CORA Cork Open Research Archive
Cartlann Taighde Oscailte Chorcaí

Title	Development and characterisation of solution processed vanadium oxide and transparent metal oxide thin films
Authors	Glynn, Colm
Publication date	2015
Original Citation	Glynn, C. 2016. Development and characterisation of solution processed vanadium oxide and transparent metal oxide thin films. PhD Thesis, University College Cork.
Type of publication	Doctoral thesis
Rights	© 2015, Colm Glynn. - http://creativecommons.org/licenses/by-nc-nd/3.0/
Download date	2026-11-15 11:45:31
Item downloaded from	https://hdl.handle.net/10468/3377



UCC
University College Cork, Ireland
Coláiste na hOllscoile Corcaigh

Development and Characterisation of Solution Processed Vanadium Oxide and Transparent Metal Oxide Thin Films



A thesis presented for the degree of Doctor of Philosophy to the National University of Ireland, Cork

By

Colm Glynn, M.Sc.

Department of Chemistry

University College Cork, Ireland

December 2015

Supervisor

Dr Colm O'Dwyer

Declaration

I, Colm Glynn, hereby confirm that the work presented in this thesis is my own research, carried out under the direction of Dr Colm O'Dwyer and due reference has been made, where necessary, to work of other authors. No part of this thesis has been previously submitted to this or any other university.

Signed

_____

Colm Glynn

Dedicated to the three people who believed in me and

supported me unconditionally over the past four years

My parents,

Assumpta and MacDara

And my fiancé

Dawn

Acknowledgements

I would first like to thank and acknowledge the great help that my supervisor Dr. Colm O'Dwyer has been to me throughout my PhD. The enthusiasm he showed for my research coupled with his experience and knowledge of the area was irreplaceable. I also wish to thank the Irish Research Council for funding my PhD.

I would like to thank the administration and technical staff of the Chemistry Department in UCC for their help throughout the years. I would like to especially thank Dr. Trevor Carey and Dr. Ian O'Connor for their support and providing me experience with laboratory demonstration.

I would like to thank all of the research, academic and technical staff who I met during my time in the University of Limerick and the Materials and Surface Science Institute.

I thank all of the current and past members of the Applied Nanoscience Group, in particular Eileen, Will, Michal, Darragh and Sally. I wish to especially thank Elaine, my next door neighbour in the office during both my time in UL and UCC, you have always been supportive and helped me to keep to my strict diet of coffee! My deepest thanks to both of our postdocs, Dr. Hugh Geaney and Dr. David McNulty both of whom endured my random requests to image the most awkward of samples.

To all of my lab colleagues in labs 115 and 343 I wish to thank you all for your welcome when I joined the department, each and every one of you made me feel a part of the community. Special thanks to John O'Connell and Timothy Collins for all of their help with XPS and AFM throughout the years.

I want to thank my collaborators in the Centre de Spectroscopie at the Institut Lavoisier de Versailles in France in particular Damien Aureau.

My family have supported me in every way throughout my PhD and I wish to express just how thankful I am to them. My brothers Macdara, Ciaran and my sister Caitriona, each of you has helped me through the years and I thank you, I also want to thank Elaine and James for their support in the short times that we can spend time together. To my parents, Assumpta and MacDara, I have no words that can express my thanks for all that you have done to help, encourage and support me for my whole academic career, without you I would not be where I am today. I am who I am because of both of you and for that I will be eternally thankful and only wish that I can repay the kindness and support that you have always given me.

Finally I would like to thank my fiancé Dawn, you have supported and cared for me during the good and bad times over the past four years and you have always been my rock, when I am with you I can weather the worst storms.

Abstract

Metal oxide thin films are important for modern electronic devices ranging from thin film transistors to photovoltaics and functional optical coatings. Solution processed techniques allow for thin films to be rapidly deposited over a range of surfaces without the extensive processing of comparative vapour or physical deposition methods. The production of thin films of vanadium oxide prepared through dip-coating was developed enabling a greater understanding of the thin film formation. Mechanisms of depositing improved large area uniform coverage on a number of technologically relevant substrates were examined. The fundamental mechanism for polymer-assisted deposition in improving thin film surface smoothness and long range order has been delivered. Different methods were employed for adapting the alkoxide based dip-coating technique to produce a variety of amorphous and crystalline vanadium oxide based thin films. Using a wide range of material, spectroscopic and optical measurement techniques the morphology, structure and optoelectronic properties of the thin films were studied. The formation of pinholes on the surface of the thin films, due to dewetting and spinodal effects, was inhibited using the polymer assisted deposition technique. Uniform thin films with sub 50 nm thicknesses were deposited on a variety of substrates controlled through alterations to the solvent-alkoxide dilution ratios and employing polymer assisted deposition techniques. The effects of polymer assisted deposition altered the crystallized VO thin films from a granular surface structure to a polycrystalline structure composed of high density small in-plane grains. The formation of transparent VO based thin film through Si and Na substrate mediated diffusion highlighted new methods for material formation and doping.

Publications from this Thesis

- Glynn, C.; Thompson, D.; Paez, J.; Collins, G.; Benavente, E.; Lavayen, V.; Yutronic, N.; Holmes, J. D.; Gonzalez, G.; O'Dwyer, C. Large directional conductivity change in chemically stable layered thin films of vanadium oxide and a 1D metal complex. *J. Mater. Chem. C* **2013,** *1*, 5675-5684.
- Glynn, C.; Creedon, D.; Geaney, H.; Armstrong, E.; Collins, T.; Morris, M. A.; O'Dwyer, C. Linking Precursor Alterations to Nanoscale Structure and Optical Transparency in Polymer Assisted Fast-Rate Dip-Coating of Vanadium Oxide Thin Films. *Sci. Rep.* **2015,** *5*, 11574.
- Glynn, C.; Creedon, D.; Geaney, H.; O'Connell, J.; Holmes, J. D.; O'Dwyer, C. Optimizing Vanadium Pentoxide Thin Films and Multilayers from Dip-Coated Nanofluid Precursors. *ACS Appl. Mater. Interfaces* **2014,** *6*, 2031-2038.
- Glynn, C.; Aureau, D.; Collins, G.; O'Hanlon, S.; Etcheberry, A.; O'Dwyer, C. Solution processable broadband transparent mixed metal oxide nanofilm optical coatings via substrate diffusion doping. *Nanoscale* **2015**, *7*, 20227-20237.
- O'Hanlon, S.; Glynn, C.; O'Dwyer, C. Effect of Annealing on the Development of Fully Transparent Ternary V-O-Na-Si Mixed Metal Oxide Thin Films from Polymer-Assisted Dip-Coated V_2O_5. *ECS J. Solid State Sci. Technol.**5***, R3100-R3106 (2015).
- Glynn, C.; Aureau, D.; O'Hanlon, S.; Daly, L.; Geaney, H.; Collins, G.; Etcheberry, A.; O'Dwyer, C. Precursor Concentration and Substrate Effects on High Rate Dip-Coated Vanadium Oxide Thin Films. *ECS Trans.* **2015,** *64*, 1-9.
- Glynn, C.; Osiak, M.; McSweeney, W.; Lotty, O.; Jones, K.; Geaney, H.; Quiroga-González, E.; Holmes, J. D.; O'Dwyer, C. (Invited) Semiconductor Nanostructures for Antireflection Coatings, Transparent Contacts, Junctionless Thermoelectrics and Li-Ion Batteries. *ECS Trans.* **2013,** *53*, 25-44.

Poster Presentations

- Uniform Thin Films of Vanadium Pentoxide from Dip-Coating, MRS Spring Meeting 2014, San Francisco, United States, April 10th 2014.
- Heterogeneous Nucleation Effects during Vanadium Pentoxide Thin Films Formed from an Alkoxide Precursor, MRS Spring Meeting 2014, San Francisco, United States, April 10th 2014.
- Evolution of Electro-Optic and Crystallinity Correlation in Dip-Coated Thin Films of Vanadium Oxide, Tyndall National Institute Postgraduate Student Poster Competition, August 26th 2015.
- Evolution of Electro-Optic and Crystallinity Correlation in Dip-Coated Thin Films of Vanadium Oxide, Institute of Physics Ireland Spring Meeting, Cork, Ireland, March 28th 2015.
- Heterogeneous Nucleation Effects during Vanadium Pentoxide Thin Films Formed from an Alkoxide Precursor, Institute of Physics Ireland Spring Meeting, Dun Laoghaire, 8th March 2014.
- Heterogeneous Nucleation Effects during Vanadium Pentoxide Thin Films Formed from an Alkoxide Precursor, Tyndall National Institute Postgraduate Student Poster Competition, July 24th 2014.
- Heterogeneous Nucleation Effects during Vanadium Pentoxide Thin Films Formed from an Alkoxide Precursor, The 18th Workshop on Dielectrics in Microelectronics (WODIM), June 9th 2014.

Other Publications

- Armstrong, E.; Osiak, M.; Geaney, H.; Glynn, C.; O'Dwyer, C., 2D and 3D vanadium oxide inverse opals and hollow sphere arrays. *CrystEngComm* **2014,** *16*, 10804-10815.
- Lotty, O.; Biswas, S.; Ghoshal, T.; Glynn, C.; O' Dwyer, C.; Petkov, N.; Morris, M. A.; Holmes, J. D., Containing the catalyst: diameter controlled Ge nanowire growth. *J. Mater. Chem. C* **2013,** *1*, 4450-4456.
- McSweeney, W.; Lotty, O.; Mogili, N. V. V.; Glynn, C.; Geaney, H.; Tanner, D.; Holmes, J. D.; O'Dwyer, C., Doping controlled roughness and defined

mesoporosity in chemically etched silicon nanowires with tunable conductivity. *J. Appl. Phys.* **2013,** *114*, 034309.

- McSweeney, W.; Lotty, O.; Glynn, C.; Geaney, H.; Holmes, J. D.; O'Dwyer, C., The influence of carrier density and doping type on lithium insertion and extraction processes at silicon surfaces. *Electrochim. Acta* **2014,** *135*, 356-367.
- Armstrong, E.; Osiak, M.; Glynn, C.; O'Dwyer, C., Investigations into Structure and Chemistry of 1D, 2D and 3D Structured Vanadium Oxide Nanomaterials for Li-Ion Batteries. *ECS Trans.* **2014,** *58*, 3-12.
- McSweeney, W.; Glynn, C.; Geaney, H.; Collins, G.; Holmes, J. D.; O'Dwyer, C., Mesoporosity in doped silicon nanowires from metal assisted chemical etching monitored by phonon scattering. *Semicond. Sci. Technol.* **2016,** *31*, 014003.
- Quiroga-Gonzalez, E.; Carstensen, J.; Glynn, C.; O'Dwyer, C.; Foll, H., Pore size modulation in electrochemically etched macroporous p-type silicon monitored by FFT impedance spectroscopy and Raman scattering. *PCCP* **2014,** *16,* 255-63.
- Padmanathan, N.; Shao, H.; Selladurai, S.; Glynn, C.; O'Dwyer, C.; Razeeb, K. M., Pseudocapacitance of α-$CoMoO_4$ nanoflakes in non-aqueous electrolyte and its bi-functional electro catalytic activity for methanol oxidation. *Int. J. Hydrogen Energy* **2015**.
- McSweeney, W.; Geaney, H.; Glynn, C.; McNulty, D.; O'Dwyer, C., Pseudocapacitive Charge Storage at Nanoscale Silicon Electrodes. *ECS Trans.* **2015,** *66*, 39-48.

Table of Contents

Declaration		ii
Acknowledgments		iv
Abstract		v
Abbreviation List		xiii
Chapter 1	Introduction	1
1.1	Motivation	2
1.2	Thesis Overview	4
1.3	References	7
Chapter 2	Literature Review	9
2.1	Introduction	10
2.1.1	Thin Film Technologies	12
2.1.2	Common Thin Film Deposition Techniques	14
2.1.3	Thin Film Analysis Techniques	15
2.2	Precursor Solutions	17
2.3	Deposition Techniques	20
2.3.1	Spin Coating	21
2.3.2	Dip Coating	23
2.3.3	Other Deposition Techniques	30
2.3.4	Polymer Assisted Deposition	33
2.4	Comparison of Thin Film Deposition for Vanadium Oxides	35
2.4.1	Thin Film Composition and Structure	35
2.4.2	Surface Morphologies	41
2.4.3	Optical Properties	44
2.5	Thin Film Applications and Devices	48
2.5.1	Electronic Materials	48
2.5.2	Optoelectronic Devices and Solution Processed TCOs	58
2.5.3	Miscellaneous Device Applications	70
2.6	Conclusions and Outlook	76
2.7	References	81

Chapter 3 Experimental 90
3.1 Introduction 91
3.2 Thin Film Preparation 91
3.2.1 V_2O_5 Precursor Solution Preparation 91
3.2.2 Deposition Techniques 93
3.2.3 Post-Deposition Processing 96
3.3 Analysis Techniques 97
3.3.1 Atomic Force Microscopy 97
3.3.2 Electron Microscopy 98
3.3.3 Raman Scattering Spectroscopy 99
3.3.4 Optical Spectroscopy 100
3.3.5 X-Ray Diffraction 103
3.3.6 X-Ray Photoelectron Spectroscopy 104
3.4 References 106

Chapter 4 Dip-Coated V_2O_5 Thin Film Formation 107
4.1 Introduction 109
4.2 Experimental 112
4.2.1 Precursor Synthesis 112
4.2.2 V_2O_5 Thin Film Preparation 112
4.2.3 Characterization Techniques 113
4.3 Results 113
4.3.1 V_2O_5 Drop-Casted Deposits 113
4.3.2 Thin Film Characteristics 120
4.3.3 Optical Transmission of Uniform Dip-coated Films 125
4.3.4 In-Plane HRTEM of PAD Processes in Oxide Thin Films 129
4.4 Discussion 134
4.5 Conclusions 144
4.6 References 147

Chapter 5 Optimizing V_2O_5 Dip-Coated Thin Film Depositions 150
5.1 Introduction 152
5.2 Experimental 155
5.2.1 Substrate Preparation and Deposition 155
5.2.2 Characterisation and Analysis Techniques 156

5.3 Results and Discussion 157
5.3.1 Surface Pinhole Formation 157
5.3.2 Pinhole Formation Analysis 159
5.3.3 Thin Film Structural Characterisation 164
5.3.4 Methods for Relieving Pinhole Development 168
5.4 Conclusions 170
5.5 References 173

Chapter 6 Transparent Thin Film Deposition via Substrate Diffusion Doping 176
6.1 Introduction 178
6.2 Experimental 182
6.2.1 Thin Film Deposition and Processing 182
6.2.2 Analysis Techniques 182
6.2.3 Sample Designations 183
6.3 Results and Discussion 183
6.3.1 Optical Properties of Inter-Diffusion Formed Thin Films 183
6.3.2 Inter-Diffusion Thin Film Surface Characterization 188
6.3.3 Time Dependent Inter-Diffusion Characterization 194
6.4 Conclusions 200
6.5 References 203

Chapter 7 Contact Transfer Doping of Solution Processed V-O-Na-Si Thin Films and Nanowires on Transparent Metal Oxide Substrates 206
7.1 Introduction 208
7.2 Experimental 209
7.2.1 Thin Film Formation and Processing 209
7.2.2 Analysis Techniques 210
7.3 Contact Diffusion Transfer 210
7.3.1 Deposition Process 210
7.3.2 Surface Morphology and Vibrational Spectra 212
7.3.3 HRTEM of Contact Diffusion V-O-Na-Si Surface 218
7.4 Planar Electrodeposition Formation of Na-SiO_2 and V-Na-SiO_2 222
7.4.1 Effect of Electrodeposition Voltage on Structure and Vibrational Characteristics 222

7.4.2 Thin Film Morphology of Na-SiO_2 and V-Na-SiO_2 Thin Films 227
7.5 Planar Electrodeposition Formation of SiO_2 and V-SiO_2 230
7.6 Templated Deposition of Na-SiO_2 and V-Na-SiO_2 238
7.7 Conclusions 244
7.8 References 247

Chapter 8 Conclusions 250
8.1 Introduction 251
8.2 Dip-Coated V_2O_5 Thin Film Formation 251
8.3 Optimizing V_2O_5 Dip-Coated Thin Film Depositions 252
8.4 Transparent Thin Film Deposition via Substrate Diffusion Doping 252
8.5 Contact Transfer Doping of Solution Processed V-O-Na-Si Thin Films and Nanowires on Transparent Metal Oxide Substrates 253
8.6 Summary of Conclusions 254
8.7 Future Work 256
8.7.1 Solution Processed Thin Film Device Applications 256
8.7.2 Precursor Solution Nanofluid 258
8.7.3 Advanced Electrodeposition Templating 260
8.8 References 262

Abbreviation List

AFM – Atomic Force Microscopy

ADDC – Angle Dependent Dip-Coating

AgNWs – Silver Nanowires

ALD – Atomic Layer Deposition

AlO_x – Aluminium Oxide

APCVD – Atmospheric Pressure Chemical Vapour deposition

As-Dep – As-Deposited

BE – Binding Energy

$BiFeO_3$ – Bismuth Ferrite

$BiVO_4$ – Bismuth Vanadate

BO – Bridging Oxygen

CCD – Charge Coupled Device

CMOS – Complimentary Metal-Oxide Semiconductor

Cu_2O – Copper Oxide

CVD – Chemical Vapour Deposition

DI – Deionised

DUV – Deep Ultra-Violet

EC – Electrochromic

ED – Electrodeposition

EDTA - Ethylenediaminetetraacetic acid

E_g – Optical Bandgap

EtOH – Ethanol

eV_2O_5 – Evaporated V_2O_5

FFT – Fast Fourier Transforms

FTIR – Fourier Transform Infrared Spectroscopy

FTO – Fluorine Doped Tin Oxide

FWHM – Full Width Half Maximum

H_2O – Water

HCL – Hydrochloric Acid

HCP – High Concentration Dilution

HCP-PEG – High Concentration Dilution with PEG

HTA – High Temperature Thermal Anneal

IC – Integrated Circuit

IGZO – Indium Gallium Zinc Oxide

In_2O_3 – Indium Oxide

IPA – Isopropyl Alcohol

ITA – Intermediate Temperature Thermal Anneal

ITO – Indium Doped Tin Oxide

k_C – calculated fraction of material in liquid film

k_E – estimated fraction of material in liquid film

$LaAlO_3$ – Lanthanum Aluminate

LCO – Lithium Cobalt Oxide

LCP – Low Concentration Dilution

LCP-PEG – Low Concentration Dilution with PEG

LED – Light Emitting Diode

LiCl – Lithium Chloride

Li-CVD – Liquid Injection Chemical Vapour Deposition

LTA – Low Temperature Thermal Anneal

LTO – Lithium Titanate

MIM – Metal Insulator Metal

MIT – Metal-Insulator Transition

MoO_x – Molybdenum Oxide

MOS – Metal Oxide Semiconductor

Na_2O – Sodium Oxide

$NaNO_3$ – Sodium Nitrate

$NaVO_3$ – Sodium Vanadate

NBO – Non-Bridging Oxygen

NEXAFS – Near Edge X-Ray Absorption Fine Structure

NIR – Near Infrared Light

NP – Nanoparticles

OT – Total Oxygen

P3HT - Poly(3-hexylthiophene-2,5-diyl)

PAD – Polymer Assisted Deposition

PEDOT:PSS - poly(3,4-ethylenedioxythiophene)

PEG – Polyethylene Glycol

PEI – Polyethylenimine

PET – Polyethylene Terephthalate

PI - Polyimide

PMMA - Poly(methyl methacrylate)

PVD – Physical Vapour Deposition

RMS – Root Mean Square

RPM – Revolutions per Minute

SAXS – Small Angle X-Ray Scattering

SEM – Scanning Electron Microscopy

Si_3N_4 – Silicon Nitride

SiO_2 – Silicon Dioxide

$SrTiO_3$ – Strontium Titanate

sV_2O_5 – Solution Processed V_2O_5

TCO – Transparent Conducting Oxide

TEM – Transmission Electron Microscopy

TEOS - Tetraethyl Orthosilicate

TFT – Thin Film Transistor

TiO_2 – Titanium Dioxide

TO – Transparent Oxide

TTF – Transparent Thin Film

TTFT – Transparent Thin Film Transistor

UHV – Ultra High Vacuum

UV – Ultraviolet

V_2O_3 – Vanadium Trioxide

V_2O_5 – Vanadium Pentoxide

VBM – Valence Band Maximum

VCL_3 – Vanadium Chloride

Vis – Visible Light

VISG – Vanadium Oxide Inorganic Precursor Solution

VNA – Vanadium Oxide Metallo Organic Precursor Solution

VO – Vanadium Oxide

VO_2 – Vanadium Dioxide

VONTs – VO_x Nanotubes

VOSG – Vanadium Oxide Organic Precursor Solution

WO_3 – Tungsten Oxide

XAS – X-Ray Absorption Spectroscopy

XPS – X-Ray Photoelectron Spectroscopy

XRD – X-Ray Diffraction

YO_x – Yttrium Oxide

ZAO – Zr Incorporated Aluminium Oxide

ZIO – Zinc Indium Oxide

ZnO – Zinc Oxide

ZnSnO – Zinc Tin Oxide

ZrO_x – Zirconium Oxide

Chapter 1

Introduction

1.1 Motivation

Thin films are a fundamental building block of modern devices and coatings.[1] Different types of thin films, with varied morphologies and materials, have uses in a large range of industries, from microelectronics[2] and optics[3] to energy generation[4]/storage[5]. Many materials can be deposited with thin film morphologies and a large range of deposition techniques are available. Thin films of metals[6], polymers[7] and metal oxides[1] can be deposited with various surface morphologies and structures. The techniques used for the formation of these thin films ranges from physical/chemical vapour depositions[8], sputtering[9] and solution processed methods.[10]

Metal oxides are a large range of materials with many applications possible. Metal oxides can be deposited with a number of different morphologies, from nanowires[11-12], nanoparticles[13], inverted opals[14-15] to free standing structures and thin films.[16] As with the above examples for thin film uses, metal oxides also see use for a range of applications, from energy storage/generation[17], electronics[18] to catalysis[19] and sensors.[20]

The deposition of metal oxides into thin film morphologies is an integral part of modern technology. The development of devices such as thin film transistors (TFTs), transparent thin film transistors (TTFTs), anti-reflection coatings, photovoltaics and optical coatings has impacted on the day to day life of the population and their use increases annually. As the demand increases each year for more advanced, smaller and, most importantly, cheaper consumer electronics, the preparation of the devices that make up the desired products must be stepped up in both scale and complexity without increasing cost. In order to achieve this, the improvement in control of solution processed deposition techniques and ways to control composition and doping and the associated changes in physical properties, is

envisaged to alleviate the reliance on sputtering, chemical/vapour assisted deposition, and atomic layer deposition techniques for some technologies.[1, 10]

Solution processed deposition techniques comprises a variety of methods that utilise liquid precursor solutions. These precursor solutions are prepared from a number of different precursors, such as nitrates, alkoxides and carboxylates.[1] The solutions are then deposited on substrates through methods including but not limited to dip-coating,[21] spin coating,[22] ink-jet printing[23] and spray pyrolysis.[24] The benefit of solution processed techniques can be attributed to the availability of low cost precursors and the versatility of the deposition techniques in rapidly depositing thin films of different thicknesses and morphologies over large surface areas.

Solution processed deposition techniques have historically suffered from detrimental deposition aspects; the difficulty in depositing complex morphologies and structures at large production scales required by the semiconductor industry is one of most difficult hurdles which must be surpassed. In recent years, strides have been made in the improvement of deposition selectivity for increasingly complex thin film devices using solution processed techniques.[25-27] These improvements have been achieved through research on the characteristics and deposition limitations of the different precursor solutions and deposition techniques available. Through research into these two aspects of the deposition, new methodologies and techniques have been developed for the production of state of the art devices using solution processed methods.[28-30]

The motivation of this thesis was to understand the processes behind vanadium pentoxide (V_2O_5) thin film formation from alkoxide-based precursors using a dip-coating technique and to link the nature of the physical effects that occur during dip-coating to the thin film structure, chemical composition, and optical

properties. By attaining a greater understanding of these processes, the goal was to develop and adapt dip-coating and control uniformity via viscosity by polymer-assisted deposition, and to find new ways of doping and controlling the optical transparency, morphology and composition of reproducible, highly uniform thin films of V_2O_5 and mixed metal oxide optical coatings on a range of technologically relevant substrates.

1.2 Thesis Overview

In **Chapter 2**, a review of the primary literature and current state of the art of solution processed deposition of metal oxide thin films is introduced and discussed. A selection of precursor solutions and solution processed deposition techniques are highlighted and examples are given of research currently being conducted within this field up to the present day. Particular emphasis is given to the fundamental research and applications of V_2O_5 deposition methods and materials from solar cells and sensors, to electronic materials and optical/electrochromic films, and their uses in modern devices. Examples are also summarised on thin film materials, structures and designs researched for electronic, optical and energy storage/generation applications in general, from solution-based methods.

The various experimental procedures conducted for the work of this thesis is provided in **Chapter 3**. An overview of the different analysis methods and techniques is also included.

Chapter 4 examines the deposition of V_2O_5 thin films on transparent substrates. The alterations to the precursor solution concentration and choice of additive were related to thin film optical, structural and morphological

characteristics. Detailed comparisons were made between the formation of the dip-coated thin films to bulk, drop-cast thick films, and to polymer-assisted coated thin films. The effect of solvent-alkoxide dilution on the structure and optoelectronic properties and crystallinity of thin films is also presented. Modelling of the thin film formation using a withdrawal speed within the fast-rate draining regime and its relation to precursor parameters is provided. Finally, the link between coating method and structure is determined through optical transmission and UV-vis spectroscopy.

In **Chapter 5**, the spinodal and dewetting processes governing pinhole formation on the surface of high-rate dip-coated V_2O_5 thin films from liquid precursors was investigated. The evolution of uniform thin film growth from hydrolysis and evaporation processes was analysed and related to the effects governing nanofluid liquid formation and the retardation of dewetting. Methods for halting the pinhole defect formation are also examined.

The preparation of a V-O-Na-Si transparent thin film (TTF) through inter-diffusion processes at the thin film-substrate interface is investigated in **Chapter 6**. The formation of a crystalline α-$NaVO_3$ material enclosed within a glassy matrix through thermal inter-diffusion processes was examined using a range of techniques including Raman scattering spectroscopy and X-Ray photoelectron spectroscopy. The TTF is shown to have a high broadband transparency across the UV-NIR spectral range while retaining uniform substrate coverage with low root-mean square (rms) surface roughness. The rate of inter-diffusion in the formation of the TTF was investigated through a time-dependent thermal treatment study.

In **Chapter 7**, methods for the deposition and formation of V-O-Na-Si materials by contact diffusing transfer is demonstrated on substrates with diffusion

barrier coatings such as FTO. A contact-diffusion technique was developed to form transparent mixed metal oxide thin films and nanowire networks of a transparent mixed metal oxide. Electrodeposited Na-SiO_2 and SiO_2 films onto conductive substrates served as ionic sources, allowing the conversion of dip-coated V_2O_5 with the TTF materials being prepared through subsequent dip-coating and thermal treatment enabled inter-diffusion. The resulting TTF material did not have as high a transparency as those prepared through inter-diffusion on the surface of borosilicate glass, however, methods for the templating of the TTF was investigated using custom 3D printed templates.

The significant conclusions of the thesis are presented in **Chapter 8** and a range of experiments are postulated for future work in this area.

1.3 References

1. Schneller, T.; Waser, R.; Kosec, M.; Payne, D., *Chemical Solution Deposition of Functional Oxide Thin Films*. 1st ed.; Springer: London, 2013; p 796.
2. Franklin, A. D. Nanomaterials in transistors: From high-performance to thin-film applications. *Science* ***349***, (2015).
3. Manning, T. D. *et al.* Intelligent Window Coatings: Atmospheric Pressure Chemical Vapor Deposition of Tungsten-Doped Vanadium Dioxide. *Chem. Mater.* ***16***, 744-749 (2004).
4. Boucle, J.; Ravirajan, P.; Nelson, J. Hybrid polymer-metal oxide thin films for photovoltaic applications. *J. Mater. Chem.* ***17***, 3141-3153 (2007).
5. Gaikwad, A. M.; Arias, A. C.; Steingart, D. A. Recent Progress on Printed Flexible Batteries: Mechanical Challenges, Printing Technologies, and Future Prospects. *Energy Technol.* ***3***, 305-328 (2015).
6. Jeon, G. H. Recent progress in thin film processing by magnetron sputtering with plasma diagnostics. *J. Phys. D: Appl. Phys.* ***42***, 043001 (2009).
7. Mukherjee, R. *et al.* Stability and Dewetting of Metal Nanoparticle Filled Thin Polymer Films: Control of Instability Length Scale and Dynamics. *ACS Nano* ***4***, 3709-3724 (2010).
8. Ohta, A.; Murakami, H.; Higashi, S.; Miyazaki, S. Determination of Energy Band Alignment in Ultrathin Hf-based Oxide/Pt System. *Journal of Physics: Conference Series* ***417***, 012012 (2013).
9. Ohta, H.; Hosono, H. Transparent oxide optoelectronics. *Mater. Today* ***7***, 42-51 (2004).
10. Pasquarelli, R. M.; Ginley, D. S.; O'Hayre, R. Solution processing of transparent conductors: from flask to film. *Chem. Soc. Rev.* ***40***, 5406-5441 (2011).
11. Jiang, J. *et al.* Recent Advances in Metal Oxide-based Electrode Architecture Design for Electrochemical Energy Storage. *Adv. Mater.* ***24***, 5166-5180 (2012).
12. O'Dwyer, C. *et al.* Bottom-up growth of fully transparent contact layers of indium tin oxide nanowires for light-emitting devices. *Nat. Nano.* ***4***, 239-244 (2009).
13. Ming, J. *et al.* Assembling metal oxide nanocrystals into dense, hollow, porous nanoparticles for lithium-ion and lithium-oxygen battery application. *Nanoscale*, (2013).
14. Armstrong, E.; O'Dwyer, C. Artificial opal photonic crystals and inverse opal structures - fundamentals and applications from optics to energy storage. *J. Mater. Chem. C* ***3***, 6109-6143 (2015).
15. Armstrong, E. *et al.* 2D and 3D vanadium oxide inverse opals and hollow sphere arrays. *CrystEngComm* ***16***, 10804-10815 (2014).
16. O'Dwyer, C.; Sotomayor Torres, C. Epitaxial growth of an antireflective, conductive, graded index ITO nanowire layer. *Front. Phys.* ***1***, (2013).
17. Osiak, M.; Geaney, H.; Armstrong, E.; O'Dwyer, C. Structuring materials for lithium-ion batteries: advancements in nanomaterial structure, composition, and defined assembly on cell performance. *J. Mater. Chem. A* ***2***, 9433-9460 (2014).
18. Fortunato, E.; Barquinha, P.; Martins, R. Oxide Semiconductor Thin-Film Transistors: A Review of Recent Advances. *Adv. Mater.* ***24***, 2945-2986 (2012).
19. Freund, H.-J.; Pacchioni, G. Oxide ultra-thin films on metals: new materials for the design of supported metal catalysts. *Chem. Soc. Rev.* ***37***, 2224-2242 (2008).
20. Beke, S. A review of the growth of V_2O_5 films from 1885 to 2010. *Thin Solid Films* ***519***, 1761-1771 (2011).

21. Brinker, C. J.; Frye, G. C.; Hurd, A. J.; Ashley, C. S. Fundamentals of sol-gel dip coating. *Thin Solid Films* ***201***, 97-108 (1991).
22. Emslie, A. G.; Bonner, F. T.; Peck, L. G. Flow of a Viscous Liquid on a Rotating Disk. *J. Appl. Phys.* ***29***, 858-862 (1958).
23. Calvert, P. Inkjet Printing for Materials and Devices. *Chem. Mater.* ***13***, 3299-3305 (2001).
24. Faber, H. *et al.* Indium Oxide Thin-Film Transistors Processed at Low Temperature via Ultrasonic Spray Pyrolysis. *ACS Appl. Mater. Interfaces* ***7***, 782-790 (2015).
25. Krebs, F. C. Fabrication and processing of polymer solar cells: A review of printing and coating techniques. *Sol. Energy Mater. Sol. Cells* ***93***, 394-412 (2009).
26. Si Joon, K.; Seokhyun, Y.; Hyun Jae, K. Review of solution-processed oxide thin-film transistors. *Jpn. J. Appl. Phys.* ***53***, 02BA02 (2014).
27. Choi, H. W.; Zhou, T.; Singh, M.; Jabbour, G. E. Recent developments and directions in printed nanomaterials. *Nanoscale* ***7***, 3338-3355 (2015).
28. Lu, L.; Xu, T.; Jung, I. H.; Yu, L. Match the Interfacial Energy Levels between Hole Transport Layer and Donor Polymer to Achieve High Solar Cell Performance. *J. Phys. Chem. C*, (2014).
29. Costa, C.; Pinheiro, C.; Henriques, I.; Laia, C. A. T. Inkjet Printing of Sol–Gel Synthesized Hydrated Tungsten Oxide Nanoparticles for Flexible Electrochromic Devices. *ACS Appl. Mater. Interfaces* ***4***, 1330-1340 (2012).
30. Park, S. *et al.* In-Depth Studies on Rapid Photochemical Activation of Various Sol–Gel Metal Oxide Films for Flexible Transparent Electronics. *Adv. Func. Mater.* ***25***, 2807-2815 (2015).

Chapter 2

Literature Review: Solution Processed Thin Films

2.1 Introduction

A metal oxide thin film is composed of a deposit of material with a continuous and defined thickness over the entire sample. The thicknesses can range from nanometres (nm) to microns (μm) depending upon the desired application. Modern devices and technologies incorporating metal oxide thin films rely on new and improved methods for their deposition.[1] New thin film device architectures and materials are investigated each year resulting in an associated increase in the range of applications available.[2] This increase in metal oxide thin film applications is reliant on cost-effective large scale deposition. The deposition of thin films for intricate devices, such as those in the semiconductor industry, has traditionally been performed using sputtering and evaporation methods coupled with some solution processed techniques. Solution processed techniques, where thin films are deposited from a precursor solution using a range of liquid deposition methods, are commonly used in the semiconducting industry for the deposition of resists.[3] The application of solution processed methods for the deposition of large-scale thin films devices is being investigated.[1-2, 4-5]

In applications requiring precise device architectures on the x-y-z scale, as in most CMOS technologies, the use of solution processed techniques may not be competitive to currently employed methods. In contrast, many emerging technologies require thin film surfaces with high surface uniformity and controllable morphologies over large areas, an area in which solution processed techniques excel. The large scale deposition of uniform thin films is useful in particular for many applications including thin film transistors (TFT's),[6-7] photovoltaics[8-9] and optical coatings.[10] An infographic on the various steps involved in depositing solution processed thin films is presented in Figure 2.1. The infographic outlines the three

different steps that will be discussed in detail in this work. The three steps required for solution processed depositions are: precursor selection/preparation, deposition method and the thin film application.

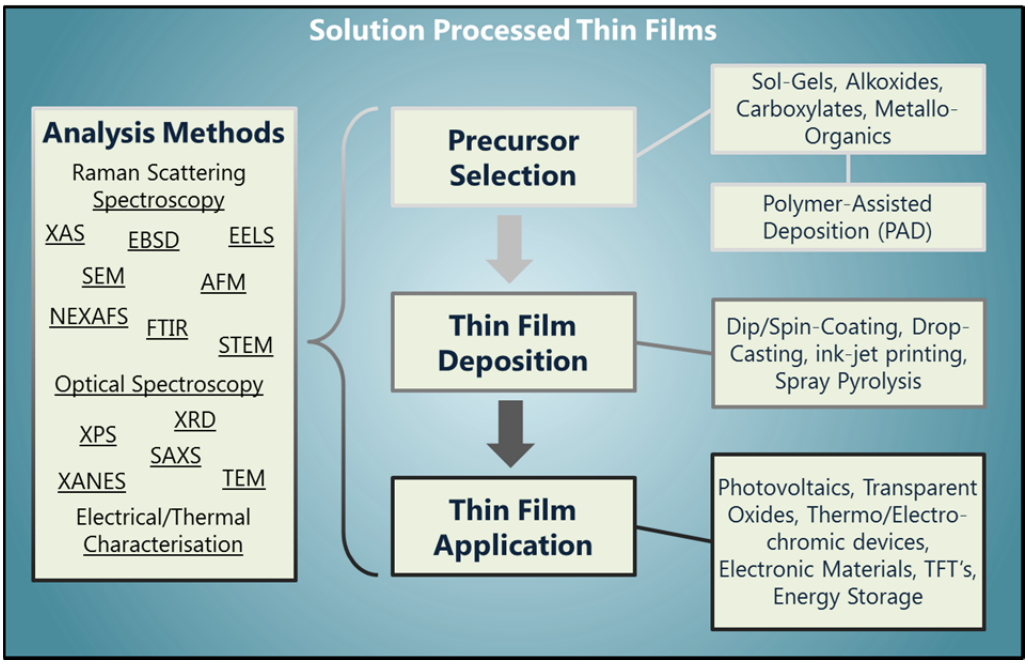


Figure 2.1. The different steps involved for the deposition of thin films through solution processed techniques. Each of the steps is outlined in the different sections of this work.

In order to produce thin films using solution processed techniques, a suitable liquid precursor must first be chosen and synthesised. These liquid precursors can be prepared using a variety of methods, from complex synthesis techniques to facile solution mixtures. Many types of precursors can be used, ranging from alkoxide/carboxylate derivatives, sol-gel mixtures to metallo-organic complexes.[1] It is important that both the chosen precursor solution and deposition method complement each other; the precursor solution can determine the most suitable deposition method. The reverse scenario is also true, where the chosen deposition method determines the best precursor solution. To complement the large variety of different liquid precursors, there are many different solution processed deposition

methods available. These deposition methods each have their own benefits and drawbacks, particularly when depositing on different substrates with varied morphologies and surface energies. Different deposition techniques each have their own strengths and weaknesses depending upon the size, shape and desired coverage of the substrate.

Further integration of solution processed thin film technologies for large-scale applications depends upon the range of thin film materials and morphologies that can be deposited. To determine the thin films composition, crystal structure, morphology and electronic/optical properties a large variety of different analysis methods can be used.[1] Thin film analysis methods are improving, with new techniques being investigated and adapted for examining a wide range of attributes that are required for characterising new thin films. Further development into analysis methods which probe the composition, morphology and application of new thin films is of interest, particularly methods that can increase throughput. In this work the different steps involved in the deposition of metal oxide thin films through solution processed methods is discussed. The range of materials and techniques involved are outlined and their advantages/disadvantages are examined. The focus of this work is to outline the ongoing work involved in the production of solution processed metal oxide thin films for cost-effective deposition of modern devices and materials.

2.1.1 Thin Film Technologies

Metal oxide thin films can be used in a wide range of applications due to the range of different materials available.[1] Device architecture design can be employed

to exploit different thin film material characteristics. The schematic in Figure 2.2 shows three possible uses of a thin film material where the intercalative, electrical or optical properties of the deposited material can be utilised for different applications. A material with favourable intercalative, electrical and optical properties, such as vanadium oxides (VO), can be used in a variety of applications due to their large range of structural and oxidative states.[11-12] Electrical properties of thin film metal oxides can be exploited for their use in modern TFT, CMOS technology and as dielectrics in the IC industry.[6, 13-14] The optical characteristics of many metal oxides are important for use in optical absorbing materials and as antireflective coatings.[10, 15-17]

Currently, an exciting area of research for thin film metal oxides is in the utilisation of the optical and electrical properties of a material in optoelectronic applications and devices. Metal oxide thin films are used in both regular and polymer thin film photovoltaic devices, where they can be utilised as different components within the devices: from the transparent conducting oxide (TCO) layer to the buffer/window and electron/hole transport layers.[9, 18-19] Other devices which utilize both the metal oxides optical and electrical properties include electro/thermo-chromic materials,[20] self-cleaning surfaces,[10] and for sensors, optics and photo-electrochemical/catalytic devices for water splitting.[21-22]

The application of metal oxide thin films in modern technology and devices is an important avenue of research. This work studies the various deposition and analysis techniques used for understanding the formation and characteristics of solution processed metal oxide thin films. Through fundamental thin film analysis both during and after deposition, and methods to control the relationship between

composition, growth and physical properties, the incorporation of thin films in modern technologies can be further improved.

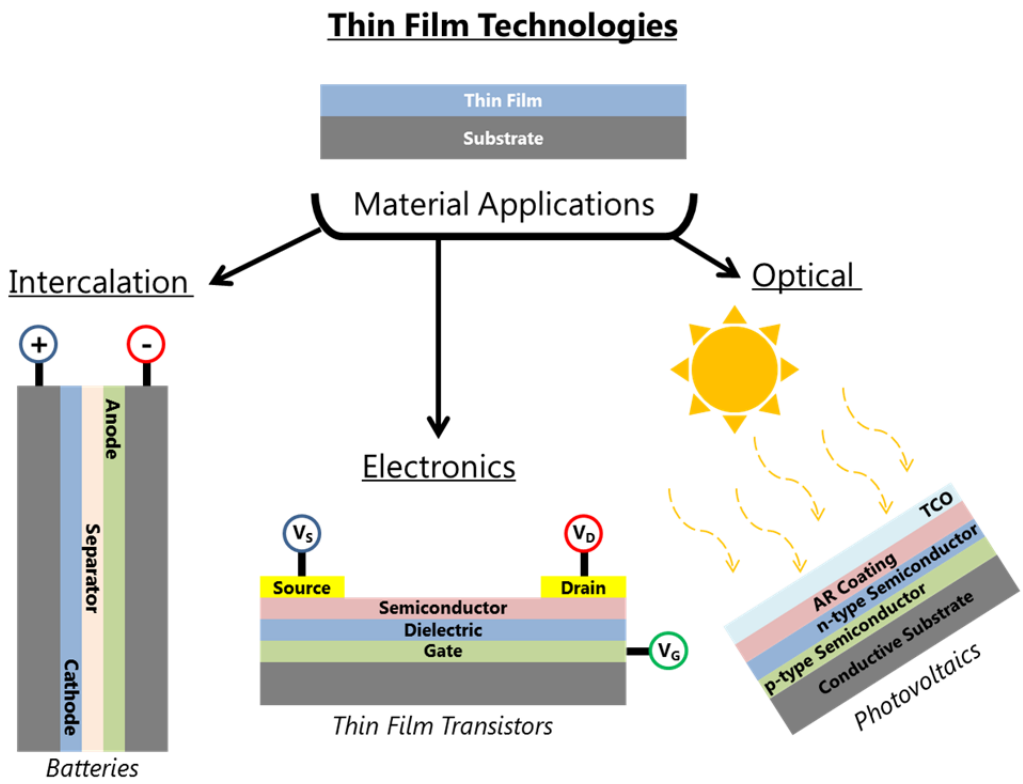


Figure 2.2. Examples of different applications exploiting a thin film materials intercalative, electronic and optical properties through different device architectures.

2.1.2 Common Thin Film Deposition Techniques

There are many types of deposition methods available for metal oxide thin films, ranging from physical (PVD)[23] and chemical (CVD)[24] vapour deposition, atomic layer deposition (ALD),[25] and solution deposited techniques.[1] The benefits and drawbacks for each of the deposition techniques can be discussed in terms of their cost, scalability, surface adhesion and coverage, the reproducibility of depositions and the types of substrate that can be used.

The thin films produced from physical vapour techniques, namely those based on sputtering of a metal target both in vacuum and under a variety of gases,

are known to have better control over the thickness and surface morphology of the thin films.[26] Physical vapour deposition techniques, such as magnetron sputtering, can deposit crystalline thin films at low substrate temperatures.[26] The crystallinity can be controlled by adjustment of the plasma energy of the sputtering system.[23]

Other methods of thin film deposition include ALD, which deposits a material by sequential atomic layer-on-layer growth by reaction of precursors at a surface.[27] Using ALD, a very uniform thin film can be deposited on the surface of a substrate with precise control of the thickness. The drawbacks to the technique are mainly due to the high cost of the apparatus and the slow sample throughput due to the number of deposition steps involved in depositing a thin film with increased thickness. The primary drawback is the cost per layer for expensive precursors, and advancements in ALD rely on alternative precursor development. Further improvements on this technique can be obtained through the adoption of a vapour based technique and using atomic vapour deposition (AVD), which is commonly known as liquid injection vapour chemical vapour deposition (Li-CVD).[28]

2.1.3 Thin Film Analysis Techniques

There is a large and diverse range of techniques available for the analysis of thin film materials, which are listed in Figure 2.1. These techniques are used for analysing the thin film structure and morphology as well as the optical, magnetic, electrical, thermal properties of the materials and devices prepared. Using increasingly sophisticated techniques, such as synchrotron radiation based methods, many analytical methods are being adapted for ex-/in-situ analysis of thin films during deposition and also the treatment steps of the process.[29-31] The in-situ

techniques allow for the mechanism of thin film formation to be studied in increased detail. Through better knowledge of the formation mechanisms, the deposition processes can be tailored to further increase the efficiency of deposition while maintaining the thin film compositional purity.

Determining a thin films' composition and crystal structure is one of the first and most important analytical steps. The chemical composition and crystallinity of a thin film material is important for ensuring the characteristics of the thin film fit the desired application. for instance, vanadium pentoxide (V_2O_5) and vanadium dioxide (VO_2) have distinct structural, thermal and electrical characteristics, and may take unique crystal structures for a large range of oxidation states, i.e. V_nO_{2n-1} and V_nO_{2n+1}, among many others. These different characteristics make each of the materials beneficial for different applications, such as gas sensors and optical absorbers.[32-34] A wide range of techniques for analysing thin film material structure are currently available. For a crystalline thin film, one of the most common methods is X-ray diffraction, where the diffraction of incident X-ray beams from a crystalline lattice can be used to identify the crystalline phase of the material.[35]

The composition and structure of a thin film can be analysed further using spectroscopy methods such as Raman scattering spectroscopy, Fourier transform infrared (FTIR) spectroscopy and X-ray photoelectron spectroscopy (XPS). Raman scattering provides vibrational data on the chemical bonds within a thin films structure. Due to the high sensitivity of the Raman scattering technique, thin films can be characterised and fingerprinted to other materials. Small changes to the thin films structure, such as size effects, morphology and intercalation or doping with other materials, can be examined both ex- and in-situ using Raman scattering spectroscopy.[36-37] A common technique to compliment Raman scattering

spectroscopy is FTIR, which measures the infrared absorption spectrum for a thin film in the near-, mid- and far-infrared region. FTIR can be used for chemical fingerprinting of the material while also providing information on changes to bond order and organic-inorganic interactions, for example.[10] One of the major benefits to techniques such as Raman scattering spectroscopy and FTIR is that they are not limited by the crystallinity of a material; both crystalline and amorphous structures can be probed using these techniques assuming that active modes are present in the structure. Absorption in the ultraviolet and visible wavelength ranges can also be examined using UV-Vis spectroscopy to provide information on the optical properties of thin films, such as identifying regions of optical absorption and determining optical bandgap energies.[38-39] More advanced techniques utilising X-Ray interactions with the material, such as XPS, X-Ray absorption spectroscopy (XAS), near edge X-Ray absorption fine structure (NEXAFS) and small-angle X-Ray scattering (SAXS) can be used to further analyse the structure and composition of the thin film materials.

2.2 Precursor Solutions

Different precursor solutions are available for solution processed deposition techniques. In its simplest form, the solutions are prepared by mixing the metal oxide precursors with a suitable solvent. Various types of catalysts (materials which increase the effectiveness of the formation of the material) or inclusions may be added to the solution for providing increased control over the dissolution of the precursor with the solvent or for beneficial effects on the deposited material. The type of precursors range from metal oxide powders[40] and nitrates[41-42], generally used in preparation of colloidal-like sol-gels, to liquid precursors containing metal oxide

complexes encapsulated by organics, such as in alkoxide[43] and carboxylate[44] materials, which facilitate the formation of the deposit through formation reactions such as hydrolysis or condensation processes.

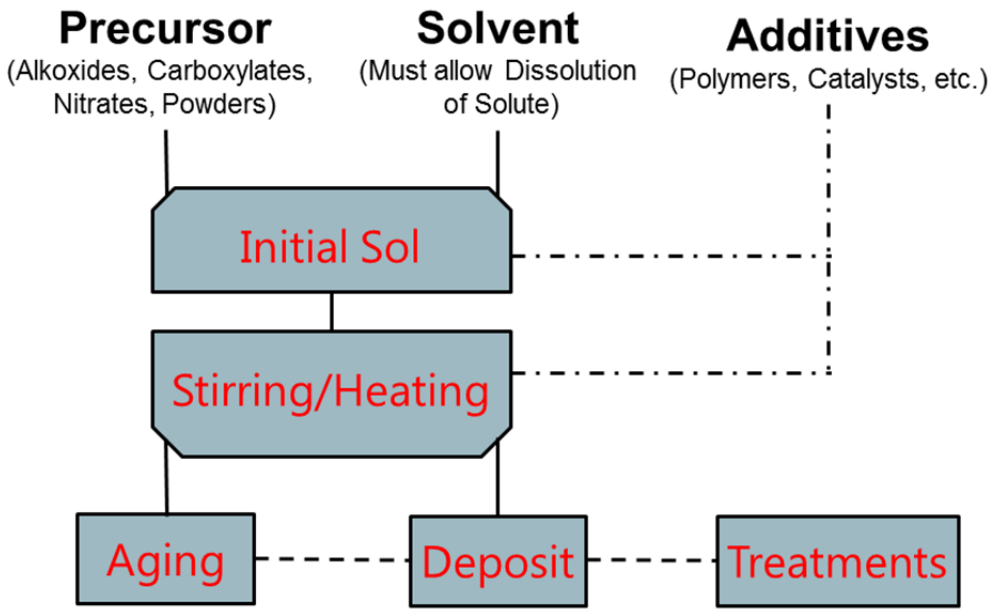


Figure 2.3. Schematic of the basic steps in preparing a solution processed precursor solution.

Figure 2.3 shows a schematic of the general steps involved in the formation of precursor solutions for a variety of solution processed techniques. In the case of alkoxide precursors, an anhydrous solvent which is generally the parent solvent of the alkoxide is added to help slow the hydrolysis reaction.[45-47] The same technique can be used for the formation of carboxylate based precursors through solvent addition.

The preparation of sols from metal oxide powders and nitrates involves the dissolution of the material with a suitable solvent with further stirring and heating required. In preparing a Zr-incorporated aluminium oxide (ZAO) thin film, Jo *et al.* dissolved both aluminium nitrate nonahydrate and zirconium(IV) acetylacetonate in 2-Mercaptoethanol (2-ME) at a variety of ratios, the solutions were then stirred for

12 h at 75 ^{o}C until the solution was clear.[48] The stirring and heating step was required for a high quality precursor solution to be prepared. This type of sol preparation is common in the literature, both with and without heating or aging steps, and is routinely used for forming materials composed of multiple metal oxides such as ZAO, IGZO etc.[41-42, 48-49]

The use of additives in solution processed techniques is not a new practice, with many different roles found in the synthesis of liquid precursor solutions for a variety of additive materials, such as acids, catalysts and polymers. One of the benefits of additives for precursor solutions is to either increase the shelf life of the solution, or to decrease the length of time for the material formation. Sanchez *et al.* discusses the effects that different additives can have on the precursor solution, such as alterations to the gelation time and improving the long term storage ability of the solution, which is of benefit due to increasing the lifetime and thus the number of depositions possible using a single batch of material.[47] Bhuiyan *et al.* discusses the use of modifying ligands, such as acetic acid or acetylacetone, which are used to chelate the alkoxides and thus reduce the sensitivity of the precursor solution to hydrolysis.[2] Bhuiyan et al. also describe how the nitrate method of precursor solution formation can be detrimental to thin film formation due to dewetting during deposition[2], however, as can be found in the literature, the detrimental effect can be overcome through the use of an additives such as ammonia.[49]

Polymer assisted deposition (PAD), has been applied to materials research since Jia *et al.* published their first paper on the subject in 2004.[50] The application of PAD in solution processed techniques involves the use of polymers to stabilise the metal precursors and increase the uniformity of the deposited thin films.[1, 50-51] PAD involves the incorporation of a polymer, originally PEI, into the solution through the

formation of additive complexes and covalent complexes between the nitrogen atoms and the metal cation as outlined by Burrell *et al*.[51] The polymer stabilises the metal complexes so that they do not experience pre-formation in the solution prior to polymer decomposition,[51] thus increasing the lifetime of the solution and encouraging the prevention of early metal oxide formation during the deposition stage.

While the precursor that comprises two solutions may be the same, the mixture ratio of the individual components, alkoxide/solvent for example, is often altered for the specific purpose of the experiment. Chen *et al.* prepared a vanadium pentoxide (V_2O_5) alkoxide precursor solution for forming thin films with an IPA-Alkoxide-H_2O mixture ratio of 76-1-19,[9] whereas the same precursor solution is also used by others at different ratios of 9-1 and 25-1.[52-53] In both cases, the end result was the formation of V_2O_5 thin films from an alkoxide precursor solution where a best-fit ratio was chosen in order to attain the desired deposit morphology.

2.3 Deposition Techniques

Choosing a precursor solution is only the first step in preparing a solution processed thin film material. As previously discussed, there are many different methods possible for depositing liquid precursors onto substrates to form a solid thin film. The range of techniques each has their own advantages and disadvantages which can depend upon the chemical and adhesion attributes of the precursor solution and the substrate. Many publications[1, 13, 54-55] have described in detail the different types of techniques available, and here, highlights of some of the most popular techniques are described together with a discussion on some of the latest

innovations that have been introduced over the years. The scope of this section also includes the deposition of other materials through solution processed methods as improvements to each technique can be applied to the deposition of metal oxide thin film materials.

2.3.1 Spin Coating

Due to the well understood processes governing the thin film formation, spin coating continues to be one of the most popular deposition techniques both within academia and industry. Figure 2.4 (a) illustrates the typical steps of the spin coating process. The precursor solution is deposited on the surface of the substrate which is held on top of a chuck within the spin coater. It is important that the solution covers the substrate surface completely prior to the spinning. The substrate is coated with solution and the spin coater accelerates rapidly to a high RPM and held at this speed for a set length of time. When the spinning is complete the thin film has been formed through a combination of liquid flow and evaporation processes. Depending on the type of precursor used the thin film may require some additional processing steps, such as heating or UV treatment, to be fully formed.

The processes involved in spin coating have undergone much experimentation and modelling so that the formation of thin films with specific as-deposited thicknesses can be formed. For most precursor solutions the as-deposited thickness of a thin film follows a general rule with regards to spin speed and duration. Figure 2.4 (b) shows a basic approximation of how changes in spin speed and duration effects film thickness; as both speed and duration increases there is an associated decrease in as-deposited thin film thickness.[2] For best results, experiments

are performed on new precursor solutions to determine the range of spin acceleration/speed/duration values required in producing a variety of thin film as-deposited thicknesses.

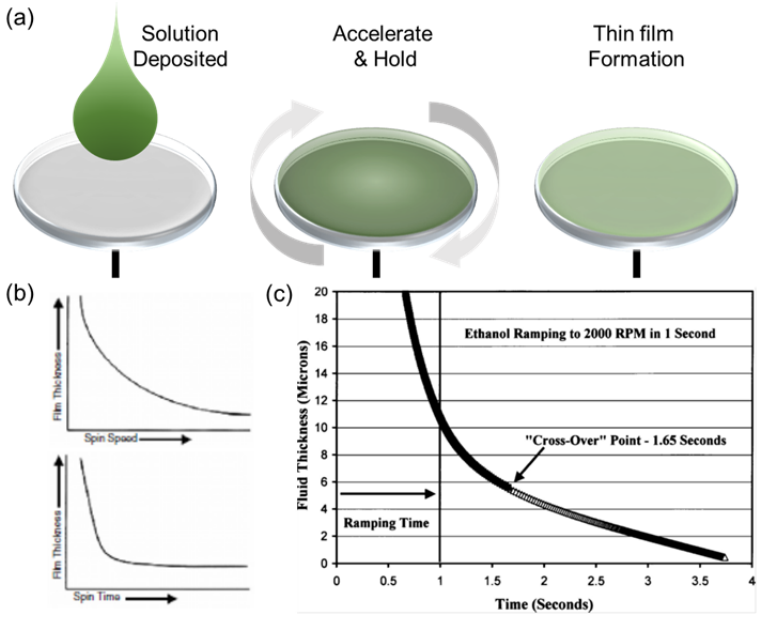


Figure 2.4. (a) Schematic of process steps involved in the formation of thin films through spin coating. (b) Graphs showing how thin film thickness is influenced by both spin speed and duration, adapted from Bhuiyan *et al.*[2] (c) How fluid of ethanol thickness evolves with respect to time at constant acceleration to 2000 RPM. The cross-over point signifies when the dominating process controlling film thickness changes from liquid flow to evaporation.[56]

The modelling of the processes involved in spin coating relies on fluid dynamics and surface interactions. The analysis of the technique is presented elsewhere in greater detail for readers that are interested in the full detail.[1, 3, 56-57] Through modelling of a solution's characteristics such as viscosity, density and evaporation rates, a model can be predicted that determines how different spin coating settings affect the as-deposited thickness of thin films. Interestingly, the analysis can also be used to determine a cross-over point during the deposition at which the dominating process controlling the thin film thickness changes. The first of the two dominating forces that determine the film thickness is the liquid flow

which can be altered by changing the acceleration and spin speed. The second dominating force is the evaporation of the precursor solution. For many of the materials discussed above in Section 2.2, the effect of evaporation would be largely due to the higher rate of evaporation compared to other solutions, particularly aqueous solutions. Figure 2.4 (c) is a plot of thickness versus time for an ethanol solution that undergoes acceleration to 2000 RPM in 1 s.[56] The analysis of Figure 2.4 (c) shows that the cross-over point is reached quickly at ~1.67 s, where after this point the thickness is dominated by evaporation effects. This analysis highlights the importance of choosing a valid ramp time, as a longer ramp time can force the cross-over point to occur during the acceleration, which could have detrimental effects on the control of uniformity and thickness of the thin film.

2.3.2 Dip Coating

The dip-coating deposition process continues to be popular for thin films on large and irregularly shaped surfaces. While the technique does not see a widespread use in the semiconductor industry as spin-coating, in part due to the amount of precursor solution initially required in the reservoir, dip-coating provides an option for many forms of material coating in industrial and academic areas. While the formation mechanism of thin films through dip-coating is well understood and characterised, high impact research is still being conducted so that the specifics of the method can be further investigated and used for more efficient depositions. While the mechanism for thin film formation continues to be investigated, moving forward there is a large demand for dip-coating techniques in forming thin films with complex and varied surface morphologies through alterations of the deposition techniques.

The experimental procedure for a normal dip-coating technique is shown in Figure 2.5 (a), where the substrate is immersed in a precursor solution and then drawn out at a controlled rate. As the substrate is removed from the solution, a liquid film forms which undergoes solvent evaporation leading to the formation of a solid thin film composed of the active agent within the precursor solution. This solid thin film can then be further processed through thermal treatments or other post-processing techniques to alter the thin film. Multiple deposition steps can be performed to prepare multi-layered thin film deposits. The thickness of the thin film is controlled primarily through changes of the withdrawal speed; however, there are also various methods available to alter the thickness such as through precursor solution alterations, varying deposition temperature and by performing the dip coating at an angle as notable examples.

In Figure 2.5 (b) a schematic produced by Brinker *et al.* shows the processes involved in thin film formation in a steady state regime.[58-59] In a steady state regime the receding drying line velocity matches the withdrawal speed. Different forces interact during steady state dip coating for forming the solid thin films which are outlined in the schematic. The forces include viscous drag, gravity, inertial forces and meniscus surface tension and gradient surface tension.[59] Through experimental design and analysis it is possible to use knowledge of the precursor solution to model the resultant thin film thickness.

A model proposed by Landau *et al.* for the deposition of a liquid film on a surface outlines how the liquid thin film is controlled by balancing the viscosity and surface tension of the material such that a continuous liquid film is formed during a constant withdrawal speed.[60] The Landau-Levich model determines that the liquid

height (h_0) is controlled by the withdrawal speed (U_0), viscosity (η), liquid density (ρ), gravity (g) and surface tension (γ) such that

$$h_0 = 0.94 \frac{(U_0\eta)^{2/3}}{\sqrt[6]{\gamma}\sqrt{\rho g}} \qquad (Eq.\ 2.1)$$

The solid thin film is then formed through evaporation, gelation and solidification of the liquid film. Therefore by manipulating the thickness of the liquid film the resulting solid thin film can be controlled. While the Landau-Levich model can be used to model the thin film thickness of a material through the solutions properties, there are other processes that must be accounted for in order for a full understanding of the thin film material to be reliably formed.

Figure 2.5 (c) shows the effect of withdrawal speed on the thickness for a variety of solution precursors. In this case, each of the solutions used ethanol as the solvent for a variety of silica and titania materials together with various acid/polymer additives for preparing the solid thin film.[61] The plot of thickness versus withdrawal speed highlights a reversal in the trend after a specific point where a higher deposition speed increases thin film thickness. Faustini *et al.* showed that this effect is due to a change in the processes that control thin film formation and solidification due to either capillary or draining forces that act on the liquid film.[61] They referred to the two stages as the capillarity/evaporation and draining/evaporation regimes, with both regimes dominating the formation of the thin film at both low and high withdrawal speeds, respectively. In the draining regime, where the Landau-Levich model dominates, the capillary forces are negligible as the withdrawal speed is high enough to negate meniscus effects. The solution wets to the surface of the substrate and excess material is drained; during the draining step, evaporation occurs, which forms the solid thin film. In the capillary regime, the thin film forms during

evaporation of the solution while it is being slowly withdrawn. The slow withdrawal results in capillary feeding from the surface tension of the solution. In this regime, the effects of viscosity and gravity coupled with the rate of evaporation influence the thickness of the thin film.[1] At intermediate withdrawal speeds a combination of capillary, draining and evaporation processes are involved, which dictate the thickness of the thin films. Faustini *et al.* also examined the effects of changes to the precursor concentration and solution temperature combined with alterations to the polymer aiding the deposition.[61]

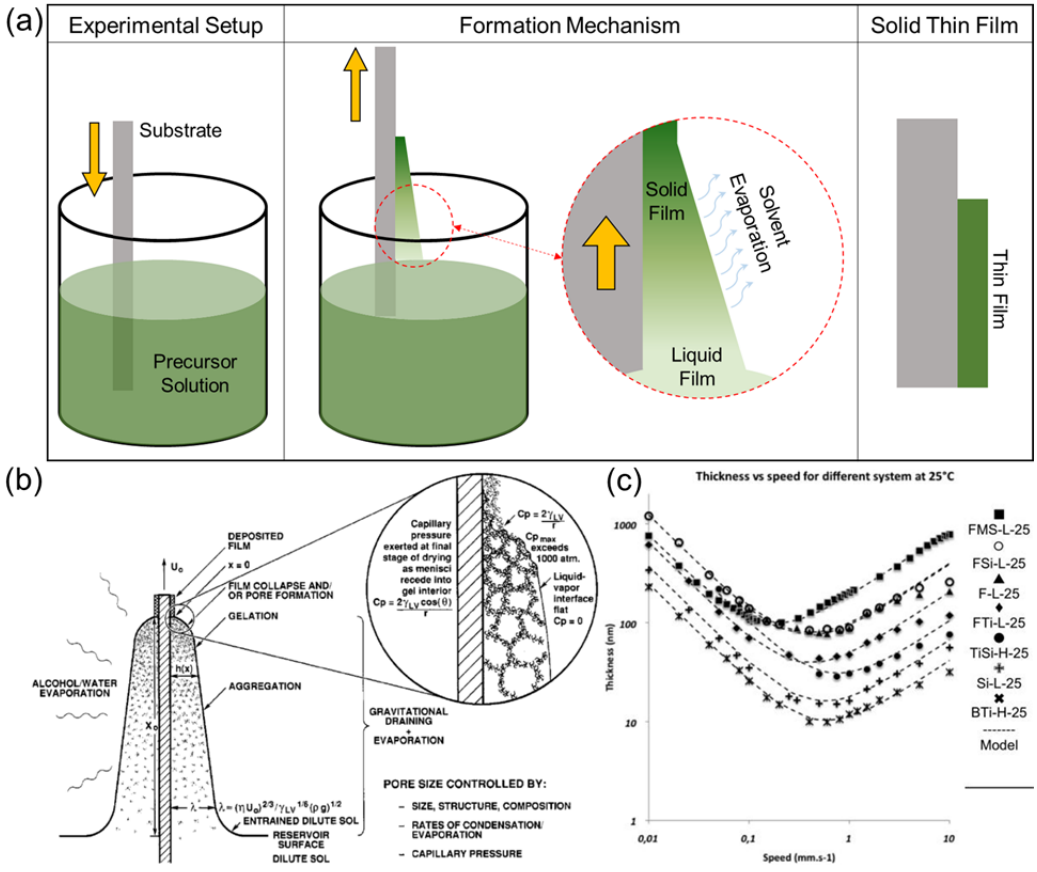


Figure 2.5. (a) Schematic of thin film formation from a dip-coating technique. The solid thin film forms through evaporation and condensation of the solvent from a dip-coated liquid film. (b) Schematic for steady state dip-coating processes showing the forces which control the thin film formation.[59] (c) Plot of thickness versus withdrawal speed, with modelled fits, for a variety of liquid precursor systems showing the characteristic trend for dip-coated thin film formation.[61]

For many dip-coating depositions an important issue must be accounted for when using many of the common precursor solutions, many of which are composed of mixtures of different components and precursors. When choosing a withdrawal rate for a new material, it is important to take into account the chemistries of the materials within the solution as large differences in the evaporation rate of different volatile additives can result in a varied formation at the drying line, where the evaporation occurs at the highest rate. When materials with different evaporation rates are mixed in a solution and dip-coated, a staggered and non-uniform film deposition can result. The staggered deposition occurs as one material evaporates prior to the other such as seen by Nishida e*t al.* where a sharp gradient was found due to a greater water content near the drying line compared to the water content of the overall solution.[1, 62] When depositing from a solution composed of a mixture of different materials it is important that the properties of each of the components, particularly those relating to evaporation and wetting ability, are accounted for when experimenting with the dip-coating procedure. For example, in a dip-coating solution composed of both relatively non-volatile H_2O and a volatile solvent, such as IPA or EtOH, there can be preferential evaporation of the solvent prior to the full formation of the liquid film and subsequent solid thin film.[62-64]

Dip-coating technologies continue to be expanded with new research focused on improving the ability to dip-coat a variety of different surfaces with new thin film structures and morphologies. Improvements in dip-coating techniques are not confined to metal oxides but can be applied to many different types of materials. Figure 2.6 highlights a selection of the different techniques currently being examined, where changes to the dip-coating attributes, ranging from the speed, substrate changes and solution alterations, can result in changes to the resultant thin

film materials. In most dip-coating applications, the withdrawal rate is kept constant. Faustini *et al.* instead deposited thin films of metal oxides with graded thickness and refractive indices by accelerating the withdrawal speed during deposition.[65] Through this acceleration deposition technique, thin films with a graded thickness index, or functionality gradient, were produced as shown in the schematic in Figure 2.6 (a).

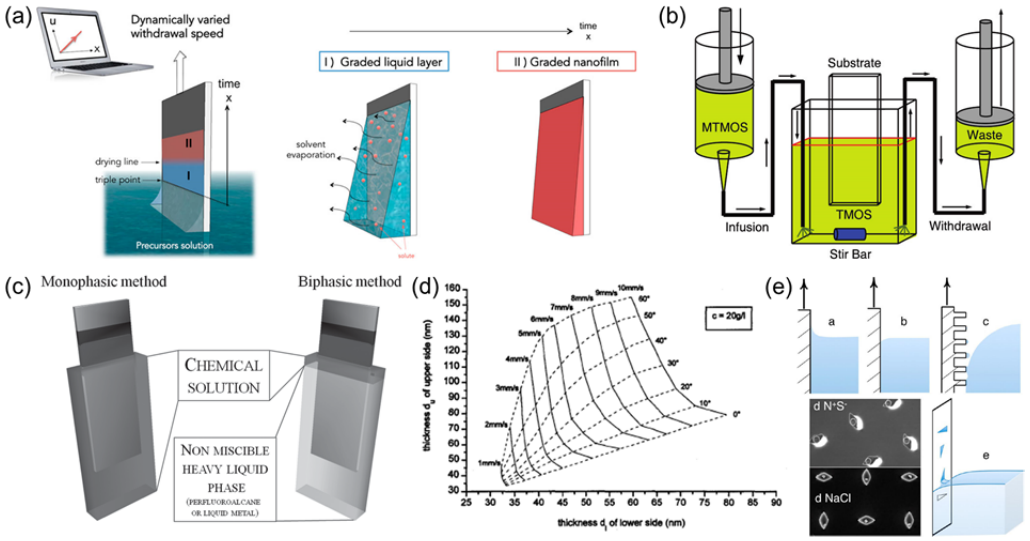


Figure 2.6. Various innovative techniques for altering dip-coated thin films. (a) Preparing graded thin films through varying withdrawal speed in-situ.[65] (b) Infusion withdrawal technique where a secondary material is infused into the solution during dip-coating.[66] (c) Large surface thin film coating technique using minimal precursor solution through use of a biphasic solution.[67] (d) Influence on both upper and lower surface thin films on the angle during angle-dependent dip-coating.[68] (e) Schematic of the deposition of chemically treated surfaces where a mix of hydrophobic and hydrophilic surfaces are dip-coated.[69]

Alterations to the precursor solutions, other than through chemical additives, can also cause changes to the thin films. Figure 2.6 (b) and (c) both show how alterations to the precursor solution can alter thin film structure or increase the efficiency of dip-coating thin films respectively. In Figure 2.6 (b) the schematic of an infusion withdrawal technique used by Ye *et al.* to deposit a thin film with a polarity gradient is shown.[66] The technique does not involve conventional dip-coating; instead the substrate is left in position while two solutions are mixed in the

reservoir by pumping in the secondary solution. As the secondary solution is pumped in, the reservoir is also emptied, thus mimicking the effect of withdrawal in conventional dip-coating. A new method for decreasing the amount of solution required while facilitating large-scale dip coating depositions was demonstrated by Ceratti *et al.* who supported a precursor solution on top of a non-miscible liquid as shown in Figure 2.6 (c).[67] This technique allows for the active precursor solution to coat the surface of the material as in conventional dip-coating techniques, while also decreasing the amount of precursor solution required, which is of particular importance for dip-coating of expensive materials.[67]

The final types of dip-coating modification discussed here involve changes to the substrate, either through mechanical or chemical means, to influence the type of thin film deposited. Angle-dependent dip-coating (ADDC) is a technique where the substrate is withdrawn at an angle rather than orthogonal to the precursor solution surface. When depositing at an angle, the thin film can be prepared at higher thickness with a lower number of sequential coatings required. Another benefit to the ADDC method is the ability to deposit thin films of the same material at different thickness on either side of the substrate. Figure 2.6 (d) shows how both deposition angle and withdrawal speed affect the thin film thickness on the top and bottom surface of ADDC deposited thin films of a set concentration of TiO_2.[68] Through this technique, a thin film of the same material can be deposited on both sides of a substrate with different thicknesses which is of particular interest for optical filter technologies.[68]

The last technique discussed in this section describes how chemical patterning can be used to render different areas on the substrate either hydrophobic or hydrophilic; when the substrate is dip-coated the hydrophobic areas are coated

while the hydrophilic surfaces remain free of deposit. As demonstrated by Wang *et al.* in Figure 2.6 (e), this technique can be applied to a variety of substrates to form complex and intricate materials on a variety of substrates, even those containing pillars and other non-planar morphologies.[69] The various innovative techniques highlighted in Figure 2.6 illustrate how the use of a dip-coating technique continues to be of great importance to the thin film industry due to the large range of alterations which can be implemented to improve the deposition processes.

2.3.3 Other Deposition Techniques

As described in Figure 2.1 there are a number of other solution processed techniques which can be applied in developing metal oxide thin film materials. These include techniques such as ink-jet printing and spray pyrolysis, both of which involve the deposition of the material by passing the solution through an opening, either as a liquid or by first atomising, and then depositing the material onto the substrate as a spray. Schematic representations for both spray pyrolysis and ink-jet printing[70] techniques are shown in Figure 2.7.

In the spray pyrolysis process, a spray of solution is directed at a substrate by first atomising the precursor solution. The atomising is accomplished through techniques ranging from simple air blasting to more advanced ultrasonic/electrostatic methods.[71-73] An important aspect of spray pyrolysis concerns the heating of the substrate during deposition, which aids in thin film crystallisation and surface cohesion. An unheated substrate can result in defective thin film depositions, often with cracks. For best results, it is advisable to adjust the substrate heating for each type of precursor solution until the desired morphology is deposited.[71] Many other

deposition attributes must also be accounted for when using a spray pyrolysis technique. The chemical attributes of the precursor solution must be compatible with the atomiser otherwise the solution can cause blockages and other detrimental effects which can both alter the deposition or cause machinery defects. To increase sample coverage, many spray pyrolysis devices incorporate a moveable stage to allow movement of the atomiser over the substrate.

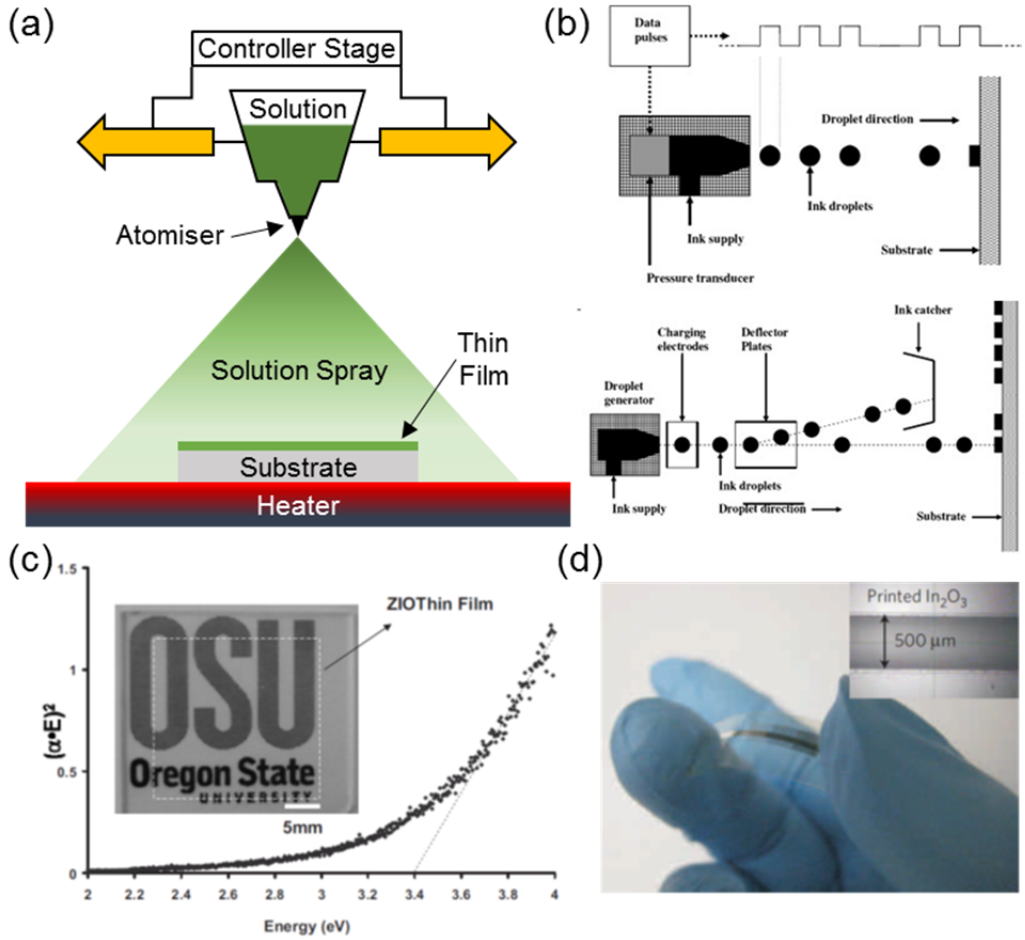


Figure 2.7. Schematic representations of (a) spray pyrolysis and (b) two ink-jet printing[70], both on-demand (top) and continuous (bottom), thin film deposition techniques. (c) Optical bandgap measurement and optical image for a inkjet printed ZIO thin film.[74] (d) Optical image of a flexible In_2O_3 TFT with the inset showing an ink-jet printed In_2O_3 line.[49]

Most applications of ink-jet printing pertain to books and other reading materials; there is currently a substantial drive in the deposition of functional

materials using the same technique since its inception.[75-76] Ink-jet printing techniques can be applied to a wide variety of materials, where the limiting factor of the method relies upon the attributes of the precursor solution and its interactions with the print head and the substrate. The precursor solution must have a high enough surface tension so as not to leak uncontrollably while also having a sufficiently low viscosity to allow for transport through the printing nozzle when required.[76] Figure 2.7 (b) shows two of the most common ink-jet printing techniques that are currently in use: in the top schematic the ink is deposited on-demand using an inducer so that droplets are selectively placed on the substrate, in the bottom schematic a continuous flow of material is fed through the nozzle and is electrostatically deflected away from the substrate into a collection tray when an area is not to be coated.[70] For depositing complex morphologies and arrays of material, the ink-jet printing head can be positioned over the surface of the substrate similar to a conventional office printer. Using this technique it is possible to deposit a large variety of materials, however, the limiting factors involve the types of inks which can be prepared and their usability. Figure 2.7 (c,d) shows two examples of inkjet printed devices. A high mobility zinc indium oxide (ZIO) transparent conducting thin film is shown in Figure 2.7 (c) which shows the capability of the ink-jet printing technique for large area depositions.[74] The smaller scale and site specific deposition of the ink-jet printing technique is highlighted in Figure 2.7 (d) where an In_2O_3 semiconductor line is deposited for use in a TFT device.[49] Ink-jet printing is a useful technique for both large and small area depositions due to its versatility and low precursor solution wastage.

2.3.4 Polymer Assisted Deposition

The addition of additives and other materials into a precursor solution to aid in the formation of thin films is not a new practice. However, in the past number of years there has been an increased drive for the development of polymer-assisted deposition (PAD) techniques for improving the deposition and material characteristics of solution processed thin films. The PAD process involves the mixture of a soluble polymer with the metal complex within the liquid precursor solution to increase the control of the solutions attributes, such as viscosity, reactivity and to increase the shelf life of the material.[50-51] PAD can thus influence the morphology, compositional consistency, thickness and the density of defects (among other attributes) during thin film formation, by the addition of a compatible polymer.

A schematic detailing two PAD processes for the deposition of TiO_2 is shown in Figure 2.8 (a,b). In the Ti complex shown in Figure 2.8 (a), a titanium triscatecholate compound was bound to PEI through dissolving and mixing in DI water with subsequent purification.[50] The resulting Ti complex is a binding of the Ti to PEI as a catecholate complex, however, the concentration of Ti present was shown to be low. The concentration of Ti ions was increased using the method detailed in Figure 2.8 (b), where the Ti was instead directly bonded to PEIC and then purified using Amicon ultrafiltration.[50] Jia *et al.* discussed how the second method produced a much more stable Ti solution, particularly toward hydrolysis reactions.[50]

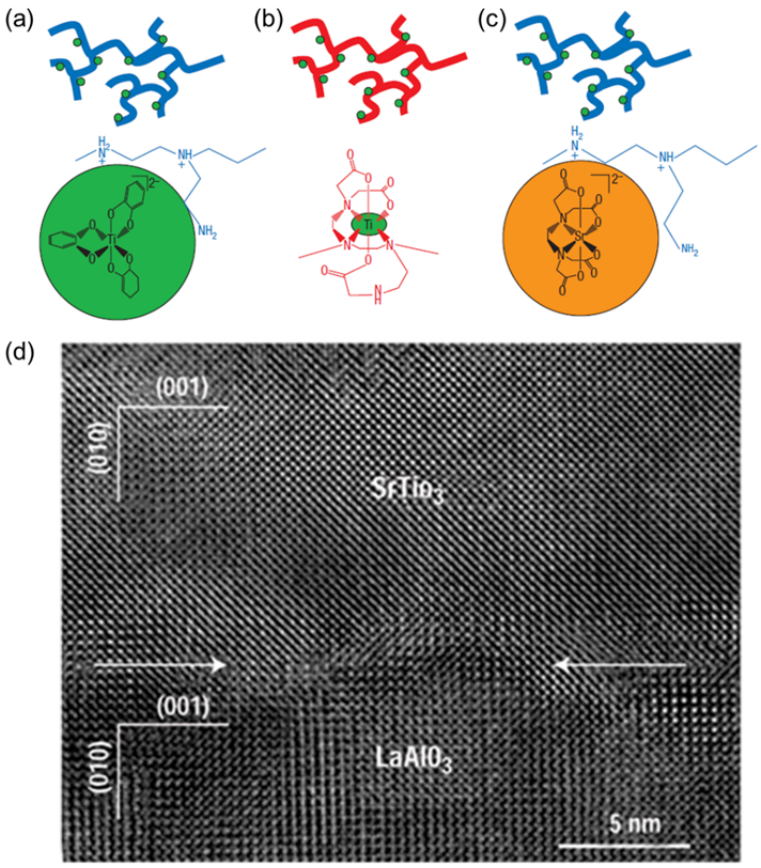


Figure 2.8. Schematic of PAD process for Ti metal ions. (a) Ti bound to PEI as a catecholate ion and to (b) PEIC directly. (c) Strontium, as an EDTA complex, bound to PEI. (d) HRTEM image of epitaxial deposition using PAD processes of $SrTiO_3$ on $LaAlO_3$.[50]

Strontium ions were also bound by Jia *et al*. to PEI for a PAD technique. Figure 2.8 (c) shows how the strontium was bound to the PEI as an EDTA complex.[50] By mixing a solution with equal molarities of Ti bound to PEIC and strontium bound to PEI, an epitaxial thin film of $SrTiO_3$ was deposited through spin coating on an $LaAlO_3$ substrate. A HRTEM image displaying the epitaxial deposition of $SrTiO_3$ on $LaAlO_3$ is shown in Figure 2.8 (d). The PAD processes utilised by Jia *et al.* allowed for a single layer epitaxial deposition of $SrTiO_3$ on $LaAlO_3$ with a dielectric constant greater than 200 and a loss of <1% at 1 MHz which is comparable to thin film dielectrics deposited using pulsed laser

deposition.[50, 77] The use of PAD techniques has increased with many studies showing the efficacy of PAD techniques particularly in the preparation of epitaxial metal oxide growth with the underlying substrate.[51, 78] The PAD technique increases the scope of the solution processed depositions allowing for an increased range of materials and stoichiometric surfaces to be prepared.

2.4 Comparison of Thin Film Deposition for Vanadium Oxides

As discussed in the preceding sections, there are many ways in which metal oxides can be deposited using a solution processed technique. In this section a comparison is made between a variety of solution processed vanadium oxide (VO) thin films. Vanadium oxide is chosen as a comparative material due to its prevalence in thin film applications and the large range of oxidative states and structures available such as V_2O_5, VO_2 and vanadium sesquioxide (V_2O_3). Different V_2O_5 thin film deposition processes are compared through analysis of the resultant thin films, where the various deposition and processing conditions are correlated to one another as a function of the different deposition and processing conditions. The morphologies and attributes discussed in this section are not exhaustive, but the review provides an overview of the range of structures and thin films possible.

2.4.1 Thin Film Composition and Structure

The analysis of thin film composition and structure is achieved using a number of different methods, including but not limited to; Raman scattering spectroscopy, XRD and XPS techniques. Different analysis techniques can be used for analysing specific attributes of a thin film, where the crystalline structure, composition or lattice

vibrational characteristics for the material can be probed and identified. A schematic of two layers of V_2O_5 are shown in Figure 2.9 (a) with the V atoms in grey and the O atoms in red.[79] V_2O_5 is the most stable oxidation state of VO materials with a crystalline orthorhombic unit and a layered structure which is beneficial for use in applications utilising intercalation such as energy storage.[80-82]

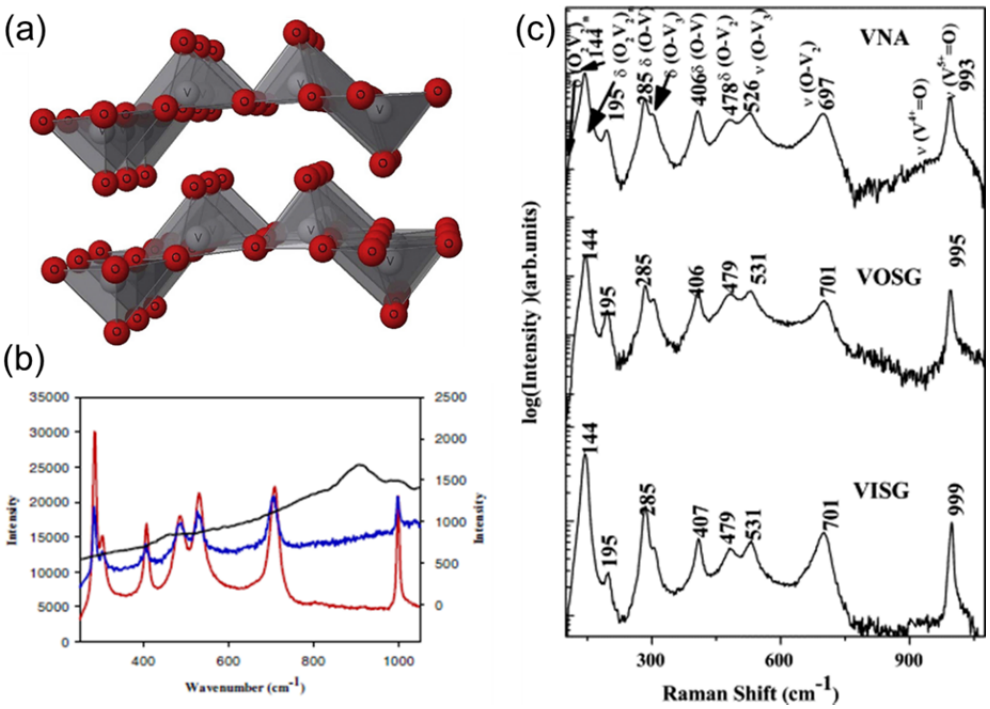


Figure 2.9. (a) Structural schematic of two layers of V_2O_5 with V atoms (grey) and O atoms (red).[79] (b) Raman scattering spectra of dip-coated V_2O_5 thin films as-deposited (black) and annealed at both 300 ^oC (blue) and 500 ^oC (red).[52] (c) Raman scattering spectra of spin coated V_2O_5 thin films formed from a metallo-organic (VNA), organic (VOSG) and inorganic (VISG) based precursor solution.[83]

The Raman scattering spectra for a dip-coated V_2O_5 thin film on ITO substrates deposited by Alsawafta *et al.* is shown in Figure 2.9 (b) where the precursor solution was prepared from a mixture of vanadium oxytriisopropoxide, IPA and acetic acid.[52] The Raman scattering spectra in Figure 2.9 (b) shows the thin films in an as-deposited state prior to annealing where no distinct Raman modes

were present that indicated the formation of orthorhombic V_2O_5, but are subsequently observed after crystallization at 500 ^oC .[52]

The deposition of orthorhombic V_2O_5 can be accomplished using a variety of different precursor solutions. In Figure 2.9 (c) Raman scattering spectra for V_2O_5 thin films deposited through spin coating using three different types of precursor is presented after annealing at 450 ^oC. The solutions were prepared from metallorganic, organic and inorganic based precursors where the resultant thin films are labelled as VNA, VOSG and VISG, respectively in Figure 2.9 (c).[83] Raman spectra show the formation of orthorhombic V_2O_5 occurs in each case with the evidence of characteristic vibrational peaks with only small discrepancies present. Shifts in the V=O bond located at 993 cm^{-1}, 995 cm^{-1} and 999 cm^{-1} respectively for the VNA, VOSG and VISG thin films is indicative of small changes to the oxidative state; a larger Raman shift corresponds to increased amount of V^{5+}. The work by Sahana *et al.* demonstrates how the use of different vanadium based precursors can be utilised for thin film deposition using identical techniques with the formation of compositionally pure V_2O_5 thin film materials. This result is important for applications where thin films are desired within a technique but a specific precursor may be unavailable.

The effect of changes to precursor molarity for V_2O_5 thin films deposited onto amorphous glass slides through a spray pyrolysis technique at constant substrate temperature is shown in the XRD data of Figure 2.10 (a).[84]. In each case there is a distinct (001) peak present while the number of peaks indexed to V_2O_5 increases as the precursor concentration increases. Akl *et al.* ascribed the increased intensity of the peaks to grain growth or an increase in the degree of crystallinity within the thin films as the concentration increased. The crystal size was tested through Voight

profile analysis of the line broadening which showed saturation at concentrations of 0.2 M, 0.3 M and 0.4 M with a sharp decrease in crystallite size for the low 0.1 M and high 0.5 M concentrations.[84] The saturation was linked to the concentrations being appropriate for crystal growth while the mobility of ions is insufficient at low concentration, but too fast at high concentrations, leading to agglomeration.[84]

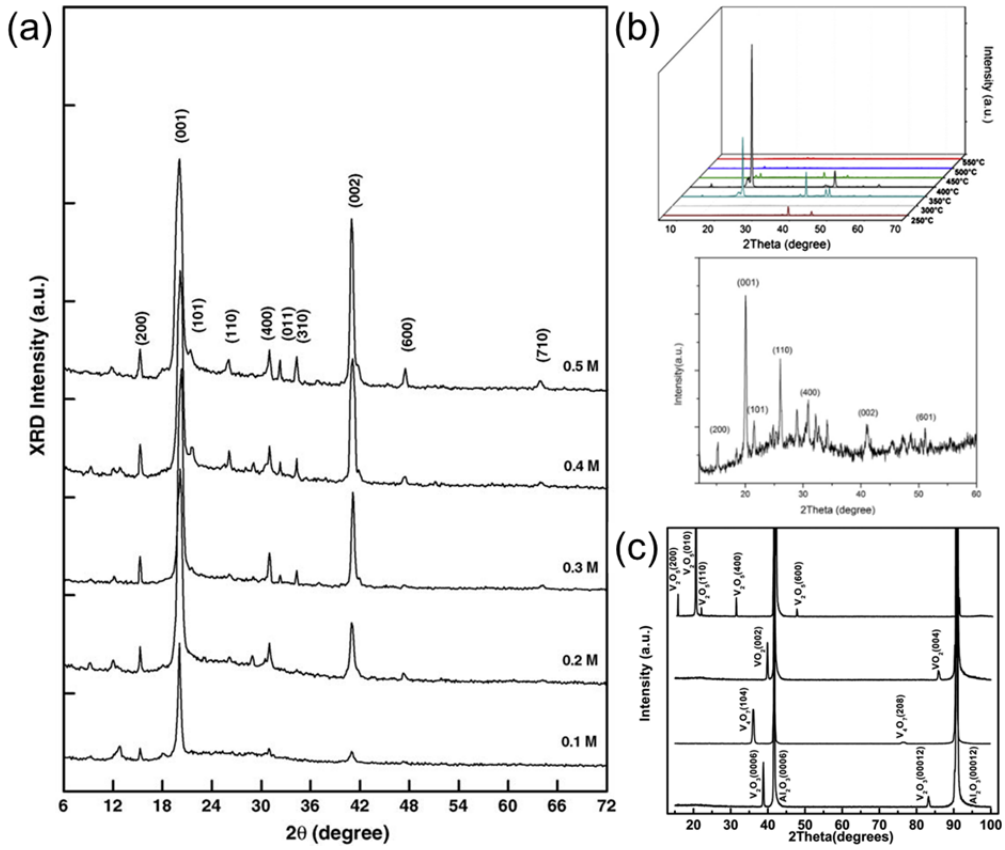


Figure 2.10. XRD pattern of V_2O_5 thin films showing effects of varying the (a) precursor solution concentration,[84] (b) substrate temperature[85] and (c) substrate and processing condition to form multiple VO materials.[86] (a, b) were deposited using a spray pyrolysis technique and (c) was deposited through a spin coating/PAD technique.

Spray Pyrolysis of V_2O_5 thin films using a VCl_3/H_2O precursor prepared by Irani *et al.* shown in Figure 2.10 (b) demonstrates that the substrate temperature also plays a key role in the formation of different VO structures.[85] The XRD patterns in Figure 2.10 (c) demonstrates how precise annealing and atmosphere control can

enable epitaxial growth of a range of VO phases other than the most stable phase which is V_2O_5.[79, 86-88]

Figure 2.11 (a) shows the XPS analysis of the V 2p peak in the characterisation of different oxidative states of VO thin films including V_2O_5, V_2O_3 and VO_2.[79] The charge state of an individual atom can be determined as shown in Figure 2.11 (a), where an increase in the core level binding energy indicates an associated increase in the positive charge of the atom.[79] Through careful data analysis it is possible to determine the oxidative state and structure of a range of VO materials.

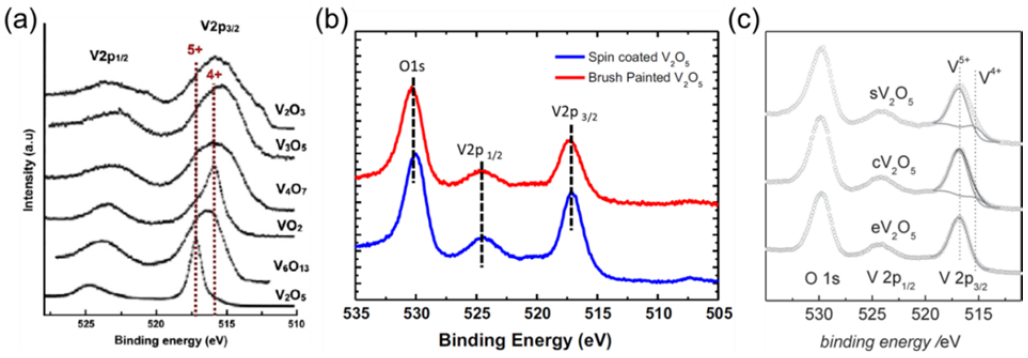


Figure 2.11. XPS spectra of the O 1s and V 2p for VO thin films. (a) XPS spectra of V_2O_5 compared to a variety of other vanadium oxide structures.[79, 89] (b) Comparison between two solution processed techniques; spin coated and brush painted V_2O_5 thin films.[90] (c) Comparison between evaporation deposited (eV_2O_5, vV_2O_5) and spin coated (sV_2O_5) thin films.[91]

In Figure 2.11 (a, c) comparisons between V_2O_5 thin films deposited through a variety of different techniques is made. Included in the XPS spectra is the O 1s peak located in close proximity to the V 2p peak discussed above. The V_2O_5 thin films studied by Cho *et al.* were deposited on ITO glasses through both a brush painting and spin coating technique from a vanadium (V) oxytriisopropoxide based precursor solution. In a brush painting deposition the precursor solution is spread over the surface with a "brush" similar to screen printing. For both the brush and

spin coating techniques the solutions were optimised for deposition.[90] A direct comparison of the V 2p and O 1s peaks can be made between the two resulting thin films and is shown in Figure 2.11 (b). For both types of depositions the V $2p_{1/2}$ is an exact match while a small shift in the binding energy of 0.3 eV for the V $2p_{3/2}$ and O 1s peaks is present.[90] The XPS analysis by Cho *et al.* demonstrates the possibility of preparing near-identical stoichiometric V_2O_5 thin films using two different solution processed techniques where the active precursor material for the solution was identical. The interchangeability of the precursor material in different solution processed techniques is important for the transition of laboratory deposition methods to industrial sized practices.

Comparisons of the O 1s and V 2p peaks for V_2O_5 thin films deposited using either a solution processed or evaporation technique is presented in Figure 2.11 (c).[91] The solution processed V_2O_5 (sV_2O_5) thin film was deposited by Zilberberg *et al.* from an IPA/vanadium (V) oxytriisopropoxide precursor solution whilst the evaporated V_2O_5 (eV_2O_5) thin films were deposited at an ultra-high vacuum. An evaporated V_2O_5 thin film sample (cV_2O_5) was exposed to air prior to XPS analysis whilst the eV_2O_5 was left under vacuum between the deposition and analysis. Analysis of the V $2p_{3/2}$ peak shows small amounts of V^{4+} present in the sV_2O_5 and cV_2O_5 thin films which is evidence that the presence of some VO_2 has formed within the thin films.[91] The analysis by Zilberberg *et al.* suggests that this formation of small amounts of VO_2 within the thin films is due to their exposure to ambient atmosphere which partially reduces the V^{5+} to V^{4+}.[91] This work highlighted the usability of solution processed techniques where the equivalent detrimental effects were experienced by both the solution processed and physical deposited thin films.

2.4.2 Surface Morphologies

Figure 2.12 shows a collection of AFM and SEM surface images of V_2O_5 thin films using various solution processed deposition techniques. Costa *et al.* ink-jet printed the thin films in Figure 2.12 (a) by depositing a precursor solution prepared from a mixture of V_2O_5 powder and hydrogen peroxide resulting in nanoparticles. The nanoparticles were suspended in water forming a stable colloidal solution.[92] This colloidal solution was deposited onto a flexible PET/ITO substrate and tested to determine surface coverage and the produced thin film morphology. Costa *et al.* observed through their AFM analysis[92] that the V_2O_5 thin film did not show the presence of spherical particles, instead both the AFM and rugosity (roughness factor) measurements show the surface of the thin film was composed of a V_2O_5 ribbon structure, a common morphology in V_2O_5 materials.[93-95]

The dip-coated thin films shown in Figure 2.12 (b) were prepared by Gökdemir *et al.* using an inorganic (V_2O_5 powder in H_2O_2) and organic (vanadium (V) triisopropoxide in IPA) based precursor solution.[96] The inorganic solution was prepared similarly to the nanoparticles used in the inkjet printing discussed in Figure 2.12 (a): a V_2O_5 powder was mixed with hydrogen peroxide and stirred to form a liquid sol. The organic based solution was prepared using vanadium (V) triisopropoxide mixed with an appropriate amount of IPA and acetic acid to form a liquid precursor solution. The thin films were dip-coated onto a variety of glass substrates including ITO coated glass at a withdrawal rate of 100 mm/min and then heated for 20 mins at 150 ^{o}C. The AFM images in Figure 2.12 (b) shows the formation of a smooth granular V_2O_5 thin film surface in both the inorganic and organic case, however, Gökdemir *et al.* discusses how the organic precursor route results in a thin film with a smoother more homogeneous surface morphology and a

smaller grain size than the inorganic.[96] These types of changes in grain size and surface homogeneity are of importance for many material properties of thin films in particular the optical characteristics.

Pinholes, a common thin film defect, are seen in the AFM image of Figure 2.12 (c), which is an example of a spin-coated V_2O_5 thin film prepared from an IPA-vanadium(V) oxytriisopropoxide solution.[97] Zilberberg *et al.* deposited the thin films on glass and ITO substrates at rotational speeds ranging from 3000 – 10000 rpm to produce controllable thicknesses between 10 – 45 nm.[97] The pinholes routinely form as a result of solution dewetting during the thin film formation stage. The pinholes were not found to strongly influence the rms roughness, which was stated to be relatively low at 0.4 nm.[97] The formation characteristics of the pinholes in thin films of either polymers or metal oxides,[98] is a commonly studied effect due in part to the deleterious effect of pinholes on electronic and optical properties; methods to prevent their formation are still being investigated.

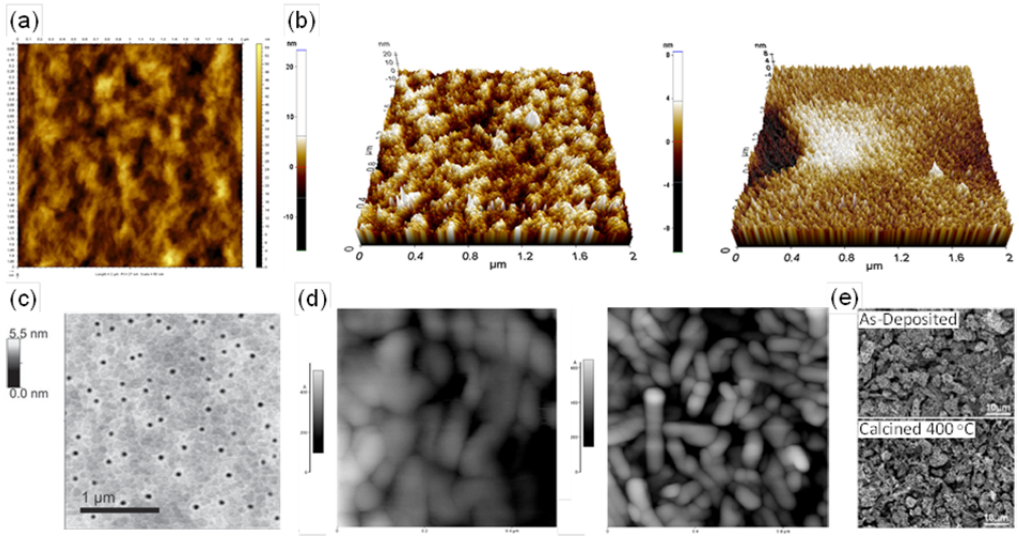


Figure 2.12. AFM and SEM Images highlighting the possible V_2O_5 surface morphologies formed using a variety of solution processed deposition techniques, namely (a) ink-jet printing[92] (b) dip-coating of two different precursor solutions[96] (c) spin-coating[97] (d) spray pyrolysis of two different molar concentrations[99] and (e) drop casted V_2O_5 precursor solution[100].

The effect of different molar concentrations on the morphology of V_2O_5 thin films deposited using a spray pyrolysis technique is shown in Figure 2.12 (d). The thin films were deposited on glass substrates at a temperature of 250 ^oC through spray pyrolysis from a vanadium trichloride solution mixed with double distilled water at both 0.4 M and 0.1 M respectively.[99] The thin films show a distinct morphology change between the two concentrations, with the 0.4 M thin films having a higher rms roughness than the equivalent 0.1 M thin film of 25 nm and 8 nm, respectively. These thin films have a much higher rms roughness compared to the others discussed in this section, however, the capabilities of large scale surface depositions with spray pyrolysis is higher than many of the alternative methods, particularly for use in energy storage[101] and optical applications.[71]

Using drop-casting techniques, large surface coverages of VOs can be achieved in a short time, albeit with a drawback in surface homogeneity. Figure 2.12 (e) shows SEM images of a drop-casted V_2O_5 film both before (top) and after (bottom) a calcination process.[100] Lim *et al.* prepared the films by synthesising the rose-like particles with a sol-gel technique involving an ethanolic-aqueous medium, vanadium triisopropoxide and hexadecylamine combined with a long-term heat treatment technique. The prepared rose-like particles were suspended in ethanol and drop-casted onto Si wafers.[100] The SEM images in Figure 2.12 (e) show that a rougher surface after calcination is found. A high surface roughness can be a beneficial attribute for a variety of applications such as energy storage and in the case of these particular films, their use as a photoswitchable super-hydrophobic/hydrophilic material.[100]

2.4.3 Optical Properties

The study of a thin films' optical properties and characteristics is required for ascertaining the suitability of a material in optoelectronic applications, optical coatings and for assessing the nature of light-matter interactions for new materials and their arrangements. One of the most common techniques involves the calculation of the effective optical bandgap. The optical bandgap is the energy threshold for light absorption of the material and can be calculated through analysis of the absorption edge using the modified Davis-Mott relation and is commonly presented as Tauc plots.[38] The optical bandgap, threshold where optical absorption can occur, can be calculated from the absorption coefficient through the relation $\alpha h\nu = A(h\nu - E_g)^n$ where α is the absorption coefficient of the thin films, A is a constant and E_g is the effective optical bandgap. The absorption coefficient determines the depth at which a given wavelength penetrates the material. The exponent n is related to the type of transition for the material. The optical bandgap can then be determined through extrapolation, where $[\alpha h\omega]^n = 0$. It is also possible to use the Moss relation to determine the refractive index from the calculated optical bandgap through $\eta_{VO}^4 E_g \sim 95\ eV$.[102-104]

For comparison to solution processed techniques, the UV-Vis spectroscopy in Figure 2.13 (a) shows V_2O_5 thin films deposited by vacuum deposition at 3 nm (top) and 30 nm (bottom) thicknesses.[105] The UV-Vis spectra of the 30 nm and 3 nm thick layers of V_2O_5 have a distinctive absorption edge at ~400 nm with expected changes in the respected transmission values across the wavelength range.[105] Comparisons can be made with these vacuum deposited thin films to the transmission characteristics of equivalent solution processed V_2O_5 thin films where changes in absolute transmission can be related to the effects of thickness whilst the

optical bandgap shifts can be related to crystallisation and structural changes in the thin films.

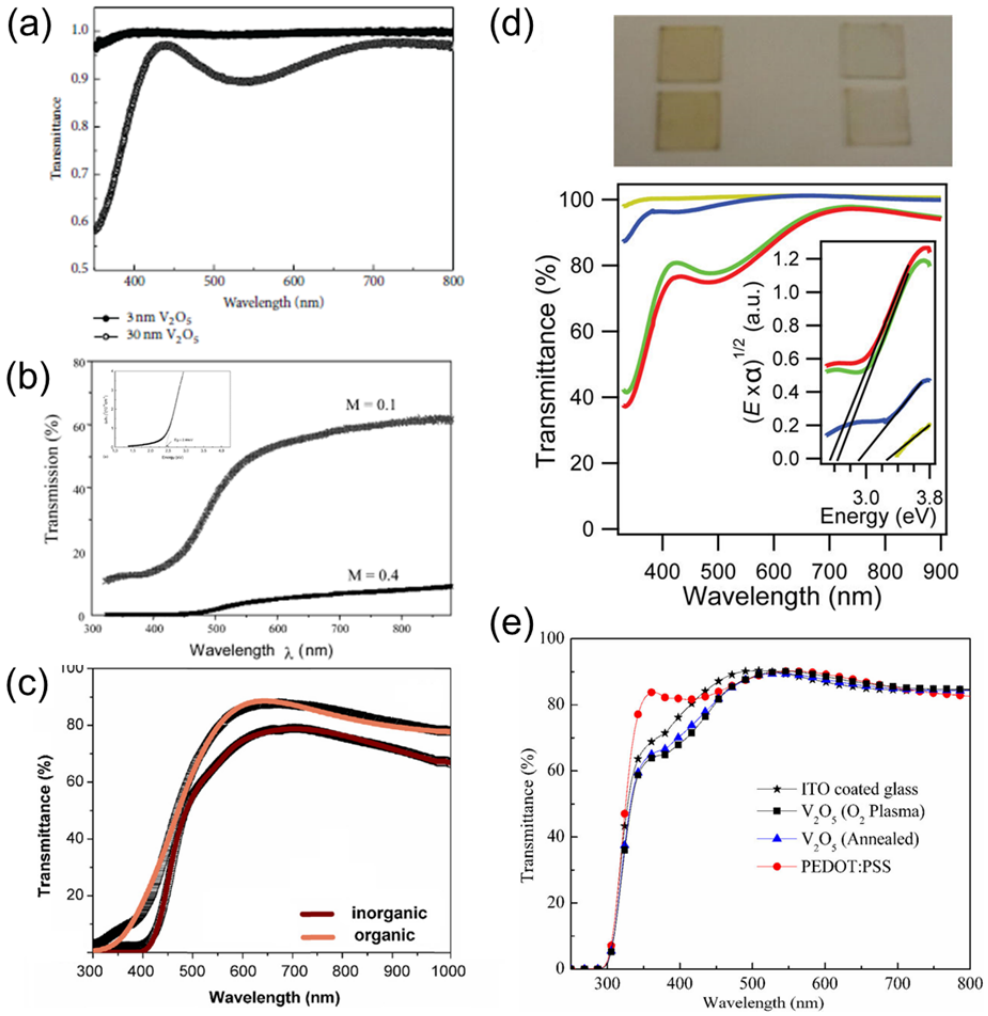


Figure 2.13. UV-Vis transmission spectra and associated analysis for a variety of V_2O_5 thin films deposited using a variety of techniques with some comparisons to contemporary materials and non-solution processable methods. (a) Transmission comparison of a 3 nm and 30 nm thick V_2O_5 sputtered thin film showing the changes in optical transmission characteristics.[105] (b) Changes in transmission due to concentration changes using spray pyrolysis and associated Tauc plot for V_2O_5 (inset).[99] (c) Transmission for dip-coated V_2O_5 thin films formed from inorganic and organic based precursors.[96] (d) Optical images and corresponding transmission and Tauc analysis for a variety of V_2O_5 thin films spin coated and annealed under varied atmospheric conditions.[106] (e) Transmission images for spin coated V_2O_5 thin film treated under different post-processing conditions thin films compared to both ITO coated glass and PEDOT:PSS.[107]

The UV-Vis transmission and related Tauc plot (inset) shown in Figure 2.13 (b) for the V_2O_5 thin films deposited by spray pyrolysis were described previously in

Section 2.4.2. The deposits were prepared from pre-formed nanoparticles with a defined size, thus while the transmission increases at lower concentrations the optical bandgap remains consistent at 2.44 eV.[99] This optical bandgap value is higher than the range expected for bulk and nanocrystalline V_2O_5 materials.[108]

Figure 2.13 (c) displays the UV-Vis transmission spectrum of the inorganic and organic thin films prepared by Gökdemir *et al.* and discussed previously in Section 2.4.2.[96] In comparison to the thin films of Figure 2.13 (b) a change in the absorption edge is seen in the transmission spectrum of Figure 2.13 (c). The changes between an inorganic and organic precursor resulted in thin films with a calculated optical bandgap of 2.64 eV and 2.10 eV respectively when an *n* value corresponding to an indirect allowed transition is used. The changes in optical bandgap energy can be related to crystalline size effects between the two deposition techniques.[96]

Post-processing techniques has an effect on the material characteristics of thin films. In Figure 2.13 (d,e) the changes which occur to the optical transmission of V_2O_5 thin films using different post processing techniques is shown. Hancox *et al.* investigated the effect of deposition and annealing atmosphere on spin coated V_2O_x thin films in Figure 2.13 (d).[106]. Thin films were spin coated under both ambient and N_2 atmosphere followed by subsequent annealing in either of the two atmospheres. The optical images in Figure 2.13 (d) shows two examples each of thin films deposited under air (left) and N_2 (right) respectively with both being annealed in air afterwards.[106] The effect of the N_2 atmosphere during the deposition can be seen in the UV-Vis transmission spectrum where the N_2 deposited (gold and blue) thin films have a higher transparency to the air deposited (green and blue) thin films.[106] The gold spectrum was both deposited and annealed in N_2 while the green spectrum was deposited in air and annealed in N_2. Hancox *et al.* demonstrated that the deposition

atmosphere had a larger effect on the optical properties of the V_2O_x thin films than the annealing atmosphere.[106] Post-processing O_2 plasma treatment of spin coated V_2O_5 thin films, as used by Bao *et al.* in Figure 2.13 (e), can be used as a low temperature method for crystallisation resulting in comparable UV-Vis transmission properties to thermally annealed thin films. Using this technique the V_2O_5 thin films can be decomposed from the as-deposited amorphous material into the desired V_2O_5 phase with no change to the optical bandgap.[107] The O_2 plasma treatment allows for a low temperature post processing step which can be utilised for incorporation into polymer solar cells where high temperature processing can be detrimental. Direct comparisons are made in Figure 2.13 (e) to both ITO, a common TCO, and PEDOT:PSS which V_2O_5 can be used for replacing in polymer solar cells as a charge extraction layer.

Through study of the optical characteristics of the V_2O_5 thin films, comparisons can be made between the various deposition and post-processing techniques used in engineering the transparency and optoelectronic properties of thin films. As with the discussion on morphology alteration outlined above, the methods for altering the optical characteristics discussed are not an exhaustive list, however they do provide an overview of the types of changes that can be applied to help control V_2O_5 thin film formation. These same methods can be applied to other solution processed materials to help in engineering thin films with beneficial attributes.

2.5 Thin Film Applications and Devices

Metal oxide thin films have many applications within the optical, electronics, optoelectronics and energy storage/generation industries. The thin films are used as a variety of components within these devices, either as the working electrode/material, dielectric, hole/electron donor or as an optical coating for anti-reflection, filtering or to increase/decrease hydrophobicity as a few examples. As outlined in previous sections there are many methods available for depositing these thin films ranging from evaporation and vapour techniques to the solution processed methods outlined in this work. The purpose of this section is to outline some of the latest developments in the use of solution processed techniques in preparing modern devices such as TFTs, photovoltaics and battery materials. The devices discussed in this section are either fully solution processed or contain major components which have been deposited using one or more of the techniques outlined in Section 2.3. In many cases it is possible for the type of solution processed techniques to be interchanged for preparing thin film components, such as replacing a spin-coating process with dip-coating.

2.5.1 Electronic Materials

A transistor is made from a semiconducting material and is capable of either amplifying or rectifying an electronic signal. The transistor is one of the most important and fundamental devices for modern computing and electronics.[109] The continued improvement in transistor technology is driven by the need to make smaller and more energy efficient devices whilst also increasing the computing power.[110] The use of thin film transistors (TFTs) in fulfilling these needs is being

examined.[111] The improvements required can be achieved by preparing TFTs that have a higher mobility, stability and uniformity. In the case of transparent TFTs a high level of optical transparency is also required. As outlined previously, the deposition of active dielectric or channel materials these devices can rely upon expensive and time consuming processes. Using solution processed techniques it is possible to cost-effectively form large scale assemblies of TFTs where each of the different components can be prepared sequentially, often on non-planar substrates.

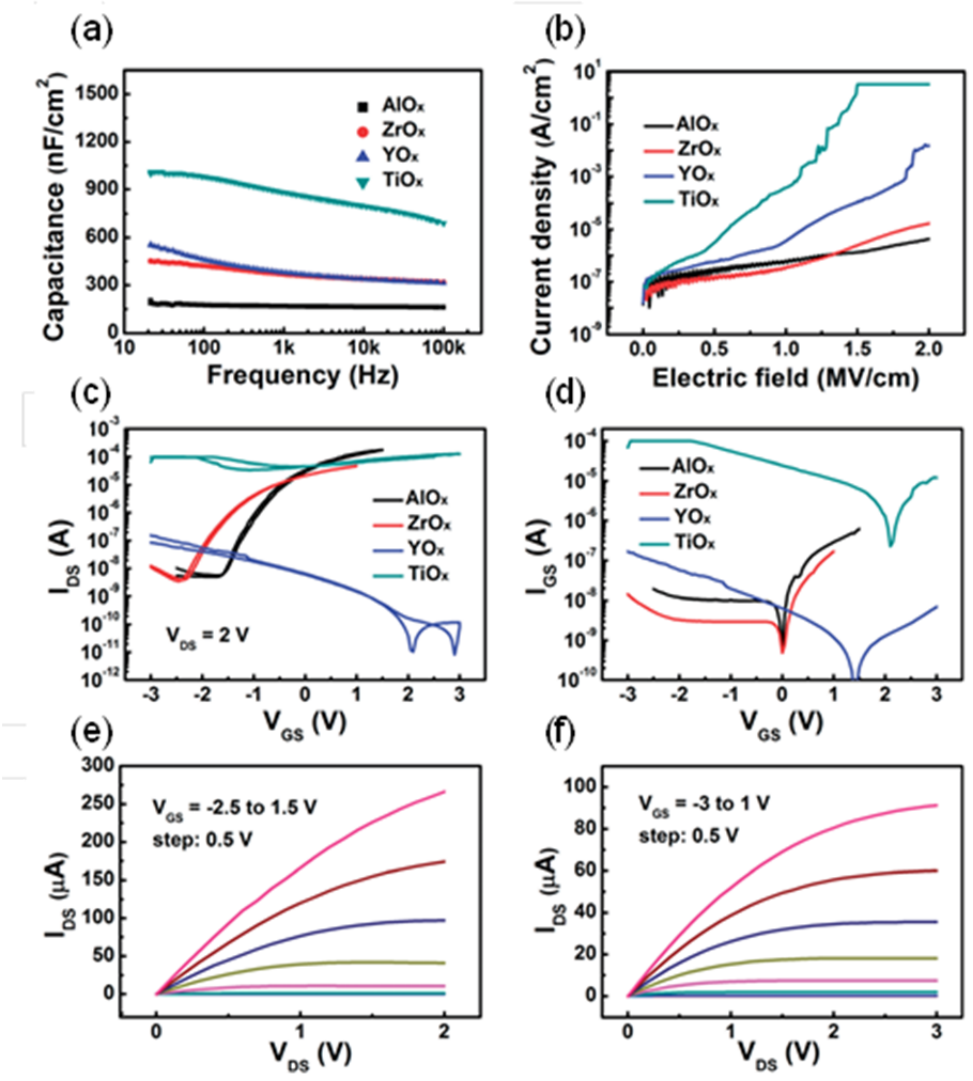


Figure 2.14. Electrical characteristics of different solution processed high-k dielectric materials showing the (a) capacitance vs. frequency, (b) leakage current density vs. electric field. (c) Transfer characteristics and (d) gate leakage characteristics of In_2O_3 TFTs with high-k solution processed dielectrics. Output characteristics of In_2O_3 TFTs with (e) AlO_x and (f) ZrO_x dielectrics.[112]

In Figure 2.14 (a, b), Xu *et al.* developed TFTs using solution processed dielectric thin films and by creating metal-insulator-metal (MIM) structures they demonstrated that the frequency dependent capacitance of the AlO_x, ZrO_x, YO_x and TiO_x had high values at low frequencies and low values at high frequencies.[112] Due to the low temperature annealing, the AlO_x, ZrO_x, YO_x and TiO_x thin films had an amorphous structure which limited the capability of determining the exact phase for each material.[112]

For high-k dielectrics the presence of defects and other non-uniformities influences the stability of the capacitance at different frequencies. As shown in Figure 2.14 (a) Xu *et al.* demonstrated a lower dispersion in the low frequency capacitance for AlO_x compared to TiO_x or YO_x dielectric thin films, which would indicate its suitability for use in a TFT. The explanation by Xu *et al.* stated that lower amount of defects and a smoother surface morphology for the AlO_x thin films contributed to the lower dispersion.[112] They also showed that processing TiO_x and YO_x dielectrics prevented breakdown and significant leakage current flow (Figure 2.14 (b)) up to electric fields of ~2 MV/cm.[112]

In Figure 2.14 (c, d) the same dielectric thin films were used in TFTs with an In_2O_3 semiconductor layer where the transfer and gate leakage characteristics were tested.[112] The behaviour of the TiO_x and YO_x dielectrics did not show suitability for the use in an efficient TFT device owing to leakage currents. The ZrO_x and AlO_x however showed a moderate and remarkable improvement respectively in their suitability as TFT dielectrics. The output characteristics of the AlO_x and ZrO_x are shown respectively for the In_2O_3 TFT in Figure 2.14 (e, f) where a good ohmic contact is demonstrated without significant current crowding, at low drain voltage (V_{DS}).[112]

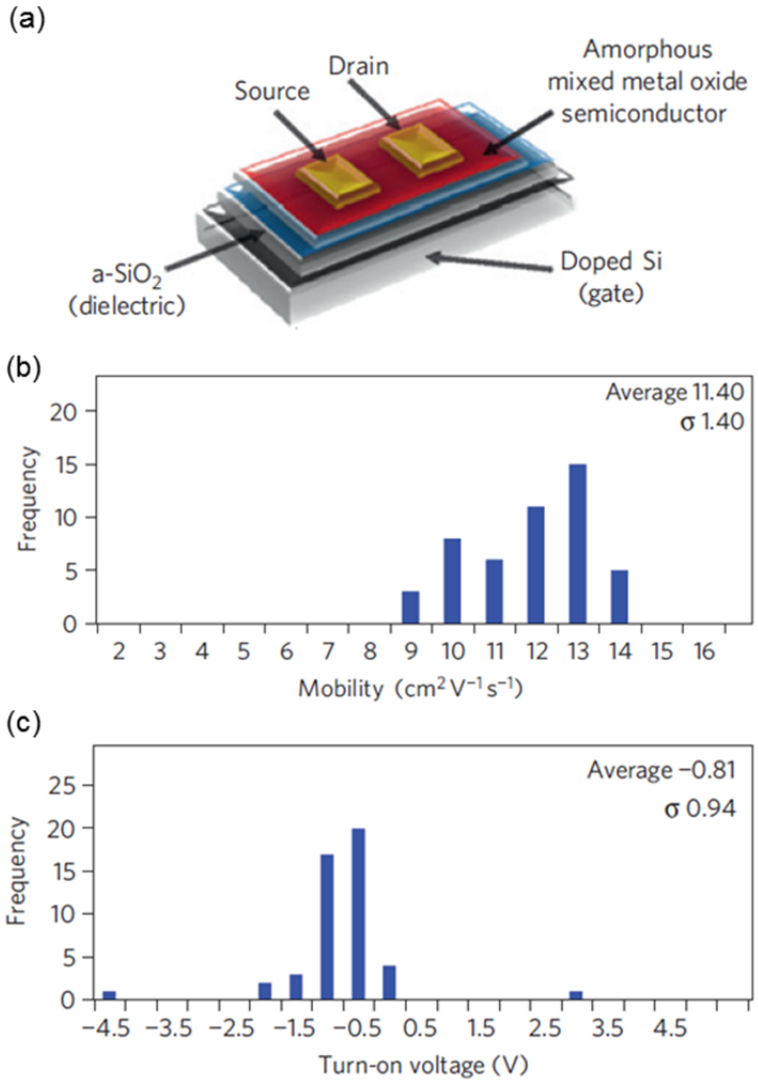


Figure 2.15. (a) IZO TFT device architecture and histograms of 49 IZO TFTs displaying their (b) mobility and (c) turn on voltages.[113]

The reproducibility of solution processed TFT designs was studied by Banger *et al.* who used a low temperature "sol gel on chip" technique to prepare TFTs with the device architecture shown in Figure 2.15 (a).[113] The thin films were deposited using alkoxide based precursors that were spin-coated onto substrates in a cleanroom environment under controlled humidity. In Figure 2.15 (b,c), the mobility and turn on voltages for 49 identically deposited TFTs where Banger *et al.* showed that the solution processed TFTs had a similar performance with small deviations in both mobility and turn-on voltage.[113] While the reproducibility of the technique would be

less than that of the current large-scale deposition techniques such as physical vapour or CMOS technologies, it is at a level of reproducibility that highlights the possibilities of the sol-gel technique for active channel material deposition in TFTs.

The upscaling of TFT production using solution processed methods is under constant investigation.[1, 13, 113-114] As outlined in previous sections, there are many different types of solution processed techniques that can be utilised for forming uniform thin films on a variety of substrates. Each of the techniques has positive and negative aspects for deposition, ranging from substrate limitations (wetting ability of precursor to substrate and irregular sizes) to their ability for upscaling of sample size and throughput. The benefit of many solution processed methods is modularity of inorganic precursor solutions and the ability to apply them using a variety of coating methods whose degree of control is related to some parameter (spin rate, viscosity, wettability, evaporation, volatility, concentration, functionalization or dielectric constant, to name a few).[114]

In Figure 2.16 a bar-coating deposition method was used by Lee *et al.* to fabricate TFTs over a large area.[114] The bar-coating technique is schematically shown in Figure 2.16 (a) and involves the deposition of precursor solution onto a substrate placed in contact with the wired-bar rolling system. The wired-bar is moved horizontally at a constant rate while the interaction of the meniscus between the solution and bar results in the formation of a thin film. The final thin film material can then be thermally annealed to form the desired layer.[114] The bar-coating technique can be further enhanced through the application of self-assembled monolayers (SAM) which can encourage uniform surface morphologies to form. The impressive transfer and output characteristics of the bar-coated MO_x TFTs shown in Figure 2.16 (b) have a high average field-effect mobility value of 5.25 $cm^2 V^{-1} s^{-1}$.[114]

Interestingly, Lee *et al.* were able to compare the average mobility values of IGZO TFTs deposited through both a spin- and bar-coating technique. In Figure 2.16 (c) the IGZO TFTs formed through a bar-coating technique had a higher average mobility value than the corresponding spin-coated deposited TFTs from the same precursor solution. It was speculated that the longer evaporation time allowed in the bar-coating process resulted in an increased thin film quality.[114] This improvement in the mobility values shows how the transition from a small- to large-scale deposition technique can have benefits with solution processed methods.

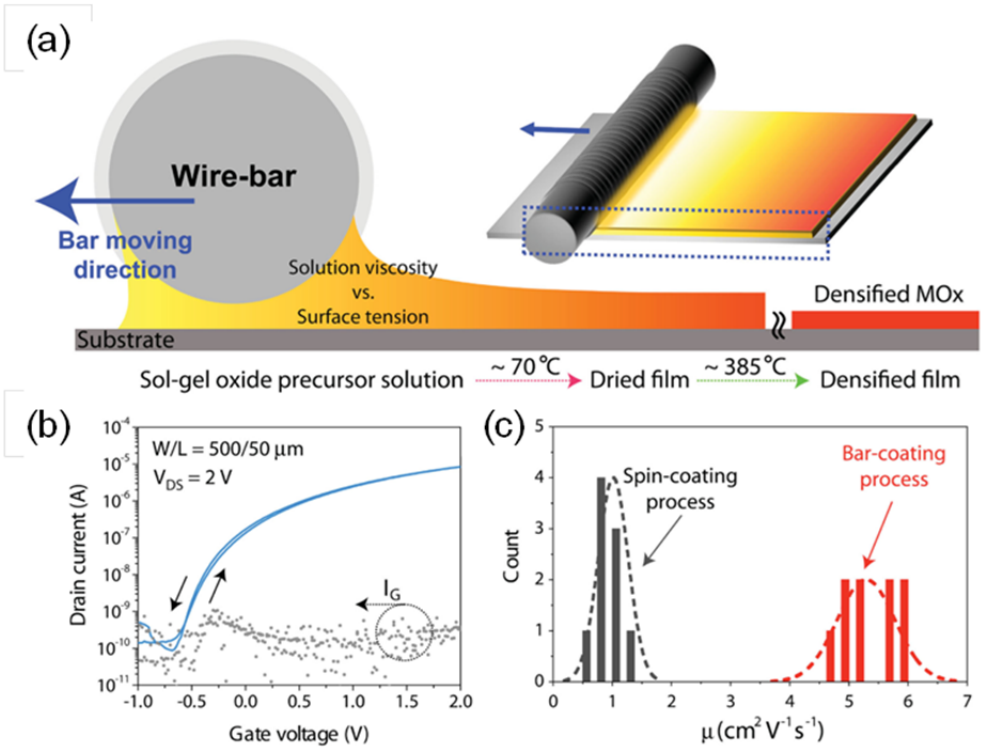


Figure 2.16. (a) Schematic for preparing thin films using a bar-coater system. (b) Representative transfer and output characteristics for all-bar-coated MO_x TFTs. (c) Comparison of statistical distributions for TFT mobility values for IGZO TFTs using either spin-coating or bar-coating deposition techniques.[114]

Different post-deposition processing techniques can be employed for treating as-deposited thin films to improve or alter many attributes of the thin films. These post-processing techniques can include thermal treatment/annealing at various

temperatures and under different atmospheres, optical processing, curing or conversion using UV light, ozone decomposition/cleaning etc. and even chemical treatments to remove contaminants or other species from the surface. As with the different types of deposition techniques, the post-processing methods must also be chosen and tuned to the specific resultant thin films.

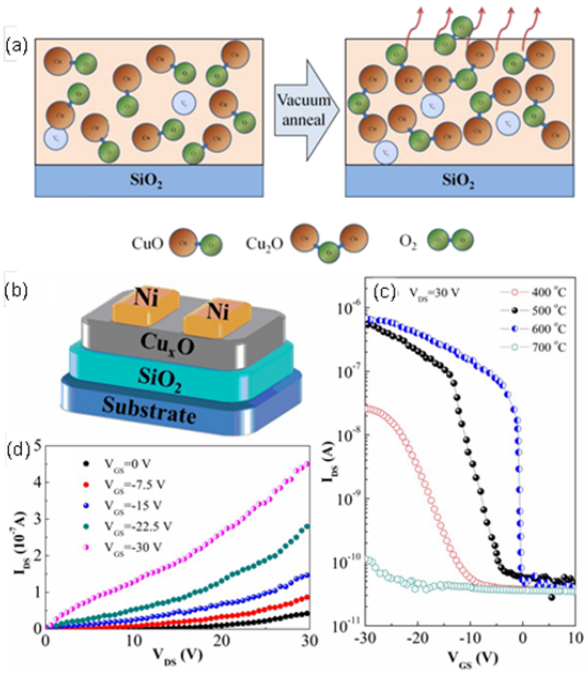


Figure 2.17. Schematic of Cu_xO thin films showing (a) effect of vacuum-annealing on thin film structure and (b) Cu_xO TFT diagram. (c) Transfer characteristics of Cu_xO thin films prepared at various thin film annealing temperatures under vacuum and (d) output characteristics of the same TFT annealed at 600 ^oC.[115]

Yu *et al*. deposited Cu_xO thin films, where x defines the variation away from stoichiometric semiconducting Cu_2O affected by annealing conditions, through spin coating of a copper acetate monohydrate based precursor solution. The investigation[115] showed that, in Figure 2.17 (a), vacuum annealing (at 2×10^{-6} Torr and 200 °C) altered the thin film structure and composition such that the initial CuO thin film was reduced to Cu_2O at increased annealing temperatures. The oxide reducing mechanism in this case was attributed to phase boundary migration induced

by oxygen out-diffusion along the moving phase boundary.[115-116] A Cu_xO TFT in Figure 2.17 (b) fabricated by the team, used a Si/SiO_2 substrate and Ni source/drain electrodes. The transfer characteristics of the same Cu_xO TFTs vacuum annealed at different temperatures in Figure 2.17 (c) improved up to an annealing temperature of 600 ^oC. At annealing temperatures above 600 ^oC the transfer characteristics degraded. The improvement at 600 ^oC is attributed to the formation of Cu_2O and subsequent beneficial changes in crystallinity and morphology whilst the degradation at temperatures above this was due to detrimental island growth.[115] While the annealing temperatures used may be too high for incorporation into current technologies, the role of the vacuum annealing can be studied for its effects at lower annealing temperatures.

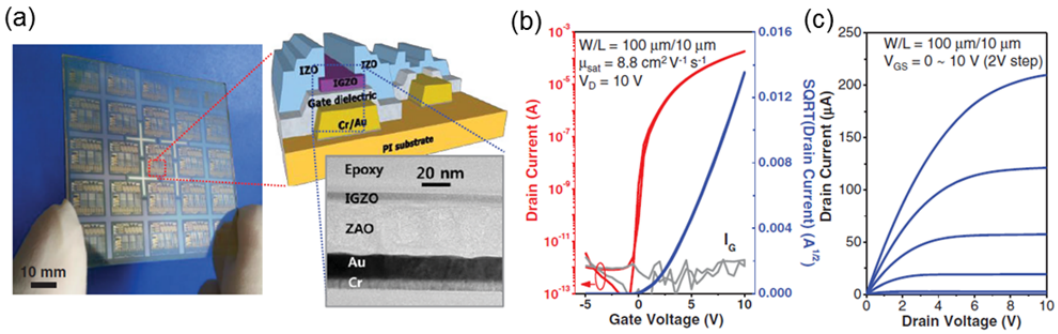


Figure 2.18. Spin coated IGZO TFTs and circuits on PI substrate. (a) Optical image, schematic and corresponding TEM cross-section. (b) Transfer and (c) output characteristics of IGZO TFTs with ZAO dielectric layer.[48]

One exciting and emerging technology currently under intense research is the formation of electronic devices on flexible substrates. These substrates allow for the incorporation of many different thin film devices within wearable and wear resistant applications such as wristwatches and e-paper displays. As with the incorporation of thin films into current devices and technologies, the application of solution processed methods in the formation of flexible electronics can be expected to be a driving force of research in the foreseeable future.[13, 117] The active interest in both flexible

electronics and the variety of solution processed deposition techniques means that the two areas complement one another in their compatibilities.[13]

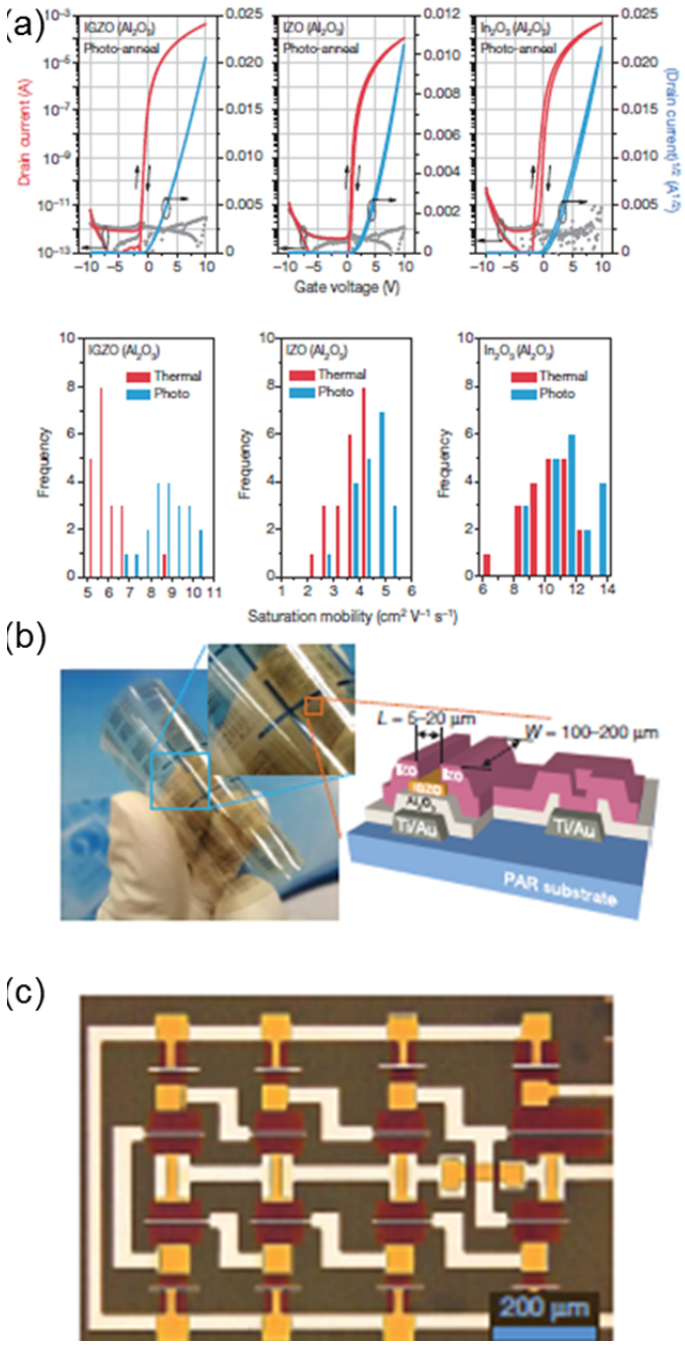


Figure 2.19. (a) Transfer characteristics and distribution of saturation mobility for both photo- and thermal-annealed GZO, IZO and In_2O_3 TFTs with an Al_2O_3 gate dielectric. (b) Optical image and schematic of IGZO TFTs and circuits on a flexible PAR polymer substrate and (c) zoomed in optical image of one of the seven-stage ring oscillator.[117]

A solution processed device deposited on a polyimide (PI) substrate composed of IGZO/ZAO TFTs and circuits by Jo *et al.*[48] is displayed in Figure 2.18

(a). Initially a PI layer was spin-coated onto a glass slide with the IGZO and ZAO TFT devices and circuits deposited afterwards. The IGZO and ZAO thin films were deposited through spin-coating while the gate electrodes were prepared with sputtering. The thin films were deposited and subsequently protected with passivation layers which allowed the samples to be peeled from the glass substrate producing a flexible electronic device. Jo *et al.* also incorporated a deep ultraviolet (DUV) photo-annealing step in forming the channel and dielectric layers so that high temperature anneals were not be required. The typical transfer and output characteristics of the IGZO/ZAO TFTs is shown in Figure 2.18 (b, c) and displays high field effect mobility of ~ 11 cm^2 V^{-1} s^{-1} with little to no hysteresis and a low gate leakage current.[48]

A comparison between the characteristic transfer and the saturation current mobility distributions of DUV photo- and thermally-annealed solution processed IGZO, IZO and In_2O_3 semiconductor layers on an Al_2O_3 gate dielectric with a source-drain voltage of 10 V is shown in Figure 2.19 (a).[117] Kim *et al.* demonstrated that the photo-annealed TFTs on glass substrates exhibited comparable or better electrical characteristics in relation to their thermally annealed counterparts. However, in order for the photo-annealing to facilitate these high-performance values, the photo-annealing stage must be performed in an inert atmosphere. In an inert atmosphere the photo-activation efficiency by the 184.9 nm emission does not undergo attenuation due to absorption of molecular oxygen.[117-118] In the presence of molecular oxygen the photo-activation efficiency is decreased resulting in poor thin film densification.[117] This photo-annealing method facilitated the formation of the flexible IGZO TFTs and circuits on a PAR polymer substrate seen in Figure 2.19 (b, c).[117] The formation of the seven ring oscillators (a common device for examples of

new hardware constructed of an odd number of logic NOT gates where feedback is used to decide a true or false signal), shows the scalability of the technique enabled by the combination of solution processed deposition and low temperature DUV photo-annealing techniques.

2.5.2 Optoelectronic Devices and Solution Processed TCOs

In electronic applications, metal oxide thin films are a promising candidate in the future development of modern technologies. In the area of optical and optoelectronic devices the use of metal oxide thin film materials is already an industry standard. The application of solution processed methods into these industries is also commonplace, however they are generally used for large blanket coatings rather than conformal coating of intricate and often high aspect ratio device architectures that are common in modern optoelectronic devices. Solution processed methods are not confined to metal oxide materials, particularly in optoelectronic and optical applications. Polymers, nitrides, sulfides and other oxides can also be deposited using these techniques which allows for a large diversity of device architectures to be made. The solution processed methods outlined in this section are commonly used with these other materials for depositing anti-reflection, self-cleaning, hydrophilic/phobic coatings and other such devices.[10, 55, 61, 119] The variety of applications in which solution processed layers of metal oxides are utilised are discussed in this section. In many of the cases each of the layers, including the metal oxide thin films, are deposited using solution processed techniques.

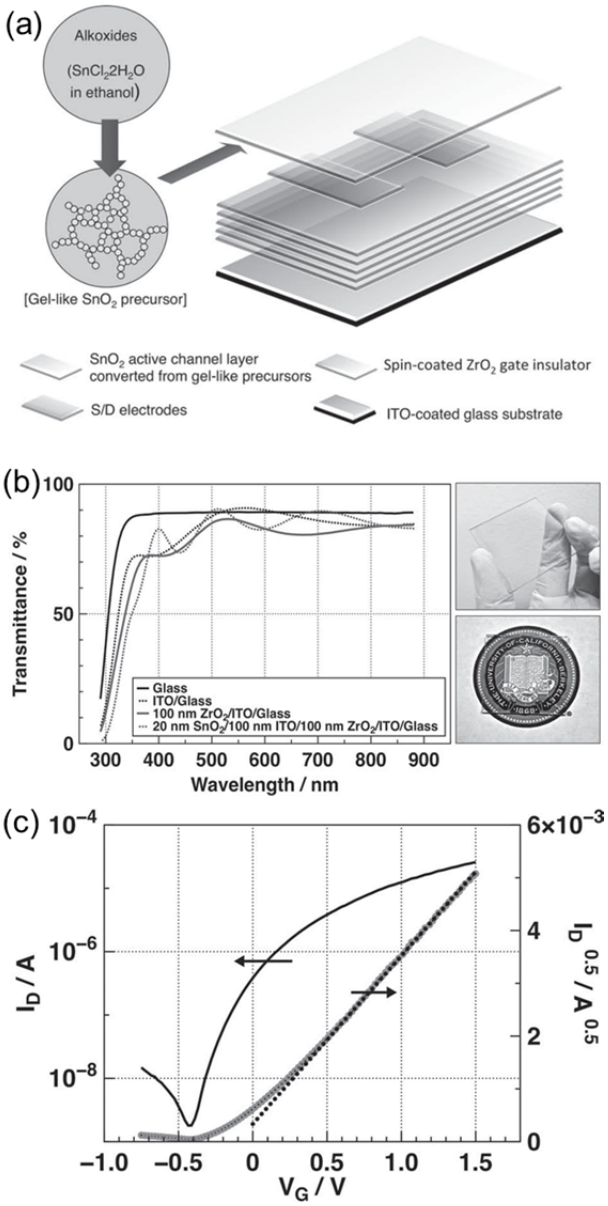


Figure 2.20. (a) Fully Transparent SnO_2/ZrO_2 TFT schematic and (b) accompanying optical transmission spectroscopy and images of the TFTs with ITO source and drain electrodes. (c) Transfer characteristics of SnO_2/ZrO_2 TFT devices.[120]

The use of transparent TFT devices is important as a key component in next-generation displays. To achieve this, TFTs discussed in the previous section must be prepared over large areas using all transparent materials. Figure 2.20 (a) shows a schematic of a fully transparent TFT formed using ITO source/drain electrodes and a SnO_2 channel layer utilising ZrO_2 insulators.[120] Both the channel and insulator layers were deposited using a spin-coating process while the source and drain electrodes

required a sputtering step. The transmission spectra and accompanying optical images in Figure 2.20 (b) illustrates the optical characteristics of the prepared TFT, which has a high visible transmission. A high visible wavelength transparency is ideal for use in optoelectronic devices intended for displays as they can be integrated into devices without lowering the optical quality. Along with the beneficial optical properties, excellent electrical performances were found for the fully transparent thin films. The transfer characteristics in Figure 2.20 (c) show a high field effect mobility of ~ 90 cm^2 V^{-1} s^{-1} possible without compromising a high transparency.[120]

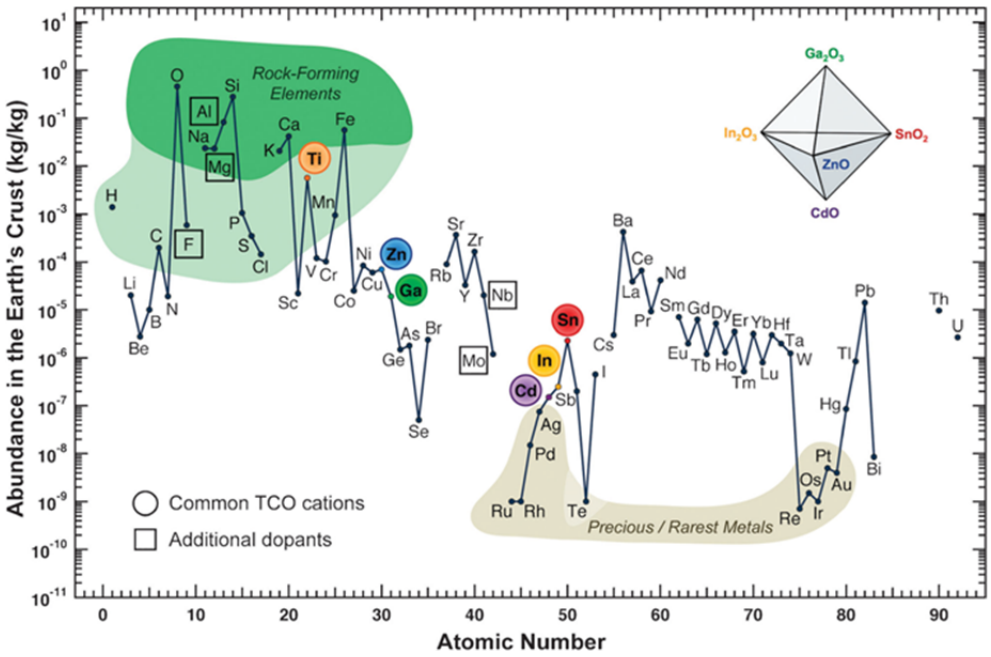


Figure 2.21. Mass fraction abundance of elements in the Earth's crust in relation to their atomic number. The common TCO cations are highlighted by coloured circles with additional possible dopants shown with squares.[121-123]

The conductive channel layer is an integral component of many electronic and optoelectronic devices. The conductive layer must retain not only a high conductivity but a good field-effect mobility, and maintain a high transparency in the wavelength range of interest. Transparent conducting oxides (TCOs) are a range of metal oxide materials which fill this requirement. In Figure 2.21, the relative abundance of the different TCO compatible elements within the Earth's crust is

shown. The lower the abundance, the higher the cost in their retrieval and thus the cost of the devices themselves.[121-123] There is a large drive in research to move away from Indium based TCO materials and instead examine more affordable and abundant materials such as Titanium, Molybdenum, Zinc and Gallium. ITO remains the industry standard due to its well-documented deposition and device characteristics but inroads are being made with other materials.[124-128]

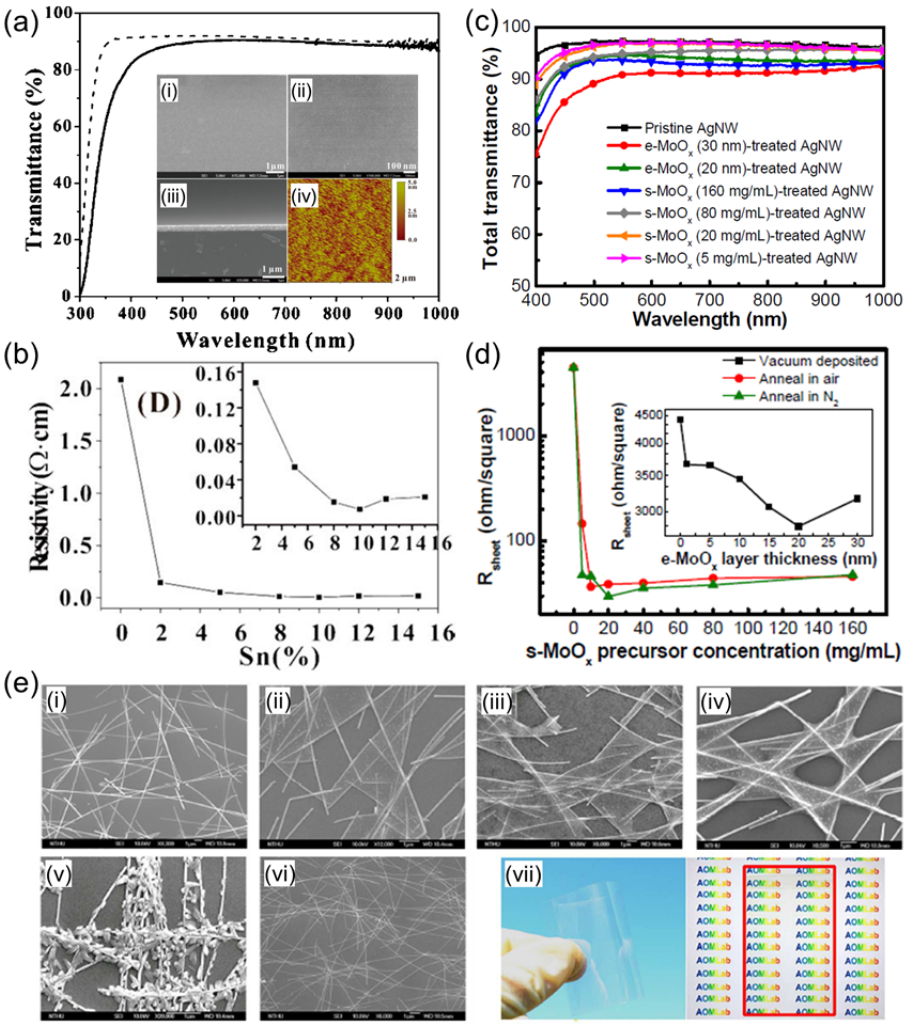


Figure 2.22. (a) ITO thin film UV-Vis transparency and SEM images of a Sn% = 10% with the accompanying glass spectra included.[124] (b) The effect of increased Sn% on the resistivity of the ITO thin film.[124] (c) UV-Vis transparency of pristine AgNW and MoO_x treated AgNWs and (d) thin film resistivity vs. MoO_x precursor concentration. (e) SEM images of (i) pristine AgNWs and AgNWs coated with MoO_x at concentrations of (ii) 5 mg/ml, (iii) 20 mg/ml, (iv) 40 mg/ml, (v) 160 mg/ml and (vi) evaporated 30 nm thin film. (vii) Optical images of flexible TCO material composed of AgNWs coated with MoO_x on a PEN substrate.[129]

While new TCO materials are being investigated so too is the layer morphology, where the morphology ranges from smooth TCO thin films to nanowire/dots and grids.[130-131] Two varieties of TCO architectures are shown in Figure 2.22, a planar deposition and a nanowire/thin film composite. The precursor concentration of the facile solution processed techniques were examined in both cases allowing TCOs with a range of conductivities to be deposited. Chen *et al.* deposited an ITO thin film with a high transparency comparable to the underlying glass substrate (Figure 2.22 (a)).[124] A high transparency is seen across the entire visible range with a decrease in the transmission shown at lower wavelengths due to the ITOs absorption edge.[124] The spin coated ITO thin films prepared by Chen *et al.* have a uniform surface morphology and thickness across a large area (inset Figure 2.22 (a)) where the percentage of Sn within the solution can lead to fine control of the resistivity of the ITO thin film (Figure 2.22 (b)).[124]

A different type of TCO thin film was prepared by Chang *et al.* from a nanowire/film architecture (Figure 2.22 (c – e)) comprised of a layer of AgNWs deposited by the bar-coating technique and coated with MoO_x by spin coating.[129] Using these two processes, they fabricated a highly conductive TCO over a large area, and importantly, demonstrated that this core-shell networked material assembly had better optical and electrical characteristics relevant to visible-frequency TCOs than either material alone. The aggregation of the MoO_x coating around the AgNWs was postulated to lower the overall junction resistance, but they did not demonstrate any optimization of the density and spatial distribution of nanowire contacts nor a percolation threshold for this material system that is correlated to maximum network conductivity for a defined overall transmittance.[129] They did demonstrate for the networks examined, in Figure 2.22 (c), that the overall optical transmission of

AgNWs treated with evaporated MoO_x is marginally better, and was a function of the MoO_x precursor concentration.[129]

As the MoO_x precursor concentration was increased by Chang *et al.* the resistivity of the MoO_x treated AgNW thin film decreases (Figure 2.22 (d)).[129] The changes in resistivity can be attributed to the MoO_x coating the AgNWs where the SEM images of Figure 2.22 (e) show increasing concentrations of the spin-coated MoO_x resulting in thicker deposits around the AgNWs which due to increased defects and agglomeration effects can be detrimental to both optical and electrical properties. The optical images of Figure 2.22 (d) (vii) show how Chang *et al.* used this technique to coat a flexible polymer substrate while maintaining high conductivity and optical transparency with a high level of mechanical strength.[129] The use of carbon nanotube meshes are also under investigation for TCO preparation similar to the AgNW case discussed by Chang *et al*.[131]

In an electrochromic (EC) material, light transmission can be reversibly varied through different values with the application of an electrical voltage.[20, 132] The use of EC materials is of great benefit in the application of green technologies such as smart windows and adjustable electronic displays. The ability to alter light absorption of windows within a modern building in an easily controllable way can decrease the level of cooling required through air-conditioning on warmer days. The EC mechanism involves the insertion and extraction of small ions, such as lithium, between a transparent conductor and EC material. In the case of an EC device, the ion is stored in a transparent film when not intercalated with the EC material.[20] The degree of optical transparency can be varied through application of an electric field with many devices facilitating degrees of transparency through voltage adjustments.

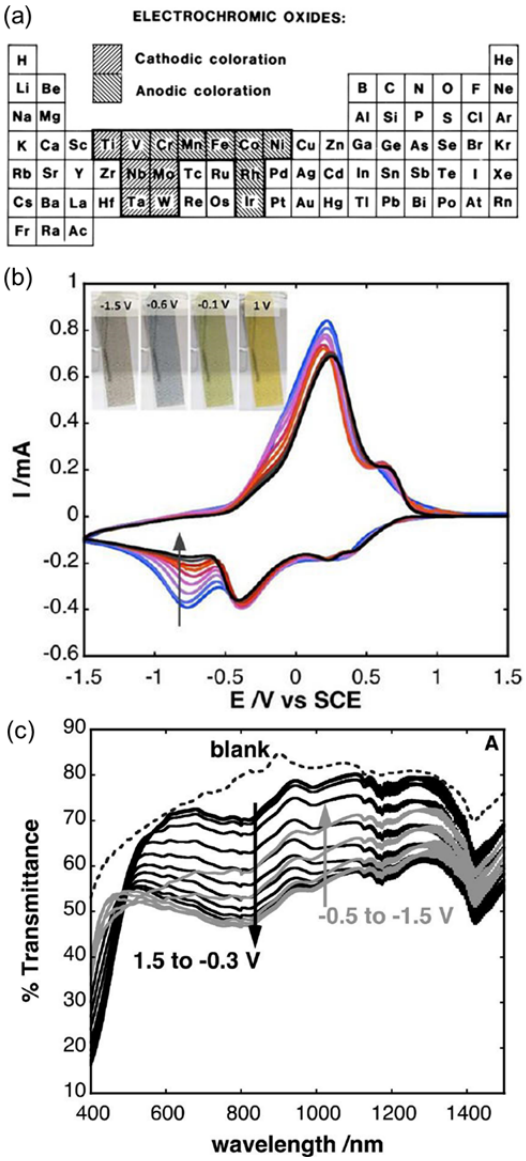


Figure 2.23. (a) Periodic table showing various metal oxides capable of displaying clear electrochromism. The different shadings indicated whether they display clear cathodic or anodic electrochromism.[20, 132] (b) Cyclic voltammetry of inkjet-printed VO thin films highlighting the change in colour at various potentials. (c) Vis-NIR spectra of a solid state VO device showing the transmission characteristics at varied applied potentials.[92]

The periodic table in Figure 2.23 (a) highlights the various metals that in oxide form are capable of varying optical transmission through EC processes.[20, 132] In an EC cathodic material, the switch from bleached to coloured states is achieved through ion insertion while an anodic material requires ion extraction. Vanadium based oxides[132] are unique as they are considered intermediates which can undergo

EC processes in both anodic and cathodic regimes depending upon their oxidative state.[20] The amount of a materials available intercalation sites and the required diffusion distance impact on the optical contrast (change in transparency between coloured and bleached states) and switching time respectively.[133-134] Therefore, by reducing the required diffusion distance and increasing the available intercalative sites of a material both the efficiency and bleaching/coloration wavelength range of a material can be increased.

An example of an inkjet-printed VO thin film EC device is displayed in Figure 2.23 (b) where a number of transparency and colouring effects can be produced through the application of different voltages related to lithium ion insertion/extraction amounts within the VO material.[92] Previously Costa *et al.* also presented the same inkjet-printing method and characterisation technique for a tungsten oxide EC material with a remarkable colour contrast, particularly in the NIR region.[135] Different optical properties can be observed in Figure 2.23 (b) for a number of applied voltages in the VO thin films deposited by Costa *et al.* The corresponding pairs of oxidation and reduction peaks for each transition is shown in the cyclic voltammetry graph of Figure 2.23 (b) with the relevant Vis-NIR transmission spectra displayed in Figure 2.23 (c).[92] Costa *et al.* have demonstrated that changes in optical transparency are not limited to the visible wavelength range but also can affect the NIR wavelengths thus allowing EC devices capable of filtering thermal energy while transmitting visible wavelengths, can be prepared.

Other “green” thin film optoelectronic technologies under investigation are those which utilise light for energy generation. Many types of devices, architectures, and various energy generation processes exist which would be too high in number and complexity to cover in this review. Instead a brief description of the most recent

advances in the application of solution processed thin film coatings for energy conversion and generation is discussed, namely in the areas of photo-catalysis and photovoltaics.

The use of photocatalytic processes in the splitting of water for the production of hydrogen as a fuel source has been under investigation for many years.[136] New techniques and methods in improving the efficiency are developed through increased research of photocatalysts, electrode materials and device architectures.[22, 137-139] Metal oxide coatings have been reported to increase the stability of semiconductors for long term photocatalytic processes[22, 138] where the variety of deposition methods available improves their functionality. TiO_2 is commonly used both by itself and in conjunction with other materials for photocatalytic applications.[137, 139-140]

One novel area which has the potential for improving the output of optical energy generation devices is the process of combining two types of devices that both harness energy from optical radiation. A common device architecture that uses this method are tandem solar cells, where multiple cells are layered on top of one another with each tuned to absorb different wavelengths, thus utilising more of the incoming radiation.[141] However, recently there has been much research into the incorporation of different types of devices so that two types of energy conversion can occur. The schematic for a combined photocatalytic and photovoltaic device is shown in Figure 2.24 (a), where both chemical and electrical energy are generated from the incoming photon radiation.[21]

In the device shown in Figure 2.24 (a), Abdi *et al.* combined an amorphous silicon solar cell with a gradient doped tungsten $BiVO_4$ photoanode using a cobalt-phosphate oxidation catalyst deposited through spray pyrolysis. The use of a

common solar cell technology coupled with a state of the art photoanode and photocatalyst resulted in a device with a solar-hydrogen efficiency of 4.9% at a photocurrent of ~ 4 mA cm^{-2}.[21] A novel aspect to the device deposition was related to the deposition method for forming the gradient doped W:$BiVO_4$ electrode. The state of the art electrode was deposited by altering the precursor concentration in-situ during the spray pyrolysis stage. The use of the cobalt-phosphate oxidation catalyst also increased the photocurrent to high levels as can be seen in Figure 2.24 (b).[21]

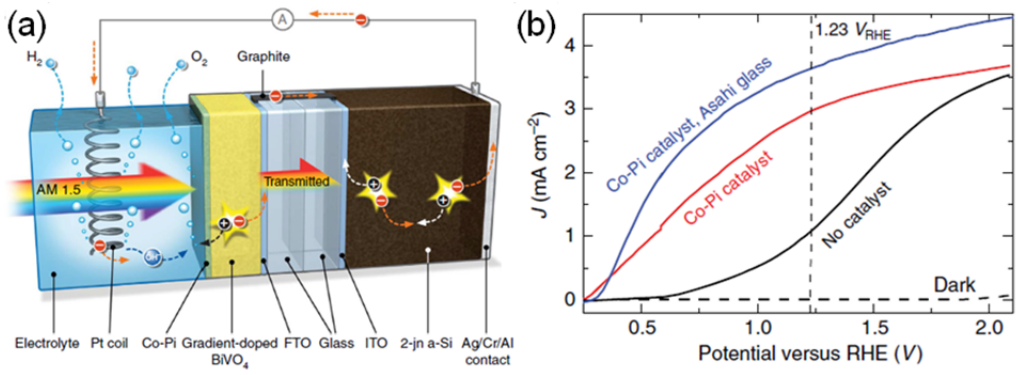


Figure 2.24. (a) A schematic representation of a combined gradient-doped W:$BiVO_4$ and amorphous-Si solar cell. (b) Photocurrent vs. voltage curve of un-catalysed and Co-Pi-catalysed gradient doped W:$BiVO_4$ electrodes. The black and red lines are for devices deposited on TEC-15 with the blue line data deposited on conductive glass substrates.[21]

The use of metal oxide thin films in photovoltaics is commonplace, with applications for different materials possible in each of the components, from the TCO, active layer and charge extraction layers. Yip *et al.* described how the use of all solution processed depositions and the incorporation of new materials and device architectures could theoretically increase the efficiency of single and tandem solar cells by ~10 % and ~15 % respectively over the next 10 years.[142] The charge extraction layer is required, particularly in polymer solar cells, where the extraction of the photo-generated charges needs to be facilitated.[91, 97] There are many options available for use as the charge extraction layer, notably PEDOT:PSS, however, in

recent years many different high bandgap transition metal oxides have been investigated due to their more stable electrical characteristics. One of the most notable transition metal oxides examined for this application is V_2O_5 with many publications on its efficacy.[9, 90, 143-145]

The deposition of VO materials has previously been discussed in this review and demonstrates that V_2O_5 can be deposited through a large range of techniques. Each of these methods can be adjusted and fine-tuned so that the desired thin film morphology can be deposited. The effect of either V_2O_5 or PEDOT:PSS hole extraction layers on the power conversion efficiency of an organic solar cell under ambient conditions is shown in Figure 2.25 (a).[97] The data shows that a V_2O_5 based device has an increased lifetime over an equivalent PEDOT:PSS device which completely degraded after 400 h in air with no photovoltaic activity recorded after this time. This drop in efficiency was attributed to the degradation of the PEDOT:PSS layers over time while the V_2O_5 layers were more robust with a longer life cycle. The power conversion efficiency for the V_2O_5 charge extraction layers at different thickness in the same organic solar cells is shown in Figure 2.25 (b). The team discovered that the highest power conversion efficiency is possible at lower V_2O_5 thicknesses. Zilberberg *et al.* postulated that at higher thicknesses, the increased optical absorption of the V_2O_5 thin films in the absorption wavelength range of the P3HT active material decreased the efficiency of the devices.[97] When the thickness of the V_2O_5 layer was too large, the benefit of the material in facilitating the extraction photo-generated charge carriers was compromised.

MoO_x is another candidate as a charge extraction layer, which similarly to V_2O_5 can be deposited using a variety of solution processed methods. In Figure 2.25 (c) an organic solar cell incorporating a MoO_x anode interfacial layer is depicted. A

comparison was made by Yi *et al.* between a PAD solution processed MoOx thin film to both evaporated MoO_x and PEDOT:PSS. The UV-Vis transparency of the different materials shows that the solution processed MoO_x has the highest transmission in the Vis-NIR range, and the highest photocurrent density of the three types of material they investigated.[146] This improvement in the PAD deposited MoO_x thin film compared to the evaporated thin film is attributed to the higher transparency at full surface coverage. The usability of solution processed methods in depositing uniform metal oxide thin films over large areas is of the utmost importance for their use in next-generation photovoltaic devices.

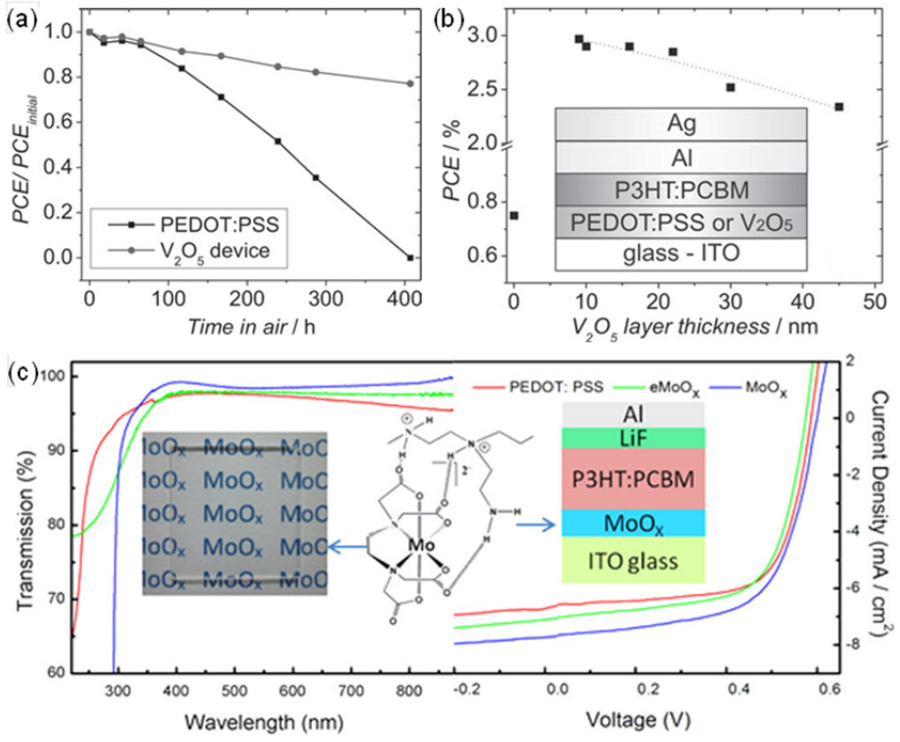


Figure 2.25. (a) Power conversion efficiency of organic solar cells utilising either a PEDOT:PSS or V_2O_5 hole extraction layer in an ambient air atmosphere. (b) Power conversion efficiency of the same organic solar cells with increasing thickness of V_2O_5 hole extraction layer. Also included is the efficiency with no V_2O_5 layer.[97] (c) UV-Vis Transmission of PEDOT:PSS, evaporated and spin-coated/PAD MoO_x (included optical image) thin films. Characteristic current density vs. voltage for the three types of films used as interfacial layers in organic solar cells.[146]

2.5.3 Miscellaneous Device Applications

As outlined in this review, significant developments have been demonstrated for solution processed metal oxide thin film deposition for a range of applications where optical, electronic, electrochemical and structural properties can not only be controlled in terms of uniformity and quality, but offer alternative methods for unique morphologies and compositions for a range of applications. The electronic and optoelectronic applications discussed above are some of the most common examples where solution processed methods are being applied. There are also a large number of other applications where niche uses are being investigated. In this section a brief overview of the use of solution processed methods in other thin film applications is discussed.

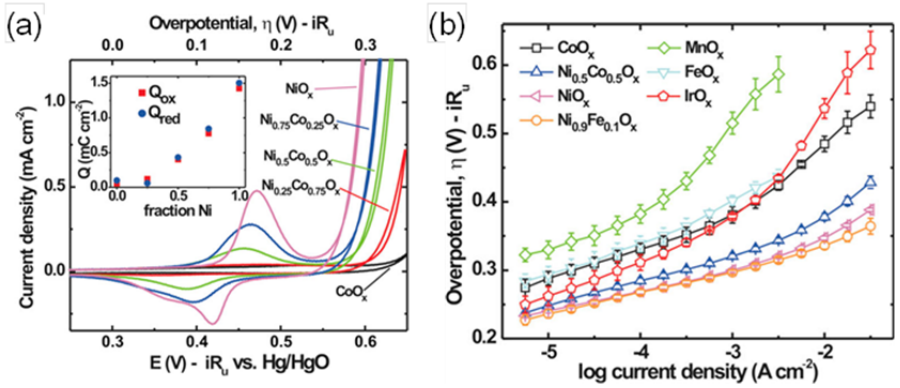


Figure 2.26. (a) Voltammetry of a number of conditioned thin films with differing Ni contents for electrocatalytic testing with an integrated charge for the redox processes as a function of Ni content. (b) Comparison of steady state Tafel measurements for different thin films in 1 M KOH.[147]

The use of metal oxide thin films in photocatalytic processes was discussed previously, however, their use in electrocatalytic devices is also important, and has received renewed interest in the last couple of years. In a water splitting electrocatalytic device, hydrogen and oxygen are produced through the electrolysis of water. A large factor for increasing their efficiency is through correct electrode

and catalyst choice, as is also the case in many photocatalytic processes. The use of thin film electrocatalysts can have many benefits such as minimising the catalysts effect on overpotential due to their thinness, controllable film composition and morphology.[147] In Figure 2.26, different thin film electrocatalysts were prepared and their oxygen evolution reactions compared. Comparisons were made between the different materials with conditioned cyclic voltammetry measurements and Tafel measurements, showing that the $Ni_{0.9}Fe_{0.1}O_x$ was a more efficient electrocatalyst than one of the best known electrocatalysts, IrO_2, for the types of measurements performed.[147] Interestingly, Trotochaud *et al.* were also able to show *in-situ* that the layered hydroxide/oxyhydroxide were the active catalyst through a structural transformation between oxide to hydroxide/oxyhydroxide.[147]

There are many types of sensors and sensing devices available, from thermal measurements using liquid cells to electronic sensors which monitor the electrical response of materials in different environments. Thin film sensors are particularly useful due to their small size and the range of materials available. The thin film sensor shown in Figure 2.27 (a) was composed of a spray deposited V_2O_5 material prepared at different pyrolysis temperatures. The sensing response curve for the V_2O_5 layers deposited at different temperatures was examined and shows that the highest response and thus most sensitive layer is that heated to 300 ^oC.[148] One of the factors that improved gas sensing responses of the V_2O_5 thin films deposited at 300 ^oC was the smaller material grain size. With a smaller grain size and an increase in surface area of the electrode, more of the surface is available for the sensing to occur and thus the sensitivity increases.[148] Possible methods for further improvement of the efficiencies may be the formation of mesoporous electrodes utilising the same materials but with greater surface areas through inverted opal morphologies.[149-150]

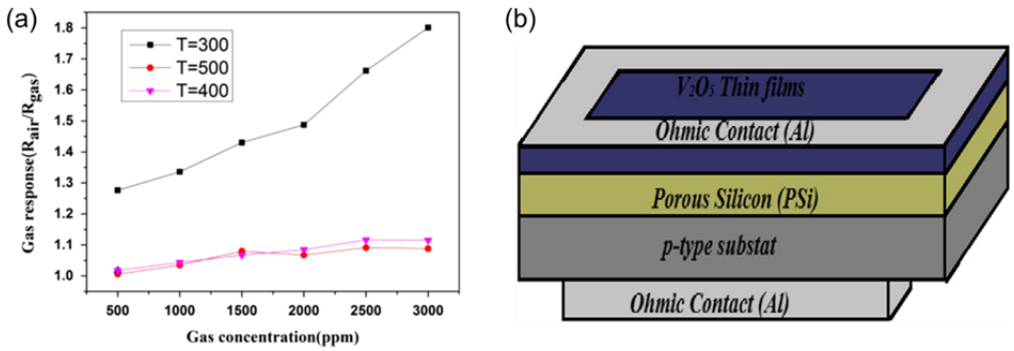


Figure 2.27. (a) Sensing response curve as a function of ethanol concentration for V_2O_5 based thin film sensors deposited through spray pyrolysis at different pyrolysis temperatures.[148] (b) Schematic of a proposed V_2O_5/porous Si/Si ethanol sensor.[95]

The incorporation of different VO's into sensing devices is commonplace due to the materials large range of oxidation states and its history as an industrial catalyst. The different VO materials can be used in a variety of sensors as either the main active material or for increasing the sensitivity, such as in the schematic shown in Figure 2.27 (d) where the V_2O_5 is deposited on top of an amorphous silicon electrode to increase the sensitivity for ethanol detection.[95] The implementation and extended use of VO materials can be expected to continue for implementation with state of the art sensors and materials.[1, 151-153]

Solution processed methods are not limited to pure electrical or optical applications, but can also be applied to areas such as energy storage. In Figure 2.28 (a) a metal-oxide-semiconductor (MOS) device for use as a capacitor was deposited through solution processed techniques. The SEM images in Figure 2.28 (a) show two different morphologies deposited using a dip-coating method on either glass or p-Si substrates.[154] The change in surface morphology is common in these types of depositions but can be adapted using many of the techniques discussed previously. The $BiFeO_3$ capacitors deposited by Cetinkaya *et al.* showed stable insulation

characteristics with a density interface states measurements equivalent to thin films deposited using more expensive techniques such as sputtering.[154]

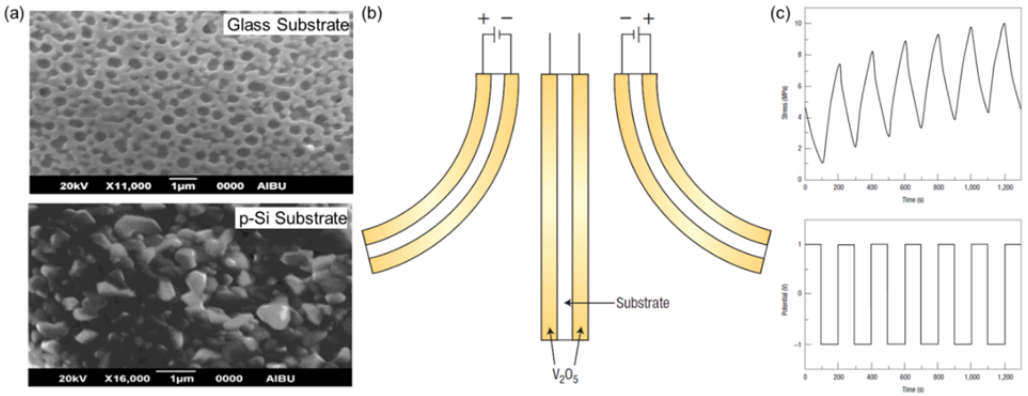


Figure 2.28. (a) SEM images of solution processed $BiFeO_3$ thin films deposited on glass and p-Si substrates for use as capacitor electrodes.[154] (b) Schematic of a V_2O_5 free standing cantilever actuator[155] and (c) Generated stress (top) and corresponding applied potential (bottom) as a function of time.[156]

The electrochemical attributes of different materials are studied for integration into energy storage, electromechanical sensors and capacitors. A novel application for V_2O_5 is demonstrated in the schematic of Figure 2.28 (a) where standalone nanofiber sheet actuators were synthesised and tested.[155-156] The nanofiber sheet actuators were synthesised from a sol-gel mixture dropped onto filter paper and peeled away. The resulting standalone layer of entangled V_2O_5 nanofibers were tested by Gu *et al.* for electromechanical actuation by immersing in a LiCl aqueous electrolyte. Upon insertion and removal of the lithium into the V_2O_5 through voltage sweeps the cantilever flexed either left or right as shown in the schematic. The mechanical stress that the layer was experiencing during the flexing was analysed by Gu *et al.* using a sophisticated optical technique.[156] The generated stress and corresponding applied voltage is presented in Figure 2.28 (c). The structure of the V_2O_5 material in this case showed a lower voltage requirement than other ferroelectric or electrostrictive materials, in part due to the ability of V_2O_5 to insert

Li-ions between the layers. Gu *et al.* theorised that the many uses and applications of V_2O_5 would lead to the materials incorporation into multifunctional devices which would take advantage of their multifunctional properties, such as multicomponent sensors.[156] The research group led by Baughman have investigated many other materials utilising this effect for artificial muscle applications.[157-158]

The possible electrochemical responses of many metal oxide thin films mean that they are not limited to use in sensors and electronic or optics but can also be of great benefit for battery technologies.[159-160] An ideal thin film battery would have a compact size while retaining high electrode surface area and a rapid charge/discharge cycle without capacity fade.[80, 161-162] These attributes can be obtained through the use and incorporation of flexible electrodes and substrates with thin film technologies. The capability of solution processed techniques in providing a battery with these capabilities while also allowing simpler doping and composition control is an area under intense research.[163-164] Pulverisation of the electrode during charge/discharge cycles caused by the stresses of insertion/removal of Li is a detrimental effect for Li-ion batteries, which tends to decrease the lifetime of devices. By wrapping and moulding the electrode and keeping the thin film to a low thickness a sufficiently high surface area can be formed. A thin film with sufficiently low thickness can accommodate the stresses caused by the insertion/removal of the Li ion in the z direction which can result in a high degree of reversibility in the cycle process.[81]

The ordered mesoporous α-Fe_2O_3 battery electrode shown in Figure 2.29 (a) was deposited from a liquid precursor through dip-coating onto various substrates such as FTO or p-Si and utilised a diblock copolymer to structure the surface morphology.[165] The cyclic voltammetry and associated stored charge vs. sweep rate

relationship for the α-Fe_2O_3 battery electrode is shown in Figure 2.29 (a) where the increased sweep rates result in less stored charge. The SEM images show that there is little large-scale degradation of the α-Fe_2O_3 thin films after 200 cycles of lithium insertion/removal.[165] The findings by Brezesinski *et al.* demonstrated that thin films of an inexpensive material such as α-Fe_2O_3 can be cost-effectively deposited using a di-block copolymer assisted solution processed technique and used to prepare a long lifetime Li-ion battery.

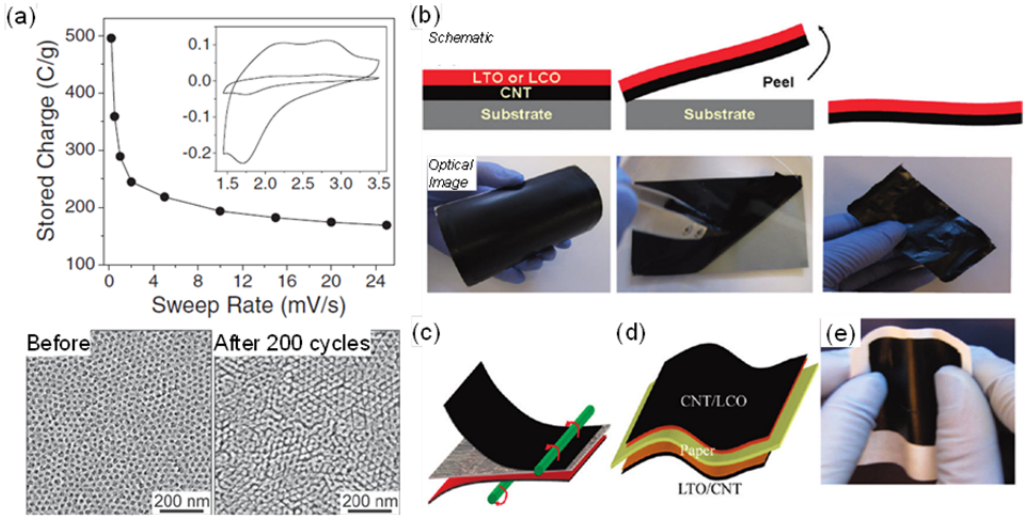


Figure 2.29. (a) Charging rates calculated from cyclic voltammetry at various sweep rates for α-Fe_2O_3 Li-ion battery electrodes. An associated cyclic voltammetry graph for two different sweep rates after 5 cycles is included in the inset.[165] (b) Fabrication schematic and corresponding optical images outlining the formation of a solution processed free standing LTO/LCO Li-ion electrode. (c) Lamination process where the free standing film is adhered to paper. (d) Schematic and (e) optical image of a Li-ion paper battery prepared from the free standing LTO/LCO Li-ion electrodes.[164]

The preparation of a thin, flexible Li-ion paper battery is shown in Figure 2.29 (b – e) where the different layers are deposited through a doctor blade technique. A carbon nanotube film is used as a conductive layer while the battery electrodes consisted of either $Li_4Ti_5O_{12}$ (LTO) or $LiCoO_2$ (LCO) materials also deposited using the same doctor blade technique.[164] As demonstrated in Figure 2.29 (a) both the carbon nanotube and active materials are deposited onto a stainless steel

substrate and then peeled off forming a free standing film. This free standing film is then laminated onto a paper substrate, Figure 2.29 (c), which is then prepared into a flexible thin film battery schematically shown in Figure 2.29 (d). An optical image of the final thin film battery is shown in Figure 2.29 (e). The final battery retained a capacity of ~110 $mAhg^{-1}$ after 20 cycles. The work by Hu *et al.* is a proof of concept for the realisation of an all solution processed flexible thin film battery for use in applications where embedded power devices are needed such as smartwatches, sensors and phones.[164]

2.6 Conclusions and Outlook

This review discussed and highlighted aspects related to the formation of metal oxide thin films. Specifically, solution processed techniques offer a wide range of possible deposition routes, ranging from the common spin-/dip-coating methods to the sophisticated printing and roll-to-roll depositions.[1] Further development of these techniques will be required for industrial scale deposition required for next-generation applications that involve not only fully solution processable devices and active materials, but coating of patterned structures and non-planar, even flexible, materials.[74, 121] As detailed in this review, many of the precursors and deposition methods and parameters in solution processed techniques are interchangeable to some degree, which facilitates scalability and flexibility in coating method, composition, and sequential deposition, ease of doping or modification of chemical, electrical and optical properties for example, and the comparative simplicity and accessibility of the infrastructure.

There is scope yet for many new material compositions through precursor design. Analogous to the influence of precursor design, chemical interactions and modes of decomposition also influence ALD; for example the rational synthesis of precursors will need to consider control over volatility, decomposition, surface interaction or immobilisation and wetting on the surface of interest. These parameters are especially important in thin film technologies where capacitance, optical transmission, absorption, dielectric constant and defects influence many physical parameters which need to be controlled to a high degree of precision. Polymer-assisted methods offer the possibility of mitigating dewetting phenomena during some methods of coating and subsequent conversion to the active materials from an inorganic precursor, sol or solution. Practically, understanding the evolution and basis of dewetting processes during thermolysis or hydrolysis is important for enhancing uniform surface coverage from dip-coated materials. Recently, several reports have shown that dewetting of thin liquid polymer films could be suppressed by the presence of "inclusions", which are often nanoparticles.[98, 166] Spinodal clustering and nucleation dewetting effects are characterized by specific pattern formation in liquid surface films that eventually solidify. This thesis also explores this effect directly, and demonstrated how pinholes and other defects are minimized in vanadium oxide thin films formed from liquid precursor due to the formation of nanoscale crystallites of the oxide within the hydrolysing film, thus maintaining uniformity within the deposit and avoiding dewetting. Dip-coating or spin-casting liquid precursors and nanofluids can in principle be extended to improve the consistency in sequential or iterative multilayer deposits of hybrid materials and provides a liquid-based route for crystallized thin vanadium oxide films with exotic thermal, electrical, and optical properties.

The analytical techniques summarised in this review are not limited to solution processed methods but serve as a means of directly comparing the depositions to the currently employed techniques, such as sputtering, evaporation and vapour assisted methods. Ultimately, any industrial deposition must involve solution chemistry and the substrate/device geometry. There are challenges that still remain for high speed coating of very large flat panels, and recent research has tackled 3D deposition onto substrates with complex or tortuous geometries. These deposition techniques are becoming increasingly important in photocatalysis, photovoltaics, angle-independent absorber and hole-conducting layers in solar cells, and in water splitting devices. Operational stability of solution processed films in certain electrochemical systems also relies on uniformity in deposition, to avoid pitting, corrosion and localised electric field-induced electrochemistry at grain boundaries, or defects in thin films formed from liquid precursors. Such defects also present reliability and integration challenges for TFT and other electronic devices. New avenues of research that look specifically at methods for stabilization of drying, hydrolysis or polymerizing thin films from liquids are thus of great importance.

For metal oxides, cross-linking between solution chemistry, inorganic syntheses and the (opto)electronic characteristics required by ultra-thin device materials may provide new avenues for non-conventional materials that may be CMOS compatible. Materials systems including mixed metallo-organic precursor systems, alkoxides, carboxylate precursors (long and short chain), and related offer advantages during thermolysis akin to ALD precursors, where interaction with the substrate, particularly complex geometrically shaped surfaces, may aid in positioning of the precursors for eventual conversion to the desired oxide phase. In addition, such phases may be converted to completely transparent films for uniform, well-

adhered optical coatings, anti-reflection layers, graded-index sequentially deposited coatings and other applications. This thesis also presents advancements in this regard, using both the film and the substrate co-operatively during crystallization to create a unique completely transparent thin oxide film.

For uniformity in electronic and photonic devices, solubility of all materials in the solvent, i.e., formation of a stable one-pot solution for a range of coating methods requires control of several critical parameters:

a) The precursor solution must be stable for a long time, for storage and roll-to-roll processing environments for example.
b) Precursor systems that are ‘pure’ after thermal treatment/pyrolysis, i.e. only oxygen and the respective metal cation(s) remain to form the uni-, bi-, ternary etc. oxide of choice.
c) Effects such as macrophase separation, unless wanted, must be avoided or prevented during the drying/thermolysis conversion processes. This may necessitate solution rheology control and the needs to prevent comet defect and streaking during spin coating for example, and solidification at the nozzle of an inkjet printing deposition method where pressure differences corresponds to large temperature changes.
d) Crack and compositional non-uniformity formation during thermal processing should be prevented, and extension to control of these effects on substrate with flat surfaces and coatings on vertical sidewalls.
e) Once formed, the films should resist degradation during operation or processing.

In the future, solution processed oxide deposition may facilitate the development of doped metal oxides that use substrate species or indeed the controlled inter-diffusion of species between dissimilar coated layers for diffusional doping, and this may be spatially isolated across a film. Such method could in principle be extended to polar oxide materials with pyro- and piezoelectric characteristics, high and low-k dielectric materials, nanocrystal embedded dielectrics, and oxide memristors, and the ability to rationally control viscosity to enable or optimize infilling of patterned surfaces or structures for optical coatings, or hard-masks, high density multi TB/sq. inch. materials for magnetic recording etc. In addition, halted dewetting of multiphasic solution processed materials, may provide embedded materials systems that can approximate composites, providing routes for thermoelectric materials whose phonon scattering and thermal conductivity reduction is based on mesoscale scattering at point defects and compositional variations including grain boundaries caused by phase separation within thin films. Solution processable materials for Li-ion batteries and other composites for energy storage, where mass loading, tap density, thickness and stable connectivity with the substrate are very important, should also be possible with continued research and development.

2.7 References

1. Schneller, T.; Waser, R.; Kosec, M.; Payne, D., *Chemical Solution Deposition of Functional Oxide Thin Films*. 1st ed.; Springer: London, 2013; p 796.
2. Bhuiyan, M. S.; Paranthaman, M.; Salama, K. Solution-derived textured oxide thin films—a review. *Supercond. Sci. Technol.* ***19***, R1 (2006).
3. Meyerhofer, D. Characteristics of resist films produced by spinning. *J. Appl. Phys.* ***49***, 3993-3997 (1978).
4. Chandra, R. D. *et al.* Tuning Electrical Properties in Amorphous Zinc Tin Oxide Thin Films for Solution Processed Electronics. *ACS Appl. Mater. Interfaces* ***6***, 773-777 (2014).
5. Si Joon, K.; Seokhyun, Y.; Hyun Jae, K. Review of solution-processed oxide thin-film transistors. *Jpn. J. Appl. Phys.* ***53***, 02BA02 (2014).
6. Park, J. S.; Maeng, W.-J.; Kim, H.-S.; Park, J.-S. Review of recent developments in amorphous oxide semiconductor thin-film transistor devices. *Thin Solid Films* ***520***, 1679-1693 (2012).
7. Park, J. H. *et al.* Low-temperature, solution-processed ZrO2:B thin film: a bifunctional inorganic/organic interfacial glue for flexible thin-film transistors. *ACS Appl. Mater. Interfaces 7*, 4494-4503 (2015).
8. Park, S. *et al.* In-Depth Studies on Rapid Photochemical Activation of Various Sol–Gel Metal Oxide Films for Flexible Transparent Electronics. *Adv. Func. Mater.* ***25***, 2807-2815 (2015).
9. Chen, C.-P.; Chen, Y.-D.; Chuang, S.-C. High-Performance and Highly Durable Inverted Organic Photovoltaics Embedding Solution-Processable Vanadium Oxides as an Interfacial Hole-Transporting Layer. *Adv. Mater.* ***23***, 3859-3863 (2011).
10. Faustini, M. *et al.* Hydrophobic, Antireflective, Self-Cleaning, and Antifogging Sol−Gel Coatings: An Example of Multifunctional Nanostructured Materials for Photovoltaic Cells. *Chem. Mater.* ***22***, 4406-4413 (2010).
11. Tepavcevic, S. *et al.* Nanostructured Bilayered Vanadium Oxide Electrodes for Rechargeable Sodium-Ion Batteries. *ACS Nano* ***6***, 530-538 (2011).
12. Glynn, C. *et al.* Large directional conductivity change in chemically stable layered thin films of vanadium oxide and a 1D metal complex. *J. Mater. Chem. C* ***1***, 5675-5684 (2013).
13. Thomas, S. R.; Pattanasattayavong, P.; Anthopoulos, T. D. Solution-processable metal oxide semiconductors for thin-film transistor applications. *Chem. Soc. Rev.* ***42***, 6910-6923 (2013).
14. Nayak, P. K. *et al.* Thin Film Complementary Metal Oxide Semiconductor (CMOS) Device Using a Single-Step Deposition of the Channel Layer. *Sci. Rep.* ***4***, 4672 (2014).
15. Eliason, C. M.; Shawkey, M. D. Antireflection-enhanced color by a natural graded refractive index (GRIN) structure. *Opt. Express* ***22***, A642-A650 (2014).
16. Song, H. *et al.* Nanocavity Enhancement for Ultra-Thin Film Optical Absorber. *Adv. Mater.* ***26***, 2737-2743 (2014).
17. Xi, J. Q. *et al.* Optical thin-film materials with low refractive index for broadband elimination of Fresnel reflection. *Nat. Photon.* ***1***, 176-179 (2007).
18. Shrotriya, V. *et al.* Transition metal oxides as the buffer layer for polymer photovoltaic cells. *Appl. Phys. Lett.* ***88***, 073508 (2006).
19. Meyer, J. *et al.* Transition Metal Oxides for Organic Electronics: Energetics, Device Physics and Applications. *Adv. Mater.* ***24***, 5408-5427 (2012).

20. Granqvist, C. G. Electrochromics for smart windows: Oxide-based thin films and devices. *Thin Solid Films* ***564***, 1-38 (2014).
21. Abdi, F. F. *et al.* Efficient solar water splitting by enhanced charge separation in a bismuth vanadate-silicon tandem photoelectrode. *Nat. Commun.* ***4***, (2013).
22. Hu, S. *et al.* Amorphous TiO_2 coatings stabilize Si, GaAs, and GaP photoanodes for efficient water oxidation. *Science* ***344***, 1005-1009 (2014).
23. Jeon, G. H. Recent progress in thin film processing by magnetron sputtering with plasma diagnostics. *J. Phys. D: Appl. Phys.* ***42***, 043001 (2009).
24. Manning, T. D. *et al.* Intelligent window coatings: atmospheric pressure chemical vapour deposition of vanadium oxides. *J . Mater. Chem. A* ***12***, 2936-2939 (2002).
25. Johnson, R. W.; Hultqvist, A.; Bent, S. F. A brief review of atomic layer deposition: from fundamentals to applications. *Mater. Today* ***17***, 236-246 (2014).
26. Ba, C. *et al.* Fabrication of high-quality VO_2 thin films by ion-assisted dual ac magnetron sputtering. *ACS. Appl. Mater. Interfaces* ***5***, 12520-12525 (2013).
27. Leskelä, M.; Ritala, M. Atomic layer deposition (ALD): from precursors to thin film structures. *Thin Solid Films* ***409***, 138-146 (2002).
28. Deepak, N. *et al.* Interesting Evidence for Template-Induced Ferroelectric Behavior in Ultra-Thin Titanium Dioxide Films Grown on (110) Neodymium Gallium Oxide Substrates. *Adv. Func. Mater.* ***24***, 2844-2851 (2014).
29. Kregsamer, P. *et al.* Synchrotron radiation-excited glancing incidence xrf for depth profile and thin-film analysis of light elements. *X-Ray Spectrom.* ***28***, 292-296 (1999).
30. Horiba, K. *et al.* A high-resolution synchrotron-radiation angle-resolved photoemission spectrometer with in situ oxide thin film growth capability. *Rev. Sci. Instrum.* ***74***, 3406-3412 (2003).
31. Lin, Y.-H. *et al.* High Electron Mobility Thin-Film Transistors Based on Solution-Processed Semiconducting Metal Oxide Heterojunctions and Quasi-Superlattices. *Adv. Sci.* ***2***, (2015).
32. Piccirillo, C.; Binions, R.; Parkin, I. P. Synthesis and Functional Properties of Vanadium Oxides: V_2O_3, VO_2, and V_2O_5 Deposited on Glass by Aerosol-Assisted CVD. *Chem. Vap. Deposition* ***13***, 145-151 (2007).
33. Kats, M. A. *et al.* Vanadium Dioxide as a Natural Disordered Metamaterial: Perfect Thermal Emission and Large Broadband Negative Differential Thermal Emittance. *Phys. Rev. X* ***3***, 041004 (2013).
34. Huotari, J.; Lappalainen, J.; Puustinen, J.; Lloyd Spetz, A. Gas sensing properties of pulsed laser deposited vanadium oxide thin films with various crystal structures. *Sens. Actuators, B* ***187***, 386-394 (2013).
35. Wang, X. J. *et al.* XRD and Raman study of vanadium oxide thin films deposited on fused silica substrates by RF magnetron sputtering. *Appl. Surf. Sci.* ***177***, 8-14 (2001).
36. Baddour-Hadjean, R.; Marzouk, A.; Pereira-Ramos, J. P. Structural modifications of $Li_xV_2O_5$ in a composite cathode ($0 \leq x < 2$) investigated by Raman microspectrometry. *J. Raman Spectrosc.* ***43***, 153-160 (2012).
37. Gouadec, G.; Colomban, P. Raman Spectroscopy of nanomaterials: How spectra relate to disorder, particle size and mechanical properties. *Prog. Cryst. Growth Charact. Mater.* ***53***, 1-56 (2007).
38. Tauc, J., *The Optical Properties of Solids*. Academic Press: New York, 1966.

39. Buchholz, D. B. *et al.* Control and Characterization of the Structural, Electrical, and Optical Properties of Amorphous Zinc−Indium−Tin Oxide Thin Films. *ACS Appl. Mater. Interfaces* ***1***, 2147-2153 (2009).
40. Wei, Y.; Li, M.; Zheng, J.; Xu, C. Structural characterization and electrical and optical properties of V_2O_5 films prepared via ultrasonic spraying. *Thin Solid Films* ***534***, 446-451 (2013).
41. Xu, W. *et al.* Facile and Environmentally Friendly Solution-Processed Aluminum Oxide Dielectric for Low-Temperature, High-Performance Oxide Thin-Film Transistors. *ACS Appl. Mater. Interfaces* ***7***, 5803-5810 (2015).
42. Faber, H. *et al.* Indium Oxide Thin-Film Transistors Processed at Low Temperature via Ultrasonic Spray Pyrolysis. *ACS Appl. Mater. Interfaces* ***7***, 782-790 (2015).
43. Glynn, C. *et al.* Precursor Concentration and Substrate Effects on High Rate Dip-Coated Vanadium Oxide Thin Films. *ECS Trans.* ***64***, 1-9 (2015).
44. Lange, F. F. Chemical solution routes to single-crystal thin films. *Science* ***273***, 903 (1996).
45. Livage, J.; Sanchez, C. Sol-gel chemistry. *J. Non-Cryst. Solids* ***145***, 11-19 (1992).
46. Nabavi, M.; Doeuff, S.; Sanchez, C.; Livage, J. Chemical modification of metal alkoxides by solvents: A way to control sol-gel chemistry. *J. Non-Cryst. Solids* ***121***, 31-34 (1990).
47. Sanchez, C.; Livage, J.; Henry, M.; Babonneau, F. Chemical modification of alkoxide precursors. *J. Non-Cryst. Solids* ***100***, 65-76 (1988).
48. Jo, J.-W. *et al.* Highly Stable and Imperceptible Electronics Utilizing Photoactivated Heterogeneous Sol-Gel Metal–Oxide Dielectrics and Semiconductors. *Adv. Mater.* ***27***, 1182-1188 (2015).
49. Kim, M.-G.; Kanatzidis, M. G.; Facchetti, A.; Marks, T. J. Low-temperature fabrication of high-performance metal oxide thin-film electronics via combustion processing. *Nat. Mater.* ***10***, 382-388 (2011).
50. Jia, Q. X. *et al.* Polymer-assisted deposition of metal-oxide films. *Nat. Mater.* ***3***, 529-532 (2004).
51. Burrell, A. K.; Mark McCleskey, T.; Jia, Q. X. Polymer assisted deposition. *Chem. Comm.*, 1271-1277 (2008).
52. Alsawafta, M.; Almoabadi, A.; Badilescu, S.; Truong, V.-V. Improved Electrochromic Properties of Vanadium Pentoxide Nanorods Prepared by Thermal Treatment of Sol-Gel Dip-Coated Thin Films. *J. Electrochem. Soc* ***162***, H466-H472 (2015).
53. Hanlon, T. J.; Walker, R. E.; Coath, J. A.; Richardson, M. A. Comparison between vanadium dioxide coatings on glass produced by sputtering, alkoxide and aqueous sol–gel methods. *Thin Solid Films* ***405***, 234-237 (2002).
54. Chueh, C.-C.; Li, C.-Z.; Jen, A. K. Y. Recent progress and perspective in solution-processed Interfacial materials for efficient and stable polymer and organometal perovskite solar cells. *Energy Environ. Sci.* ***8***, 1160-1189 (2015).
55. Si, Y.; Guo, Z. Superhydrophobic nanocoatings: from materials to fabrications and to applications. *Nanoscale* ***7***, 5922-5946 (2015).
56. Birnie, D., III; Hau, S.; Kamber, D.; Kaz, D. Effect of ramping-up rate on film thickness for spin-on processing. *J. Mater. Sci. Mater.* ***16***, 715-720 (2005).
57. Emslie, A. G.; Bonner, F. T.; Peck, L. G. Flow of a Viscous Liquid on a Rotating Disk. *J. Appl. Phys.* ***29***, 858-862 (1958).

58. Brinker, C. J.; Frye, G. C.; Hurd, A. J.; Ashley, C. S. Fundamentals of sol-gel dip coating. *Thin Solid Films* ***201***, 97-108 (1991).
59. Brinker, C. J. *et al.* Review of sol-gel thin film formation. *J. Non-Cryst. Solids* ***147–148***, 424-436 (1992).
60. Landau, L.; Levich, B. Dragging of a liquid by a moving plate. *Acta Physicochim. URSS* ***17***, 12 (1942).
61. Faustini, M. *et al.* Preparation of Sol−Gel Films by Dip-Coating in Extreme Conditions. *J. Phys. Chem. C* ***114***, 7637-7645 (2010).
62. Nishida, F. *et al.* In-situ fluorescence imaging of sol-gel thin film deposition. *J. Sol-Gel Sci. Technol.* ***2***, 477-481 (1994).
63. Alan, J. H., Evaporation and Surface Tension Effects in Dip Coating. In *The Colloid Chemistry of Silica*, American Chemical Society: 1994; Vol. 234, pp 433-450.
64. Hurd, A. J.; Brinker, C. J. Optical sol-gel coatings : ellipsometry of film formation. *J. Phys. France* ***49***, 1017-1025 (1988).
65. Faustini, M. *et al.* Engineering Functionality Gradients by Dip Coating Process in Acceleration Mode. *ACS Appl. Mater. Interfaces* ***6***, 17102-17110 (2014).
66. Ye, F. *et al.* Fluorescence Spectroscopy Studies of Silica Film Polarity Gradients Prepared by Infusion-Withdrawal Dip-Coating. *Chem. Mater.* ***22***, 2970-2977 (2010).
67. Ceratti, D. R. *et al.* A New Dip Coating Method to Obtain Large-Surface Coatings with a Minimum of Solution. *Adv. Mater.* ***27***, 4958-4962 (2015).
68. Arfsten, N. J.; Eberle, A.; Otto, J.; Reich, A. Investigations on the angle-dependent dip coating technique (ADDC) for the production of optical filters. *J. Sol-Gel Sci. Technol.* ***8***, 1099-1104 (1997).
69. Wang, Y.; McCarthy, T. J. Dip-coating deposition on chemically patterned surfaces: a mechanistic analysis and comparison with topographically patterned surfaces. *Langmuir* ***30***, 2419-2428 (2014).
70. Krebs, F. C. Fabrication and processing of polymer solar cells: A review of printing and coating techniques. *Sol. Energy Mater. Sol. Cells* ***93***, 394-412 (2009).
71. Perednis, D.; Gauckler, L. Thin Film Deposition Using Spray Pyrolysis. *J. Electroceram.* ***14***, 103-111 (2005).
72. Chen, C. H.; Kelder, E. M.; Schoonman, J. Effect of layer morphology on the lithium-ion diffusion in thin Li_xCoO_2 films. *J. Mater. Sci. Lett.* ***16***, 1967-1969 (1997).
73. Arya, S. P. S.; Hintermann, H. E. Growth of Y-Ba-Cu-O superconducting thin films by ultrasonic spray pyrolysis. *Thin Solid Films* ***193–194, Part 2***, 841-846 (1990).
74. Lee, D. H.; Chang, Y. J.; Herman, G. S.; Chang, C. H. A General Route to Printable High-Mobility Transparent Amorphous Oxide Semiconductors. *Adv. Mater.* ***19***, 843-847 (2007).
75. Liu, X.; Tarn, T.-J.; Huang, F.; Fan, J. Recent advances in inkjet printing synthesis of functional metal oxides. *Particuology* ***19***, 1-13 (2015).
76. de Gans, B.-J.; Schubert, U. S. Inkjet Printing of Polymer Micro-Arrays and Libraries: Instrumentation, Requirements, and Perspectives. *Macromol. Rapid Commun.* ***24***, 659-666 (2003).
77. Findikoglu, A. T.; Jia, Q. X.; Reagor, D. W.; Wu, X. D. Electrical characteristics of coplanar waveguide devices incorporating nonlinear dielectric thin films of $SrTiO_3$ and $Sr_{0.5}Ba_{0.5}TiO_3$. *Microw. Opt. Techn. Let.* ***9***, 306-310 (1995).

78. Zhai, P. *et al.* Transparent p-type epitaxial thin films of nickel oxide. *Chem. Comm.* ***50***, 1854-1856 (2014).
79. Beke, S. A review of the growth of V_2O_5 films from 1885 to 2010. *Thin Solid Films* ***519***, 1761-1771 (2011).
80. McNulty, D.; Buckley, D. N.; O'Dwyer, C. Synthesis and electrochemical properties of vanadium oxide materials and structures as Li-ion battery positive electrodes. *J. Power Sources* ***267***, 831-873 (2014).
81. Armstrong, M.; O'Dwyer, C.; Macklin, W.; Holmes, J. D. Evaluating the performance of nanostructured materials as lithium-ion battery electrodes. *Nano Res.* ***7***, 1-62 (2014).
82. O'Dwyer, C. *et al.* Reduced Surfactant Uptake in Three Dimensional Assemblies of VO_x Nanotubes Improves Reversible Li+ Intercalation and Charge Capacity. *Adv. Func. Mater.* ***19***, 1736-1745 (2009).
83. Sahana, M. B. *et al.* Electrochemical properties of V_2O_5 thin films deposited by spin coating. *Mater. Sci. Eng., B* ***143***, 42-50 (2007).
84. Akl, A. A. Effect of solution molarity on the characteristics of vanadium pentoxide thin film. *Appl. Surf. Sci.* ***252***, 8745-8750 (2006).
85. Irani, R.; Rozati, S. M.; Beke, S. Structural and optical properties of nanostructural V_2O_5 thin films deposited by spray pyrolysis technique: Effect of the substrate temperature. *Mater. Chem. Phys.* ***139***, 489-493 (2013).
86. Ji, Y. D. *et al.* Epitaxial growth and metal-insulator transition of vanadium oxide thin films with controllable phases. *Appl. Phys. Lett.* ***101***, (2012).
87. Livage, J. Vanadium pentoxide gels. *Chem. Mater.* ***3***, 578-593 (1991).
88. Livage, J. Optical and electrical properties of vanadium oxides synthesized from alkoxides. *Coord. Chem. Rev.* ***190–192***, 391-403 (1999).
89. Demeter, M.; Neumann, M.; Reichelt, W. Mixed-valence vanadium oxides studied by XPS. *Surf. Sci.* ***454–456***, 41-44 (2000).
90. Cho, S.-P. *et al.* Brush painted V_2O_5 hole transport layer for efficient and air-stable polymer solar cells. *Sol. Energy Mater. Sol. Cells* ***132***, 196-203 (2015).
91. Zilberberg, K. *et al.* Inverted Organic Solar Cells with Sol–Gel Processed High Work-Function Vanadium Oxide Hole-Extraction Layers. *Adv. Func. Mater.* ***21***, 4776-4783 (2011).
92. Costa, C.; Pinheiro, C.; Henriques, I.; Laia, C. A. T. Electrochromic Properties of Inkjet Printed Vanadium Oxide Gel on Flexible Polyethylene Terephthalate/Indium Tin Oxide Electrodes. *ACS Appl. Mater. Interfaces* ***4***, 5266-5275 (2012).
93. Livage, J. Hydrothermal Synthesis of Nanostructured Vanadium Oxides. *Materials* ***3***, 4175-4195 (2010).
94. Chan, C. K. *et al.* Fast, Completely Reversible Li Insertion in Vanadium Pentoxide Nanoribbons. *Nano Lett.* ***7***, 490-495 (2007).
95. Chebout, K. *et al.* Electrical characterization of ethanol sensing device based on Vanadium oxide/Porous Si/Si structure. *Solid State Ionics* ***253***, 164-168 (2013).
96. Gökdemir, F. P.; Özdemir, O.; Kutlu, K. Comparison of Structural and Electrochemical Properties of V_2O_5 Thin Films Prepared by Organic/Inorganic Precursors. *Electrochim. Acta* ***121***, 240-244 (2014).
97. Zilberberg, K.; Trost, S.; Schmidt, H.; Riedl, T. Solution Processed Vanadium Pentoxide as Charge Extraction Layer for Organic Solar Cells. *Adv. Energy Mater.* ***1***, 377-381 (2011).
98. Amarandei, G. *et al.* Effect of Au Nanoparticle Spatial Distribution on the Stability of Thin Polymer Films. *Langmuir* ***29***, 6706-6714 (2013).

99. Bouzidi, A. *et al.* First synthesis of vanadium oxide thin films by spray pyrolysis technique. *Mater. Sci. Eng., B* ***95***, 141-147 (2002).
100. Lim, H. S. *et al.* UV-Driven Reversible Switching of a Roselike Vanadium Oxide Film between Superhydrophobicity and Superhydrophilicity. *J. Am. Chem. Soc.* ***129***, 4128-4129 (2007).
101. Chidembo, A. *et al.* Globular reduced graphene oxide-metal oxide structures for energy storage applications. *Energy Environ. Sci.* ***5***, 5236-5240 (2012).
102. Moss, T. S. Relations between the Refractive Index and Energy Gap of Semiconductors. *Phys. Status Solidi B* ***131***, 415-427 (1985).
103. Ravindra, N. M.; Ganapathy, P.; Choi, J. Energy gap–refractive index relations in semiconductors – An overview. *Infrared Phys. Techn.* ***50***, 21-29 (2007).
104. Reddy, R. R.; Nazeer Ahammed, Y. A study on the Moss relation. *Infrared Phys. Techn.* ***36***, 825-830 (1995).
105. Zhan, Z. *et al.* Role of Vanadium Pentoxide Hole-Extracting Nanolayer in Rubrene C_{60} Based Small Molecule Organic Solar Cells. *J Nanomater.* ***2014***, 1-7 (2014).
106. Hancox, I. *et al.* Optimization of a High Work Function Solution Processed Vanadium Oxide Hole-Extracting Layer for Small Molecule and Polymer Organic Photovoltaic Cells. *J. Phys. Chem. C* ***117***, 49-57 (2013).
107. Bao, X. *et al.* Simple O_2 Plasma-Processed V_2O_5 as an Anode Buffer Layer for High-Performance Polymer Solar Cells. *ACS Appl. Mater. Interfaces* ***7***, 7613-7618 (2015).
108. Ramana, C. V. *et al.* Correlation between Growth Conditions, Microstructure, and Optical Properties in Pulsed-Laser-Deposited V_2O_5 Thin Films. *Chem. Mater.* ***17***, 1213-1219 (2005).
109. Kuo, Y. Thin Film Transistor Technology--Past Present and Future. *Electrochem. Soc. Interface* ***22***, 55-61 (2013).
110. Kuo, Y., *Thin film transistors. 1. Amorphous silicon thin film transistors*. Springer Science & Business Media: 2004; Vol. 1.
111. Kuo, Y.; Kozlowski, P. M. Polycrystalline silicon formation by pulsed rapid thermal annealing of amorphous silicon. *Appl. Phys. Lett.* ***69***, 1092-1094 (1996).
112. Xu, W.; Wang, H.; Ye, L.; Xu, J. The role of solution-processed high-k gate dielectrics in electrical performance of oxide thin-film transistors. *J. Mater. Chem. C* ***2***, 5389-5396 (2014).
113. Banger, K. K. *et al.* Low-temperature, high-performance solution-processed metal oxide thin-film transistors formed by a 'sol–gel on chip' process. *Nat. Mater.* ***10***, 45-50 (2011).
114. Lee, W.-J. *et al.* Large-Scale Precise Printing of Ultrathin Sol–Gel Oxide Dielectrics for Directly Patterned Solution-Processed Metal Oxide Transistor Arrays. *Adv. Mater.* ***27***, 5043-5048 (2015).
115. Yu, J. *et al.* Solution-processed p-type copper oxide thin-film transistors fabricated by using one-step vacuum annealing technique. *J. Mater. Chem. C*, (2015).
116. Li, J.; Wang, S. Q.; Mayer, J. W.; Tu, K. N. Oxygen-diffusion-induced phase boundary migration in copper oxide thin films. *Phys. Rev. B* ***39***, 12367-12370 (1989).
117. Kim, Y. H. *et al.* Flexible metal-oxide devices made by room-temperature photochemical activation of sol-gel films. *Nature* ***489***, 128-U191 (2012).

118. Clark, T. *et al.* A New Application of UV−Ozone Treatment in the Preparation of Substrate-Supported, Mesoporous Thin Films. *Chem. Mater.* ***12***, 3879-3884 (2000).
119. Mizoshita, N.; Ishii, M.; Kato, N.; Tanaka, H. Hierarchical Nanoporous Silica Films for Wear Resistant Antireflection Coatings. *ACS Appl. Mater. Interfaces* ***7***, 19424-19430 (2015).
120. Jang, J. *et al.* Transparent High-Performance Thin Film Transistors from Solution-Processed SnO_2/ZrO_2 Gel-like Precursors. *Adv. Mater.* ***25***, 1042-1047 (2013).
121. Pasquarelli, R. M.; Ginley, D. S.; O'Hayre, R. Solution processing of transparent conductors: from flask to film. *Chem. Soc. Rev.* ***40***, 5406-5441 (2011).
122. Greenwood, N. N.; Earnshaw, A., *Chemistry of the Elements*. Elsevier: 2012.
123. Lide, D. R., *CRC handbook of chemistry and physics*. CRC press: 2004.
124. Chen, Z. *et al.* Fabrication of Highly Transparent and Conductive Indium–Tin Oxide Thin Films with a High Figure of Merit via Solution Processing. *Langmuir* ***29***, 13836-13842 (2013).
125. O'Dwyer, C.; Sotomayor Torres, C. Epitaxial growth of an antireflective, conductive, graded index ITO nanowire layer. *Front. Phys.* ***1***, (2013).
126. Sunde, T. O. L. *et al.* Transparent and conducting ITO thin films by spin coating of an aqueous precursor solution. *J. Mater. Chem.* ***22***, 15740-15749 (2012).
127. Watcharotone, S. *et al.* Graphene−Silica Composite Thin Films as Transparent Conductors. *Nano Lett.* ***7***, 1888-1892 (2007).
128. Kim, A. *et al.* Highly Transparent Low Resistance ZnO/Ag Nanowire/ZnO Composite Electrode for Thin Film Solar Cells. *ACS Nano* ***7***, 1081-1091 (2013).
129. Chang, J. H. *et al.* A solution-processed molybdenum oxide treated silver nanowire network: a highly conductive transparent conducting electrode with superior mechanical and hole injection properties. *Nanoscale* ***7***, 4572-4579 (2015).
130. O'Dwyer, C. *et al.* Bottom-up growth of fully transparent contact layers of indium tin oxide nanowires for light-emitting devices. *Nat. Nano.* ***4***, 239-244 (2009).
131. Ellmer, K. Past achievements and future challenges in the development of optically transparent electrodes. *Nat. Photon* ***6***, 809-817 (2012).
132. Granqvist, C. G., *Handbook of inorganic electrochromic materials*. Elsevier: 1995.
133. Tong, Z. *et al.* Improved electrochromic performance and lithium diffusion coefficient in three-dimensionally ordered macroporous V_2O_5 films. *J. Mater. Chem. C* ***2***, 3651-3658 (2014).
134. Wang, Y.; Takahashi, K.; Lee, K. H.; Cao, G. Z. Nanostructured Vanadium Oxide Electrodes for Enhanced Lithium-Ion Intercalation. *Adv. Func. Mater.* ***16***, 1133-1144 (2006).
135. Costa, C.; Pinheiro, C.; Henriques, I.; Laia, C. A. T. Inkjet Printing of Sol–Gel Synthesized Hydrated Tungsten Oxide Nanoparticles for Flexible Electrochromic Devices. *ACS Appl. Mater. Interfaces* ***4***, 1330-1340 (2012).
136. Miller, E. L. Photoelectrochemical water splitting. *Energ. Environ. Sci.* ***8***, 2809-2810 (2015).
137. Wang, Y. *et al.* $Ag_2O/TiO_2/V_2O_5$ one-dimensional nanoheterostructures for superior solar light photocatalytic activity. *Nanoscale* ***6***, 6790-6797 (2014).
138. Kumar, S. G.; Devi, L. G. Review on Modified TiO_2 Photocatalysis under UV/Visible Light: Selected Results and Related Mechanisms on Interfacial Charge Carrier Transfer Dynamics. *J. Phys. Chem. A* ***115***, 13211-13241 (2011).

139. Peng, Q. *et al.* Solution-Processed, Antimony-Doped Tin Oxide Colloid Films Enable High-Performance TiO_2 Photoanodes for Water Splitting. *Nano Lett.* ***13***, 1481-1488 (2013).
140. Arin, M. *et al.* Inkjet printing of photocatalytically active TiO_2 thin films from water based precursor solutions. *J. Eur. Ceram. Soc.* ***31***, 1067-1074 (2011).
141. Ameri, T.; Dennler, G.; Lungenschmied, C.; Brabec, C. J. Organic tandem solar cells: A review. *Energy Environ. Sci.* ***2***, 347-363 (2009).
142. Yip, H.-L.; Jen, A. K. Y. Recent advances in solution-processed interfacial materials for efficient and stable polymer solar cells. *Energ. Environ. Sci.* ***5***, 5994-6011 (2012).
143. Lu, L.; Xu, T.; Jung, I. H.; Yu, L. Match the Interfacial Energy Levels between Hole Transport Layer and Donor Polymer to Achieve High Solar Cell Performance. *J. Phys. Chem. C*, (2014).
144. Li, X. C. *et al.* MoO_x and $V2O_x$ as hole and electron transport layers through functionalized intercalation in normal and inverted organic optoelectronic devices. *Light-Sci. Appl.* ***4***, e273 (2015).
145. Liu, S. Y.; Ho, S. H.; Chen, Y.; So, F. Passivation of Metal Oxide Surfaces for High-Performance Organic and Hybrid Optoelectronic Devices. *Chem. Mater.* ***27***, 2532-2539 (2015).
146. Yi, Q. *et al.* Aqueous Solution-Deposited Molybdenum Oxide Films as an Anode Interfacial Layer for Organic Solar Cells. *ACS Appl. Mater. Interfaces* ***7***, 18218-18224 (2015).
147. Trotochaud, L.; Ranney, J. K.; Williams, K. N.; Boettcher, S. W. Solution-Cast Metal Oxide Thin Film Electrocatalysts for Oxygen Evolution. *J. Am. Chem. Soc.* ***134***, 17253-17261 (2012).
148. Abbasi, M.; Rozati, S. M.; Irani, R.; Beke, S. Synthesis and gas sensing behavior of nanostructured V_2O_5 thin films prepared by spray pyrolysis. *Mater. Sci. Semicond. Process.* ***29***, 132-138 (2015).
149. Armstrong, E.; O'Dwyer, C. Artificial opal photonic crystals and inverse opal structures - fundamentals and applications from optics to energy storage. *J. Mater. Chem. C* ***3***, 6109-6143 (2015).
150. Armstrong, E. *et al.* 2D and 3D vanadium oxide inverse opals and hollow sphere arrays. *CrystEngComm* ***16***, 10804-10815 (2014).
151. Niklaus, F.; Vieider, C.; Jakobsen, H. In *MEMS-based uncooled infrared bolometer arrays: a review*, 2007; pp 68360D-68360D-68315.
152. Sung, M. *et al.* 'Focused' assembly of V_2O_5 nanowire masks for the fabrication of metallic nanowire sensors. *Nanotechnology* ***18***, 205304 (2007).
153. Vieira, N. *et al.* Ion-sensing properties of 1D vanadium pentoxide nanostructures. *Nanoscale Res. Lett.* ***7***, 1-5 (2012).
154. Cetinkaya, A. O. *et al.* Structural and electrical characterizations of $BiFeO_3$ capacitors deposited by sol–gel dip coating technique. *Thin Solid Films* ***590***, 7-12 (2015).
155. Livage, J. Actuator materials: Towards smart artificial muscle. *Nat. Mater.* ***2***, 297-299 (2003).
156. Gu, G. *et al.* V_2O_5 nanofibre sheet actuators. *Nat. Mater* ***2***, 316-319 (2003).
157. Baughman, R. H. *et al.* Carbon Nanotube Actuators. *Science* ***284***, 1340-1344 (1999).
158. Baughman, R. H. Playing Nature's Game with Artificial Muscles. *Science* ***308***, 63-65 (2005).

159. Bhatt, M. D.; O'Dwyer, C. Recent progress in theoretical and computational investigations of Li-ion battery materials and electrolytes. *Phys. Chem. Chem. Phys.* ***17***, 4799-4844 (2015).
160. Osiak, M.; Geaney, H.; Armstrong, E.; O'Dwyer, C. Structuring materials for lithium-ion batteries: advancements in nanomaterial structure, composition, and defined assembly on cell performance. *J. Mater. Chem. A* ***2***, 9433-9460 (2014).
161. McSweeney, W. *et al.* The influence of carrier density and doping type on lithium insertion and extraction processes at silicon surfaces. *Electrochim. Acta* ***135***, 356-367 (2014).
162. McSweeney, W.; Geaney, H.; O'Dwyer, C. Metal-assisted chemical etching of silicon and the behavior of nanoscale silicon materials as Li-ion battery anodes. *Nano Res.* ***8***, 1395-1442 (2015).
163. Gaikwad, A. M.; Arias, A. C.; Steingart, D. A. Recent Progress on Printed Flexible Batteries: Mechanical Challenges, Printing Technologies, and Future Prospects. *Energy Technol.* ***3***, 305-328 (2015).
164. Hu, L. *et al.* Thin, Flexible Secondary Li-Ion Paper Batteries. *ACS Nano* ***4***, 5843-5848 (2010).
165. Brezesinski, K. *et al.* Ordered Mesoporous α-Fe_2O_3 (Hematite) Thin-Film Electrodes for Application in High Rate Rechargeable Lithium Batteries. *Small* ***7***, 407-414 (2011).
166. Amarandei, G.; O'Dwyer, C.; Arshak, A.; Corcoran, D. Fractal Patterning of Nanoparticles on Polymer Films and Their SERS Capabilities. *ACS Appl. Mater. Interfaces* ***5***, 8655-8662 (2013).

Chapter 3

Experimental

3.1 Introduction

The experimental methods used for the fabrication of different V_2O_5 thin films are presented in this chapter. Synthesis methods for the different precursor solutions and dilutions are outlined. Both dip-coating and drop-casting are used for the controlled deposition of thin film and bulk film deposits. Many different characterisation methods were used for examining the morphological, structural, compositional and optical properties. The deposition and characteristion of SiO_2/V_2O_5 thin films is outlined in this chapter.

3.2 Thin Film Preparation

3.2.1 V_2O_5 Precursor Solution Preparation

Vanadium oxide precursor solution was prepared from an alkoxide based precursor mixed with IPA. Additives were added to the precursor to affect the resultantly deposited thin films. The alkoxide precursor vanadium (V) triisopropoxide $OV(OCH(CH_3)_2)_3$ was purchased from Sigma-Aldrich. The alkoxide was mixed by volume with isopropyl alcohol (IPA) and the additives, such as PEG-400 or H_2O, at a number of different ratios. The different precursor solutions were then referenced by their different dilutions. The dilution ratios between the IPA, alkoxide and additive were altered in order to test the resulting thin film characteristics. The IPA was kept at a larger dilution to the alkoxide and additive. The alkoxide: additive dilution ratio was kept to a constant 10:1 ratio.

Due to the possible reactions, such as unwanted hydrolysis/condensation, between the additive and alkoxide precursor that can occur when mixed prior to dilution, the two solutions were pre-mixed with half of the IPA and then combined.

The IPA/additive is added dropwise to the V_2O_5/IPA mixture. A schematic detailing the preparation of the precursor solutions is shown in Figure 3.1. The desired dilution of the solution is chosen and the correct volume of IPA is split between two containers. The shelf life of the precursor solutions was extended through addition of 4 Å molecular sieves and by sealing the container lids with Parafilm in-between depositions. The containers were also stored in a desiccator box.

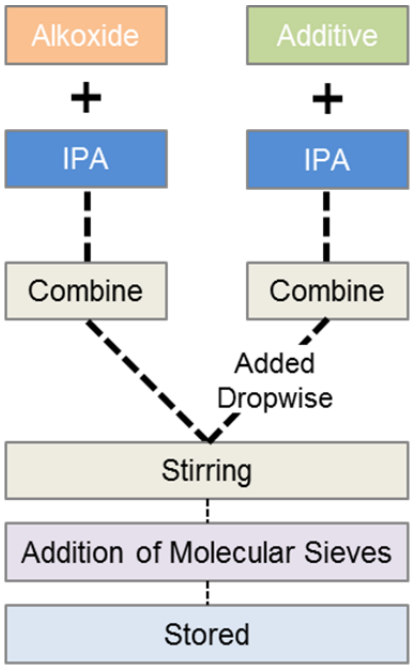


Figure 3.1. Schematic detailing preparation of precursor solutions from alkoxide, IPA and additive.

Both additives were chosen for the precursor solutions due to their respective capabilities for affecting the thin film depositions. These additives were combined with the alkoxide during the initial synthesis stage as shown in Figure 3.1. The two additives were H_2O and PEG-400 and were mixed by volume to synthesis the precursor solutions.

3.2.2 Deposition Techniques

Numerous substrates were used throughout this work with each being sized and cleaned prior to deposition. For thin film depositions on Au substrates, borosilicate glass cantilevers, 60 mm in length and 3 mm in width, were coated with a 10 nm Ti adhesion layer and a 250 nm Au layer by high vacuum thermal evaporation. The Au coated substrates were thermally annealed at 650 ^{o}C for 90 s prior to deposition of the precursor to produce larger Au grains and prevent delamination occurring during the thin film deposition. Optical grade ITO-coated glass substrates were purchased from Sigma-Aldrich with a nominal ITO thickness of 15 - 30 nm. Thin films were also deposited onto FTO coated glass with the FTO ~350 nm thick grown by atmospheric pressure CVD on a float glass line. Borosilicate Thermo Scientific Microscope Slides with a thickness of 1 mm were used as glass substrates for diffusion testing. An acetone, IPA, DI water wash combined with sonication was used to ensure that the surface was clean of surface contaminants prior to thin film deposition. A UV-Ozone treatment was performed for 30 mins using a Novascan UV ozone system to further remove any contaminants from the surface. The surface wettability of the thin films to the substrates can be affected by the UV-Ozone cleaning directly after exposure: to ensure identical deposition conditions, substrates were coated between 2 – 12 hours after UV-Ozone treatment.

Thin films were deposited using two different methods. Uniform controlled deposition was performed using a PTL-MM01 desktop dip coater which is shown in Figure 3.2 (a). A withdrawal speed of 150 mm/min (2.5 mm/s) was applied for thin film depositions on ITO, Au and FTO substrates. Multiple coatings could be applied by allowing sufficient time between layer depositions. The precursor solutions were

kept sealed between depositions in order to limit the length of time with exposure to ambient atmosphere. The back of the substrates were coated with polyimide tape to ensure that only one side was coated, this was particularly important when depositing on transparent substrates. The tape was applied prior to the UV-Ozone cleaning step.

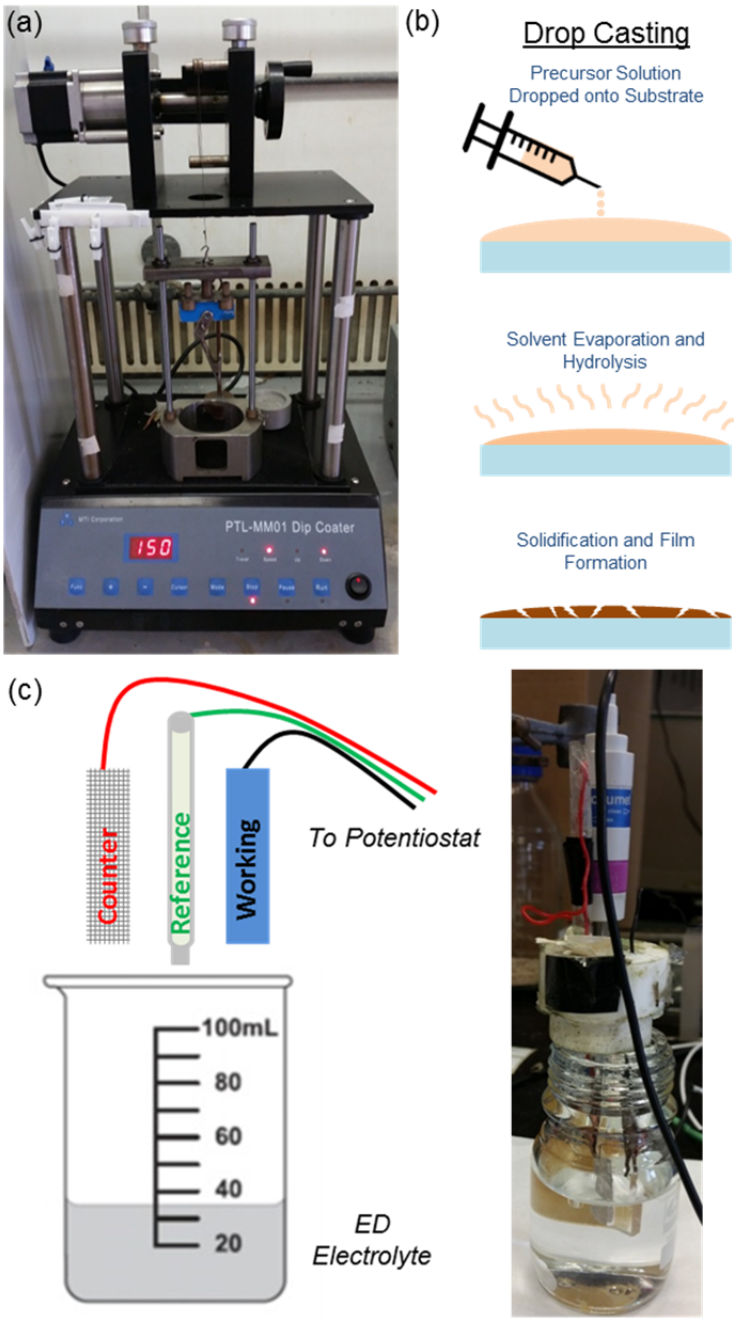


Figure 3.2. (a) Image of dip-coating apparatus. (b) Schematic of drop-casting deposition. (c) Schematic and optical image of the electrodeposition apparatus.

The formation of unconstrained films was performed through drop-casting. The films were deposited by dropping the liquid precursor directly onto the substrate as depicted in Figure 3.2 (b). The liquid film spreads over the substrate during the evaporation and hydrolysis stages. The formation of a rougher film with "bulk-like" characteristics occurred due to the precursor solution being unconstrained and able to form as an irregular surface. The liquid films formed into their preferred orientations which resulted in an irregular and rough surface. The drop-casting technique allowed for comparisons to be directly made to the dip-coating technique in preparing thin films.

Na-SiO_2 thin films were prepared using an electrodeposition apparatus. A schematic and corresponding optical image for the electrodeposition apparatus is shown in Figure 3.2 (c). The electrodeposition technique employed was adapted from that of Walcarious *et al.*[1] The electrodeposition electrolyte was prepared by first mixing 40 ml EtOH with 6 ml Tetraethyl Orthosilicate (TEOS) and then mixing for three hours with a 40 ml aqueous solution of 0.1M Sodium Nitrate ($NaNO_3$) and 10^{-3} M Hydrochloric Acid (HCL). The electrolyte was mixed prior to electrodeposition. A second electrodeposition electrolyte was prepared without the $NaNO_3$ salt in order to deposit pure SiO_2 films and electrodeposition was employed for ascertaining the salts effect on the SiO_2 deposition.

For electrodeposition an FTO coated glass substrate was used as the working electrode with a platinum mesh counter electrode and calomel reference electrode. The thin films were electrodeposited at a constant potential in the range –0.8 to –2.5 V, and all potentials were referenced to a Saturated Calomel electrodes (SCE). A Pt mesh was used as the counter electrode. Custom 3D printed templates were made using a MakerBot 2X system. Templated FTO substrates were used to form

templated Na-SiO_2 thin films. Plastic 3D printed templates were secured to the front of the FTO to ensure electrical contact with only the uncovered surface.

3.2.3 Post-Deposition Processing

After deposition a range of thin film processing methods were employed. A combination of ovens and furnaces were used for annealing processing steps. A Binder convection oven was used for annealing at and up to 300 ^{o}C with heating rates of 1 – 10 ^{o}C/min possible, the convection oven allowed for ambient air to flow through during the annealing. For annealing at higher temperatures with ambient air flow a Lenton CSC-12 tube furnace open at both ends was used with temperature ramp rates of 1 – 25 ^{o}C/min available. A Carbolite enclosed furnace, ECF 11/148, was used for high temperature anneals for which a constant flow of ambient air was not required with temperature ramp rates of 1 – 25 ^{o}C/min available. For each type of oven the ramp rate for heating could be adjusted and was chosen for the specific sample being processed ranging from 1 ^{o}C/min for slow heating applications and 5 ^{o}C/min for faster controlled heating. The annealing times ranged from 10 h - 24 h and were adjusted for consistency between comparable samples and depending upon the type of experiment being performed. A further processing step involving UV-Ozone treatment using a Novascan UV-Ozone system to remove any leftover surface contaminants both pre- and post-thermal treatments was employed. A UV-Ozone treatment was not used on thin films containing PEG to avoid photodegradation and decomposition of the polymer prior to annealing.

3.3 Analysis Techniques

A range of characterisation techniques were used for analysing the chemical, structural, morphological, spectroscopic and optical properties of the thin films. The specific details of each method for the work in this thesis are provided in the following sections.

3.3.1 Atomic Force Microscopy

The surface topography and roughness of the prepared samples were collected through atomic force microscopy (AFM). AFM is a sensitive surface analysis technique which raster scans a sharp tipped probe over the surface of a sample.[2] The probe is held at the end of a cantilever and the deflection of the cantilever is measured using the reflected image of a laser beamed onto a sensitive photodetector. The photodetector allows for the z-position of the cantilever, and thus the probe tip, to be measured to a high resolution of ~ 0.1 nm. The x-y resolution of an AFM is controlled using a microcontroller and the x-y resolution of many systems is lower than that of the z resolution.

Scans were performed on a Park XE-100 AFM system in non-contact mode with SSS-NCHR enhanced resolution tips, the XY and Z resolution are ~ 2 nm and 0.05 nm respectively. Using the AFM technique, thin film thicknesses can be determined. To determine thicknesses samples were scribed with a scalpel blade and AFM images were taken at the interface between the substrate and thin film surface to determine the thin film thickness. For analysing the AFM images both XEI and Gwyddion software packages were used, which provided numerical algorithms to

analyse thin film surface topography attributes such as root mean square (rms) roughness and thicknesses directly from the AFM data.

3.3.2 Electron Microscopy

The surface morphologies and topography of the thin films were studied using scanning electron microscopy (SEM). In SEM a beam of electrons is focused and raster scanned across the surface of a sample. Secondary electrons are released from the surface through an inelastic scattering effect which are then detected and used to prepare a high magnification image of the surface.[3-4] An SEM has a high depth of field and thus the images provide a highly detailed image of the sample showing any surface discontinuities or structures on the surface. SEM images can be used in conjunction with AFM topography images to fully characterise the surface of a sample as the SEM can provide high magnification images over large areas and the AFM shows high resolution surface topography of the same regions. The SEM captures detailed images of sample surfaces for which AFM measurements would be impractical or overly time consuming, such as on samples with non-planar morphologies or a high peak to peak roughness. SEM analysis was performed on an FEI Quanta 650 FEG high resolution SEM equipped with an Oxford Instruments X-MAX 20 large area Si diffused EDX detector. Images were collected at an operating voltage of 10-20 kV.

For atomic scale imaging, a transmission electron microscope (TEM) was used. In TEM a focused beam of electrons travels through the sample.[5-6] If the sample is thin enough, the beam interacts with the material allowing for high-resolution images of the atomic structure to be reconstructed from the resulting electron beam diffraction by the crystal structure of the material. Using selected

apertures, electron diffraction patterns were also acquired from regions of interest. In this work, the in-plane structure of the thin films was determined by HRTEM using a JEOL 2100 high resolution TEM operating at 200 kV. To allow for the in-plane structure to be examined, single layer thin films were dip-coated onto the surface of 15 nm Si_3N_4 – coated TEM grid windows.

3.3.3 Raman Scattering Spectroscopy

Raman scattering spectroscopy is a tool used for the measurement of vibrational modes of phonons within a material.[7] In Raman spectroscopy monochromatic light interacts with the material and information on the vibrational modes of the sample is recorded through analysis of this scattered light. The Raman Effect is an inelastic scattering technique where vibrational energy is exchanged between the sample and the incident photon. In a Raman scattering event the light is excited to a virtual energy level and then inelastically drops to an energy level other than the ground state. Through analysis of the energy difference between the ground and second state information on the vibrational modes of the material can be obtained using a high resolution Raman spectrometer. The change of energy can be related to the molecular vibrations and structure of the sample and is a highly selective technique allowing for various chemical species and molecules to be distinguished. This technique is a powerful method for site-specific measurements, particularly when coupled with a microscope allowing for finer focusing of the site to be analysed.

There are nine characteristic Raman scattering modes for orthorhombic V_2O_5 as shown in Figure 3.3.[8] The symmetry mode assignments for orthorhombic V_2O_5 is shown in Figure 3.3 and the various modes can be related to different V-O bonds from both within the orthorhombic lattice and the connections between the V_2O_5

layers. Orthorhombic V_2O_5 is characterised by point group symmetry of D_{2h} with 21 allowed Raman modes.[8] The 195 cm^{-1}. 147 cm^{-1} and 105 cm^{-1} vibrational modes derive from the relative motion of the V_2O_5 unit cells along the x-, y- and z-axis respectively. The mode at 995 cm^{-1} corresponds to the short V=O bond while the remaining modes correspond to O-V-O, V-O-V and V-O stretching modes.[9]

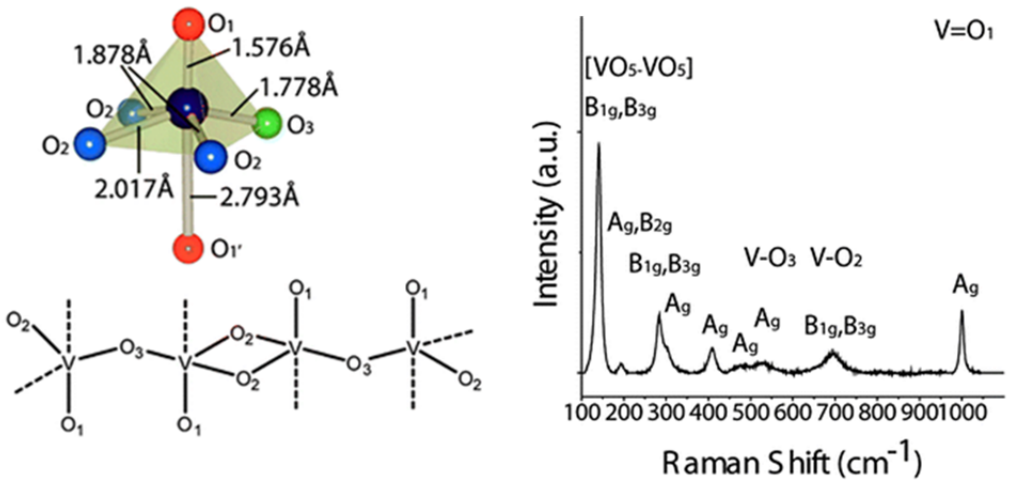


Figure 3.3. V_2O_5 bond structure, bond lengths and associated Raman spectrum for orthorhombic V_2O_5 with the symmetry labelling used for each of the modes given.[8]

Raman scattering spectroscopy was collected with a Renishaw InVia Raman spectrometer equipped with a 2400 lines/mm grating using a 514 nm 30 mW Argon Ion laser, spectra were collected using a RenCam CCD camera. The beam was focused onto the samples using either a 20×/50× objective lens. The laser power density was adjusted to ensure that the thin film surfaces did not undergo sample heating during the full spectral acquisition time.

3.3.4 Optical Spectroscopy

To study the optical properties of all thin films studied in this thesis, a range of optical spectroscopy techniques were used to probe the transmission of the thin

films in the UV-Vis-NIR wavelength ranges. The optical transmission measurements were also used to examine the optical constants for each thin film. The optical absorption edge, where the absorption increases in the optical region, was extracted and correlated to the effective optical bandgap (E_g).

The E_g value is estimated through the modified Davis-Mott relation,

$$\alpha h\nu = A(h\nu - E_g)^n$$

(Eq.3.1)

where α is the absorption coefficient of the thin films, A is a constant and E_g is the effective optical bandgap.[10] The exponent n is related to the type of transition for the material, where n = 1/2 for an direct allowed transition. A Tauc plot, $[\alpha h\omega]^{1/n}$ vs. E (eV), is used to estimate the E_g value by extrapolating the linear region determined where $[\alpha h\omega]^{1/n} = 0$. The refractive index ($n$) can be estimated from the Eg through the Moss[11-12] relation where,

$$n_{VO}^4 E_g \sim 95 \text{ eV} \qquad (Eq.\ 3.2)$$

Different optical setups were used to obtain the transmission spectra of the thin films over the range of UV-Vis-NIR wavelengths and are presented in Figure 3.4. The optical transparency of the thin films can be measured over large and small planar surface areas with site-specific measurements. To measure the thin film optical transparency in the 200 – 1000 nm range with a 0.5 nm resolution over a large planar area, a Thermo Scientific Evolution 60S UV-Visible spectrophotometer illuminated with a Xenon light source was used with a custom sample holder as shown in Figure 3.4 (a).

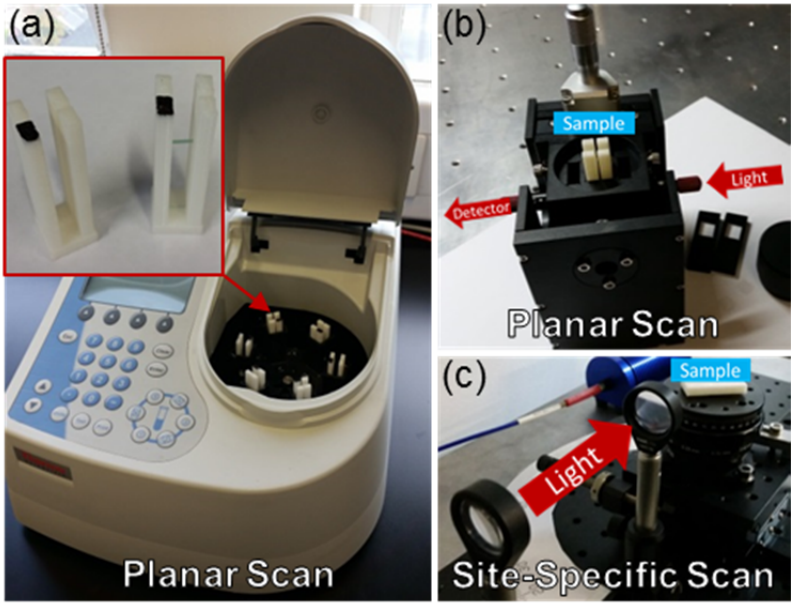


Figure 3.4. Different optical transparency measurement devices for measuring over larger planar thin film surfaces and site-specific areas. (a) Multi sample holder for planar UV-Vis transparency measurements using custom 3D printed sample holders. (b) Sample holder for planar transparency measurements using a connected UV-Vis or NIR spectrometer. (c) UV-Vis transparency measurement device for small area site-specific testing through collimated beam focusing.

To examine the planar optical transmission from thin films in the NIR wavelength range of 1000 nm – 2500 nm an OceanOptics NIRQuest256-2.5 spectrometer with a 9.5 nm spectral resolution was used in conjunction with the sample holder shown in Figure 3.4 (b). An OceanOptics HL-2000 tungsten halogen source was used for illumination for NIR transmission measurements and was directed through the lens as shown and collected after interacting with the sample held with the 3D printed holder. For UV-Vis transmission characteristics of smaller regions of interest on thin films for site specific scans, tests were performed using the optical setup shown in Figure 3.4 (c). The thin film samples were illuminated with white light from a Halogen bulb, which was incident normal to the surface and collimated to a beam diameter of ~1 mm. Spectra of the transmitted light were collected using an Ocean Optics USB2000+VIS-NIR-ES CCD spectrometer in the wavelength range 200 nm – 950 nm with a resolution of ~4 nm.

3.3.5 X-Ray Diffraction

X-ray diffraction (XRD) was used to determine the crystal structure of the drop-casted thin films. In XRD, a beam of X-rays is directed at a sample with the resulting elastic scattering of the X-rays caused by the atomic arrangements of the material being collected at different angles. By counting the number of X-rays diffracted at each angle, Braggs law, $n\lambda = 2d \sin\theta$, can be applied to determine the interplanar distance (d) of the crystal, where λ is the wavelength of the X-rays and θ is the angle at which the diffracted X-rays were detected. The different XRD patterns can be compared to the literature and online databases to determine the composition and phases of the sample. Powder XRD analysis was performed using a Phillips Xpert PW3719 diffractometer using Cu Kα radiation (40 kV and 40 mA) scanned between 10^{o} - 70^{o}. Thin film X-Ray diffraction was performed with a Philips X'pert equipped with a θ–θ goniometer. A Cu anode provided X-ray photons with a wavelength of λ = 0.15956 nm.

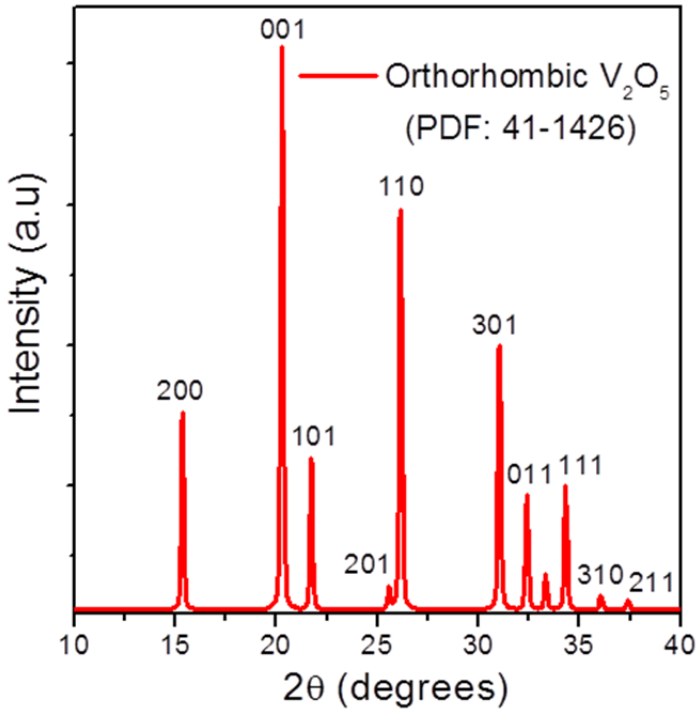


Figure 3.5. Star XRD pattern for orthorhombic V_2O_5 highlighting the peaks for diffraction from individual crystal planes.

The XRD pattern for the star pattern of orthorhombic V_2O_5 is displayed in Figure 3.5. The pattern is taken from PDF file 41-1426 for Shcherbinaite, the mineral form of orthorhombic V_2O_5. Orthorhombic V_2O_5 is part of the Pmmn space group with cell parameters of a = 11.516 Å, b = 3.5656 Å, c = 4.3727 Å.[13]

3.3.6 X-Ray Photoelectron Spectroscopy

In the X-ray photoelectron spectroscopy (XPS) technique, the surface of a sample is exposed to X-rays and the resulting kinetic energies of the released electrons are measured which are released through the photoelectric effect.[14] Through analysis of the range of energies of the released electrons it is possible to determine the core energy values of the elements comprising the sample. XPS is a surface sensitive technique, where only the top nanometers to the surface of the sample is probed. In this work two types of XPS systems were used. XPS spectra were acquired on an Oxford Applied Research Escabase XPS system equipped with a CLASS VM 100 mm mean radius hemispherical electron energy analyzer with multichannel detectors in an analysis chamber with a base pressure of 3.0×10^{-9} mbar. Survey scans were recorded between 0-1100 eV with a step size of 0.7 eV, dwell time of 0.5 s and pass energy of 100 eV. Core level scans were acquired at the applicable binding energy range with a step size of 0.1 eV, dwell time of 0.5s and pass energy of 20 eV averaged over 10 scans. A non-monochromated Al-Kα X-ray source at 150 W was used for all scans. All spectra were acquired at a take-off angle of 90º with respect to the analyzer axis. XPS spectra were also collected on a Thermo Electron K-Alpha spectrometer at the Centre de Spectroscopie at the Institut Lavoisier de Versailles in France, using a monochromatic Al K_α X-ray source (1486.6 eV). Core level spectra from 100 scans were referenced to the C 1s core-

level peak at 284.3 eV. The XPS spectra were processed using a Shirley background correction followed by peak fitting to Voigt profiles.[15] The Shirley correction was employed to remove the background due to photoelectrons which experienced energy loss. The FWHM were allowed to vary within reasonable value ranges in order to achieve best fit.

3.4 References

1. Walcarius, A.; Sibottier, E.; Etienne, M.; Ghanbaja, J. Electrochemically assisted self-assembly of mesoporous silica thin films. *Nat. Mater.* ***6***, 602-608 (2007).
2. Meyer, E. Atomic force microscopy. *Progress in Surface Science* ***41***, 3-49 (1992).
3. Joy, D. C.; Howitt, D. G., Scanning Electron Microscopy. In *Encyclopedia of Physical Science and Technology (Third Edition)*, Meyers, R. A., Ed. Academic Press: New York, 2003; pp 457-467.
4. Zhou, W.; Apkarian, R.; Wang, Z.; Joy, D., Fundamentals of Scanning Electron Microscopy (SEM). In *Scanning Microscopy for Nanotechnology*, Zhou, W.; Wang, Z., Eds. Springer New York: 2007; pp 1-40.
5. Williams, D. B.; Carter, C. B., *The transmission electron microscope*. Springer: 1996.
6. Reimer, L., *Transmission electron microscopy: physics of image formation and microanalysis*. Springer: 2013; Vol. 36.
7. Gouadec, G.; Colomban, P. Raman Spectroscopy of nanomaterials: How spectra relate to disorder, particle size and mechanical properties. *Prog. Cryst. Growth Charact. Mater.* ***53***, 1-56 (2007).
8. Horrocks, G. A.; Likely, M. F.; Velazquez, J. M.; Banerjee, S. Finite size effects on the structural progression induced by lithiation of V_2O_5: a combined diffraction and Raman spectroscopy study. *J. Mater. Chem. A* ***1***, 15265-15277 (2013).
9. Baddour-Hadjean, R.; Marzouk, A.; Pereira-Ramos, J. P. Structural modifications of $Li_xV_2O_5$ in a composite cathode ($0 \leq x < 2$) investigated by Raman microspectrometry. *J. Raman Spectrosc.* ***43***, 153-160 (2012).
10. Tauc, J., *The Optical Properties of Solids*. Academic Press: New York, 1966.
11. Ravindra, N. M.; Ganapathy, P.; Choi, J. Energy gap–refractive index relations in semiconductors – An overview. *Infrared Phys. Techn.* ***50***, 21-29 (2007).
12. Akaltun, Y.; Yıldırım, M. A.; Ateş, A.; Yıldırım, M. The relationship between refractive index-energy gap and the film thickness effect on the characteristic parameters of CdSe thin films. *Opt. Commun.* ***284***, 2307-2311 (2011).
13. McNulty, D.; Buckley, D. N.; O'Dwyer, C. Polycrystalline Vanadium Oxide Nanorods: Growth, Structure and Improved Electrochemical Response as a Li-Ion Battery Cathode Material. *J. Electrochem. Soc* ***161***, A1321-A1329 (2014).
14. Siegbahn, K. *et al. Nova Acta Regiae Soc. Sci. Ups., Ser. IV*, (1967).
15. Shirley, D. A. High-Resolution X-Ray Photoemission Spectrum of the Valence Bands of Gold. *Phys. Rev. B* ***5***, 4709-4714 (1972).

Chapter 4

Dip-Coated V_2O_5 Thin Film Formation

Adapted From

Glynn, C. *et al.* Linking Precursor Alterations to Nanoscale Structure and Optical Transparency in Polymer Assisted Fast-Rate Dip-Coating of Vanadium Oxide Thin Films. *Sci. Rep.* **5**, 11574 (2015).

Abstract

Solution processed metal oxide thin films are important for modern optoelectronic devices ranging from thin film transistors to photovoltaics and for functional optical coatings. Solution processed techniques, such as dip-coating, allows for thin films to be rapidly deposited over a large range of surfaces including curved, flexible or plastic substrates without extensive processing of comparative vapour or physical deposition methods. To increase the effectiveness and versatility of dip-coated thin films, alterations to commonly used precursors can be made that allow for controlled thin film deposition. The effects of polymer assisted deposition and changes in solvent-alkoxide dilution on the morphology, structure, optoelectronic properties and crystallinity of vanadium pentoxide thin films was studied using a dip-coating method at a speed within the fast-rate draining regime. The formation of sub-100 nm thin films could be achieved rapidly from dilute alkoxide based precursor solutions with high optical transmission in the visible, linked to the phase and film structure. The effects of the polymer addition was shown to change the crystallized vanadium pentoxide thin films from a granular surface structure to a polycrystalline structure composed of a high density of smaller in-plane grains, resulting in a uniform surface morphology with lower thickness and roughness.

4.1 Introduction

Metal oxide thin films are an integral part of modern electronic devices and see use in energy storage,[1-2] supercapacitors,[3-5] field emission devices,[6-7] photovoltaics,[8] thermochromics [9-11] and as components of the working electrodes in sensing devices.[12-13] The deposition methods for producing uniform and stoichiometric thin films in current integrated circuit (IC) devices relies heavily upon methods such as chemical/physical vapour depositions[14] and sputtering techniques[15] which can have low sample throughput and high deposition times compared to comparative solution based techniques.

Thin films deposited from solution processed techniques, such as ink-jet printing, spin coating and dip-coating, use a low-cost liquid precursor solution to form morphologically/compositionally uniform thin films.[16] The increased interest in solution processed methods is mirrored by an increase in the development of analytical techniques to correlate precursor and solution changes to their effects on the composition, structure and morphology of the resultant thin film. Better understanding of the factors that affect thin film materials deposited through solution processed techniques is critical for their future uses within modern device infrastructures where the nanoscale characteristics are increasingly important.

The interaction between the substrate and precursor influences the homogeneity of the thin film, where a match can enable epitaxial growth of the desired thin film.[17-18] Dip-coating is a widely used solution processed deposition technique which is an alternative to the more costly deposition methods. In dip-coating, through both substrate and precursor selection, a fine control over the thin film thickness and morphology is possible.[19] Dip-coating techniques continue to be improved,[20] with various methods devised for producing thin films with different

characteristics such as: optical constant gradation from a single coating through dip-coating acceleration[21] and adjustments to the precursor *in-situ* resulting in polarity gradients within the thin film.[22]

The precursor should complement the chosen deposition method and the desired resultant thin film whilst avoiding undesirable reactivity that might alter the final phase.[23] Polymer assisted deposition (PAD) can be utilized to further influence the characteristics of the thin film through the addition of a polymer to the precursor as an additive.[16, 24] Avoiding gelation or demixing of constituent inorganic and organic phases during preparation, hydrolysis and film crystallization[25] are key requirements for uniform and single phase deposition the thin films. Choosing the appropriate precursor and additive is a key consideration for the formation of metal oxide thin films from solution processed techniques.

For dip-coating techniques, the withdrawal speed influences the formation of the resulting thin films: a low deposition rate produces thin films with a low sample throughput, by increasing the deposition rate, sample throughput is improved but the resultant thin films will be thicker. At dip-coating speeds below ~0.1 mm/s, known as the capillary regime, the formation of the thin film occurs through evaporation at the capillary/air interface and is dependent upon the evaporation of the solvent to form the thin film.[21] Dip-coating speeds at 1 mm/s or above are within the draining regime and at these speeds the formation of the thin film follows the Landau-Levich-Derjaguin model, where gravity-mediated drainage affects the liquid film from which the resultant solid thin film forms after solvent evaporation.[26-27]

At deposition speeds within the draining regime, different methods are proposed for increasing the control over the thickness and morphology of the thin films. To prepare thin films with a low thickness and a uniform surface morphology

whilst retaining higher sample throughput using a dip-coating technique, methods must be employed to counter the drawbacks of the draining regime.[28-29] One such method is to utilise a combination of an alkoxide precursor with the application of a PAD technique that influences viscosity, the nature of the precursor and its conversion to a (uniform) oxide.

For PAD techniques, the choice of polymer additive in the solution precursor must a) prevent demixing at any stage during deposition, b) set the viscosity to maintain uniform coating, c) prevent the incorporation of impurities into the film during clean calcination or thermal treatment, and d) provide ordered, continuous or even epitaxial films to the underlying substrate. Challenges for sol–gel processing methods for reactive and multivalent metal-oxides include the identification of a system in which the solvent and organometallic precursors are compatible. Attempts have been made where polymers were added during sol preparation to increase the formation of crack-free critical thin films.[30] However, the formation and understanding of thin films with controllable phase, crystallinity, uniformity and coverage by simple polymer addition remains a significant challenge for solution based depositions of important oxides.

In this chapter, a combination of techniques was chosen for their compatibility in studying the composition and morphology of solution processed V_2O_5 thin films and provides a mechanistic understanding for polymer-assisted formation and crystallization of V_2O_5 thin films from liquid precursor solutions.

4.2 Experimental

4.2.1 Precursor Synthesis.

Four types of precursor solutions were prepared to produce V_2O_5 thin films where the dilution of the alkoxide to the solvent and also the effect of two different types of additives to the precursor could be studied. For preparing the low and high dilution precursors, the IPA was mixed by volume with the vanadium oxytriisopropoxide precursor and the chosen additive at a volume ratio of 1000:10:1 and 250:10:1 (IPA : Alkoxide : Additive) respectively. Deionized water was added as an additive to the precursor solution to aid the hydrolysis and was replaced by the same liquid volume of PEG-400 in the polymer-assisted deposition (PAD) precursor solutions. Four types of precursor solution were prepared: a low concentration dilution (LCP) and high concentration dilution (HCP) solution where the additive was deionized H_2O, the precursor solutions prepared using PEG-400 as an additive were a low (LCP-PEG) and high (HCP-PEG) dilution mixture.

4.2.2 V_2O_5 Thin Film Preparation.

Drop-casting technique was used to prepare bulk-like samples of the materials while dip-coating at a constant withdrawal rate of 2.5 mm/s was used to deposit uniform thin films. All samples in this chapter were prepared on high quality ITO-coated glass substrates with a nominal ITO thickness of 15 - 30 nm. The substrates were cut to be a uniform size of 12.5 mm in length and 5 mm in width. Crystallization was performed in a convection oven ramped up to 300 ^{o}C at a rate of 1 ^{o}C/min and held for 14 hours. For thermal treatments of the drop-casted samples at 450 ^{o}C a tube furnace was used with a ramp rate of 1 ^{o}C/min and heated for 14 hours.

4.2.3 Characterization Techniques

Surface morphologies were examined using scanning electron microscopy (SEM) and atomic force microscopy (AFM). Samples were scribed with a scalpel blade and AFM images were taken at the interface between the substrate and thin film surface to determine the thin film thickness.

The phase of the films post-crystallisation was tested using Raman scattering spectroscopy collected with a Renishaw InVia Raman spectrometer at 514 nm. XRD of the drop-casted samples was performed using a Phillips Xpert PW3719 diffractometer using Cu Kα radiation (40 kV and 40 mA) scanned between 10^{o} - 40^{o}.

UV-Vis transmission spectroscopy was performed by illuminating samples with white light from a Halogen bulb incident normal to the sample surface and collimated to a beam diameter of ~1 mm. Spectra of the transmitted light were collected using an Ocean Optics USB2000+VIS-NIR-ES CCD spectrometer in the wavelength range 200 – 950 nm. A baseline of the corresponding ITO substrate was taken before each scan.

The in-plane structure of the thin films was determined through HRTEM using a JEOL 2100 high resolution TEM at 200 kV. Single layer thin films were dip-coated onto the surface of 15 nm coated Si_3N_4 TEM grid windows. Thermal treatments were performed in a conventional oven at 300 ^{o}C in air for 14 hours.

4.3 Results

4.3.1 V_2O_5 Drop-Casted Deposits

By drop casting onto the ITO substrate, the bulk-like properties of the precursor were studied. In the drop-casting test, the LCP and LCP-PEG precursors

were dropped onto the substrate and the resulting deposits were studied both pre- and post-thermal treatment. The precursor was dropped onto the substrate as a liquid and hydrolysed slowly due to the large amount of precursor present and the need for the solvent to evaporate, resulting in a slow rate of hydrolyzation. During the initial hydrolysis stage, the liquid precursor was able to flow unconstrained on the substrate prior to solidifying and forming a solid deposit. The effect of increased concentration on the drop casted samples was found to hasten hydrolysis of the deposit, the morphology of the deposit was found to be dependent instead upon the constituents of the precursor.

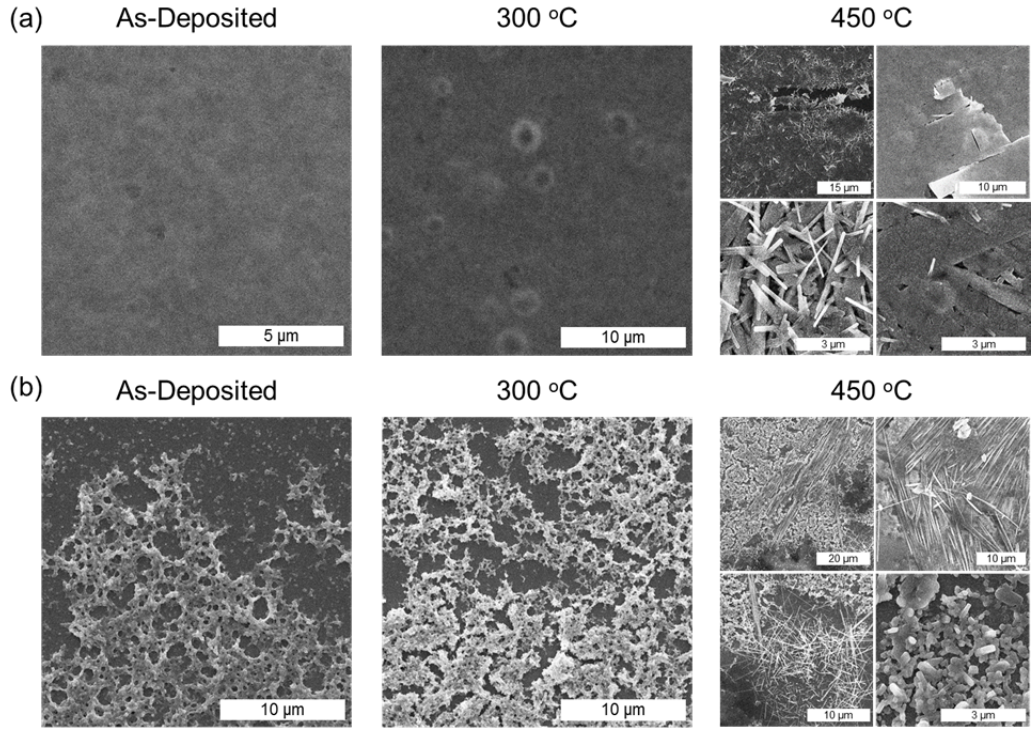


Figure 4.1. SEM surface images showing the surface morphology of as-deposited and thermally treated drop-casted films of VO deposits formed from (a) LCP and (b) LCP-PEG precursors. SEM images of each of the deposits formed at both a thermal treatment of 300 ^{o}C and 450 ^{o}C for 14 hours respectively, is shown.

The drop-casted deposits were thermally treated at two different temperatures, 300 ^{o}C and 450 ^{o}C, under ambient conditions. The deposits were thermally treated at 300 ^{o}C as it is the temperature at which the thin films

crystallized to orthorhombic V_2O_5 without subsequent damage to the film which was found to occur at higher temperatures, where the thin films would experience delamination and surface cracking at temperatures higher than 300 ^oC. A thermal treatment at the increased temperature was performed to correspond to the common crystallising temperatures from the literature.[12, 31]

Surface SEM images of the as-deposited and post-thermally treated LCP and LCP-PEG samples highlighting the differences in surface morphology at both crystalizing temperatures are shown in Figure 4.1 (a, b) respectively. The morphology of the as-deposited deposits is shown to be affected by the additive. The morphology of the as-deposited surfaces for the LCP and LCP-PEG samples differ. The LCP samples form a smoother surface than the LCP-PEG samples which has a rough and irregular morphology. After thermal treatment at 300 ^oC (the temperature used to crystallise the corresponding thin films) the morphology of the LCP samples roughens slightly with the formation of surface defects in the form of pinholes due to the densification of the sample during the thermal treatment. The morphology of the LCP-PEG samples heated at 300 ^oC however undergoes a larger change which results in an increased surface roughness.

After thermal treatment at 450 ^oC both samples show the formation of different structures of VO. The surface of the LCP samples roughens further with increased temperature and also shows the formation of rod-like structures on the surface. The same rod structures are seen in the corresponding LCP-PEG samples, however, the length of the rod structures is larger in the LCP-PEG samples. There is also the formation of crystallites on the surface of the LCP-PEG samples heated at 450 ^oC. The rougher morphology of the thermally treated LCP-PEG sample is attributed to the demixing and removal of the PEG during the thermal treatment as

the VO crystallizes. The PEG demixes from the as-deposited stoichiometric deposit as the temperature increases and is then removed as the temperature further increases. During the removal process, the surface of the crystallising V_2O_5 fractures, resulting in the surface morphology seen in Figure 4.1 (b). Crystalline rods are a common morphology for orthorhombic V_2O_5,[32] however, the size variations of the rods and other crystallites seen on the surface may be indicative of the presence of other forms of VO which are to be studied using XRD and Raman scattering spectroscopy.

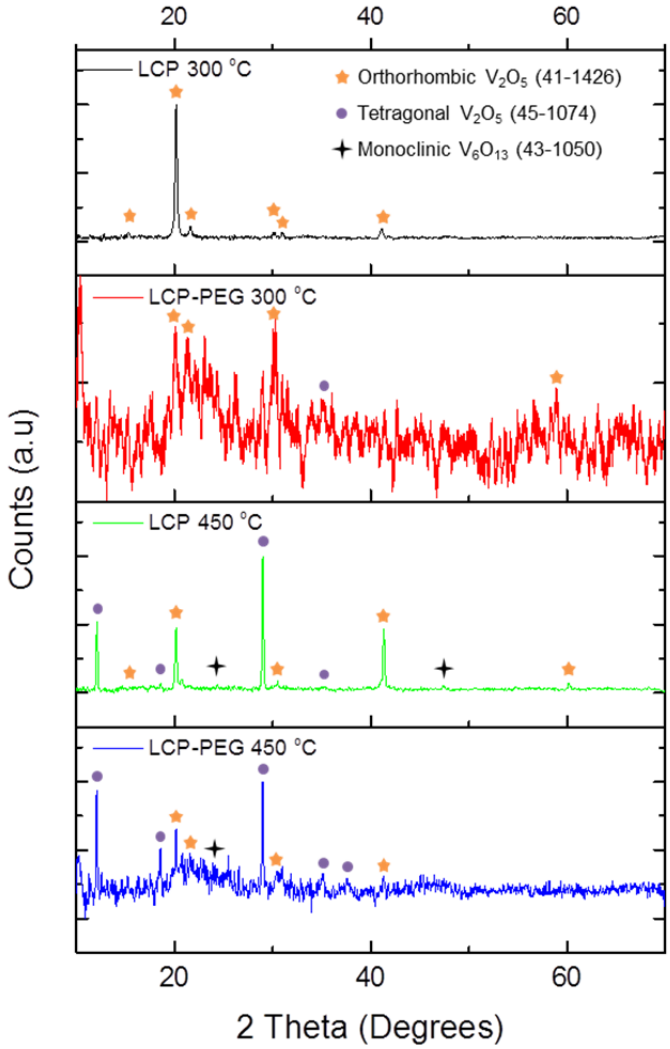


Figure 4.2. XRD patterns of LCP and LCP-PEG drop-casted films thermally treated at 300 °C and 450 °C for 14 hours. The indexed XRD patterns for a variety of VO oxidative states are highlighted.

Figure 4.2 shows the XRD patterns of the drop-casted deposits after thermal treatment. XRD analysis of the deposits after thermal treatment at 300 ^{o}C shows the formation of predominantly orthorhombic V_2O_5 for the LCP deposit with small amounts of tetragonal V_2O_5 also found in the LCP-PEG deposit. After thermal treatment at 450 ^{o}C both the LCP and LCP-PEG deposits show the formation of orthorhombic and tetragonal V_2O_5 with small amounts of V_6O_{13} also apparent in the deposits.

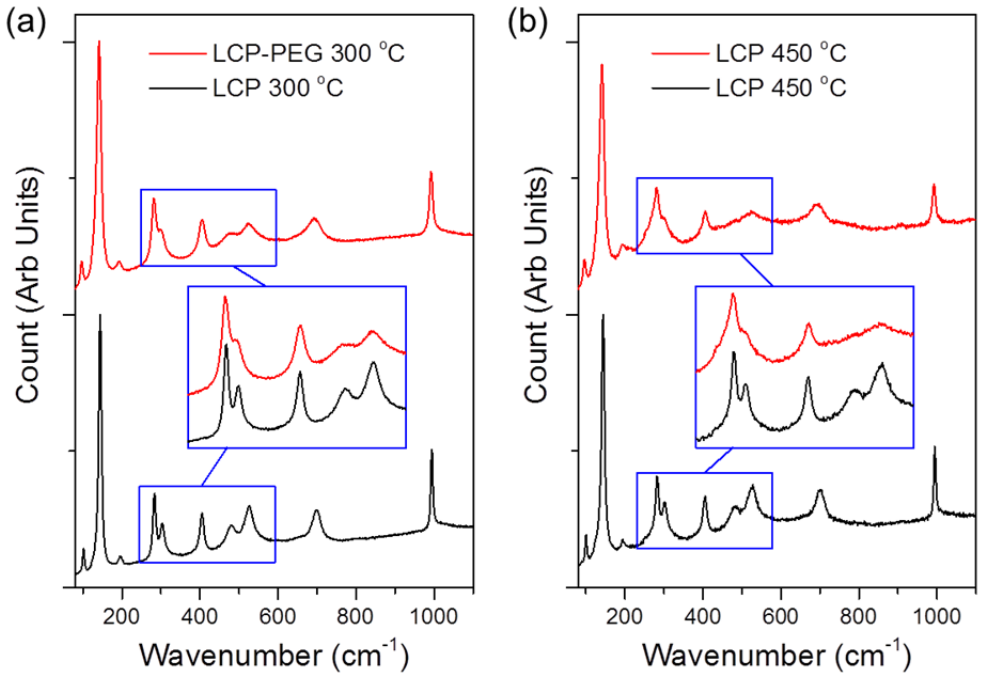


Figure 4.3. Raman scattering spectroscopy of drop casted deposits of (a) LCP and LCP-PEG thermally treated at 300 ^{o}C showing the formation of V_2O_5. (b) Two regions from the LCP deposit thermally treated at 450 ^{o}C showing the deformation of regions the V_2O_5 vibrations due to the presence of small quantities of different VO phases.

The Raman spectra for the LCP and LCP-PEG deposits treated at 300 ^{o}C are shown in Figure 4.3 (a). The Raman spectra show the formation of orthorhombic V_2O_5. The Raman scattering spectra for two regions of the LCP deposits formed at 450 ^{o}C are presented in Figure 4.3 (b) and show the formation of predominantly orthorhombic V_2O_5 with some areas exhibiting some deformation to the highlighted

regions due to the presence of some other vibrations due to different VO phases, in this case most probably that of tetragonal V_2O_5.

As seen in the SEM images in Figure 4.1, the LCP-PEG deposits underwent a large surface change in different regions of the deposit during thermal treatment at 450 ^oC with the formation of long crystalline rods and crystallites. The Raman scattering spectra for three regions on the surface of the deposit is presented in Figure 4.4 (a). The Raman spectra for region one is that of orthorhombic V_2O_5 and is the dominant spectrum found in the deposit, however, areas such as region two and three are interspersed through the surface and the vibrations differ from those of orthorhombic V_2O_5. Figure 4.4 (b) is a deconvolution of the Raman scattering spectrum for regions two and three. The corresponding vibrations which make up the spectra were extracted and used to help determine the VO phases which are present. The vibrations from the deconvoluted spectra were not correlated to one VO phase in particular, the vibrations of both region two and three were instead attributed to the vibrations from a combination of V_6O_{13}, V_2O_3 and VO_2 respectively.[33-34]

The presence of other phases of VO in the XRD spectra is attributed to the crystallization of the disordered as-deposited material. The disorder in the material and likely facilitates crystallization at different rates forming small amounts of different phases of VO. The lack of evidence for different phases of VO in the Raman scattering spectra shows that the amounts of the other VO phases in the deposit are minimal and are more easily detected in a larger area by XRD.

Morphological and structural analysis of the drop-casted V_2O_5 samples provided information on the formation of other phases within the samples at different temperatures. Low concentration solution precursors were used for analysis of the drop-casted V_2O_5 samples as the technique facilitates the formation of bulk-like

deposits regardless of concentration due to the unconstrained nature of the deposition method. At the lower 300 ^{o}C crystallising temperature, the drop casted samples showed that traces of other VO phases can form in the samples; this was applicable to the corresponding thin films for which the smaller amount of other VO phases proved to be difficult to quantify.

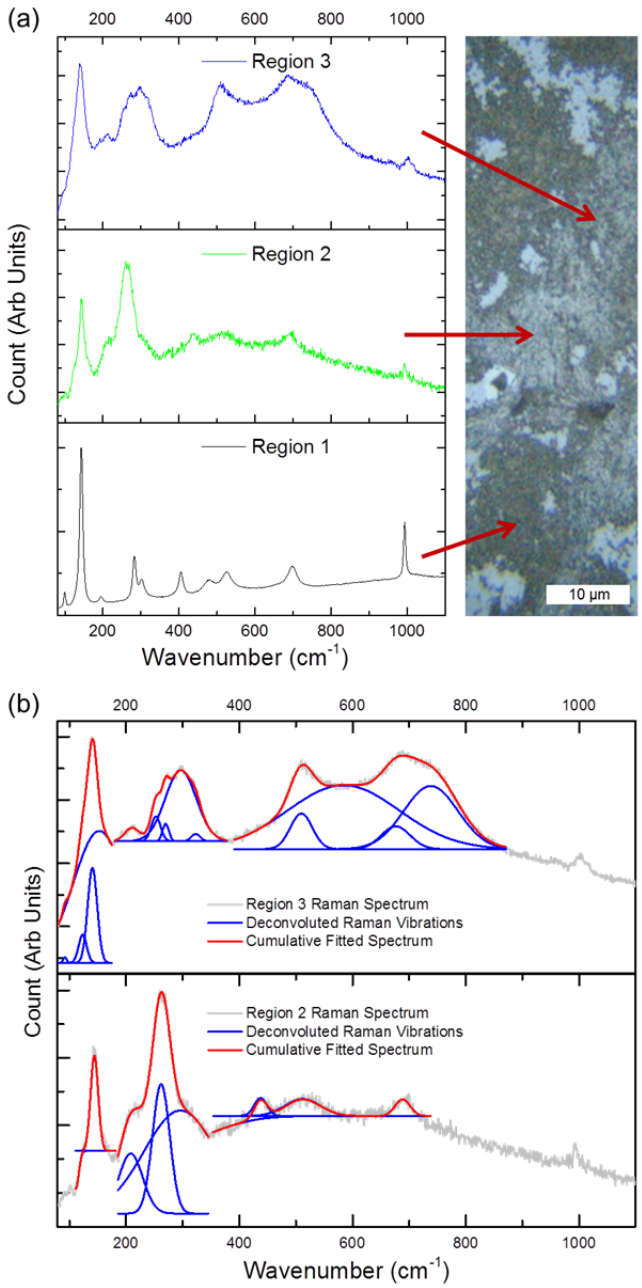


Figure 4.4. (a) Raman scattering spectra and image of the different regions of the LCP-PEG samples thermally treated at 450 °C showing the varied spectra found at each region. (b) Deconvolution of the Raman scattering spectra for region 2 and 3 to characterize the contributing vibrations of the spectra.

4.3.2 Thin Film Characteristics

Alterations to the IPA/alkoxide dilution ratio and the effect of PAD through PEG addition to V_2O_5 precursor solutions for thin film solution processed depositions were studied by preparing four precursor solutions and depositing through a dip-coating technique. Each of the solutions was a dilution mixture of V_2O_5 alkoxide and IPA with either deionized H_2O or PEG-400 as an additive. Four types of precursor solution were prepared: a low concentration dilution (LCP) and high concentration dilution (HCP) solution where the additive was deionized H_2O, the precursor solutions prepared using PEG-400 as an additive were a low (LCP-PEG) and high (HCP-PEG) dilution mixture.

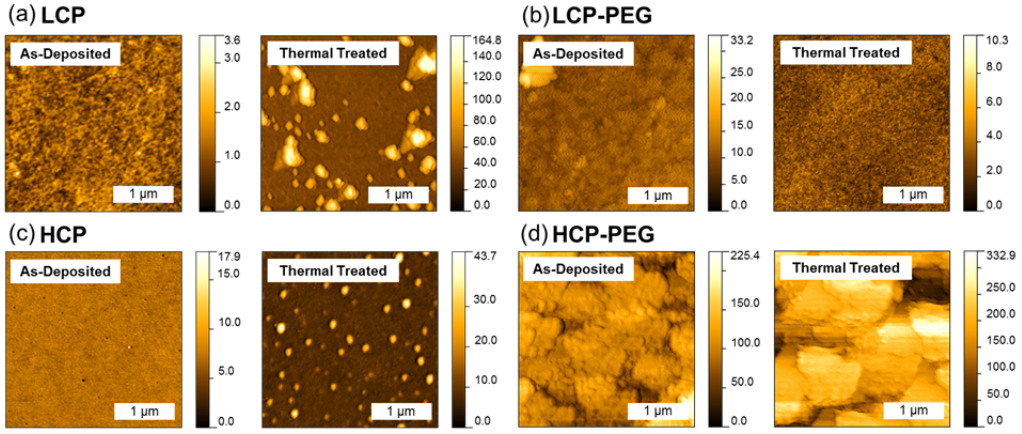


Figure 4.5. AFM surface images of as-deposited stoichiometric and post-thermally treated orthorhombic V_2O_5 films dip-coated from (a) LCP (b) LCP-PEG (c) HCP and (d) HCP-PEG solutions.

AFM surface images of the as-deposited and post-thermally treated dip-coated thin films formed from LCP, LCP-PEG, HCP and HCP-PEG precursors are shown in Figure 4.5 (a-d) respectively. Corresponding SEM images of the surfaces can be seen in Figure 4.6. The average RMS surface roughness for each thin film obtained from AFM measurements is summarized in Table 4.1. The as-deposited LCP and HCP thin films have a low RMS roughness value of 0.2 nm and 0.4 nm respectively that increases to 7.8 nm and 4.8 nm after thermal treatment at 300 °C for

14 h. The increase in surface roughness is expected and occurs during crystallization and densification of the thin film coupled with the formation of crystallites on their surfaces during thermal treatment.

The thin films formed from the PEG-containing solutions exhibited a more uniform surface morphology to those without PEG which can be prone to pin-hole development. Factors which affect the formation of pinholes were shown to be both environmental and chemical which can be adjusted through changes to the deposition conditions and through PAD processes (see Chapter 5). After thermal treatment, the LCP-PEG thin film surface roughness decreased from 1.2 nm to 0.2 nm, with a corresponding reduction in the density of observable surface crystallites. The as-deposited HCP-PEG samples had a high roughness of 8.7 nm which rose to 23.1 nm after thermal treatment. This increase was evident in both the AFM and SEM images of Figure 4.5 (d) and Figure 4.6 (d) respectively; where the surface of the thin films was seen to be covered by large crystals of V_2O_5 with evidence of surface cracking and void formation.

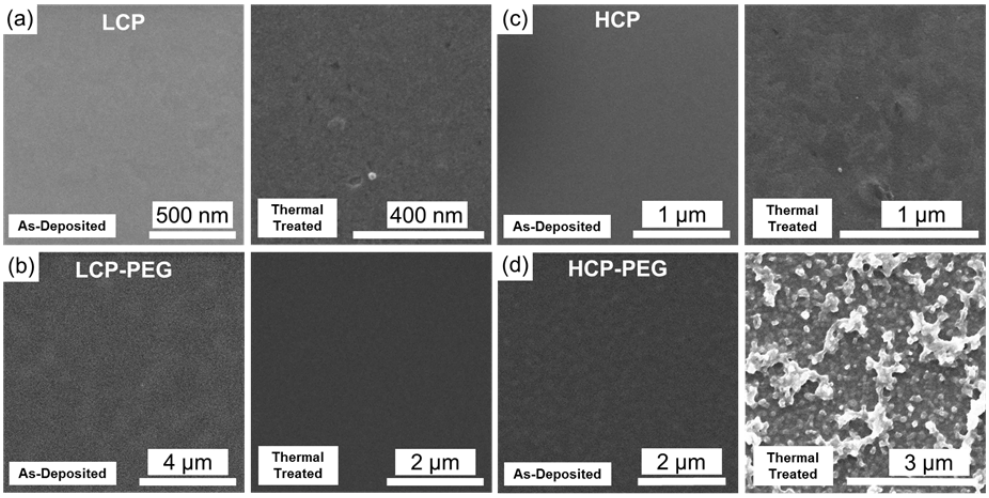


Figure 4.6. SEM surface images of as-deposited stoichiometric and post-thermally treated orthorhombic V_2O_5 films dip-coated from (a) LCP (b) LCP-PEG (c) HCP and (d) HCP-PEG solutions.

Raman scattering spectroscopy analysis in Figure 4.7 (a) confirms the formation of crystalline V_2O_5 after thermal treatment for each of the thin films due to the presence of the vibrational frequencies characteristic of orthorhombic V_2O_5.[35] Additional vibrations seen at 168 cm^{-1}, 845 cm^{-1}, 880 cm^{-1} and 935 cm^{-1} are attributed to small amounts of V_6O_{13} present in the samples due to a displacement of one of the vanadyl-oxygen bonds in the orthorhombic crystal, which can be caused by pseudosymmetry breaking in the layered orthorhombic structure.[36] The vibrational frequencies attributed to these phases is more distinct in thin films formed from the solutions with a high IPA/alkoxide dilution. The peaks at 848 cm^{-1} and 936 cm^{-1} were previously assigned by Su *et al.* to a mode of VO_2 and the peak at 167 cm^{-1} interpreted as a VO_x layered structure.[37] Several reports interpret these symmetric and asymmetric modes as inherent to curvature in the crystal unit cell from VO_x nanotubes (VONTs), or a phase seen in VONTs at low annealing temperatures before the nanotube structure is decomposed and re-arranged to form V_2O_5.[38-41] One report does demonstrate the link between these modes and the corresponding XRD pattern, suggesting a mixed phase of V_6O_{13} and V_2O_5.[36]

The V-O-V in-plane mode depicted in Figure 4.7 (a) can theoretically exhibit an anti-phase stretch with B_{2g} symmetry. This mode is a pseudo centro-symmetric bending in pristine orthorhombic, layered V_nO_{2n-1}. This mode is predicted at ~848 cm^{-1} when the centro-symmetry is broken and the resulting Raman intensity greatly increases. Higher intensity modes at 881 cm^{-1} and 935 cm^{-1} are not predicted based on distortions to the V-O-V and V-O bonds in the D_{2h} space group of orthorhombic V_2O_5 and may arise from VO in another phase such as V_6O_{13} as described above.

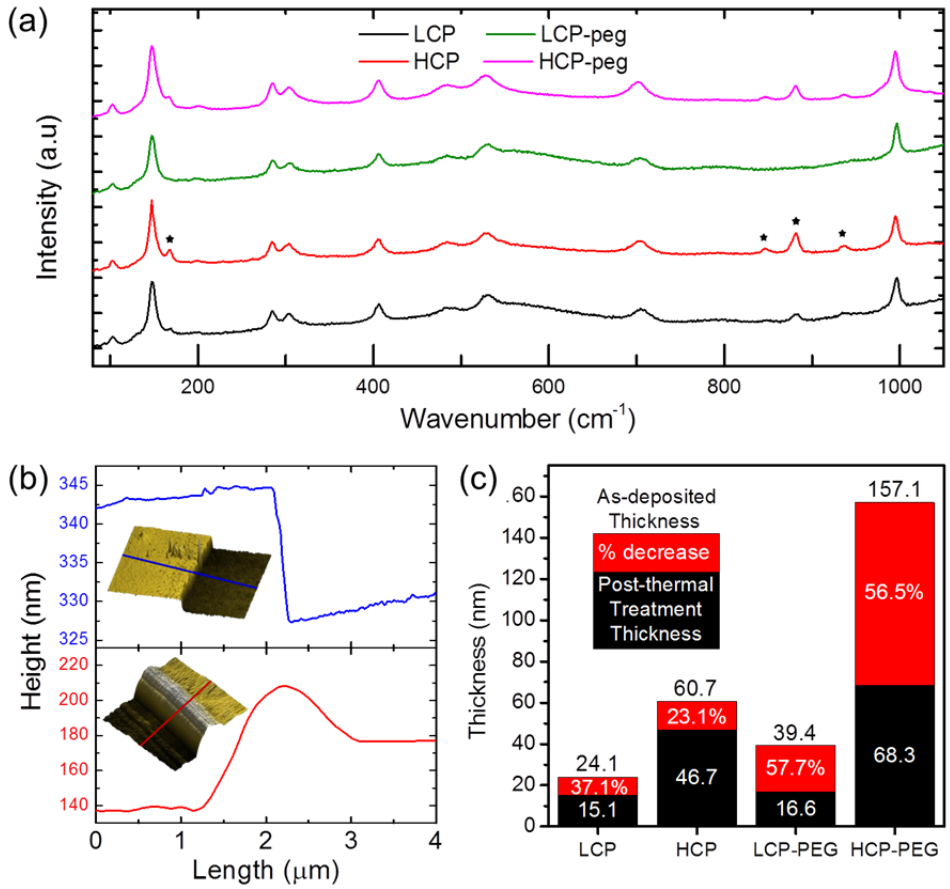


Figure 4.7. (a) Raman scattering spectroscopy of orthorhombic V_2O_5 thin films formed from different precursor solutions. Vibrations seen at 168 cm^{-1}, 845 cm^{-1}, 880 cm^{-1} and 935 cm^{-1} are attributed to the formation of small amounts of V_6O_{13} in the thin films due to a vanadyl-oxygen bond displacement. (b) Thickness profiles of a scribed portion of LCP and LCP-PEG thin film with the associated AFM image (inset). (c) Thickness of as-deposited and post-thermally treated two layer thin films of V_2O_5 formed from each solution. The percent decrease of the thin film due to crystallisation at 300 ^oC for 14 h is provided.

To specifically confirm the resultant phase formation in thin films from PAD dip-coating, thicker drop-casted films were also prepared to examine the bulk-like behaviour of the precursor solutions, i.e. to probe if the crystal structure is representative of the solution composition or influenced by the crystallization mechanism during shear thinning or Marangoni-like instabilities from surface tension variations within the nanofluid precursor solutions. Drop-cast samples allow a comparative bulk-like examination of the final crystal phase and composition. The

liquid films hydrolyze to form a solid amorphous thin film of stoichiometric VO which contains the additive, H_2O or PEG, present in the precursor. The drop-casted samples show the formation of predominantly V_2O_5 after thermal treatments identical to that of the thin films. Drop-casted deposits treated at 450 ^oC showed the formation of tetragonal V_2O_5 and monoclinic V_6O_{13}. Regions on the surface of the deposits with varied morphologies were noted which is indicative of the various phases of VO present. Mendialdua *et al.* confirmed through detailed XPS analyses of various VO phases that if carbon contaminated V_2O_5 is heated at 300 °C in UHV, it reduces to V_4O_9 and subsequently to V_6O_{13} if further heated to 500 °C.[42]

The thicknesses of the thin films formed from different precursor solutions were studied to examine the effects of concentration and additive changes on the as-deposited and crystallised film thicknesses. Samples were prepared with two layers of as-deposited VO thin films deposited in a staircase configuration using iterative dip-coating, allowing for the thickness of the single and double layers to be measured using AFM. Figure 4.7 (b) shows two examples of the AFM images and corresponding line profiles for two thin film thickness measurements. The thicknesses of the as-deposited VO first layer on ITO were generally larger than each subsequent layer of VO. The as-deposited first layer thicknesses were 14.3 nm, 39.6 nm, 29.9 nm and 69.3 nm respectively for the LCP, HCP, LCP-PEG and HCP-PEG precursors. An increase in the alkoxide-IPA ratio resulted in an increase in the thickness of each thin film. The HCP film thicknesses were 2.4 – 2.8× greater than LCP thin films. An increase in thickness by a factor of 1.6 – 2.1× was also found between the LCP-PEG to that of the LCP films. The HCP-PEG thin films are thickest due to the increase in concentration and the addition of PEG which resulted in a rough, irregular surface. The thickness of single layers of crystallized V_2O_5

could not be reliably measured in the LCP and LCP-PEG samples due to the tendency of the thin films to crack during the scribing step due to the thinness of the single layers; therefore, crystallised thickness effects was studied for double layers of the thin films which could be reliably measured after thermal treatment.

For uniform coverage with good interfacial adhesion to the substrate and on preformed films in iterative or multilayer deposits, the mechanism of crystallization from a nanofluid precursor-polymer mixture is important (see Chapter 5). The crystallization of the thin films was studied by comparing the as-deposited thickness to the thermally treated thickness of double layer thin films of each solution. Figure 4.7 (c) presents the total thicknesses of two successively dip-coated thin films (as-deposited and thermally treated) from LCP, HCP, LCP-PEG and HCP-PEG precursor solutions.

4.3.3 Optical Transmission of Uniform Dip-coated Films

The optical transmission of the polymer-free and PAD amorphous and crystallized thin films is shown in Figure 4.8 (a). All films, at low or high solution dilutions and with or without polymer addition, show a decrease in optical transmission after thermal treatment and crystallization. Thin film densification and additive removal occurs during the thermal treatment and crystallization step. Figure 4.8 (a) shows that the as-deposited LCP-PEG thin films have a higher transmittance in the visible region (>80-95%) beyond their respective absorption edges, in spite of being 1.6 – 2.1× thicker than LCP thin films. Uniform mixing of the PEG-blended solution decreases the opacity of the thin films prior to crystallisation, and based on microscopy analyses (*vide infra*), are inherently more uniform, preventing scattering at wavelengths greater than the absorption edge. These thicker films are largely

composed of the PEG-400 polymer with amorphous V_2O_5 inclusions and thus are more transparent than thin films that are composed of the amorphous V_2O_5 inclusions alone. Drude absorption beyond the plasma frequency is not a contributory factor in the visible frequency range for these films, and since the thickness is sub-wavelength (less than $\lambda/30$ at 650 nm for LCP and LCP-PEG).

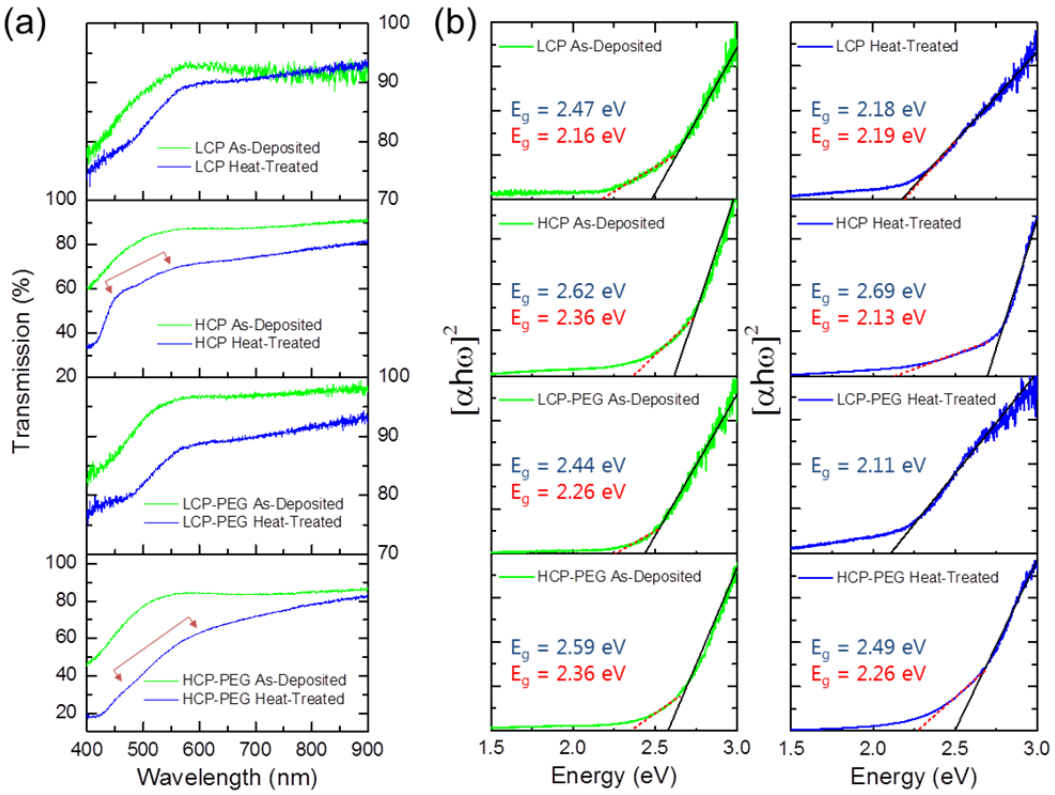


Figure 4.8. (a) UV-Vis transmission spectroscopy of as-deposited and post-thermally treated V_2O_5 thin films formed from both low and high dilution solutions with/without PEG. [Arrows indicates change in transmission spectra between HCP and HCP-PEG thin films] (b) Plot of $[\alpha h\omega]^2$ versus photon energy for the as-deposited and thermal-treated thin films. For the thin films which exhibit the secondary energy gap, the values are shown in red.

As the effect of substrate interface reflections is taken into account by referencing (subtracting) the transmission of the substrate alone from that of the coated substrate, the differences in transmission are thus dominated by the reflectivity caused by crystallization (reduction in void content and increase in refractive index) and by PEG removal in polymer-assisted deposited thin films.

Frequency-dependent thin film interference oscillations are not found in the visible range while the drop in transmission is characteristic of these compact crystalline thin films.

The effective optical bandgap (E_g) of the VO thin films after thermal treatment was calculated by employing the modified Davis-Mott relation in Figure 4.8 (b) and presented as Tauc plots.[43] The absorption coefficient is related to the band-gap through the relation:

$$\alpha h\nu = A(h\nu - E_g)^n \qquad (Eq.\ 4.1)$$

where α is the absorption coefficient of the thin films, A is a constant and E_g is the effective optical bandgap. The exponent n is related to the type of transition for the material, in this case $n = 1/2$ for a direct allowed transition, determined where $[\alpha h\omega]^2 = 0$. The index step change from glass to ITO has been accommodated in the effective gap fits in Figure 4.8.

Table 4.1. Precursor solution and thin film data for orthorhombic V_2O_5 thin film samples prepared in this work. The refractive index of ITO is 1.848 at 650 nm. *r* values calculated at 650 nm. Note, the transmission values in Figure 4.8 have the ITO interface background subtracted.

Precursor Solutions	**Avg. Thin Film RMS Roughness (nm)**		**Avg. Second Layer Thickness (nm)**		**Calc. E_g (eV) [±0.01 eV]**		**Effective η**		**Interfacial reflectance, *r***	
	As-deposited	**Thermal Treated**	**As-deposited**	**Thermal Treated**	**As-deposited**	**Thermal Treated**	**As-deposited**	**Thermal Treated**	**As-deposited**	**Thermal Treated**
LCP	0.2	7.8	24.1	15.1	2.47	2.18	2.49	2.57	0.29	0.31
LCP-PEG	1.2	0.2	39.4	16.7	2.44	2.11	2.50	2.59	0.29	0.32
HCP	0.4	4.8	60.7	46.7	2.62	2.69	2.45	2.44	0.28	0.27
HCP-PEG	8.7	23.1	157.1	68.3	2.59	2.49	2.46	2.48	0.28	0.29

A lower indirect optical transition energy is found in PEG-containing thin films: the effective bandgap values for the LCP and HCP thin films are 2.18±0.01 eV and 2.69±0.01 eV, while those for the LCP-PEG and HCP-PEG films are 2.11±0.01 eV and 2.49±0.01 eV respectively. An increase in the dilution of solutions for LCP to HCP and LCP-PEG to HCP-PEG thin films is correlated with a blue-shift in the effective optical bandgap by 0.51±0.01 eV and 0.38±0.01 eV respectively.

Transmission intensity effects of nano-inclusions or from discontinuities in any of the films is discounted as the primary reason for the shift in absorption, due to sub-wavelength sizes and Rayleigh scattering from solidified features in a solid film 20-100 nm in thickness is less likely to influence the optical transmission. LCP and LCP-PEG films on ITO glass comprise two interfaces with their individual refractive index contrast. In order to explain contributory reasons to reduction in transmission intensity after crystallization and densification in uniform films pre- and post-heating, reflection losses during transmission at two interfaces is considered, where the film is as-deposited, mixed with PEG (and thus thicker), or crystallized and more dense. Thus from wave optics, the reflectivity is related to the modulus of the electric fields via the three-phase Fresnel equations for light reflection at the ITO-VO interface (*i*) and that at the VO thin film-air interface (*j*), and can be expressed as

$$R_{ij} = \left|R_{ij}\right| \exp\left[-2\left(\delta_i + \delta_j\right)\right] \qquad \textit{(Eq. 4.2)}$$

where,

$$\left|R_{ij}\right| = \left[\left(\eta_i - \eta_j\right)/\left(\eta_i + \eta_j\right)\right] \qquad \textit{(Eq. 4.3)}$$

and the phase thickness of each layer in the film-substrate system is

$$\delta_i = 2\pi\eta_i \cos\theta_i d_i/\lambda \qquad \textit{(Eq. 4.4)}$$

where θ_i is the angle of refraction and d_i is the actual layer thickness. As with

antireflection coatings for instance, the changes in refractive index of each film reported here (at thicknesses much less than $\lambda/4$) should affect the total transmittance, and measured values are thus related to thickness and effective index based on phase and structure. The reflectance from each interface of the two-film systems for each type of thin film prepared that reduces total transmittance,

$$r = [\eta_{air}\eta_{ITO} - \eta_{VO}^2/\eta_{air}\eta_{ITO} + \eta_{VO}^2]^2 \qquad \textit{(Eq. 4.5)}$$

are summarised in Table 4.1. Using Mott theory, the effective bandgaps from Figure 4.8 were related to the refractive index according to

$$\eta_{VO}^4 E_g \sim 95\ eV \qquad \textit{(Eq. 4.6)}$$

and the values are shown in Table 4.1. Since the ITO transmittance and reflectance are subtracted as background in Figure 4.8 (a), the variations in transmission at 650 nm, are influenced by effective index contrast reflectance at the VO-air interface, as the reduction in thickness of the film (with and without PEG and pre- and post-heating) does not account for the decrease in optical transmission at wavelengths where band edge material absorption does not occur.

4.3.4 In-Plane HRTEM of PAD Processes in Oxide Thin Films

Thin films were dip-coated from the LCP and LCP-PEG precursor solutions onto the surface of the Si_3N_4 TEM grids, allowing examination of in-plane crystal structure by HRTEM, high resolution AFM and Raman scattering spectroscopy. A schematic of V_2O_5 dip-coated onto a Si_3N_4 coated TEM grid is shown in Figure 4.9 (a): the in-plane structure of the films can be probed by HRTEM without complications from separate entities of material overlapping in projection as found in TEM samples prepared through exfoliation methods.

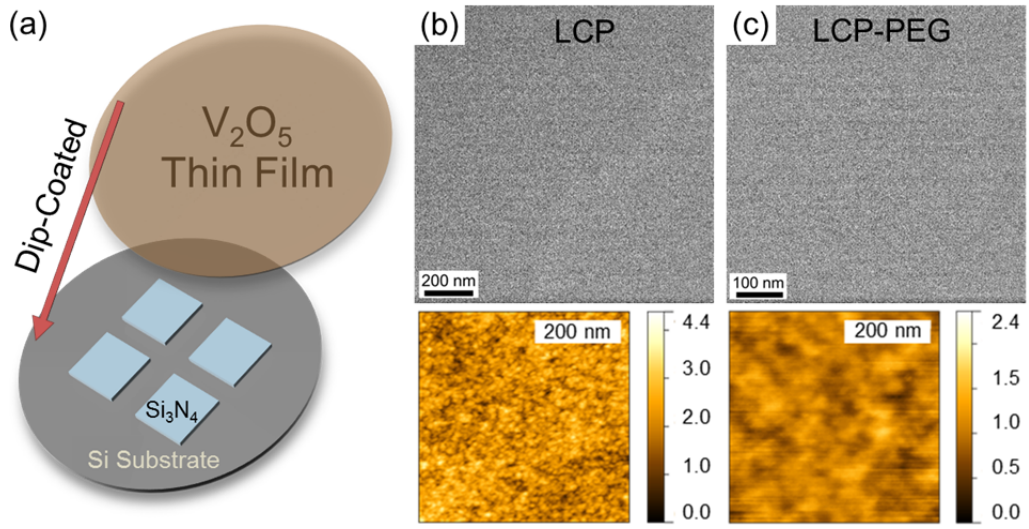


Figure 4.9. (a) Schematic of Si_3N_4 membrane TEM grids with dip-coated V_2O_5 thin films for investigation of their in-plane structure. In-plane TEM images and corresponding AFM images of as-deposited stoichiometric V_2O_5 thin films dip-coated from (b) LCP and (c) LCP-PEG solutions.

Single thin film layers deposited from the low dilution concentration solutions were formed on the Si_3N_4 TEM grids so that the effect of PEG on the in-plane crystallization could be examined. HRTEM and high resolution AFM (inset) images for the LCP and LCP-PEG as-deposited thin films are shown in Figure 4.9 (b, c) respectively. There is no evidence of crystalline structure evident prior to thermal treatment in the HRTEM images for either deposit as expected from the XRD and Raman scattering spectroscopy performed previously in this work. The as-deposited thin films are amorphous as they are formed from un-heated vanadium alkoxide precursor which does not crystallise until thermally-treated. High-resolution AFM images show that the amorphous LCP and LCP-PEG films have a granular surface morphology where the individual features are composed of inclusions of stoichiometric amorphous V_2O_5. The LCP-PEG samples appear to have comparatively larger individual inclusions. These larger inclusions are attributed to the continual coarsening of hydrolyzing alkoxide into solid V_2O_5 and the

development of instabilities in the PEG that are retarded by the increasing density of inclusions with time.

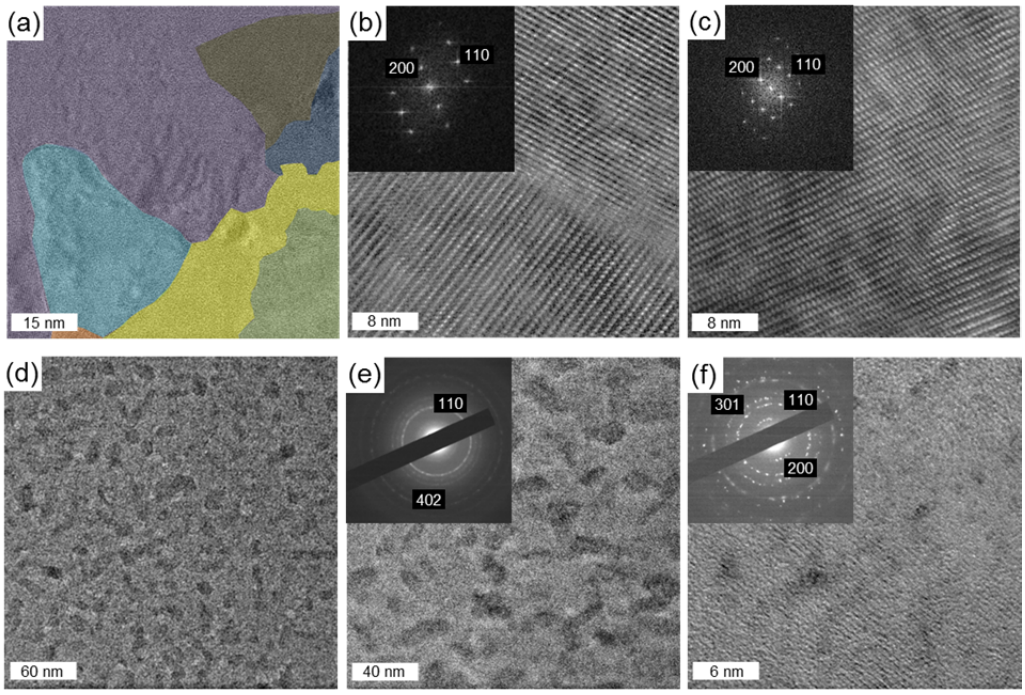


Figure 4.10. Post-thermal treated in-plane HRTEM images and corresponding FFT or diffraction patterns of orthorhombic V_2O_5 thin films formed from (a-c) LCP and (d-f) LCP-PEG solutions. Thin films formed from LCP precursor solutions show the formation of grains of orthorhombic V_2O_5 with defined grain boundaries. Thin films formed from LCP-PEG precursors have a polycrystalline orthorhombic V_2O_5 structure.

The V_2O_5 coated grids were thermally treated for 14 hours at 300 ^oC and the HRTEM and AFM analyses were repeated. Figure 4.10 (a-c) shows the HRTEM and related fast Fourier transforms (FFT) patterns for the thermally treated LCP samples, while Figure 4.10 (d-f) shows the corresponding images for the LCP-PEG samples. The LCP thin film crystallization results in individual crystalline grains of orthorhombic V_2O_5 in a patchwork arrangement; the different grains indexed to orthorhombic V_2O_5 are highlighted in Figure 4.10 (a-c). The HRTEM in Figure 4.10 (a) is reshown in Figure 4.11 without the colour coding of the V_2O_5 grains.

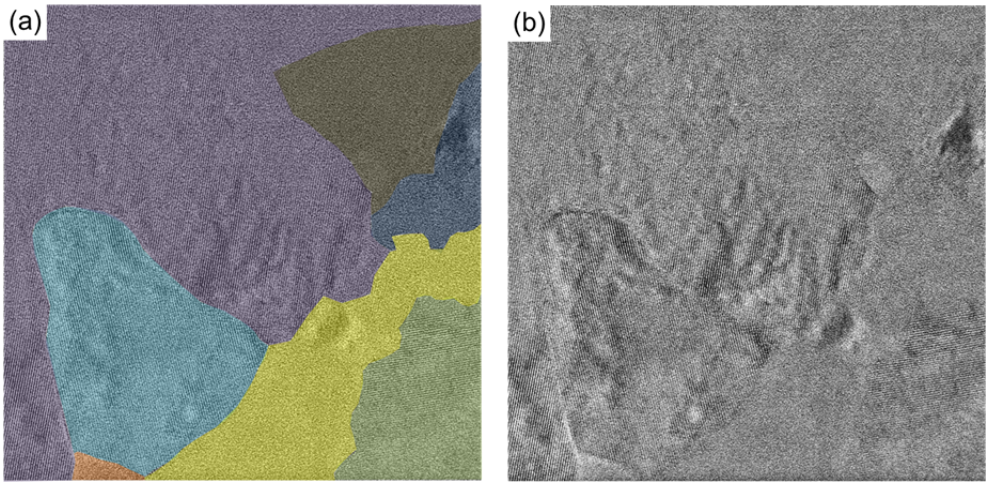


Figure 4.11. (a) TEM image of the different crystalline grains of the LCP thin films thermally treated at 300 °C on a Si_3N_4 coated TEM grid (b) corresponding TEM image without the grains highlighted.

The LCP-PEG thin film shown in Figure 4.10 (d) has a pockmarked morphology in the HRTEM images where the presence of individual crystalline grains is not apparent as found with the LCP thin films. In such films, the removal of the polymer results in high density, small grains that form a polycrystalline film (Figure 4.10 (e, f)), which from Figure 4.5, is uniform and of low surface roughness. Polycrystalline orthorhombic V_2O_5 is also found at higher magnification (Figure 4.10 (f)), and single crystalline grains are not characteristic of calcined PAD V_2O_5 thin films at atomic resolution. The data confirm that polymer-assisted synthesis using PEG-containing precursors alters the hydrolysis and gelation point of the nanofluid, forming high density grains within the structure. Regions of the thermally treated LCP-PEG thin films exhibited a porous morphology as seen in Figure 4.12. These regions are small and interspersed on the sample and show an increase in the porosity of the thin films due to the effects of the PEG on the hydrolysis and gelation point of the nanofluid stage.

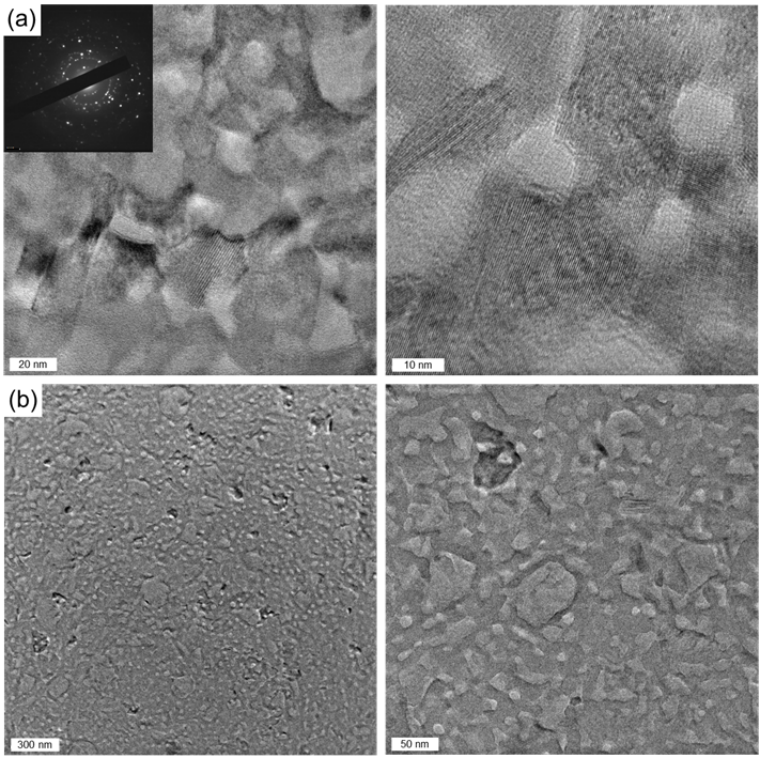


Figure 4.12. (a, b) TEM images of different regions of the LCP-PEG thin film deposited onto Si_3N_4 TEM grids. These regions show the formation of porous thin films of the V_2O_5 attributed to the effects of the PEG on the crystallization of the thin film.

The high-resolution AFM images of the thermally-treated LCP and LCP-PEG thin films on the Si_3N_4 TEM grids are shown in Figure 4.13 (a, b) respectively. The single crystalline grains of V_2O_5 for the LCP thin films are seen in Figure 4.13 (a) as found in the corresponding HRTEM images. The pockmarked and smaller polycrystalline structure of the LCP-PEG thin films can be characterized from Figure 4.13 (b) due to the presence of smaller structures and a similar surface morphology as seen in the HRTEM images.

Raman scattering spectroscopy was performed on the V_2O_5 thin films deposited on the Si_3N_4 coated TEM grids after thermal treatment. Figure 4.13 (c) is an optical microscopy image of the surface of the grids showing the thin films deposited onto the Si_3N_4 window and the surrounding regions. The Raman scattering

spectra shown in Figure 4.13 (d) confirm the formation of orthorhombic V_2O_5 for both the LCP and LCP-PEG thin films after thermal treatment. The low intensity of the vibrational modes is attributed to the thinness of a single dip-coated film on the Si_3N_4.

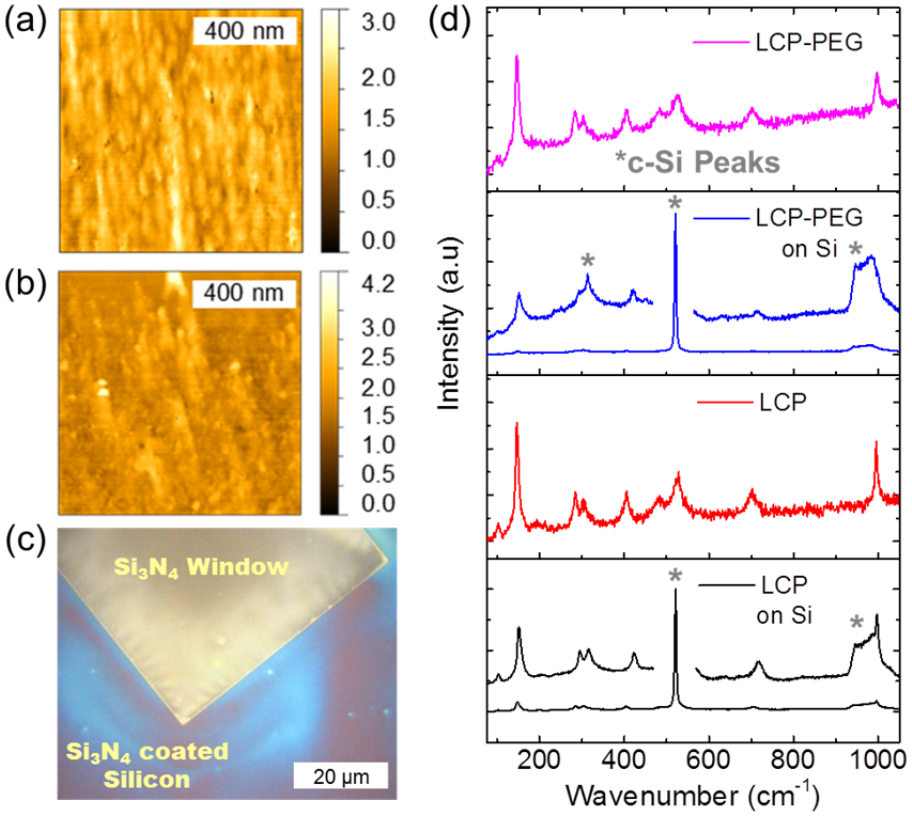


Figure 4.13. AFM surface images of (a) LCP and (b) LCP-PEG orthorhombic V_2O_5 thin films deposited onto Si_3N_4 TEM grids after thermal treatment. (c) Optical microscope image of a thin film of V_2O_5 on a Si_3N_4 coated TEM grid. (d) Raman scattering spectroscopy of the thin films formed on Si_3N_4 windows. The vibrational contributions from the underlying Si substrate are highlighted by asterisks (*).

4.4 Discussion

As described by Sanchez *et. al.* the role of chemical modifications to alkoxide based liquid solutions is to affect the hydrolyzation and condensation reactions such that the resultant solution is adjusted and improvements to the deposition of the solid materials can be made.[44] Both the H_2O and PEG-400

additives can have different effects on the formation reaction of the alkoxide based precursor due to their specific chemistry. The low volume of the H_2O additive is insufficient to fully hydrolyse the precursor solution. The addition of the H_2O is to facilitate the triggering of the hydrolysis of the liquid thin film in the initial stages of the deposition stage, so that the solid thin film has increased adhesion to the surface of the substrate during its formation. The source of H_2O reactant for the hydrolysis of the deposited liquid film for forming a solid thin film comes from the deposition environment after the initial dip-coating. The role of PEG-400 as an additive is to form a mixed vanadium-PEG alkoxide derivative in the liquid solution; during the formation reaction with environmental H_2O the effects of the polymer on the hydrolyzation and condensation alters the morphology of the resultant thin film.[44] The effect of the PEG additive on the thin films can be considered in terms of the chemistry of the solution but must also be considered mechanistically in the method it mixes and demixes within the as-deposited thin film before and during thermal treatment. The different alterations to the precursor solution affect the structural, morphological and optoelectronic properties of the thin films in a variety of ways as shown in the results above.

The roughened surface morphology seen in the HCP-PEG thin films is attributed to the higher concentration of PEG and alkoxide within the as-deposited thin film. During the thermal treatment, the PEG demixes and carbonizes, while the amorphous VO crystallizes into orthorhombic V_2O_5. The as-deposited AFM images in Figure 4.5 and for the HCP-PEG films show an already roughened surface where the PEG has non-uniformly spread through the thin film during the deposition process. As the temperature further increases, the demixed PEG is removed from the film and results in surface fracturing and the formation of nanoscale sub-wavelength

voids in the solidifying V_2O_5. Uniform films before and after thermal treatment are possible from LCP-PEG thin films where an optimum dilution between the IPA, alkoxide and PEG allows for decomposition and removal of the PEG additive while the crystallizing V_2O_5 forms a coherent thinner thin film (Figure 4.5 (b)).

The relative thickness reduction for PEG-containing solutions is consistently highest after heating at 300 ^oC for 14 hours. Using the high dilution concentration of alkoxide increases the rate of hydrolyzation compared to LCP-PEG thin films where the PEG spreads uniformly through the film. Consequently, AFM and thickness measurements indicate that discontinuous demixing and subsequent PEG decomposition affects the overall uniformity. Crystallized film uniformity is improved through a PAD technique with the addition of PEG, but with lower IPA/alkoxide concentration.

The processes which control the formation of alkoxide based thin films dip-coated within the draining regime were examined so a greater understanding of thin film formation could be examined. At dip-coating rates within the Landau-Levich-Derjaguin draining regime, Faustini *et al.* reaffirm that thin film thicknesses can be constrained, with minimal variation, for relatively fast deposition rates of ~1-10 mm/s.[21, 27]

The formation process for thin films deposited using fast- and slow-rate dip-coating are shown in Figure 4.14. At fast-rates, the liquid film is deposited on the surface of the substrate prior to the evaporation, hydrolysis and subsequent formation of the solid thin film. At slow-rates for dip-coating, the same evaporation, hydrolysis and solidification processes occur whilst the substrate is still being withdrawn from the precursor. Capillary action affects the formation of the thin film as it is still in contact with the meniscus of the liquid.

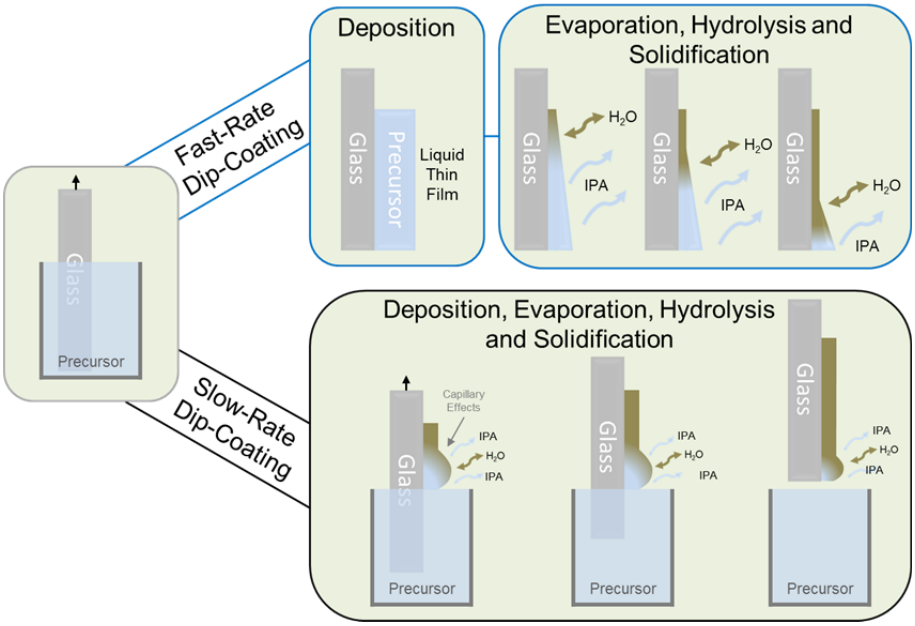


Figure 4.14. Formation processes of fast- and slow-rate dip-coated thin films.

The thickness of a liquid coating that remains on the surface of a substrate at high speed withdrawal rates is dependent upon gravity induced drainage which dominates over capillary and meniscus effects. Therefore, the thickness of the liquid coating is related to the drainage balancing surface tension such that

$$\rho g h \gamma / \eta \sim u \qquad \textit{(Eq. 4.7)}$$

where u is the withdrawal rate, h is the liquid thin film thickness, γ is the surface tension, η is the viscosity, ρ is the solution density and g is the standard gravity. At faster deposition rates that initially overcome gravitational forces (>1 mm/s), the thickness of the liquid film can be approximated with

$$h \sim D\,[U]^{2/3} \qquad \textit{(Eq. 4.8)}$$

where D can be calculated using constant values of the deposited liquid,[21, 26]

$$D = \frac{0.94\,\eta^{2/3}}{\gamma^{1/6}\,(\rho g)^{1/2}} \qquad \textit{(Eq. 4.9)}$$

For each precursor solution studied in this work, the low molar volume fraction of the alkoxide and additive at both concentrations approximates to that of the density

of the main component, IPA. The impact of the alkoxide and additive on the wetting characteristics of the IPA is also negligible due to their small comparative overall volume within the solution. Therefore, the thickness of the IPA film at a withdrawal speed of 2.5 mm/s can be approximated by using the constants for IPA. Using literature values for IPA (γ = 2.212×10^{-3} kg/m, ρ = 786 kg/m^3, η = 2.3703×10^{-3} kg/ms) an estimate for the static liquid film thickness prior to drainage and formation of the solid thin film through hydrolysis formed at high withdrawal rate of 2.5 mm/s is 9 – 10 μm.

To account for the transition from a liquid to solid thin film through evaporation processes, a material proportion constant (*k*) term can be introduced such that:

$$h \sim kD\,[U]^{2/3} \qquad \textit{(Eq. 4.10)}$$

The *k* term is specific to the initial precursor in each case and is a volume proportion constant for the material mixture within the liquid solution and defined by

$$k = \frac{CM}{\alpha\rho} \qquad \textit{(Eq. 4.11)}$$

where *C* is the inorganic precursor concentration, *M* is the inorganic material molar weight, α is the fraction of the material in the film and ρ is the density of the inorganic material.[26] (Note: α_i was originally calculated by Faustini *et. al*. through comparison of the initial and final refractive index of the material.[21] As the value is given as "the fraction of material in the liquid film", the percentage amount of the vanadium oxide and additive was calculated through their respective molar masses within each precursor and used in calculating the k_E value)

An estimate for an equivalent *k* value (k_E) for the LCP and HCP precursors is 0.76 and 0.79 respectively. A *k* value can be calculated (k_C) for each solution using

the experimentally obtained thin film thickness; the k_C for the LCP and HCP precursors is 1.69×10^{-3} and 4.08×10^{-3} respectively, which is two orders of magnitude lower than that of the estimated k_E. The k_E and k_C values for the different precursors is shown in Table 4.2. The k_C value is two orders of magnitude smaller than k_E. It can therefore be assumed that the solid thin film which results from the initial liquid thin film cannot be calculated through a simple relationship between the "solid" materials in the precursor; instead, the thin film forms through the evaporation and phase change that occurs after deposition during this time. The experimentally calculated k_E value incorporates this process for each precursor.

Table 4.2. Calculated *k* values for each of the precursors:

Precursor	**k_E**	**k_C**	**k_C / k_E**
LCP	0.76	1.69×10^{-3}	452.94
LCP-PEG	0.76	3.52×10^{-3}	214.17
HCP	0.79	4.08×10^{-3}	195.35
HCP-PEG	0.77	7.13×10^{-3}	106.94

Typically, *k* is cited for sol-gel systems with a large volume fraction of inorganic material. In the present case, the molar volume fraction of inorganic V-O species in each solution is several orders of magnitude smaller than that of the IPA. Also, unlike many sol-gel systems, thin films formed from alkoxides and carboxylates do not form through evaporation of the solvent alone, but also convert from one compound to another when transitioning from their liquid film phase to a solid thin film phase due to hydrolysis and condensation effects. To explain the

difference in the estimated and calculated *k* values the formation processes of the thin film were examined optically during deposition.

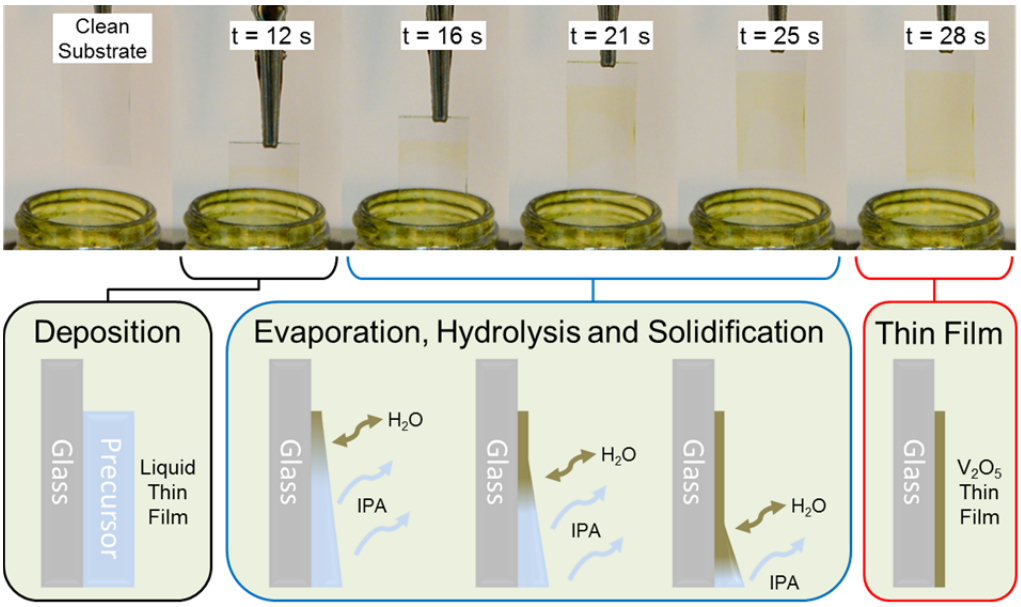


Figure 4.15. Optical images of a glass substrate being dip-coated over time. The formation process from a liquid solution film to a solid stoichiometric V_2O_5 thin film through a combination of evaporation, hydrolysis and solidification is shown optically and schematically.

The formation process of the V_2O_5 thin films during deposition is demonstrated in Figure 4.15, where the initial liquid film is first deposited onto the substrate using fast-rate dip-coating to an estimated thickness of ~9.7 µm. The solid V_2O_5 thin film forms through the evaporation of IPA and the subsequent hydrolysis of the alkoxide and additive into a solid thin film; a process which begins at the top of the deposit and proceeds down the substrate over time. This formation process is shown in the optical image of Figure 4.15 and the accompanying movie hosted online (http://www.nature.com/article-assets/npg/srep/2015/150630/srep11574/extref/srep11574-s2.mov).

The change in thin film thickness occurs during the short hydrolyzation and condensation step after IPA evaporation. The liquid/solid phase change of the alkoxide precursor is the mechanism through which the solid thin films are formed

after the initial liquid film is formed; the estimated *k* value does not take this change into account resulting in a lower estimated thin film thickness. The experimental results provide an empirical value for *k* which takes into account the phase change processes for each of the precursors. It is due to this phase change process which is characteristic to the alkoxide based precursor solution which allows for thin films with nanometre scale thicknesses to be deposited at a dip-coating rate of 2.5 mm/s which is within the Landau-Levich draining regime.

The effects of the PEG additive within the thin film pre- and post-thermal treatment is shown to influence the long range order of the deposit and therefore the optical characteristics of the thin film are affected. The higher dilution concentration of alkoxide/PEG to IPA in the HCP-PEG thin films and the influence of PEG addition respectively results in a different morphology, surface roughness, thickness (see Figure 4.5 and Figure 4.7) and optical transmission characteristic for the HCP and LCP-PEG thin films. The profile of the transmission spectra for the HCP-PEG thin films in Figure 4.8 (a) shows extra features, indicated by an arrow, when compared to the spectra for the corresponding HCP thin film, particularly after thermal treatment. During deposition, the PEG does not have sufficient time during the hydrolyzation step to spread homogenously throughout the thin film; instead the PEG clusters around the amorphous V_2O_5 inclusions resulting in a rougher surface morphology as shown in the AFM data above. The rougher morphology subsequently allowed for selectively higher PEG decomposition during the thermal treatment resulting in the formation of voids and surface fracturing as was also observed for the drop-cast films shown in Figure 4.1 (b).

This change is attributed to an increase in disorder within the thin films from the higher IPA:alkoxide dilution which resulted in a more densely packed thin film

with a higher optical conductivity. The thin films crystallise from amorphous deposits, but optical data is acquired at room temperature, thus no insulating phase transition accounts for a change in optical conductivity and transparency. The presence of other phases of reduced vanadia may explain absorption due to intra-bandgap states; the exact reason is as-yet unclear. The films formed from these precursors can comprise some V_6O_{13} and tetragonal V_2O_5 altering the total absorbance of the thin films.

Oxygen emission at temperatures >300 °C is known to occur in V_2O_5, and in the present case of thin films from PAD methods, other phases such as tetragonal V_2O_5 and monoclinic V_6O_{13} result from vanadyl oxygen vacancy formation in orthorhombic V_2O_5. Creating donors due to oxygen vacancies can increase optical conductivity (n = [donors] – [acceptors]), and lower transparency (or at least shift the onset of absorption to the red due to a Burnstein-Moss shift). Based on HRTEM analysis of the crystallization mechanism and the densification of nanoscale crystallites of V_2O_5 during thin film formation, the reduction in optical transparency is likely caused by changes to the optical constants by an increase in the effective refractive index. Our measurements confirm that inherent porosity and voids of non-V_2O_5 regions define an effective medium with a lower effective index[45-47]. These thin film optical coatings with uniform coverage provide higher transmission without undergoing a metal-insulator transition (MIT) due to a phase change, but alter optical constants due to the nanofluid-like composite structure of the coating prior to crystallization and densification. In trying to explain MIT effects in V_2O_5 thin films[48] the structure of the film and void content, which can significantly alter optical constants and provide high grain-density resistance paths for conduction should be

considered, as it defines the optical conductivity and transparency of conductive thin films.[49]

While the amorphous as-deposited films (with and without PEG) have optical transitions indicated by extrapolation from a single linear region in Figure 4.8 (b), the crystallized thin films show two linear regions at energies higher than the Urbach tail, suggesting absorption contributions from multiple VO phases. For the thin films which exhibit this lower energy gap the absorption edge and value are highlighted in red in Figure 4.8 (b). The energy difference between the higher and lower energy region in the crystallized thin films is larger for the films from high-dilution precursors.

The thermal processes that lead to different thickness, uniformity, roughness and crystallinity of the V_2O_5 thin films after thermal treatment were further studied by dip-coating onto Si_3N_4 TEM window grids. Analogous to liquefied polymer films, dilution which alters the molecular weight of the overall precursor also alters the viscosity, density of V_2O_5 formation and thus processes and forces associated with dewetting and phase separation.[50-51] The dynamic formation of V_2O_5 inclusions during hydrolysis is similar to nanoparticle covered and nanoparticle-embedded polymer films, where the nanoparticles prevent dewetting and control the development of patterning and roughness development during solidification.[52-54] Embedded nanoscale inclusions can potentially enhance the stability of films formed during polymer-assisted deposition, yet the process of oxide formation during film growth under faster withdrawal speeds that negate dominant effects of meniscus and drying fronts at the air-liquid interface (hydrolysis occurs *after* the dip-coating in the 'draining' regime, which defines the thickness) has not been investigated.

In-plane HRTEM, AFM and Raman scattering spectroscopy showed that the presence of PEG in the as-deposited thin films of VO does not impede the formation of orthorhombic V_2O_5 after a thermal treatment at 300 ^oC. The effect of the removal of PEG from the LCP-PEG samples was only evident in the formation of a pockmarked structure which was visible by HRTEM imaging shown in Figure 4.12. The comparison between the surface morphology of thin films produced from a low dilution solution with/without PEG addition shows that the surface morphology of these thin films differs in their smoothness as shown by AFM. Thin films formed without the addition of PEG have a surface composed of single crystalline grains of V_2O_5 with well-defined in-plane grain boundaries on the atomic scale. Thin films prepared with the addition of PEG are composed of a polycrystalline V_2O_5 due to the heterogeneously mixed polymer in the as-deposited thin films necessitating the formation of small crystal grains.

4.5 Conclusions

Thin films of V_2O_5 of varied surface morphologies and characteristics were deposited using fast-rate dip-coating such that the effects of PAD and dilution changes between the alkoxide/additive pair and the IPA solvent of an alkoxide based precursor were studied. Alterations to the precursor solution were shown to have significant effect on the thin film morphology and structure both pre- and post-thermal treatment. The optical properties, including conductivity and transparency associated with non-uniform demixing of polymers within the thin films, was also examined for the resultant amorphous as-deposited thin films and shows that uniform mixing of the polymer additive within the amorphous film is required to maintain long range order. The production of thin films by single dip or iterative dip

coating at high rate with sub 100 nm thicknesses is possible due to the phase change of the alkoxide based precursor during hydrolysis and condensation after the formation and subsequent evaporation of the carrier solvent film.

Thin films containing discontinuities that contribute to higher roughness via demixing/dewetting effects can form surface cracks and surface-bound crystallites when crystallized. The presence of other phases of VO was also found for these samples and was attributed to pseudosymmetry breaking in the layered orthorhombic crystal structure: the small proportion of extra phases of VO are likely contributors to additional absorption in the transmission spectra as the thickness and discontinuities are sub-wavelength and do not contribute to significant scattering. Samples deposited from a low dilution precursor solution with the addition of PEG-400 for PAD effects produced the most uniform thin films of orthorhombic V_2O_5 with a low surface roughness both pre- and post-crystallisation. In these thin films, a significant presence of other VO phases was not found through either Raman scattering or UV-Vis spectroscopy.

Using a combination of HRTEM, AFM and Raman scattering techniques, the effects of PAD on the crystallisation of V_2O_5 thin films were studied in an in-plane configuration. PAD effects on the V_2O_5 thin films were shown to alter the crystallisation mechanism such that a polycrystalline structure composed of small high density grains was formed as opposed to a larger granular structure which forms without PAD effects. The smaller grains of the thin films formed through PAD processes are attributed to the heterogeneous mixing of PEG within the as-deposited thin film resulting in smaller crystal grains forming during thermal treatment. The small crystal grains were shown through in-plane HRTEM and AFM to result in a uniformly smooth surface morphology with a low rms roughness.

The study of the type formation characteristics and subsequent analysis of alkoxide based fast-rate dip-coated thin films in this work indicates a promising method for optoelectronic oxide material deposition in thin film transistors, functional coatings and as oxides for electronic devices that are processed on flexible substrates or plastic electronics (amorphous room-temperature oxides, or crystallized films on polyimides for example). The applications of the PAD process is potentially a useful solution-processable low cost approach for controlling the types of thin films that can be deposited. By cataloguing the effects of the precursor alterations, unwanted thin film attributes such as roughness can be systematically removed, or enhanced for influencing light-matter interactions as desired. This particular approach does not necessitate new precursor development and outlines how the rheology and chemical conversion characteristics of precursor solutions can provide a range of uniform thin films.

4.6 References

1. Gershinsky, G.; Yoo, H. D.; Gofer, Y.; Aurbach, D. Electrochemical and Spectroscopic Analysis of Mg^{2+} Intercalation into Thin Film Electrodes of Layered Oxides: V_2O_5 and MoO_3. *Langmuir* ***29***, 10964-10972 (2013).
2. McNulty, D.; Buckley, D. N.; O'Dwyer, C. Synthesis and electrochemical properties of vanadium oxide materials and structures as Li-ion battery positive electrodes. *J. Power Sources* ***267***, 831-873 (2014).
3. Bao, J. *et al.* All-solid-state flexible thin-film supercapacitors with high electrochemical performance based on a two-dimensional $V_2O_5.H_2O$/graphene composite. *J. Mater. Chem. A* ***2***, 10876 (2014).
4. Jeyalakshmi, K.; Vijayakumar, S.; Nagamuthu, S.; Muralidharan, G. Effect of annealing temperature on the supercapacitor behaviour of β-V_2O_5 thin films. *Mat. Res. Bull.* ***48***, 760-766 (2013).
5. Zhu, J. *et al.* Building 3D structures of vanadium pentoxide nanosheets and application as electrodes in supercapacitors. *Nano Lett.* ***13***, 5408-5413 (2013).
6. Kim, G. T. *et al.* Field-effect transistor made of individual V_2O_5 nanofibers. *Appl. Phys. Lett.* ***76***, 1875-1877 (2000).
7. Zhai, T. *et al.* Centimeter-Long V_2O_5 Nanowires: From Synthesis to Field-Emission, Electrochemical, Electrical Transport, and Photoconductive Properties. *Adv. Mater.* ***22***, 2547-2552 (2010).
8. Jung, H. H. *et al.* Doping-free silicon thin film solar cells using a vanadium pentoxide window layer and a LiF/Al back electrode. *Appl. Phys. Lett.* ***103***, 073903 (2013).
9. Minch, R.; Moonoosawmy, K. R.; Solterbeck, C.-H.; Es-Souni, M. The influence of processing conditions on the morphology and thermochromic properties of vanadium oxide films. *Thin Solid Films* ***556***, 277-284 (2014).
10. Granqvist, C. G. Electrochromics for smart windows: Oxide-based thin films and devices. *Thin Solid Films* ***564***, 1-38 (2014).
11. Kats, M. A. *et al.* Ultra-thin perfect absorber employing a tunable phase change material. *Appl. Phys. Lett.* ***101***, - (2012).
12. Li, Z. *et al.* Ir Detectors: Ultrahigh Infrared Photoresponse from Core–Shell Single-Domain-VO_2/V_2O_5 Heterostructure in Nanobeam *Adv. Func. Mater.* ***24***, 1820-1820 (2014).
13. Nicholas, F.; Sean, M. P.; Mark, W. H.; Bharadwaja, S. S. N. Electrical properties of vanadium oxide thin films for bolometer applications: processed by pulse dc sputtering. *J. Phys. D: Appl. Phys.* ***42***, 055408 (2009).
14. Kakiuchi, H.; Ohmi, H.; Yasutake, K. Atmospheric-pressure low-temperature plasma processes for thin film deposition. *J. Vac. Sci. Technol., A* ***32***, - (2014).
15. Nayak, P. K. *et al.* Thin Film Complementary Metal Oxide Semiconductor (CMOS) Device Using a Single-Step Deposition of the Channel Layer. *Sci. Rep.* ***4***, 4672 (2014).
16. Schneller, T.; Waser, R.; Kosec, M.; Payne, D., *Chemical Solution Deposition of Functional Oxide Thin Films*. 1st ed.; Springer: London, 2013; p 796.
17. Carretero-Genevrier, A. *et al.* Mesoscopically structured nanocrystalline metal oxide thin films. *Nanoscale* ***6***, 14025-14043 (2014).
18. Carretero-Genevrier, A. *et al.* Soft-Chemistry–Based Routes to Epitaxial α-Quartz Thin Films with Tunable Textures. *Science* ***340***, 827-831 (2013).
19. Brinker, C. J.; Frye, G. C.; Hurd, A. J.; Ashley, C. S. Fundamentals of sol-gel dip coating. *Thin Solid Films* ***201***, 97-108 (1991).

20. Ohta, H.; Hosono, H. Transparent oxide optoelectronics. *Mater. Today* ***7***, 42-51 (2004).
21. Faustini, M. *et al.* Engineering Functionality Gradients by Dip Coating Process in Acceleration Mode. *ACS Appl. Mater. Interfaces* ***6***, 17102-17110 (2014).
22. Ye, F. *et al.* Fluorescence Spectroscopy Studies of Silica Film Polarity Gradients Prepared by Infusion-Withdrawal Dip-Coating. *Chem. Mater.* ***22***, 2970-2977 (2010).
23. Lange, F. F. Chemical solution routes to single-crystal thin films. *Science* ***273***, 903 (1996).
24. Jia, Q. X. *et al.* Polymer-assisted deposition of metal-oxide films. *Nat. Mater.* ***3***, 529-532 (2004).
25. Valenzuela, C. D. *et al.* Solid State Pathways to Complex Shape Evolution and Tunable Porosity during Metallic Crystal Growth. *Sci. Rep.* ***3***, 2642 (2013).
26. Faustini, M. *et al.* Preparation of Sol−Gel Films by Dip-Coating in Extreme Conditions. *J. Phys. Chem. C* ***114***, 7637-7645 (2010).
27. Landau, L.; Levich, B. Dragging of a liquid by a moving plate. *Acta Physicochim. URSS* ***17***, 12 (1942).
28. Grosso, D. How to exploit the full potential of the dip-coating process to better control film formation. *J. Mater. Chem.* ***21***, 17033-17038 (2011).
29. Chen, D. *et al.* An extremely rapid dip-coating method for self-assembly of octadecylphosphonic acid and its thermal stability on an aluminum film. *J. Mater. Chem. C* ***2***, 9941-9948 (2014).
30. Yu, S.; Yao, K.; Shannigrahi, S.; Hock, F. T. E. Effects of poly(ethylene glycol) additive molecular weight on the microstructure and properties of sol-gel-derived lead zirconate titanate thin films. *J. Mater. Res.* ***18***, 737-741 (2003).
31. Goltvyanskyi, Y. *et al.* Structural transformation and functional properties of vanadium oxide films after low-temperature annealing. *Thin Solid Films* ***564***, 179-185 (2014).
32. Pelletier, O. *et al.* A Detailed Study of the Synthesis of Aqueous Vanadium Pentoxide Nematic Gels. *Langmuir* ***16***, 5295-5303 (2000).
33. Kuroda, N.; Fan, H. Y. Raman scattering and phase transitions of V_2O_3. *Phys. Rev. B* ***16***, 5003-5008 (1977).
34. Chen, X.-B.; Shin, J.-H.; Kim, H.-T.; Lim, Y.-S. Raman analyses of co-phasing and hysteresis behaviors in V2O3 thin film. *J. Raman Spectrosc.* ***43***, 2025-2028 (2012).
35. Chou, J. Y.; Lensch-Falk, J. L.; Hemesath, E. R.; Lauhon, L. J. Vanadium oxide nanowire phase and orientation analyzed by Raman spectroscopy. *J. Appl. Phys.* ***105***, 034310 (2009).
36. Manning, T. D.; Parkin, I. P. Vanadium(IV) oxide thin films on glass and silicon from the atmospheric pressure chemical vapour deposition reaction of $VOCl_3$ and water. *Polyhedron* ***23***, 3087-3095 (2004).
37. Su, Q. *et al.* Formation of vanadium oxides with various morphologies by chemical vapor deposition. *J. Alloys Compd.* ***475***, 518-523 (2009).
38. Souza Filho, A. G. *et al.* Raman Spectra in Vanadate Nanotubes Revisited. *Nano Lett.* ***4***, 2099-2104 (2004).
39. Huotari, J.; Lappalainen, J.; Puustinen, J.; Lloyd Spetz, A. Gas sensing properties of pulsed laser deposited vanadium oxide thin films with various crystal structures. *Sens. Actuators, B* ***187***, 386-394 (2013).
40. Lavayen, V. *et al.* Towards thiol functionalization of vanadium pentoxide nanotubes using gold nanoparticles. *Mater. Res. Bull.* ***42***, 674-685 (2007).

41. O'Dwyer, C. *et al.* Vanadate Conformation Variations in Vanadium Pentoxide Nanostructures. *J. Electrochem. Soc.* ***154***, K29-K35 (2007).
42. Mendialdua, J.; Casanova, R.; Barbaux, Y. XPS studies of V_2O_5, V_6O_{13}, VO_2 and V_2O_3. *J. Electron Spectrosc. Relat. Phenom.* ***71***, 249-261 (1995).
43. Tauc, J., *The Optical Properties of Solids*. Academic Press: New York, 1966.
44. Sanchez, C.; Livage, J.; Henry, M.; Babonneau, F. Chemical modification of alkoxide precursors. *J. Non-Cryst. Solids* ***100***, 65-76 (1988).
45. Eliason, C. M.; Shawkey, M. D. Antireflection-enhanced color by a natural graded refractive index (GRIN) structure. *Opt. Express* ***22***, A642-A650 (2014).
46. O'Dwyer, C. *et al.* Bottom-up growth of fully transparent contact layers of indium tin oxide nanowires for light-emitting devices. *Nat. Nano.* ***4***, 239-244 (2009).
47. Xi, J. Q. *et al.* Optical thin-film materials with low refractive index for broadband elimination of Fresnel reflection. *Nat. Photon.* ***1***, 176-179 (2007).
48. Kang, M. *et al.* Metal-insulator transition without structural phase transition in V_2O_5 film. *Appl. Phys. Lett.* ***98***, 13907 (2011).
49. Ji, Y. D. *et al.* Epitaxial growth and metal-insulator transition of vanadium oxide thin films with controllable phases. *Appl. Phys. Lett.* ***101***, (2012).
50. Reiter, G. Dewetting of thin polymer films. *Phys. Rev. Lett.* ***68***, 75-78 (1992).
51. Mukherjee, R. *et al.* Stability and Dewetting of Metal Nanoparticle Filled Thin Polymer Films: Control of Instability Length Scale and Dynamics. *ACS Nano* ***4***, 3709-3724 (2010).
52. Faupel, F.; Zaporojtchenko, V.; Strunskus, T.; Elbahri, M. Metal-Polymer Nanocomposites for Functional Applications. *Adv. Eng. Mater.* ***12***, 1177-1190 (2010).
53. Amarandei, G.; O'Dwyer, C.; Arshak, A.; Corcoran, D. The stability of thin polymer films as controlled by changes in uniformly sputtered gold. *Soft Matter* ***9***, 2695-2702 (2013).
54. Amarandei, G. *et al.* Effect of Au Nanoparticle Spatial Distribution on the Stability of Thin Polymer Films. *Langmuir* ***29***, 6706-6714 (2013).

Chapter 5

Optimizing V_2O_5 Dip-Coated Thin Film Depositions

Adapted From

Glynn, C. *et al.* Optimizing Vanadium Pentoxide Thin Films and Multilayers from Dip-Coated Nanofluid Precursors. *ACS Appl. Mater. Interfaces* **6**, 2031-2038 (2014).

Abstract

Using an alkoxide based precursor, a strategy for producing highly uniform thin films and multilayers of V_2O_5 is demonstrated using dip-coating. Defect free and smooth films of V_2O_5 on different surfaces can be deposited from liquid precursors. The formation of pinholes due to heterogeneous nucleation during hydrolysis as the precursor forms a nanofluid is shown. Using knowledge of instability formation often found in composite nanofluid films, and the influence of cluster formation on the stability of these films, it is shown how polymer-precursor mixtures provide optimum uniformity and very low surface roughness in amorphous V_2O_5 and also orthorhombic V_2O_5 after crystallization by heating. Pinhole and roughness instability formation during the liquid stage of the nanofluid on gold and ITO substrates is suppressed giving a uniform coating. Practically, understanding evolution pathways that involve dewetting processes, nucleation, decomposition or hydrolysis in complex nanofluids provides a route for improved uniformity of thin films. The method could be extended to improve the consistency in sequential or iterative multilayer deposits of a range of liquid precursors for functional materials and coatings.

5.1 Introduction

In Chapter 4, the preparation of solution processed V_2O_5 thin films was examined. In this chapter, the formation of defects within these thin films and methods for halting their formation is studied. Thin films grown from liquid precursors or solutions are often subject to sol-gel processes that influence uniformity.[1] Thin films, hybrid films and nanocomposite derivatives are important since their mode of processing often mimics that of polymer films, and often possess the properties of both the inorganic and organic phases. These different levels of complexity make controlled assembly or uniformity over a large dimension a major challenge of modern materials chemistry.[2] Thin films of alternative composite materials, those formed by the addition of nanoparticles of inorganic species to polymer films, i.e. nanofluids, offer the possibility of creating materials with features on the nano/microscale[3] with tunable properties due to nanoparticle-matrix, and nanoparticle-nanoparticle interactions.[4-7] While there has been significant research on the stability of thin polymer films, on particle aggregation, and the controlled assembly of monolayer and assemblies of nanoparticles[8], the knowledge of the stability of films of hybrid materials, those where inorganic units are formed *in situ* by molecular precursors, is still being developed.[9]

Hybrid thin films, and indeed many physical and chemical vapour deposited thin films, rely on a high degree of uniformity and low roughness, and such degrees of morphology and composition control are difficult to produce in dip-coated or spin-cast liquid precursors due to their sensitivity to dewetting on various substrates. This difficulty is compounded by complications arising from the chemical decomposition and phase changes during hydrolysis or pyrolysis, which can often lead to a high density of inorganic units within the originally liquid film. Many of

the classical inorganic solid state materials are formed using solid precursors and high temperature processes, which are often not compatible with the presence of organic groups because they are decomposed at elevated temperatures.[2] In some cases, this decomposition can prove useful when forming a metal oxide from a more complex organometallic or related derivative, and subsequent incorporation of polymeric/organic species can then influence growth.

Dewetting effect of liquids on surfaces can limit the spreading uniformity of liquid precursors, and applies to deposition on planar and non-planar substrates; the phenomenon is found with oil on a hot pan to more complex examples such as spin cast polymer films that are heated.[10] Research into bottom-up deposition methods is important for complex oxide films[11-12], and directed self-assembly and block copolymer based techniques[13] augment well-known processes involving sol-gel or molecularly engineered clusters such as organometallic, covalently or coordinatively designed precursors to help in the design of new functional materials, assemblies, arrays or coatings.[14-16]

Several reports have shown that dewetting of thin liquid polymer films could be suppressed by the presence of 'inclusions', typically nanoparticles or small additives, with the resulting polymer film exhibiting spinodal character.[5, 17] Spinodal clustering and nucleation dewetting effects are characterized by specific pattern formation in surface films that are defined by a definite wavelength in their distribution.[16, 18] This wavelength is indicative of a perturbative instability that forms within the liquid resulting in a random orientation of features, where each feature is equidistant in all directions from the next-nearest neighbour.[19] These effects are likely in liquid alkoxides and similar precursors[20] that solidify in time to form another phase that is amenable to a thin film deposit. Recent papers identified

definite control over polymer film smoothness and patterning by using Au nanoparticle networks on the surface of films, or C_{60} fullerene structures within PMMA films, or even by the addition of colloidal quantum dot nanocrystals within polymer films as a composite.[5, 10, 17, 21-22] In all cases, beading of the polymer into typical Voronoi tessellations is prevented and several models have been advanced to explain these effects.[9]

During alkoxide hydrolysis, a system that is chemically well understood, the solidification during oxide formation is as a result of an ever increasing density and association of oxide entities within a liquid that increases in viscosity until a solid film forms.[23] Such a system is reported upon and shows that these effects are not only similar to nanoparticle-loaded liquid polymer films that do not fully dewet a surface, but help to understand the underlying process that defines the hydrolysis of an alkoxide of vanadium to vanadium oxide, and influences the resulting morphology of the nominally layered material.[24-25] The production of devices from thin films of amorphous metal oxides has been recently studied and new techniques are always being examined for their synthesis.[26-28]

It is demonstrated that the well-known alkoxide of the transition metal vanadium, in liquid form on a surface to which it wets, undergoes a mechanism of competitive nucleation dewetting and solidification via hydrolysis that influences and defines the final structure and morphology of the film.[20, 29]

The potential similarity to polymer-NP composited films inspired the search for the underlying mechanism of this classic phase formation process and to develop a protocol allowing optimization of the uniformity of thin films from liquid based precursors that solidify through hydrolysis. The addition of polyethylene glycol

(PEG) or an increase in the viscosity of the alkoxide mixture can minimize pinhole formation and non-uniformities in coated thin films.

5.2 Experimental

5.2.1 Substrate Preparation and Deposition

Two of the solution processed deposition techniques were used for preparing the samples studied in this chapter. Drop casting was used to deposit irregular bulk-films of V_2O_5 while dip coating was used to form uniform thin films. Thin films were dip-coated onto both Au and ITO coated glass substrates due to their prevalence as current collectors for applications involving V_2O_5. A precursor solution composed of IPA : Alkoxide : H_2O prepared at a ratio of 1000:10:1 was used for the depositions which formed surface pinholes. A withdraw rate of 2.5 mm/s was used for depositing the thin films in this work. The Au substrates were composed of borosilicate glass cantilevers, 60 mm in length and 3 mm in width, coated with a 10 nm Ti adhesion layer and a 250 nm Au layer. The Au coated substrates were thermally annealed at 650 ^oC for 90 s prior to deposition of the precursor to produce larger Au grains and prevent delamination of the Au occurring during the thin film deposition. The growth in grain size due to annealing is shown in Figure 5.1 (a,b). The ITO coated glass was cleaved into strips 25 mm in length and 3 mm wide for direct comparison to the Au substrates. Multiple coatings were performed through dip-coating to produce thin films with a desired thickness. To examine the changes between subsequent layers, “staircase” samples (see Figure 5.2) were prepared by successively dip-coating thin films with shorter film lengths on top of underlying layers such that the morphology of each successive layer could be

examined on a single sample. After deposition, the samples were UV-Ozone treated for 30 minutes.

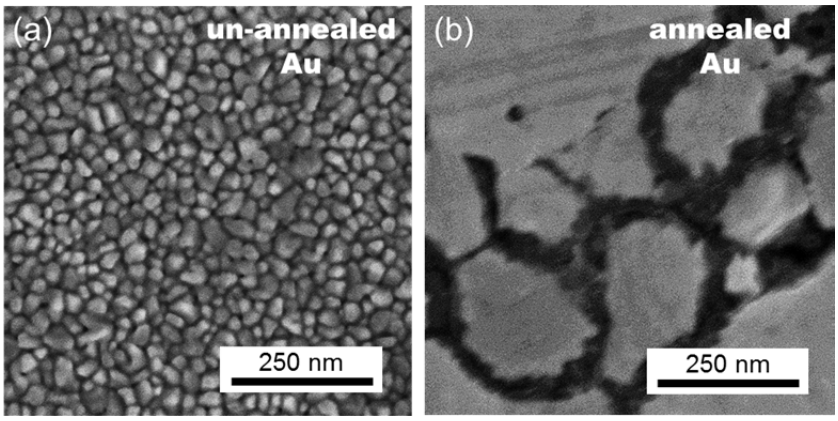


Figure 5.1. SEM images of Au substrate (a) un-annealed and (b) annealed, illustrating the increase in the grain size.

5.2.2 Characterisation and Analysis Techniques

The films were characterised using Raman scattering spectroscopy collected with a Renishaw InVia Raman spectrometer at 514 nm. XRD of the drop-casted samples was performed using a Phillips Xpert PW3719 diffractometer using Cu Kα radiation (40 kV and 40 mA) scanned between 10^{o} - 40^{o}. Surface morphologies were examined using SEM and AFM. XPS spectra were acquired on an Oxford Applied Research Escabase XPS system.

Structure factors used for examining the spatial arrangment of pinholes within films were acquired by carefully thresholding digital images and obtaining fast Fourier transforms (FFTs). Random distributions of features without any definitive wavelength in position give a decaying intensity from the maximum intensity (000) central mode.

5.3 Results and Discussion

5.3.1 Surface Pinhole Formation

Thin films of V_2O_5 were prepared using two deposition techniques: Drop casting and dip coating. During drop casting, the precursor is dropped onto the substrate to initiate the hydrolysis step, and is unconstrained. The length of time for the hydrolysis step to completely form a V_2O_5 solid film is dependent upon the alkoxide concentration. While still in liquid form, the precursor can spread across the surface of the substrate (unlike the case of dip-coating) until the hydrolysis is complete. Unlike most transition metal alkoxides that form particulate structures, the layered molecular structure of vanadium oxide allows a dominant layering of the crystal structure parallel to the substrate.[25, 30] Recently it has been shown that dip-coating of vanadium alkoxide precursors can result in surface cracking of the thin films.[31]

During dip-coating the substrate is drawn from the precursor at a controlled rate with the hydrolysis occurring once exposed to air. The hydrolysis of the alkoxide to its oxide after dip-coating occurs rapidly so that an amorphous V_2O_5 thin film is formed and the increased dewetting and beading normally experienced by the drop casted liquid thin films is prevented.

Figure 5.2 (a) is an SEM image of the surface of a thin film of as-deposited V_2O_5 on an Au substrate. The sample was deposited in a staircase configuration, depicted in the schematic in Figure 5.2 (a) which is composed of iterative dip coats after hydrolysis has occurred to form a multi-layered deposit. The low magnification SEM image shows the film surface and interfaces for the Au substrate and the first two successive layers of V_2O_5. The interfacial regions are highlighted for visual aid. Each successive layer thickness of V_2O_5 is measured to be 15 – 18 nm. The AFM

insets show the surface morphology of each of the surfaces respectively. The first dip-coated layer of V_2O_5 on Au exhibits a similar morphology to the Au grains while the AFM image shows the formation of pinholes on the surface of layer 2. The AFM surface image of layer 2 is that of a typical V_2O_5 film formed on top of a previously formed V_2O_5 film on an Au substrate, i.e. the second, third, etc. layers. Small 25 – 35 nm diameter pinholes, which are between 6 and 10 nm deep, were revealed by AFM analysis. These features are characteristic of oxide thin film formation from liquid alkoxide precursors based on our examinations. The pinholes are only apparent on the AFM image; their shallow depth and the secondary electron intensity from the underlying Au substrate beneath the film reduce the visibility of small defects in the V_2O_5 film from SEM images as can be seen in Figure 5.3.

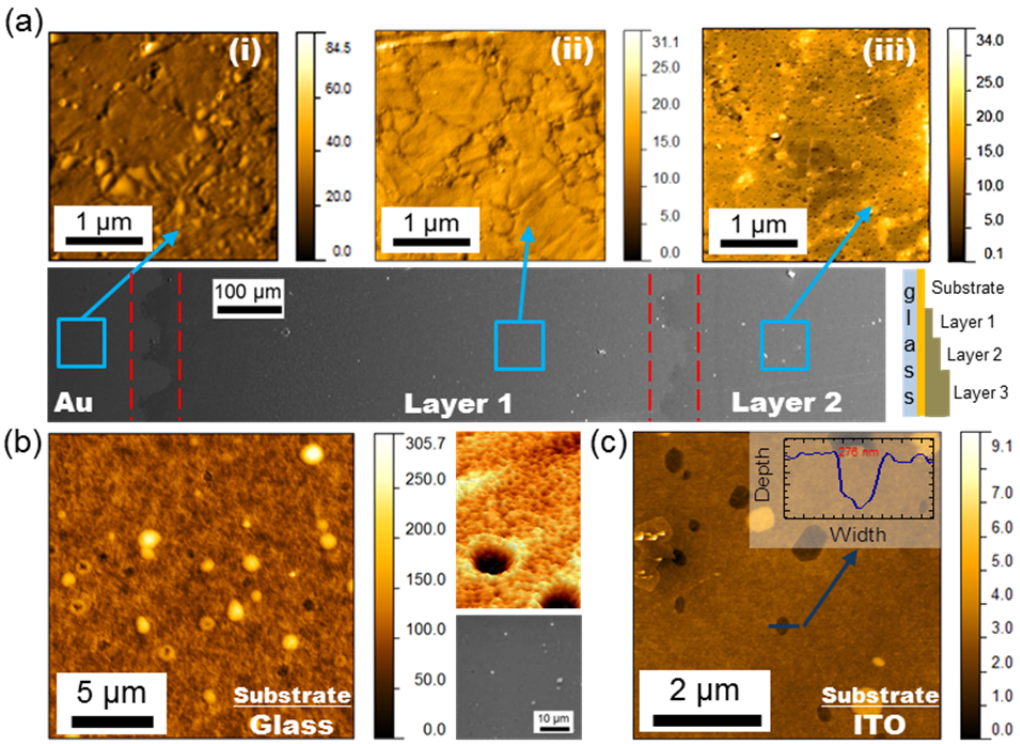


Figure 5.2. (a) AFM and SEM images of as-deposited V_2O_5 film on an Au substrate with the interfaces highlighted between each successive layer. AFM images showing the morphology of the (i) Au substrate, (ii) first layer of V_2O_5 film and (iii) second layer of V_2O_5 film with formation of pinholes visible. The schematic architecture of a 'staircase' thin film sample. (b) AFM and SEM images of V_2O_5 drop casted on glass. (c) AFM image of dip-coated V_2O_5 film on an ITO substrate. Pinholes of different distributions and sizes are present in these samples compared to films formed on Au substrates. The unit for the AFM sidebars is in nm.

The as-deposited surface images from AFM and SEM for drop casted films on glass are shown in Figure 5.2 (b). Due to the increased hydrolyzation time involved in drop casting (compared to dip-coating of thinner films), V_2O_5 films formed on different substrates by drop casting share similar morphologies. Both surface bound hillock features and pinholes are present in the thicker drop casted film in Figure 5.2 (b) as seen from both the top down and AFM images, confirmed by SEM showing the presence of hillock features on the surface. The surface roughness of the drop casted film from the AFM images displays a labyrinthine topology that is similar to spinodal instability (buckling and undulations) effects[10, 22] seen in polymer thin films, and that such features of fully hydrolysed amorphous V_2O_5 films are seen when thicker drop cast films are examined.[19]

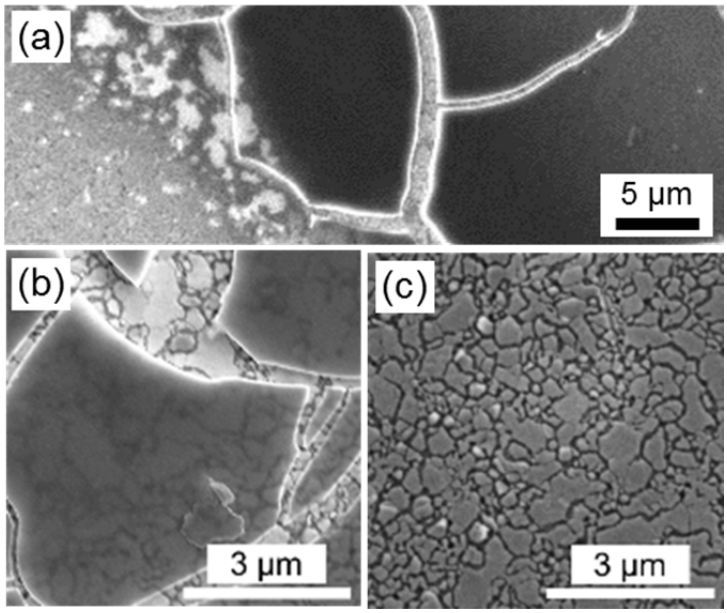


Figure 5.3. (a-c) SEM images of thin films of V_2O_5 deposited on an Au substrate highlighting the visibility of the Au grains beneath the V_2O_5.

5.3.2 Pinhole Formation Analysis

The formation of pinholes that are similar to nucleation dewetting effects in composite liquid polymer films, is also observed on dip-coated V_2O_5 thin films

formed on ITO substrates shown in Figure 5.2 (c). The pinholes formed on the ITO have a characteristically larger size and shape compared to those formed on the rougher, granular Au surface. The pinholes formed on ITO have a lower spatial distribution on the thin film surface compared to those on Au. The pinholes on ITO are also formed from the first layer and maintained in subsequent dip-coated layers. As-deposited amorphous V_2O_5 thin films deposited on ITO also contain hillocks of material on their surfaces, as seen in Figure 5.2 (c); hillock formation is a common trait between the thin films formed on both Au and ITO substrates. It is not entirely clear from measurement of multilayer deposition if the movement of material during pinhole formation is related to the density and size of hillocks, but typically, their density and position is not spatially correlated to the distribution of the pinhole features in the first and subsequent layers.

Table 5.1. Total percentage area coverage and average size of pinholes on the surface of thin films of V_2O_5 deposited onto Au and ITO substrates.

Substrate	**Percentage of Total Area (%)**	**Average Size (nm)**
Au	7.0	25.1
ITO	7.9	111.5

The Au substrates are measured to have a greater rms roughness (5.43 nm) than the transparent ITO substrates (2.03 nm). The roughness of the amorphous thin films formed on the Au and ITO substrates are 2.61 nm and 0.68 nm respectively: for both types of films the rms roughness of the amorphous thin films is less than that of the respective metal or ITO substrates.

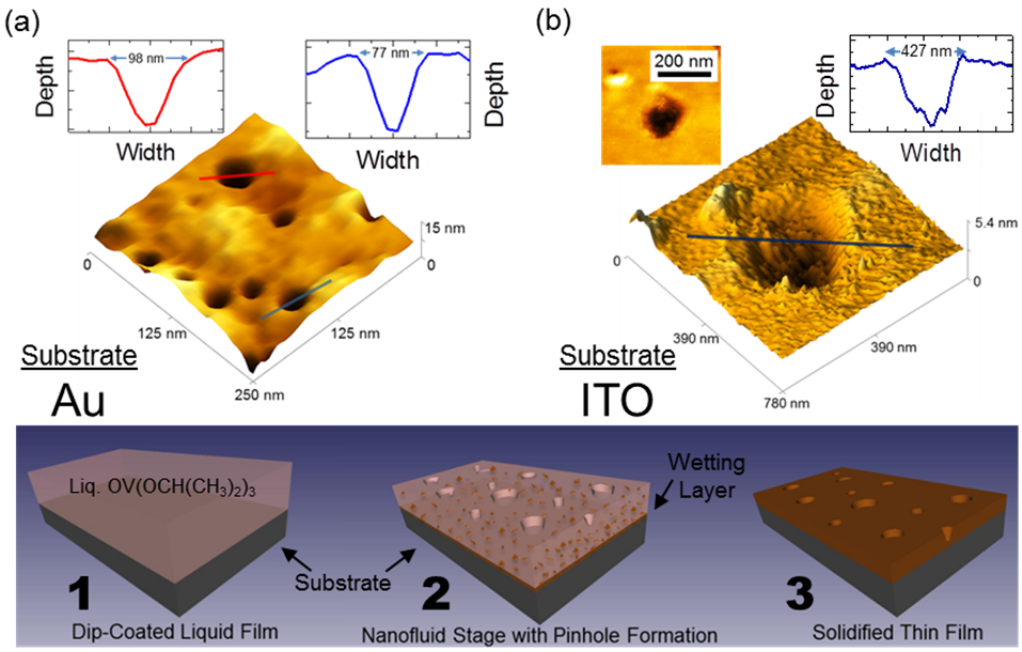


Figure 5.4. AFM images, topology and depth profiles for pinholes formed on (a) Au and (b) ITO substrates. The schematic illustrates the various phases of film hydrolysis: (1) dip-coating of liquid precursor that (2) develops a hydrolysed wetting layer to the surface with the continual formation of oxide clusters within the hydrolysing films which leads to the formation of (3) a roughened, pinhole-containing solid film.

During the hydrolysis step, the liquid film forms clusters of hydrolysed amorphous V_2O_5 which are suspended in the liquid precursor until hydrolysis is complete and the solid film has formed. This effect may be described as a thin film mixture where the solvent and solute are the liquid precursor and hydrolysed amorphous V_2O_5 respectively, similar to Class I hybrid nanocomposite blends. The deposit is somewhat analogous to network modifiers in sol-gel processes involving blends of molecular building blocks, but here, these building blocks form *in-situ* during the chemical change.[32] Similar systems have been examined in the case of thin polymer films containing mixtures and suspensions.[9] Recently, a gradient dynamics description was proposed for films of mixtures and suspensions involving a concentration-dependent wettability for liquid films containing suspensions.[9] The model details an ability of a film containing a suspension to modulate its thickness

and concentration simultaneously, giving rise to feature formation. In the present case, the increasing viscosity during hydrolysis to a solid oxide from its alkoxide complicates the comparison to particle-loaded liquid polymer films, but motivated the experimental investigation into improving the uniformity in thin film formation by supressing instabilities that can form in the thin film in its liquid state prior to solidification by hydrolysis.

Figure 5.4 (a-b) shows the morphological characteristics of the two types of pinholes formed on Au and ITO substrates respectively. The pinholes formed on Au substrates are generally smaller (in width) but consistently deeper (6 – 9 nm), compared to shallower (3 – 5 nm) pinholes in V_2O_5 films on ITO. On ITO the pinholes are predominantly non-circular with a significantly larger width to those on Au. As the precursor hydrolyses and solidifies after deposition, the form of dewetting process, including instabilities caused by lateral variations in nanoscale oxide cluster density throughout the films, thickness variations and changes in material parameters during hydrolysis to it oxide form, are halted by solidification leaving a solid film with a random distribution of pinhole defects. These defects are also observed on secondary, tertiary and further sequential layers of the thin film multilayer.

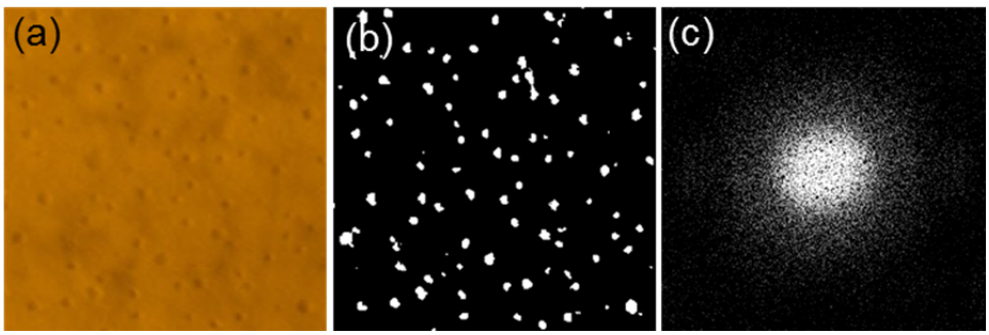


Figure 5.5. Example of technique for acquiring FFT images of pinhole distribution on the surface of V_2O_5 thin films. (a) AFM image of pinholes on a V_2O_5 film, (b) Thresholded binary image of pinhole distribution, (c) FFT of thresholded image illustrating the average distribution of the pinholes on the surface.

The distribution of the pinhole diameters formed on Au is shown in the graph for Figure 5.6 (a), the pinholes form in varying sizes with an average diameter (longest axis) of 27.3 nm. Statistical analysis of AFM images shows that the pinholes cover less than 8% of the total surface area for both types of substrates (this information is summarized in Table 5.1).

The distribution of the pinholes on Au was examined using Fast Fourier Transforms (FFT) of the AFM data. The FFTs were performed to ascertain any periodicity in the distribution of the pinholes, the method used in calculating the FFTs of the pinholes is outlined in Figure 5.5. The FFTs for the two layers shown in Figure 5.6 (b-c) indicate that the pinholes are randomly distributed on the surface of both Au and ITO surfaces due to the lack of evidence for a characteristic inter-feature wavelength expected in samples that undergo defined instabilities, such as spinodal decomposition, or influences from lateral concentration variations[17] (Marangoni and other instabilities that assume the oxide clusters are mobile).

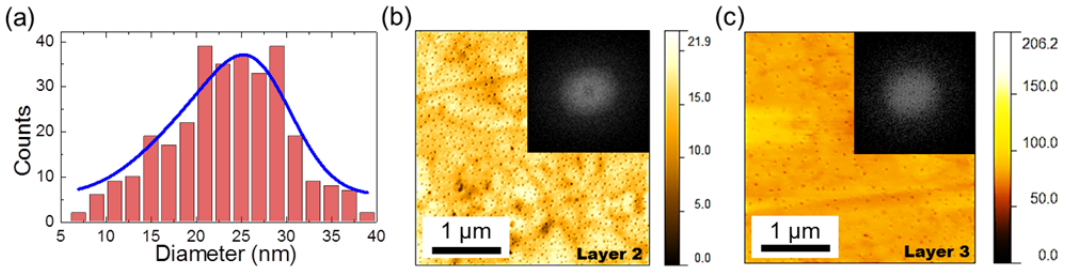


Figure 5.6. (a) Diameter distribution of pinholes formed on the surface of an Au substrate. (b-c) AFM surface image and corresponding FFT of pinhole distribution for two subsequent layers of V_2O_5 thin films on Au. The FFTs illustrate the random distribution of the pinholes.

Pinhole formation in liquid polymer films that contain nanoscale inclusions that prevent complete dewetting typically result from heterogeneous nucleation. Pinholes formed through this mechanism that open right down to the substrate become pinned in liquid films, but typically are not found in the present case even during the early stages when the dip-coated film is liquid. This effect is believed to

be due to a very thin wetting layer that instantaneously hydrolyses due to the presence of adsorbed water molecules on the substrate as shown in the schematic of Figure 5.4. AFM measurements in all cases consistently show a lesser pinhole depth compared to the average final film thickness.

5.3.3 Thin Film Structural Characterisation

To examine the influence of crystallization on the morphology of thin films, the V_2O_5 films were crystallized in air using a convection oven at 300 ^oC for 12 hours. The surface of the films was examined post-crystallisation to ascertain the changes to the thin film morphology after the phase change from amorphous to orthorhombic V_2O_5.[33-34]

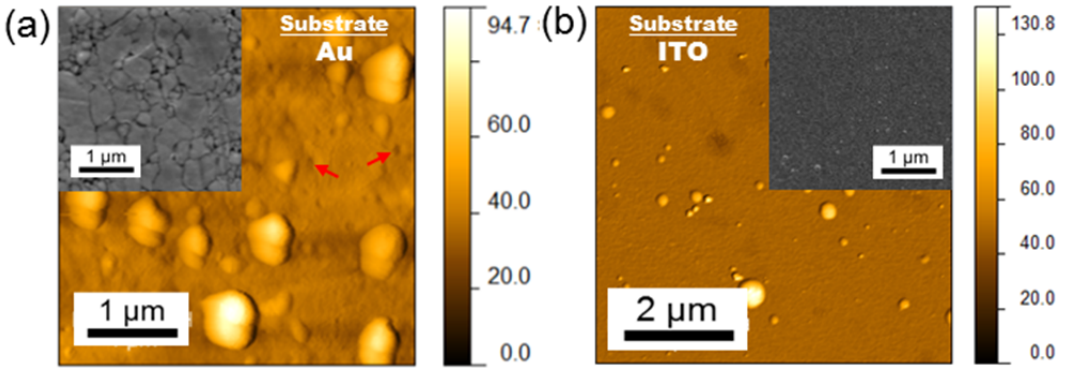


Figure 5.7. Post-crystallization AFM and SEM (insets) images of V_2O_5 thin films on (a) Au and (b) ITO substrates. The images show the formation of dispersed crystallites on the surface. Evidence of pinhole remnants are highlighted with arrows in (a)

Figure 5.7 (a-b) show the AFM and SEM surface images of the crystallized V_2O_5 films on both Au and ITO substrates respectively. In both cases crystallites of V_2O_5 form on the surface of the thin films with an average height of 31.7 nm and 36.8 nm on both Au and ITO respectively. In the case of the thin films on Au, the pinholes are still apparent on the AFM images, highlighted with red arrows, while their average depth is reduced to 4.8 nm. The rms roughness of the orthorhombic

V_2O_5 thin films on Au and ITO is 9.7 nm and 5.9 nm respectively. The increase in roughness is predominantly related to the changes caused by crystallization, the greatest roughening found for thin films on Au.

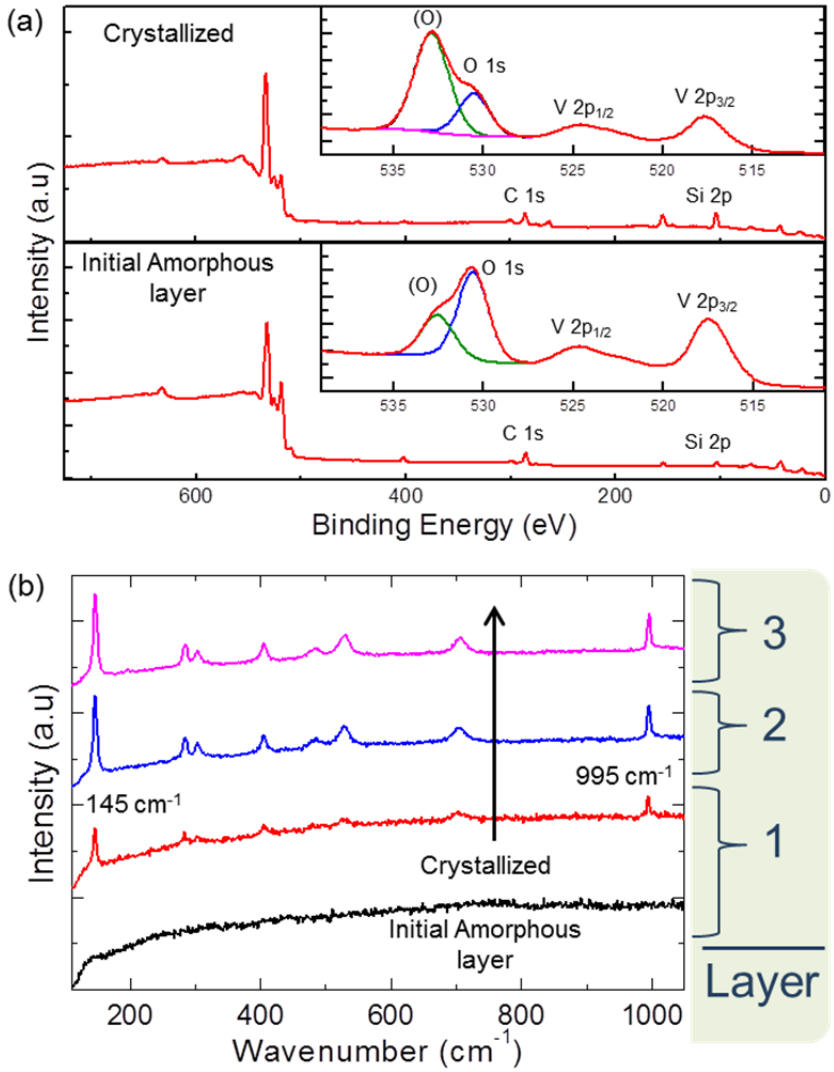


Figure 5.8. (a) XPS spectra of amorphous and crystalline V_2O_5 thin films on ITO showing the contribution of photoelectron emission from the underlying substrate due to the thinness of the film. (b) Raman scattering spectra of the as-deposited and crystallized films for successive films in the multilayer.

An XPS spectrum, Figure 5.8 (a), was acquired for both an as-deposited amorphous and crystallized single layer thin film of V_2O_5 deposited on an ITO substrate. The as-deposited and crystallised spectra show the expected $V2p_{3/2}$, $V2p_{1/2}$ and O 1s XPS peaks for V_2O_5 at 517.5 eV, 524.6 eV and 530.6 eV respectively.[35]

The presence of the oxygen XPS peak at 532.6 eV is not attributed to the formation of another vanadium oxidative state in the film.[35-36]

The O 1s core-level emission is due to contributions from the ITO conductive layer and the SiO_2 substrate underneath the V_2O_5 thin film.[37-38] The low intensity 3d core-levels peaks for Sn and In are shown in Figure 5.9. The presence of XPS peaks for the substrate underneath the thin film is due to the thinness of the single layer of V_2O_5. The XPS study demonstrates that the V_2O_5 films are free of surface contaminants from the alkoxide precursor or other sources. Additionally, the oxidation state for as-deposited and crystallized films remains unchanged.

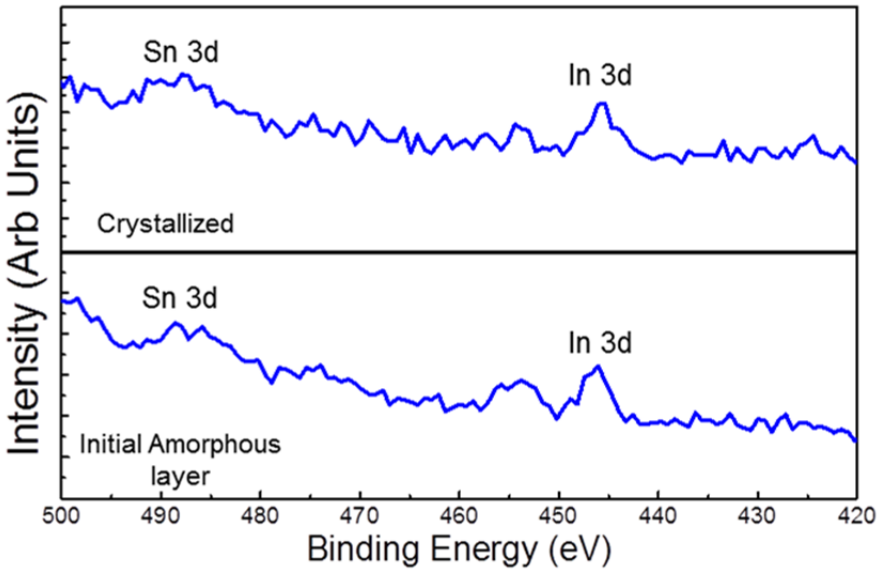


Figure 5.9. XPS spectrum showing the presence of the Sn 3d and In 3d XPS peaks corresponding to the ITO substrate beneath the V_2O_5 thin film.

Figure 5.8 (e) shows the Raman scattering spectra of the V_2O_5 thin film coatings on Au before and after crystallization. The as-deposited thin film is amorphous V_2O_5, thus no specific phonon modes from the known V-O bond structure are found. Post-crystallization, the characteristic vibrational peaks for orthorhombic V_2O_5 are present, and identical to that expected from the lamellar phase for the material.[39-40] Multilayers of V_2O_5 from iterative dip-coating also crystallize to orthorhombic V_2O_5, a stoichiometric phase that can be difficult to

control using CVD, ALD and related physical vapour deposition methods. Conventional XRD was found to be inadequate in determining the crystal structure of the thin films. To correlate the Raman scattering spectra of the thin films to X-ray diffraction characteristics of V_2O_5, a thick film with a high surface area was produced by drop casting the precursor followed by crystallization. The (001) reflection for orthorhombic V_2O_5 at ~20.5^o is shown in Figure 5.10 (a) and can be correlated to the Raman scattering spectra for orthorhombic V_2O_5 in Figure 5.10 (b). Additionally, the uniformity in the morphology and consistent low roughness is remarkable for single and multilayer deposits on metallic and transparent conducting oxide (TCO) substrates.

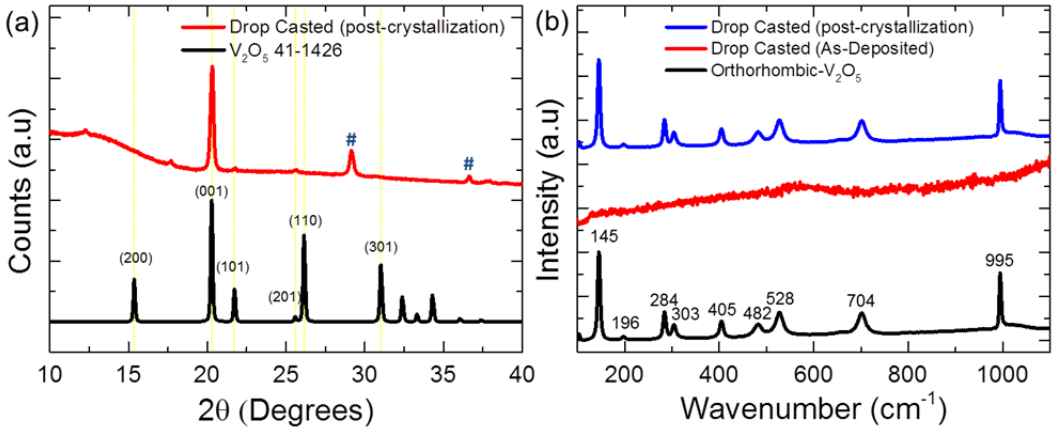


Figure 5.10. (a) XRD and (b) Raman scattering spectroscopy of drop-casted V_2O_5 film showing the formation of orthorhombic V_2O_5 after crystallization. (Peaks highlighted with a # in the XRD pattern are artefacts of the machine)

Most polymers are immiscible with alcohols, particularly alcohols released during the hydrolytic sol-gel process and phase separation becomes a problem for uniform film coverage. Utilizing polymers that are soluble with decomposition alcohols as the liquid film hydrolyzes as a cluster-containing solid film, could potentially alleviate concentration variations and unwanted structuring from these effects, which are detrimental to functional electronic and optical coatings and films.[41]

5.3.4 Methods for Relieving Pinhole Development

As with liquid polymer films, a change in molecular weight of the precursor and the viscosity fundamentally affects processes such as dewetting, nucleation, demixing and phase separation, and in those cases are fundamentally linked to gelation via hydrolysis where the material essentially contains internal 'pores' that allow the release of the alcohol, and eventual solidification. Furthermore, this uniformity should also be maintained when crystallizing the thin films after deposition. To improve film consistency and suppress pinhole formation through nucleation effects, a precursor was prepared utilizing polymer-assisted V_2O_5 thin film synthesis. The hydrophilic and alcohol-soluble PEG-400 (m.w. = 400 g/mol) was added to the precursor to bind the amorphous V_2O_5 clusters together during the hydrolysis of the liquid precursor stage. The AFM surface images for the corresponding V_2O_5 thin films, pre- and post-crystallization, formed using this polymer-assisted alteration are shown in Figure 5.11 (a).

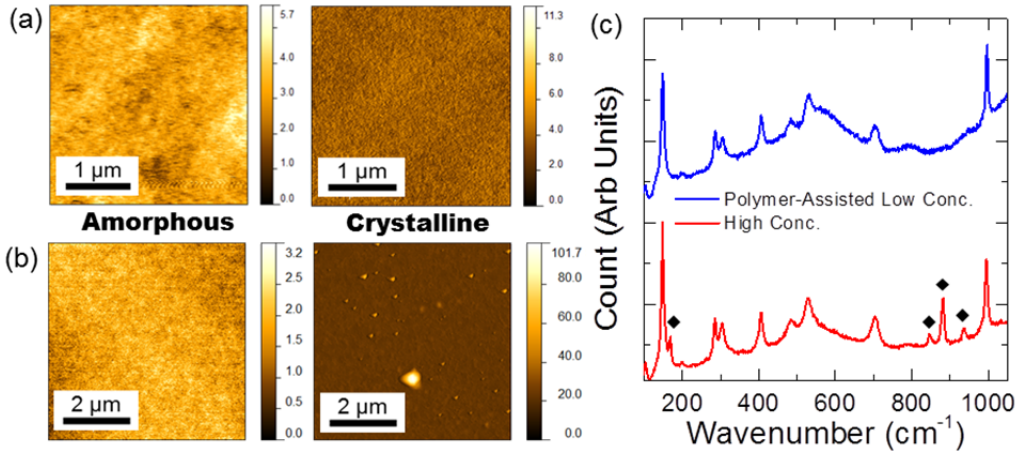


Figure 5.11. AFM images pre- and post-crystallization for (a) polymer-assisted low concentration and (b) high concentration V_2O_5 thin films formed on ITO. (c) Raman scattering spectra showing the formation of crystalline orthorhombic V_2O_5 from both films. The peaks marked with diamonds are due to the layered structure of the films and the presence of small amounts of VO_2. The broad background seen in the polymer-assisted spectra between 400 cm^{-1} – 700 cm^{-1} is due to the thinness of the film and the interaction with the ITO and glass substrate.

The resultant thin films have a uniform surface morphology and no evidence of pinhole formation is found. The Raman scattering spectrum, included in Figure 5.11 (c), shows the formation of orthorhombic V_2O_5 after the thermal treatment. The surface rms roughness for the amorphous and orthorhombic polymer-assisted V_2O_5 thin films is 0.57 nm and 0.74 nm respectively. Crystallization also calcines the mixture, removing the organic component and from Figure 5.11; the organic phase decomposition does not adversely affect the morphology of the thin films as shown previously in Chapter 4. Additionally, during the hydrolysis, the PEG is soluble in evaporating alcohols and may aid in preventing material cracking, and promote a smoothening of the surface topology by preventing instabilities forming within the hydrolysing film. By utilizing the polymer-assisted blend, a uniform non-defective thin film of orthorhombic V_2O_5 was prepared with a surface roughness an order of magnitude below that of thin films prepared without the addition of a polymer.

A secondary method for smoothing the surface topology is demonstrated by increasing the concentration of the precursor in the IPA-alkoxide mixture. This decreases the hydrolyzation time of the liquid film, and is found to suppress the formation of pinholes in the initial amorphous layer. The decrease in hydrolyzation time does increase the thickness of the single layer to 35 – 40 nm per layer. As in the case with the polymer-assisted films, the resultant thin films have a uniform surface morphology with a low rms roughness of 0.56 nm. However, after crystallization of higher concentration alkoxides (without PEG), large crystallites form on the surface and the rms roughness increases to 5.61 nm, which correlates to similar crystallization behaviour of the thin films without polymer addition. Raman scattering spectra in Figure 5.11 (c) show the characteristic vibrational peaks for orthorhombic V_2O_5, however, the presence of extra peaks at 168 cm^{-1}, 846 cm^{-1}, 880

cm^{-1} and 935 cm^{-1}, are attributed to contributions from the layered structure, or the presence of VO_2 in the polymer-assisted thin films as discussed in Chapter 4.[42] VO_2 phases in thin films with textured surface have been grown from vanadium triisopropoxides under atmospheric pressure chemical vapour deposition (APCVD).[43-45] While increasing the concentration of the precursor can halt the formation of pinholes and surface texturization from grains or nanoscale clusters in V_2O_5 thin films at the nanofluid stage, the polymer-assisted method with more dilute alkoxide mixtures has the additional benefits of lower single layer thicknesses (V_2O_5 only) and a very low surface roughness both before and after crystallization.

5.4 Conclusions

Using an alkoxide based precursor and cost-effective dip-coating techniques, a rational strategy for the deposition of highly uniform thin film and multilayers of V_2O_5 on a range of surfaces from liquid based precursors was demonstrated. The nature of hydrolysis of the layered material V_2O_5 from its alkoxide has been shown to strongly influence the uniformity of thin films formed on Au and ITO substrates as single thin films and as thin film multilayers. Utilizing knowledge of instability formation in liquid thin films and the influence of clusters as a nanofluid on the stability of such films, the addition of polymers to the nanofluid drastically improves uniformity and smoothness for amorphous and crystalline phases of V_2O_5 that can exceed that of physical and chemical vapour deposition methods.

The choice of substrate was found to have an effect on the type of pinholes formed. Small diameter pinholes with a high distribution are found for V_2O_5 films deposited on granular sputtered Au films, while those on ITO substrates have a large irregular size and lower distribution. AFM and electron microscopy confirmed

pinhole formation in addition to a specific surface roughness that is correlated to heterogeneous nucleation dewetting effects caused when the alkoxide was in its liquid state. The surface roughness and wettability of the substrates combined with the alkoxide to solvent ratio of the precursor are associated with the formation of the pinholes.

The primary difference between the two systems is that due to the hydrolysis effect experienced by the alkoxide precursor in the formation of the V_2O_5, the thin films produced solidify prior to the full dewetting and nucleation process can finish as found in polymer films. To reverse the formation of pinholes and hillocks in the V_2O_5, a polymer assisted synthesis using PEG-400 altered the hydrolysis and gelation point of the nanofluid during solidification such that an ultra-smooth surface is possible without pinholes or roughness linked to instabilities from the liquid stage that becomes frozen-in upon solidification.

Practically, understanding evolution pathways that involves dewetting processes, nucleation, decomposition or hydrolysis that includes evaporation in complex nanofluids gives routes to improved surface coverage of useful stoichiometry of V_2O_5 using dip-coating. While further theoretical work would strongly benefit additional experimental investigations to fully explain the phenomenon, the method may prove useful for deposition of thin uniform films for a variety of applications on planar or possibly non-planar substrates (which form shadows and blank regions in many vapour-phase depositions). Dip-coating or spin casting liquids precursors and nanofluids can be extended to improve the consistency in sequential or iterative multilayer deposits of hybrid materials, and provides a liquid-based route for crystallized thin vanadium oxide films with exotic thermal, electrical and optical properties. In parallel with CVD and related plasma based

deposition methods, such control of thin film uniformity gives another alternative for atmospheric pressure, open air methods for uniform films or coatings.

5.5 References

1. Brinker, C. J.; Frye, G. C.; Hurd, A. J.; Ashley, C. S. Fundamentals of sol-gel dip coating. *Thin Solid Films* ***201***, 97-108 (1991).
2. Ozin, G. A., *Nanochemistry: a chemical approach to nanomaterials*. Royal Society of Chemistry: 2009.
3. Valenzuela, C. D. *et al.* Solid State Pathways to Complex Shape Evolution and Tunable Porosity during Metallic Crystal Growth. *Sci. Rep.* ***3***, 2642 (2013).
4. Mukherjee, R. *et al.* Stability and Dewetting of Metal Nanoparticle Filled Thin Polymer Films: Control of Instability Length Scale and Dynamics. *ACS Nano* ***4***, 3709-3724 (2010).
5. Amarandei, G.; O'Dwyer, C.; Arshak, A.; Corcoran, D. Fractal Patterning of Nanoparticles on Polymer Films and Their SERS Capabilities. *ACS Appl. Mater. Interfaces* ***5***, 8655-8662 (2013).
6. Faupel, F.; Zaporojtchenko, V.; Strunskus, T.; Elbahri, M. Metal-Polymer Nanocomposites for Functional Applications. *Adv. Eng. Mater.* ***12***, 1177-1190 (2010).
7. Kaune, G. *et al.* In Situ GISAXS Study of Gold Film Growth on Conducting Polymer Films. *ACS Appl. Mater. Interfaces* ***1***, 353-360 (2008).
8. Bigioni, T. P. *et al.* Kinetically driven self assembly of highly ordered nanoparticle monolayers. *Nat. Mater.* ***5***, 265-270 (2006).
9. Thiele, U.; Todorova, D. V.; Lopez, H. Gradient Dynamics Description for Films of Mixtures and Suspensions: Dewetting Triggered by Coupled Film Height and Concentration Fluctuations. *Phys. Rev. Lett.* ***111***, 117801 (2013).
10. Wong, H. C.; Cabral, J. T. Spinodal clustering in thin films of nanoparticle-polymer mixtures. *Phys. Rev. Lett.* ***105***, 038301 (2010).
11. Osborne, I.; Lavine, M.; Coontz, R. Looking Beyond Silicon. *Science* ***327***, 1595 (2010).
12. Mannhart, J.; Schlom, D. G. Oxide Interfaces—An Opportunity for Electronics. *Science* ***327***, 1607-1611 (2010).
13. Bang, J. *et al.* Block Copolymer Nanolithography: Translation of Molecular Level Control to Nanoscale Patterns. *Adv. Mater.* ***21***, 4769-4792 (2009).
14. Herminghaus, S. *et al.* Spinodal Dewetting in Liquid Crystal and Liquid Metal Films. *Science* ***282***, 916-919 (1998).
15. Lopes, W. A.; Jaeger, H. M. Hierarchical self-assembly of metal nanostructures on diblock copolymer scaffolds. *Nature* ***414***, 735-738 (2001).
16. Higgins, A. M.; Jones, R. A. L. Anisotropic spinodal dewetting as a route to self-assembly of patterned surfaces. *Nature* ***404***, 476-478 (2000).
17. Amarandei, G.; O'Dwyer, C.; Arshak, A.; Corcoran, D. The stability of thin polymer films as controlled by changes in uniformly sputtered gold. *Soft Matter* ***9***, 2695-2702 (2013).
18. Seemann, R.; Herminghaus, S.; Jacobs, K. Dewetting Patterns and Molecular Forces: A Reconciliation. *Phys. Rev. Lett.* ***86***, 5534-5537 (2001).
19. Xie, R. *et al.* Spinodal Dewetting of Thin Polymer Films. *Phys. Rev. Lett.* ***81***, 1251-1254 (1998).
20. Livage, J. Synthesis of polyoxovanadates via "chimie douce". *Coord. Chem. Rev.* ***178–180, Part 2***, 999-1018 (1998).
21. Wong, H. C.; Cabral, J. o. T. Mechanism and Kinetics of Fullerene Association in Polystyrene Thin Film Mixtures. *Macromolecules* ***44***, 4530-4537 (2011).

22. Amarandei, G. *et al.* Effect of Au Nanoparticle Spatial Distribution on the Stability of Thin Polymer Films. *Langmuir* ***29***, 6706-6714 (2013).
23. Livage, J. Vanadium pentoxide gels. *Chem. Mater.* ***3***, 578-593 (1991).
24. Riou, D.; Roubeau, O.; Férey, G. Evidence for the Solid State Structural Transformation of the Network-Type Decavanadate $(NC_7H_{14})_4[H_2V_{10}O_{28}]$ into a Lamellar Topology $(NC_7H_{14})[V_4O_{10}]$. *Z. Anorg. Allg. Chem.* ***624***, 1021-1025 (1998).
25. Petkov, V. *et al.* Structure of $V_2O_5 \cdot nH_2O$ Xerogel Solved by the Atomic Pair Distribution Function Technique. *J. Am. Chem. Soc.* ***124***, 10157-10162 (2002).
26. Nomura, K. *et al.* Room-temperature fabrication of transparent flexible thin-film transistors using amorphous oxide semiconductors. *Nature* ***432***, 488-492 (2004).
27. Wang, L. *et al.* High-performance transparent inorganic-organic hybrid thin-film n-type transistors. *Nat. Mater.* ***5***, 893-900 (2006).
28. Banger, K. K. *et al.* Low-temperature, high-performance solution-processed metal oxide thin-film transistors formed by a 'sol–gel on chip' process. *Nat. Mater.* ***10***, 45-50 (2011).
29. Sanchez, C.; Livage, J.; Henry, M.; Babonneau, F. Chemical modification of alkoxide precursors. *J. Non-Cryst. Solids* ***100***, 65-76 (1988).
30. Glynn, C. *et al.* Large directional conductivity change in chemically stable layered thin films of vanadium oxide and a 1D metal complex. *J. Mater. Chem. C*, (2013).
31. Jung, H.-M.; Um, S. Modification of electrical and surface properties of V_2O_3 multilayer films on resin-impregnated highly oriented pyrolytic graphite composite substrates by shrinkage stress relaxation with chemical additives. *Thin Solid Films* ***548***, 98-102 (2013).
32. Kickelbick, G. Concepts for the incorporation of inorganic building blocks into organic polymers on a nanoscale. *Prog. Polym. Sci.* ***28***, 83-114 (2003).
33. O'Dwyer, C. *et al.* Vanadate Conformation Variations in Vanadium Pentoxide Nanostructures. *J. Electrochem. Soc.* ***154***, K29-K35 (2007).
34. Baddour-Hadjean, R.; Pereira-Ramos, J. P. New structural approach of lithium intercalation using Raman spectroscopy. *J. Power Sources* ***174***, 1188-1192 (2007).
35. Silversmit, G. *et al.* Determination of the V 2p XPS binding energies for different vanadium oxidation states (V^{5+} to V^{0+}). *J. Electron. Spectrosc. Relat. Phenom.* ***135***, 167-175 (2004).
36. Mendialdua, J.; Casanova, R.; Barbaux, Y. XPS studies of V_2O_5, V_6O_{13}, VO_2 and V_2O_3. *J. Electron Spectrosc. Relat. Phenom.* ***71***, 249-261 (1995).
37. So, S. K. *et al.* Surface preparation and characterization of indium tin oxide substrates for organic electroluminescent devices. *Appl. Phys. A* ***68***, 447-450 (1999).
38. Gross, T. *et al.* An XPS analysis of different SiO_2 modifications employing a C 1s as well as an Au 4f7/2 static charge reference. *Surf. Interface Anal.* ***18***, 59-64 (1992).
39. Wang, X. J. *et al.* XRD and Raman study of vanadium oxide thin films deposited on fused silica substrates by RF magnetron sputtering. *Appl. Surf. Sci.* ***177***, 8-14 (2001).
40. Sanchez, C.; Livage, J.; Lucazeau, G. Infrared and Raman study of amorphous V_2O_5. *J. Raman Spectrosc.* ***12***, 68-72 (1982).
41. Driscoll, T. *et al.* Memory Metamaterials. *Science* ***325***, 1518-1521 (2009).
42. Su, Q. *et al.* Formation of vanadium oxides with various morphologies by chemical vapor deposition. *J. Alloys Compd.* ***475***, 518-523 (2009).

43. Manning, T. D. *et al.* Intelligent window coatings: atmospheric pressure chemical vapour deposition of vanadium oxides. *J. Mater. Chem.* ***12***, 2936-2939 (2002).
44. Vernardou, D. *et al.* A study of the electrochemical performance of vanadium oxide thin films grown by atmospheric pressure chemical vapour deposition. *Sol. Energy Mater. Sol. Cells* ***95***, 2842-2847 (2011).
45. Gao, Y. *et al.* Phase and shape controlled VO_2 nanostructures by antimony doping. *Energy Environ. Sci.* ***5***, 8708-8715 (2012).

Chapter 6

Transparent Thin Film Deposition via Substrate Diffusion Doping

Adapted From

Glynn, C. *et al.* Solution Processable Broadband Transparent Mixed Metal Oxide Nanofilm Optical Coatings via Substrate Diffusion Doping. *Nanoscale* **7**, 20227-20237 (2015).

Abstract

Devices composed of transparent materials, particularly those utilizing metal oxides, are of significant interest due to increased demand from industry for higher fidelity transparent thin film transistors, photovoltaics and a myriad of other optoelectronic devices and optics that require more cost-effective and simplified processing techniques for functional oxides and coatings. A facile solution processed technique for the formation of a transparent thin film through an inter-diffusion process involving substrate dopant species at a range of low annealing temperatures compatible with processing conditions required by many state-of-the-art devices is reported. The inter-diffusion process facilitates the movement of Si, Na and O species from the substrate into the as-deposited vanadium oxide thin film forming a composite fully transparent $V_{0.04}O_{0.54}Si_{0.41}Na_{0.01}$. Thin film X-ray diffraction and Raman scattering spectroscopy show the crystalline component of the structure to be α-$NaVO_3$ within a glassy matrix. This optical coating exhibits high broadband transparency, exceeding 90-97% absolute transmission across the UV-to-NIR spectral range, while having low roughness and free of surface defects and pinholes. The production of transparent films for advanced optoelectronic devices, optical coatings, and low- or high-k oxides is important for planar or complex shaped optics or surfaces. It provides opportunities for doping metal oxides to new ternary, quaternary or other mixed metal oxides on glass, encapsulants or other substrates that facilitate diffusional movement of dopant species.

6.1 Introduction

Many modern applications and technologies are based on materials deposited upon transparent glass substrates.[1-2] Devices formed on glass substrates are used in a wide range of applications such as electrochromics[3], thin film solar cells[4-5], water splitting devices[6-7] that could benefit from transparent electrodes,[8] optical coatings[9-11] and transparent thin film transistor (TTFT) technologies.[12-14] The type of coating deposited depends upon the transparent device application. Deposits can be used as electrical/active components or as buffer/dielectrics[15], both high- and low-k, between the substrate and active layers.[16] There are a variety of methods for depositing onto glass substrates, ranging from chemical/vapour depositions[17], sputtering[18] or solution processed[19] techniques. Each of these depositions typically entails a thin or thick film of the coating material being deposited onto the glass substrate and treated under a variety of processing conditions to attain the desired structure and morphology.[20-22] For optical coatings, the ability to conformally coat thin films on glass optics, non-planar surfaces that are index-matched to an application, or indeed as fully transparent invisible barrier or protection layers, are important for optics and photonics.

Transparent oxides (TO) see use in many modern technologies due to their novel metal oxide material characteristics coupled with high optical transparency over a range of wavelengths. TO materials can be used as a conductive channel in the case of transparent conducting oxides (TCO)[23-24], as anti-reflection coatings[25] in optoelectronic devices and as active layers in thin film solar cells.[9, 19] Many of the transparent oxide materials, particularly TCO's, contain costly elements such as Indium or Gallium which in turn increases device costs; suitable replacement materials are crucial for some technologies, and atomic layer deposition (ALD) is a

leading but expensive method for their production.[1] Device fabrication costs are also linked to the complexity and number of processing steps during production. Therefore, since s-orbital states from the metallic species facilitate conduction in ionic mixed metal oxides of In, Ga, Zn and Sn for example, and not strongly influenced by structural defects and an amorphous state, considerable research is being conducted involving a replacement range of more abundant materials that are solution processable, particularly at processing temperatures <300 °C. Solution processed techniques are already a cost-effective deposition technique, where a liquid solution of the chosen material is prepared and deposited using a variety of methods such as spin-coating[22], dip-coating[26] and inkjet printing[27-28]. Using the solution processed techniques, the desired deposit can be formed through adjustments to the precursor solution and/or the deposition parameters[29], and for optoelectronic devices, these routes offer low-temperature, solution-processable materials with excellent performance achievable with crystalline semiconductors, particularly in future applications where an electrically insulating optical material is required, such as in TTFTs featuring low-k materials.[30]

Many metal oxide materials have been extensively investigated in the search for new TCOs and in TTFT applications.[8] For each TO application a vast range of different materials and nanoscale assemblies exist. In TCO development, a variety of metal oxides can be used, most common of which being ITO,[8, 31-32] however, porous arrangements of metal nanowire meshes[33] and composite materials utilizing graphene[34] with acceptable sheet resistances are under investigation. The nanoscale assembly, ranging from nanoparticles to nanowires, affects the optical and electrical characteristics of the material in both advantageous and disadvantageous ways. For example, an ITO thin film composed of epitaxial grown nanowires can exhibit high

electrical conductivity and optical transparency while also benefiting from anti-reflective properties.[35] The benefit of TO materials in TFTs over Si based devices for TTFT technologies may require easier methods of deposition while retaining relatively high carrier and field effect mobilities, and a defined optical transparency.[36] Advancements in TTFT technologies have benefited from the use of a variety of TO materials, in particular ZnO, IGZO and ZnSnO.[28, 37-38] Through varied deposition conditions, thin films are produced with many different structures and compositions, ranging from amorphous to crystalline and importantly for many applications, using low temperature processing techniques.[39]

Many vanadium oxide (VO) materials see use in a variety of applications due to their optical and electrical properties depending upon the specific VO structure used, such as vanadium pentoxide (V_2O_5), dioxide (VO_2) and sesquioxide (V_2O_3).[40] The various VO materials are used as components in optoelectronic devices with applications in photovoltaics[4], metamaterials[41-42], and electro/thermo-chromics.[3, 43] However, under normal deposition conditions the VO materials are not transparent by themselves in the visible spectral region. Controlling the diffusion process when doping metal oxides or forming ionic metal oxide mixtures with negligible surface irregularity remains a challenge. By utilizing a known thermally activated inter-diffusion effect experienced by some materials deposited on borosilicate glass, a ternary mixed metal oxide V-O-Na-Si composite material is shown to be formed that is fully transparent from the UV to NIR spectral range at a processing temperature of 300 °C.

A uniform, continuous and smooth ternary mixed metal oxide transparent thin film (TTF) material is achieved from low temperature annealing of high-rate dip-coated VO based liquid precursors from inter-diffusion of substrate and

precursor species in the film. The nature of the transparent mixed metal oxide thin film and formation process are examined using detailed Raman scattering, atomic force and electron microscopy, X-ray photoelectron and optical spectroscopy. Optical transparency, film structure and surface morphology of the TO material is demonstrated to depend upon the initial VO thin film thickness and both the temperature and duration of the thermal annealing step. Intermediate stages exist at lower annealing temperatures where separate diffusion and crystallisation effects form multi-layered structures, each with unique optical and material characteristics. A low surface rms roughness of < 1 nm is retained for the TO thin films at each stage while the main absorption edge of the transparent material blue shifts to an E_g value of 3.7 eV, widening the broadband transmission window together with an increase in transmission to 90-97% across the UV to NIR spectral range, from reduced index and reflectivity. The surface composition of the thin films shows a predominantly O bonded Si glassy matrix, however, a complex structure is present due to the vanadia species dispersed within the material resulting in the formation of a $V_{0.04}O_{0.54}Si_{0.41}Na_{0.01}$ TTF material. The facile solution-processed technique that forms a transparent thin film material may be important for optical elements, optical coatings, photonic devices including LEDs, solar cells and those requiring low processing temperatures, and possibly as a low- and high-k film growth and invisible protective barrier layers.

6.2 Experimental

6.2.1 Thin Film Deposition and Processing

The thin films were deposited onto 1 mm thick borosilicate Thermo Scientific Microscope Slides with a precursor solution composed of IPA : Alkoxide : H_2O prepared at a ratio of 1000:10:1. The composition of the glass slides is: SiO_2 72.20%, Na_2O 14.30%, CaO 6.40%, MgO 4.30%, Al_2O_3 1.20%, K_2O 1.20%, SO_3 0.30% and Fe_2O_3 0.03%. The initial V_2O_5 thin films were dip-coated at a constant withdraw rate of 2.5 mm/s. Thermal treatments were performed at a variety of temperatures and times using a conventional oven in an ambient air atmosphere.

6.2.2 Analysis Techniques

Atomic force microscopy (AFM) was performed on a Park XE-100 AFM system in non-contact mode with SSS-NCHR enhanced resolution tips. Raman scattering spectroscopy was collected on a Renishaw InVia Raman spectrometer using a 514 nm 30 mW laser source. Spectra were collected and focused onto the samples using a 50× objective lens.

To measure the optical transparency of the samples in the 200 – 1000 nm range a Thermo Scientific Evolution 60S UV-Visible spectrophotometer illuminated with a Xenon light source with an accuracy of ±0.8 nm was used with a custom sample holder. To examine the optical transmission in the wavelength range of 1000 – 2500 nm an OceanOptics NIRQuest256-2.5 spectrometer was used with a 9.5 nm spectral resolution. An OceanOptics HL-2000 tungsten halogen source was used for illumination. Thin film X-Ray diffraction (XRD) was performed with a Philips X'pert equipped with a θ–θ goniometer. A Cu anode provided X-ray photons with a wavelength of $\lambda = 0.15956$ nm.

X-ray photoelectron spectra (XPS) spectra were collected on a Thermo Electron K-Alpha spectrometer using a monochromatic Al K_α X-ray source (1486.6 eV). Core level spectra from 100 scans were referenced to the C 1s core-level peak at 284.3 eV. The XPS spectra were processed using a Shirley background correction followed by peak fitting to Voigt profiles. The FWHM were allowed to vary within reasonable value ranges in order to achieve best fit.

6.2.3 Sample Designations

Each of the samples in this work was prepared with either 5 or 10 separate dip-coated layers of VO from the alkoxide based precursor. The samples under study are the untreated as-deposited (As-Dep) thin films and the same samples thermally annealed at low, intermediate and high temperatures (LTA, ITA, HTA), 200 ^{o}C, 250 ^{o}C and 300 ^{o}C respectively.

6.3 Results and Discussion

6.3.1 Optical Properties of Inter-Diffusion Formed Thin Films

Figure 6.1 (a) shows the evolution of a 10 layer dip-coated VO thin film on glass to a completely transparent thin film (TTF) material formed after annealing. Optical images in Figure 6.1 (a) show the initial dip-coated as deposited film and its intermediate stage formed through an intermediate thermal anneal (ITA) treatment, where the characteristic green-yellow colour changes to a dark yellow. Remarkably, the samples formed through a high thermal anneal (HTA) treatment at 300 ^{o}C show a complete transformation to a fully transparent coating, cleared entirely of its colour. The solution processed technique also allows for non-planar substrates to be used,

such as the borosilicate glass tube shown in Figure 6.1 (a). Both the inner and outer diameter of the tube can be conformally coated through dip-coating and the TTF subsequently formed through a HTA treatment.

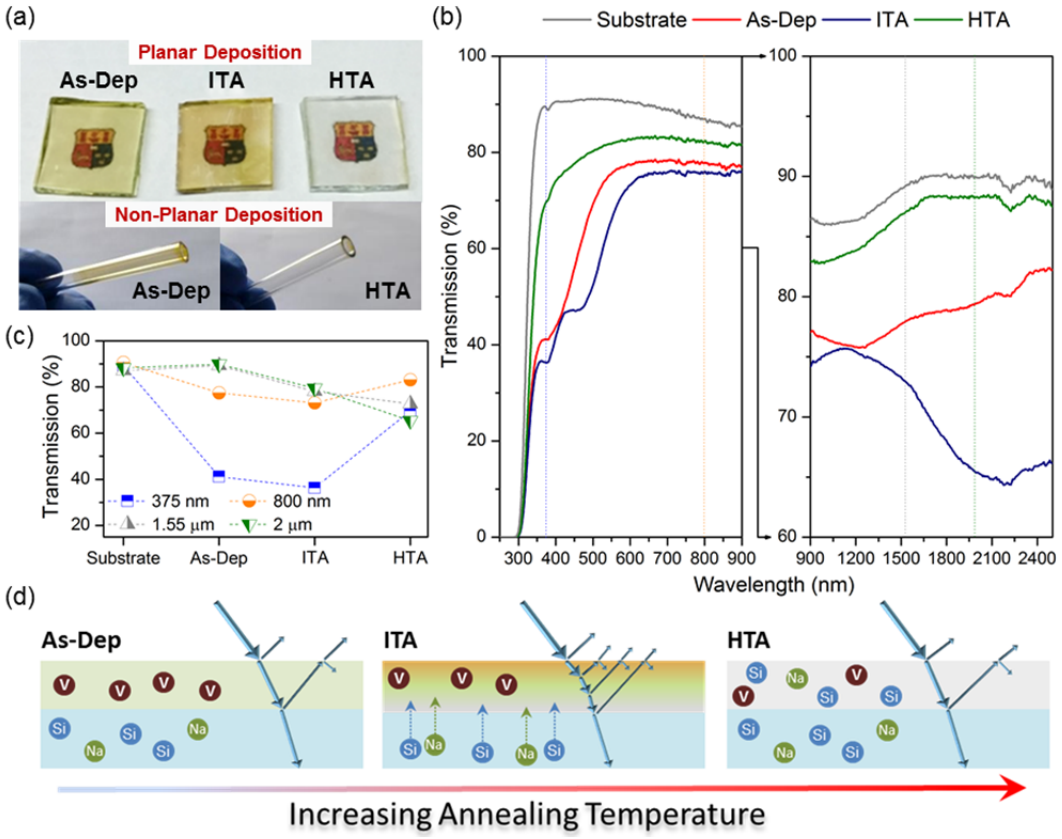


Figure 6.1. (a) Optical images of the As-Dep, ITA and HTA treated thin films on planar and non-planar glass substrates and (b) UV-Vis-NIR transmission spectra of the respective planar samples using air as the normalized background for 100% transmission (background spectrum shown in Figure 6.2 (a)). (c) Variation in total transmission at different wavelengths spanning UV to NIR ranges for each thin film. (d) Schematic of the formation of the TTF through inter-diffusion processes.

The optical transmission from 300 – 2500 nm, including that of the underlying glass substrate, for the As-Dep, ITA and HTA treated thin films is shown in Figure 6.1 (b) with a comparison of the transmission at select wavelengths presented in Figure 6.1 (c). In Figure 6.1 (b), a distinctive change to almost complete visible transparency occurs due to the inter-diffusion between the substrate and the VO thin film. During the transition to optically cleared transparency (ITA samples

annealed at 250 ^{o}C), the absolute transmission initially decreases below that of the as-deposited thin film across the broadband UV-NIR spectral range due to the crystallisation and densification of the thin film prior to its conversion to a full TO. This decrease in transmission is also observed in thin films of V_2O_5 deposited onto ITO coated glass substrates where the ITO acts as a diffusion barrier, and thus is related to crystallization and densification of the VO film (*vide infra*). However, the optical transmission markedly increases in the HTA thin film with a noticeable blue-shift in the absorption edge and increase in broadband transparency.

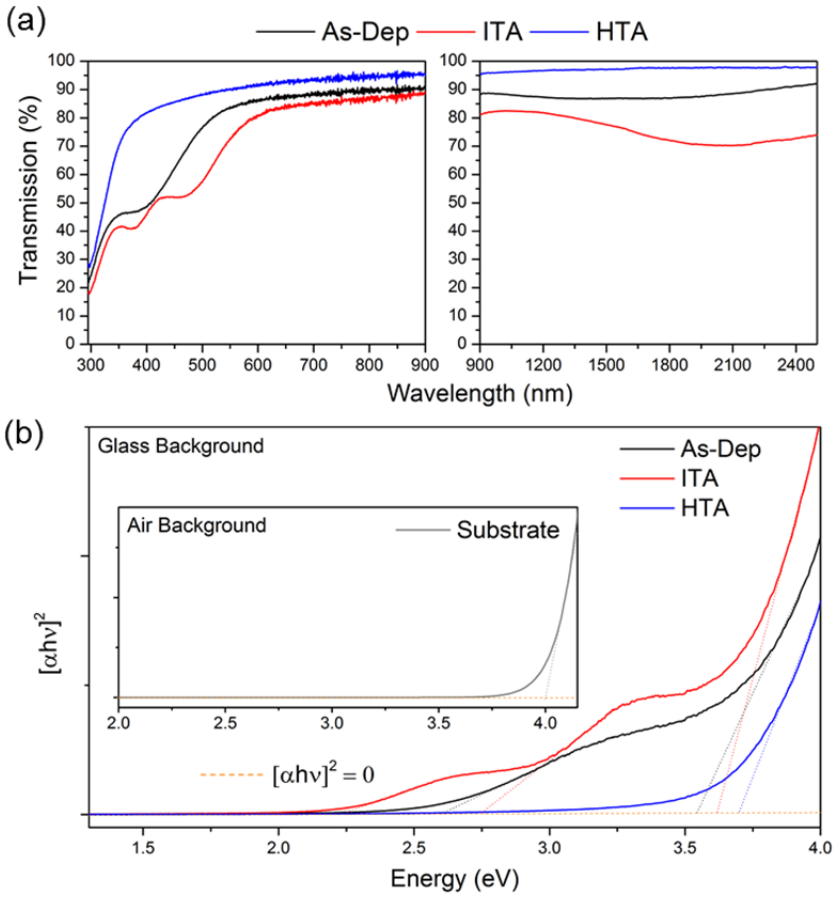


Figure 6.2. (a) UV-Vis transmission spectra of the As-Dep, ITA and HTA samples using the glass substrate as the 100% transmission background. (b) $[\alpha h\nu]^2$ versus energy (Tauc) plot of As-Dep, ITA and HTA thin films.

During conversion to a TTF, three distinct absorption edges are found in the ITA film and a reduction in total transmission at all wavelengths from 300 nm – 2.5

μm is observed. These additional absorption edges will be shown to be attributed to the initial formation stages of the TTF due to diffusion at the glass-VO interface coupled with the crystallisation of the VO thin film at the VO-Air interface, and are characteristic of the initial stages of conversion to the ternary metal oxide. After the completely transparent film is formed, a slight decrease in optical transmission >1100 nm is observed, uniquely after optical clearing. The reduction in transparency is consistent with a reduction in dielectric constant and increase in free carriers at energies less than the plasma frequency (Figure 6.1 (b), right), where the ITA treated film has a reduced transparency at lower frequencies – observing some opacity in the NIR region for the intermediate films indicates a change in electrical conductivity and film composition, due to the variation in effective refractive index.

The fully transparent HTA treated thin film exhibits just an 8 – 10% reduction in absolute transmission compared to the glass substrate in the 300 – 900 nm range, and a 3 - 5% reduction in the 900 – 2500 nm region, after accounting for the reduced reflectivity from index matching at the TTF-glass interface. From AFM images, the film thickness for this As-Dep thin film, formed from a 10–layer coating of the initial VO film, is ~ 95 - 105 nm (See Figure 6.3 (a)). Diffusion of Na and Si species from the substrate into the thin film results in a phase conversion that promotes optimum transparency of the TTF after annealing at 300 ^{o}C. The UV-Vis spectra show a distinct blue shift in the absorption edge similar to the response of the underlying glass substrate, and broadband transmission is likely limited by the UV absorption in the glass substrate. The final TTF, once fully formed, no longer exhibits any secondary or tertiary supra band-gap absorption edges as found in the As-Dep and intermediate ITA treated films (Figure 6.1 (b)).

An effective optical bandgap (E_g) related to each of the absorption edges observed during the conversion from As-Dep to TTF film was estimated using the modified Davis-Mott relation as outlined in Chapter 4.[44] The refractive index (n) of the material was then estimated using the Moss[45-46] relation where;

$$n_{VO}^4 E_g \sim 95 \text{ eV} \qquad (Eq.\ 6.1)$$

The respective E_g and n values for each of the samples are summarised in Table 6.1.

As the transparency of the thin films increases, an associated increase of the primary E_g value and a decrease in the respective refractive index values is noted. The Tauc plot of the As-Dep, ITA and HTA thin films is shown in Figure 6.2 (b). The As-Dep VO film exhibited two absorption edges that can be correlated with E_g values of 2.6 eV and 3.54 eV respectively, while the ITA treated sample displayed three absorption edges at 2.22 eV, 2.74 eV and 3.62 eV. The HTA treated sample has a calculated E_g of 3.7 eV while the glass substrates absorption edge is calculated to be ~4.01 eV. The TTF formation thus mimics the optical transmission of the glass substrate with a consistent high transparency down to 300 nm. The interfacial region thus show index matching with absorption edges close to the substrate. Both the secondary E_g value found in the As-Dep film and the tertiary E_g value seen in the ITA treated films can be attributed to the amorphous and crystalline V_2O_5 thin films deposited using the same technique on an ITO substrate as discussed in Chapter 3. The secondary absorption edge found for the ITA samples is due to the presence of a region between the layer formed at the glass-VO and VO-Air interfaces, illustrated in Figure 6.1 (d). The n values for each of the primary, secondary and tertiary E_g values were calculated and presented in Table 6.1. The absorption edges can be attributed to different layers (*vide infra*) formed within the thin film due to both crystallisation and diffusion-based changes in composition.

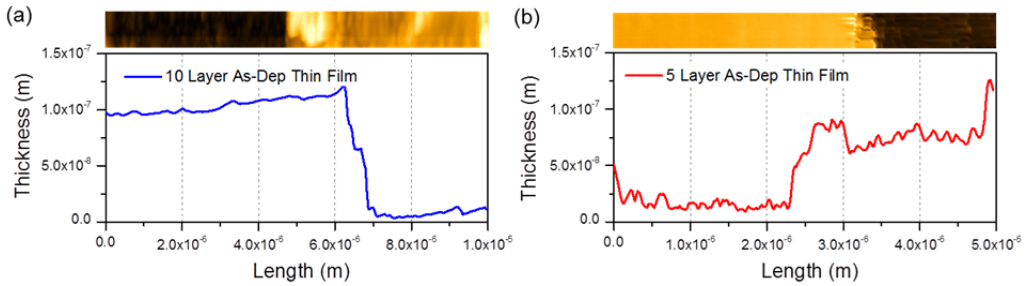


Figure 6.3. Plot of thickness profile and corresponding AFM image for (a) 10 layer and (b) 5 layer As-Dep thin films on glass substrates measured using AFM.

6.3.2 Inter-Diffusion Thin Film Surface Characterization

The surface morphology of the thin films was examined using AFM and are presented in Figure 6.4 (a), and additional AFM surface images can be seen in Figure 6.5. The AFM analysis shows small changes to the surface morphology and grain density during thermal treatment, including a slight increase in surface roughness. During conversion, the ITA films show a granular morphology with inter-grain voids that eventually merge to a fused-grain structure when completely transparent. The average rms surface roughness measured for the As-Dep, ITA and HTA treated films is <1 nm. As seen in both the optical images in Figure 6.1 (a) and in the corresponding AFM images in Figure 6.4 (a), the surface of the TTF remains relatively continuous and consistent over the entire sample area.

Using Raman scattering spectroscopy, the vibrational bonds of the As-Dep, ITA and HTA treated films were analysed and compared to that of orthorhombic V_2O_5 in Figure 6.4 (b). The As-Dep thin films are composed of amorphous stoichiometric V_2O_5 and show no discernible vibrational bonds – V_2O_5 never crystallizes in the presence of the dopant interacting species. When a transparent diffusion barrier such as ITO or FTO is present between the As-Dep film and the glass substrate, the formation of orthorhombic V_2O_5 occurs, which has an intense

and well-defined Raman scattering spectrum. The characteristic diffusion process has been shown to occur at very high thermal treatment temperatures in VO and tungsten oxide (WO_3) thin films where the diffusion initiates from the glass substrate, through an ITO coating layer to form islands of the material[47-48]. In such a case, the resulting surface film is non-homogeneous and discontinuous allowing species diffusion through voids or gain boundaries.[47-48] The lack of a diffusion barrier layer on the substrate facilitates diffusion to form a continuous TTF material on the surface of the glass.

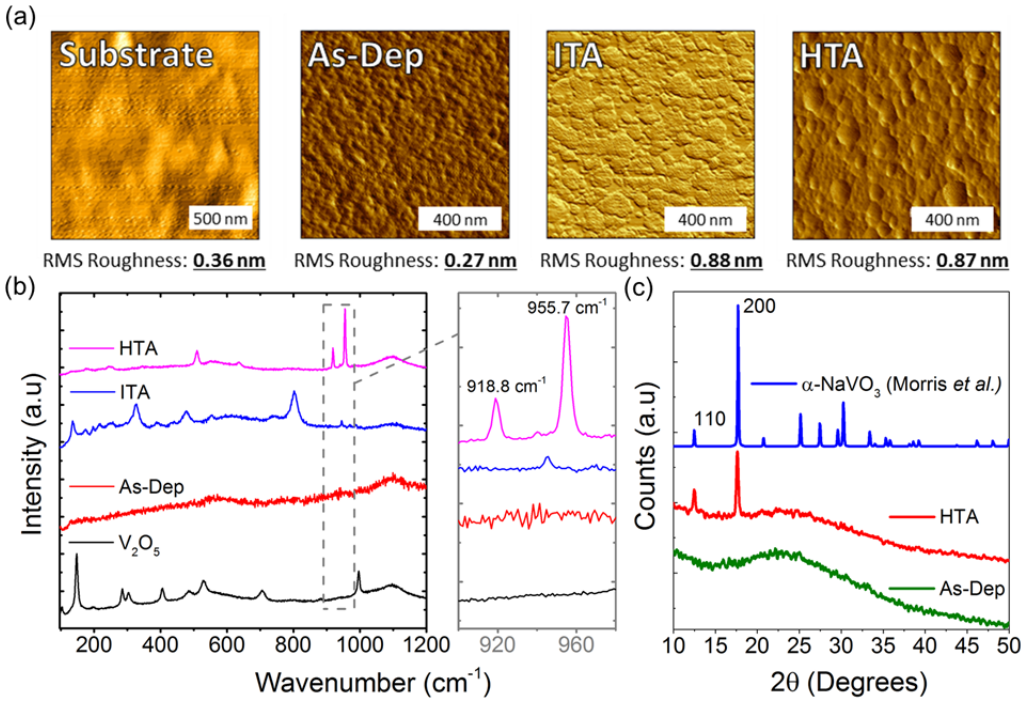


Figure 6.4. (a) AFM images and respective RMS roughness values for the substrate, As-Dep, ITA and HTA treated thin films. (b) Raman scattering spectroscopy of orthorhombic V_2O_5 on a diffusion layer substrate and As-Dep, ITA and HTA treated thin films on glass substrates showing the formation of the transparent TTF phase. (c) Thin film XRD pattern of As-Dep and HTA thin film confirms the presence of a crystalline metamunirite α-$NaVO_3$ component in the TTF material.

The TTF material formed in this study has distinct Raman scattering modes at 509.7 cm^{-1}, 918.8 cm^{-1} and 955.7 cm^{-1}. The TTF vibrational modes are attributed to specific O bonds between the Si, Na and V formed through the diffusion process.

Some of the prominent Raman modes are attributed to the formation of a crystalline α-$NaVO_3$ component within the TTF thin film.[49-50] Many of the Raman scattering modes for the ITA treated films matches superimposed amalgamated spectra for each of the intermediate layers.

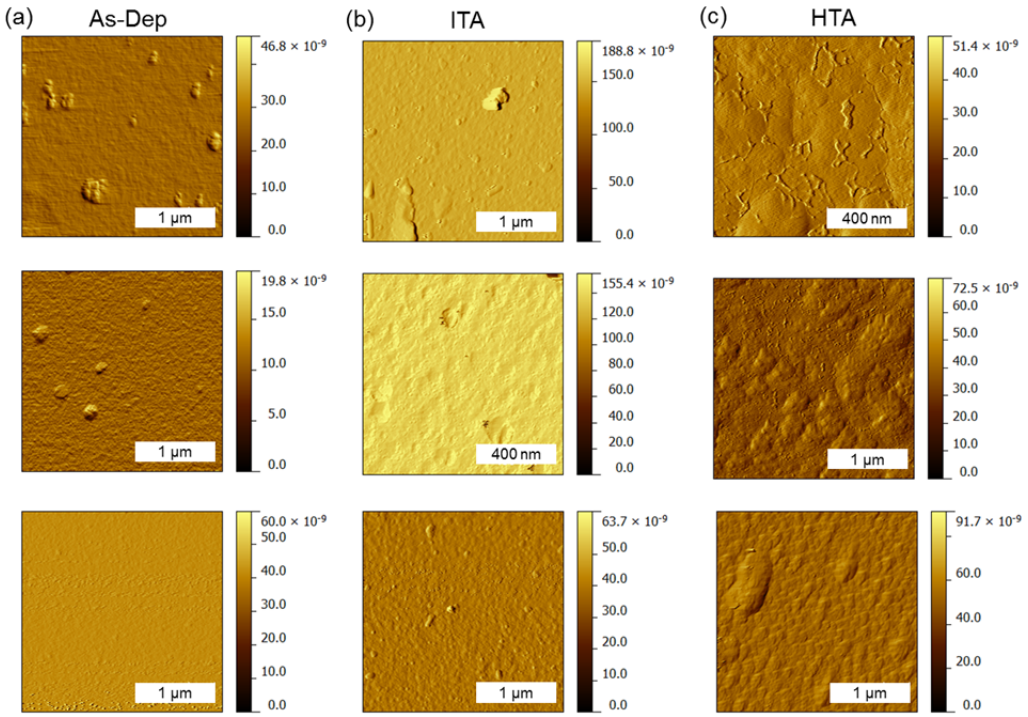


Figure 6.5. AFM images of the surface for (a) As-Dep, (b) ITA and (c) HTA samples.

The thin film XRD patterns in Figure 6.4 (c) confirm the formation of crystalline α-$NaVO_3$ within the TTF thin film where diffraction from the α-$NaVO_3$ (110) and (200) planes is present.[51] The (110) and (200) planes in α-$NaVO_3$ are also present in β-$NaVO_3$ indexed to (020) and (110) respectively.[52] The presence of only two diffraction peaks for the TTF, both of which are common to α-$NaVO_3$ and β-$NaVO_3$, means definite predictions of the crystalline phase cannot be made through XRD alone. However, the Raman scattering spectra shows the vibrational spectra for predominantly α-$NaVO_3$, allowing the crystalline component to be indexed to α-$NaVO_3$. The amorphous profile of the As-Dep and HTA XRD patterns located below

40° implies that the crystalline α-$NaVO_3$ material is surrounded by a non-crystalline glassy matrix.

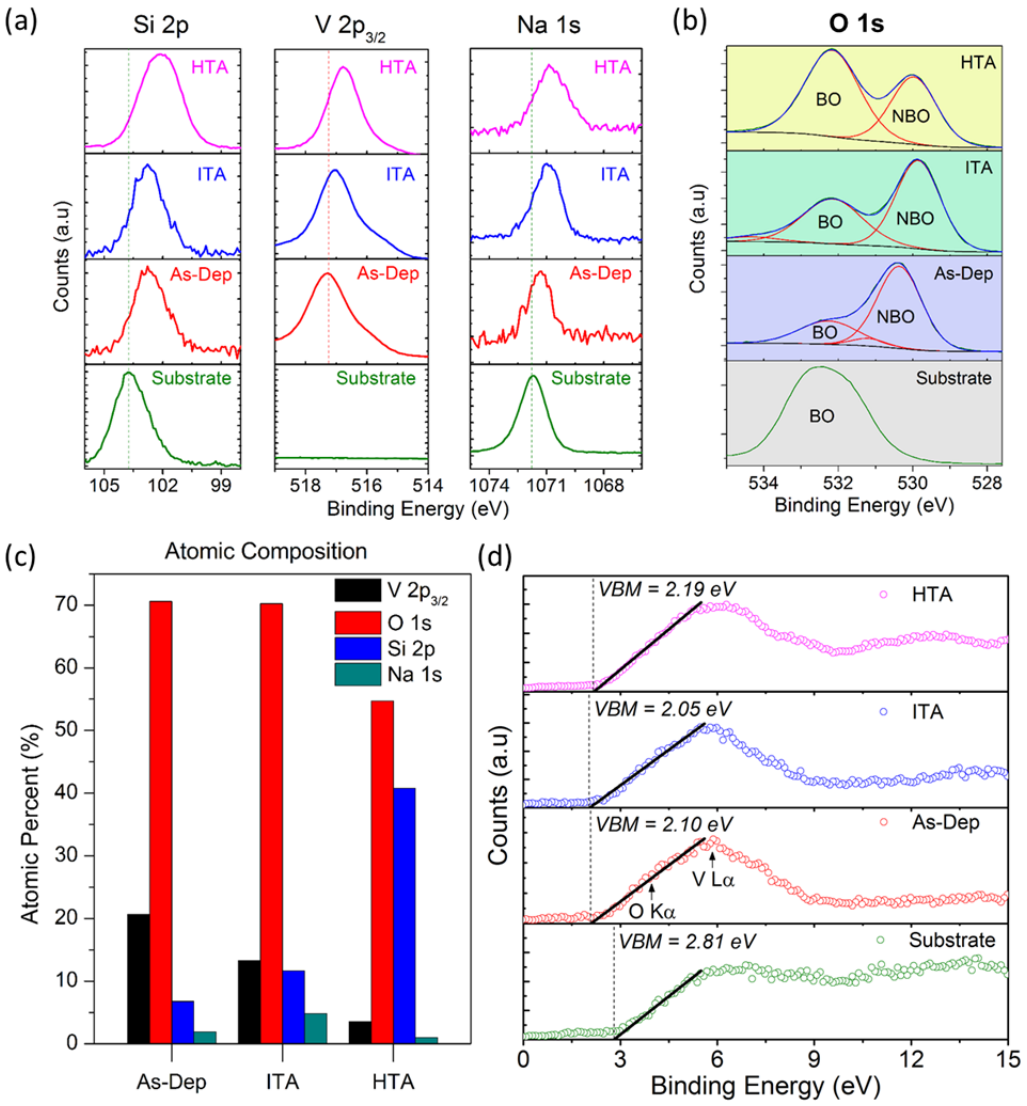


Figure 6.6. (a) XPS analysis showing the changes in the Si, V and Na spectra during thermal treatment and subsequent diffusion between the substrate and the VO thin film. (b) XPS spectra of the O 1s peaks showing the BO and NBO contributions of the glass substrate, As-Dep, ITA and HTA samples. (c) Relative atomic composition of the surface of the thin films from XPS data during conversion to the $V_{0.04}O_{0.54}Si_{0.41}Na_{0.01}$ TTF. (d) Valence band (VB) spectra and VBM estimates for the glass substrate, As-Dep, ITA and HTA treated films.

XPS was used to examine the composition during annealing, which leads to the formation of the TTF. The XPS spectra of the Si 2p, V $2p_{3/2}$ and Na 1s peaks for the substrate, As-Dep, ITA and HTA treated films are shown in Figure 6.6 (a).

Survey scans were recorded with the adventitious C 1s photoemission at 284.3 eV as a reference (the reference shifts are consistent when using C 1s or O 1s as no scattering of binding energy (BE) values from measurement is observed). A decrease in the BE of ~1.6 eV and ~0.8 eV is measured between the Si 2p and Na 1s core-level photoelectrons of the glass substrate compared to the fully formed TTF. The same associated decrease is found in Na_2O-SiO_2 glasses where an increased amount of Na_2O present in the glass results in a reduced BE of both the Si 2p and Na 1s peaks.[53] In the case of the TTF, the reduction in the Si 2p and Na 1s BE is attributed to the presence of the vanadia species. A small shift in energy of ~0.5 eV is observed for the V $2p_{3/2}$ peak after conversion from the As-Dep to the TTF. This small BE shift is attributed to the conversion of the stoichiometric As-Dep VO thin film to a TTF formed of a crystalline α-$NaVO_3$ within an overall glassy matrix approximating $V_{0.04}O_{0.54}Si_{0.41}Na_{0.01}$.

The glass substrate shows a single contribution to the O 1s peak in Figure 6.6 (b) while the As-Dep, ITA and HTA treated films contain two O 1s contributions arising from variations in the bridging of the O atoms to the other species within the thin film.[53] The O 1s peak at a higher BE is assigned to bridging oxygen (BO) atoms while the lower BE peak is due to non-bridging oxygen (NBO) atoms. In a BO system, two Si atoms are bonded by an O (Si-O-Si) while in an NBO system the Si, Na and V atoms can be O bonded in a number of ways (Si-O-V/Na, V=O, Na-O-V).[54] The ratio between the NBO and total O (O_T) peak areas is presented in Table 6.1 and highlights the dominant type of O bonding within each film. During TTF formation (ITA and HTA treated samples), the NBO/O_T ratio is found to reduce as the quantity of Si species within the thin film increases.

Table 6.1. Surface roughness, optical and material properties of the glass substrate and the respective thick As-Dep, ITA and HTA treated films. The Eg values for each of the films was calculated for the absorption edges present in the UV-Vis transmission spectra. The n values were calculated from the corresponding Eg values.

Sample	**Avg. RMS Roughness (nm)**	**E_g (eV)**	**n**	**NBO / O_T**	**ΔE_{BO-NBO} (eV)**
Glass	0.36	4.01	1.5171*	n/a	n/a
As-Dep	0.27	3.54, 2.60	2.28, 2.46	0.686	1.8
ITA	0.88	3.62, 2.74, 2.22	2.26, 2.43, 2.56	0.506	2.3
HTA	0.87	3.70	2.25	0.181	2.2

*Refractive index provided from Thermo Scientific, n = 1.5171 at λ = 546.07 nm.

The atomic composition of the thin films was studied using XPS and the calculated Si, Na, O and V at. % for the As-Dep, ITA and HTA treated samples are shown in Figure 6.6 (c). The calculated compositions for each of the films are $V_{0.19}O_{0.75}Si_{0.05}Na_{0.01}$ (As-Dep), $V_{0.13}O_{0.71}Si_{0.12}Na_{0.04}$ (ITA) and $V_{0.04}O_{0.54}Si_{0.41}Na_{0.01}$ (TTF), respectively. Note, the small Si and Na concentration (in at%) in the As-Dep stoichiometric V_2O_5 thin film is attributed to photoelectron emission from the glass caused by penetration of the X-rays and photoelectron escape through intergrain boundaries in the thin film that is otherwise thicker than the X-ray penetration depth. Analysis of the O 1s spectrum (*vide ante*) shows the majority of the diffused Si, making up ~40% of the TTF composition, is bonded to O in a BO system while the remaining O bonded Si is NBO bonded with the V and Na. Vanadia and Na species constitute ~ 3.5% and 1% of the TTF composition respectively, the majority of which is assumed to be O bonded in an NBO system; the bonded O BE shifts towards the VB edge as the TTF forms (see Figure 6.6 (d)) and the strong hybridization of V 3d–O 2p orbitals characteristic of the defined VB spectrum of V_2O_5 (As-Dep) is lost upon conversion to the TTF. The relative V and Na species in

the overall ternary composition agrees very well with theoretical V_2O_5 and Na_2O ratios for α-$NaVO_3$ of 74.6 and 25.4 wt%, respectively.[52]

Valence band spectra were also extracted from XPS data from the substrate, As-Dep, ITA and HTA treated films to determine how phase conversion to the mixed metal oxide TTF via the inter-diffusion affects the effective bandgap and density of states. Figure 6.6 (d) shows the XPS valence band spectra for the As-Dep, ITA and HTA films and the calculated valence band maximum (VBM) was estimated by extrapolation of the leading edge of the photoemission onset.[55] The borosilicate substrate VBM is ~2.89 eV, less than that of pure SiO_2, ~5 eV[55-56]. The drop in the VBM is attributed to the other species within the substrate. A decrease in the VBM of the As-Dep and ITA films is observed, while the HTA treated thin film exhibits a VBM of 2.19 eV once the TTF is fully formed. Interestingly, the formation of the TTF results in the reappearance of a secondary peak in the 11 – 14 eV region previously found in the substrate, but not present in the As-Dep film. The reappearance of this mode could be due to the inter-diffusion mechanism and attributed to O 2p (Si 3p, Si 3s) bonding states within the TTF film[56] which reappear in the spectra due to the diffusion of Si and O species to the surface of the thin film.

6.3.3 Time Dependent Inter-Diffusion Characterization

To establish the effect of annealing duration on TTF formation, a time-dependent experiment was performed over varying annealing temperatures at set periods of time. Five layer As-Dep thin films (~50 - 60 nm, see Figure 6.3 (b)) were prepared and cut into multiple pieces. Annealing was performed at 200 ^oC (LTA), 250 ^oC and 300 ^oC with separate samples removed and characterized each hour. A

thinner As-Dep thin film was chosen so that TTF conversion could be mapped over a short period of annealing time. Due to the thinner As-Dep thin film, the intermediate stage studied previously is bypassed in short time and complete transparency is rapidly developed. Figure 6.8 (a) shows UV-Vis-NIR transmission spectra of the As-Dep, LTA, ITA and HTA treated samples as a function of annealing time. The corresponding optical images of the samples are included as insets in Figure 6.8 (a). The corresponding optical images of the films, including the 48 h and 72 h LTA films, are shown Figure 6.7.

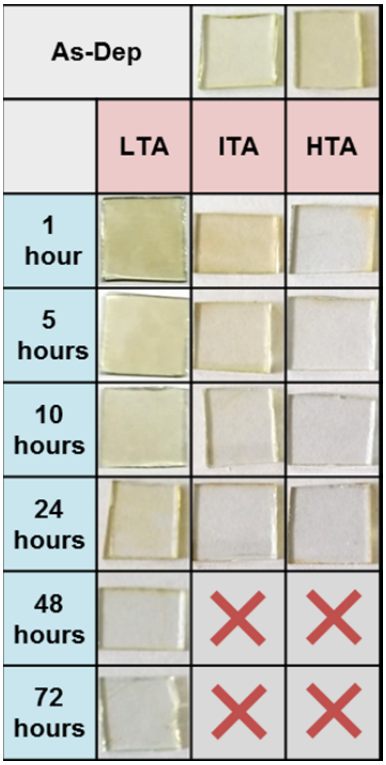


Figure 6.7. Optical images of the As-Dep, LTA, ITA and HTA samples over time showing the changes to transparency of the samples due to diffusion effects.

Optical transmission analysis shows that a fully formed TTF occurs after 24 h from both the ITA and HTA treated thin films. The LTA treated films, annealed at a lower temperature of 200 °C, do not form a fully transparent TTF after 24 h due to limited substrate species diffusion and phase change. Optical images of the LTA

samples after subsequent heating for 48 and 72 h, see Figure 6.7, appear to show the LTA thin films to be optically transparent, however, corresponding UV-Vis-NIR transmission data in Figure 6.8 proves that the transparency in the NIR region is reduced compared to ITA and HTA films owing to remnant electro-optic conductivity from limited phase conversion from V_2O_5-based As-Dep film to the ternary oxide TTF.

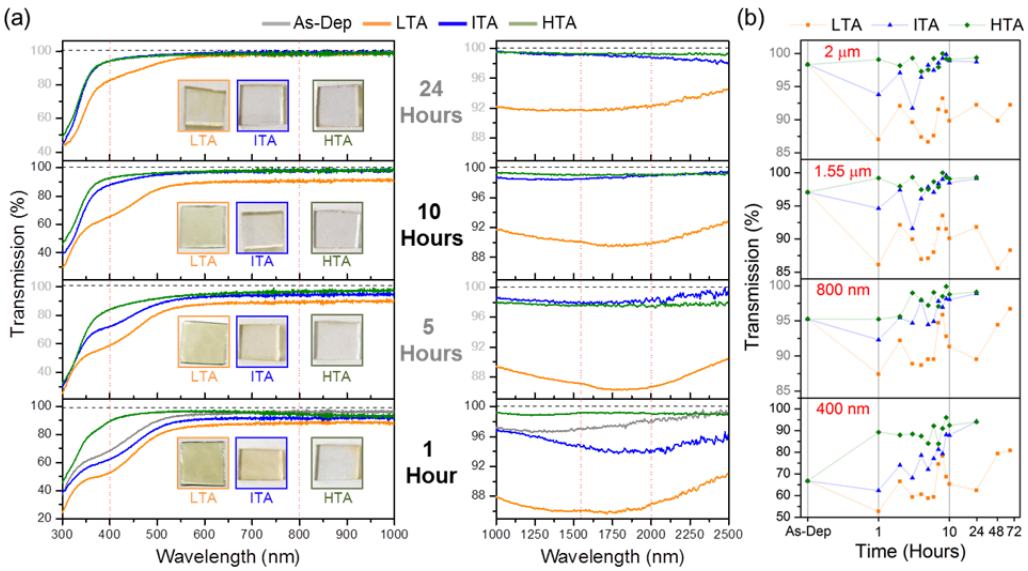


Figure 6.8. (a) UV-Vis-NIR transmission spectra and optical images of the LTA, ITA and HTA treated samples over time and (b) corresponding percentage transmission at λ = 400 nm, 800 nm, 1.55 µm and 2 µm.

The time-dependent transmission for the As-Dep, LTA, ITA and HTA treated films was measured at 400 nm, 800 nm, 1.55 µm and 2 µm and compared in Figure 6.8 (b). The annealing interval at the intermediate stage, which decreases absolute transmission due to densification of the crystalline grains prior to phase conversion to the ternary TTF, is shorter in the 5 layer as-deposited thin film. The thinner as-deposited thin film requires less time ($\sim t^{1/2}$) due to a shorter diffusion length (assuming an invariant ionic diffusion coefficient in the converting phase) to form the TTF. The formation of the TTF from dip-coated films at lower annealing

temperatures is beneficial for incorporation into devices that cannot withstand high temperature processing conditions and for optical coatings on curved or bespoke shaped glass and glassy encapsulants, such as the glass tube in Figure 6.1 (a). The E_g values for each of the films over time is shown in Figure 6.9 (a). Two absorption edges are present in spectra for LTA and ITA treated films. The secondary absorption edge value is attributed to the remnants of the intermediate stage within the thin film, which disappear in the late stage of the annealing in ITA films when modified to complete transparency. The primary E_g value of ~3.6 eV of the TTF forms in both the ITA and HTA films after 24 h annealing while in the LTA films a primary E_g value higher than 3.6 eV at the time points prior to 24 h. The higher LTA primary absorption E_g value is attributed to a contribution from the underlying glass substrate and the ITA film which due to a lower temperature does not form the TTF through diffusion processes until a late stage in the annealing; therefore the glass substrate with a higher absorption edge influences the absorption edge of the ITA films.

By comparison of refractive index data in Figure 6.9 (a) and transmission characteristics in Figure 6.8 (b), an enhanced transmission from optical clearing of the film to a TTF is found and occurs because of a phase change to a ternary mixed metal oxide that widens the transmission window and overall transparency, and from reduced interfacial reflectivity with the glass substrate.

Raman scattering spectroscopy shown in Figure 6.9 (b) was used to map the phase conversion via diffusion during TTF formation, by monitoring the onset of the two characteristic vibrational peaks at 918.8 cm^{-1} and 955.7 cm^{-1} respectively over time for the LTA, ITA and HTA films. The full time-dependent Raman scattering spectra can be seen in Figure 6.10. The characteristic vibrational peaks indicative of

crystallized phase conversion to the ternary mixed oxide TTF appear after only 1 h of annealing at 300 ^{o}C (HTA), after 4 h under annealing at 250 ^{o}C (ITA), and begins to appear after 10 h when heated at 200 ^{o}C (LTA). The intensity and resolution of the 918.8 cm^{-1} and 955.7 cm^{-1} vibrational peaks also markedly increases in each case with time once the TTF begins to form, until all films are transparent. While the absolute transmission of the LTA films never matches that of the ITA and HTA treated films, the LTA treated samples do show the formation of the same characteristic Raman vibrational peaks.

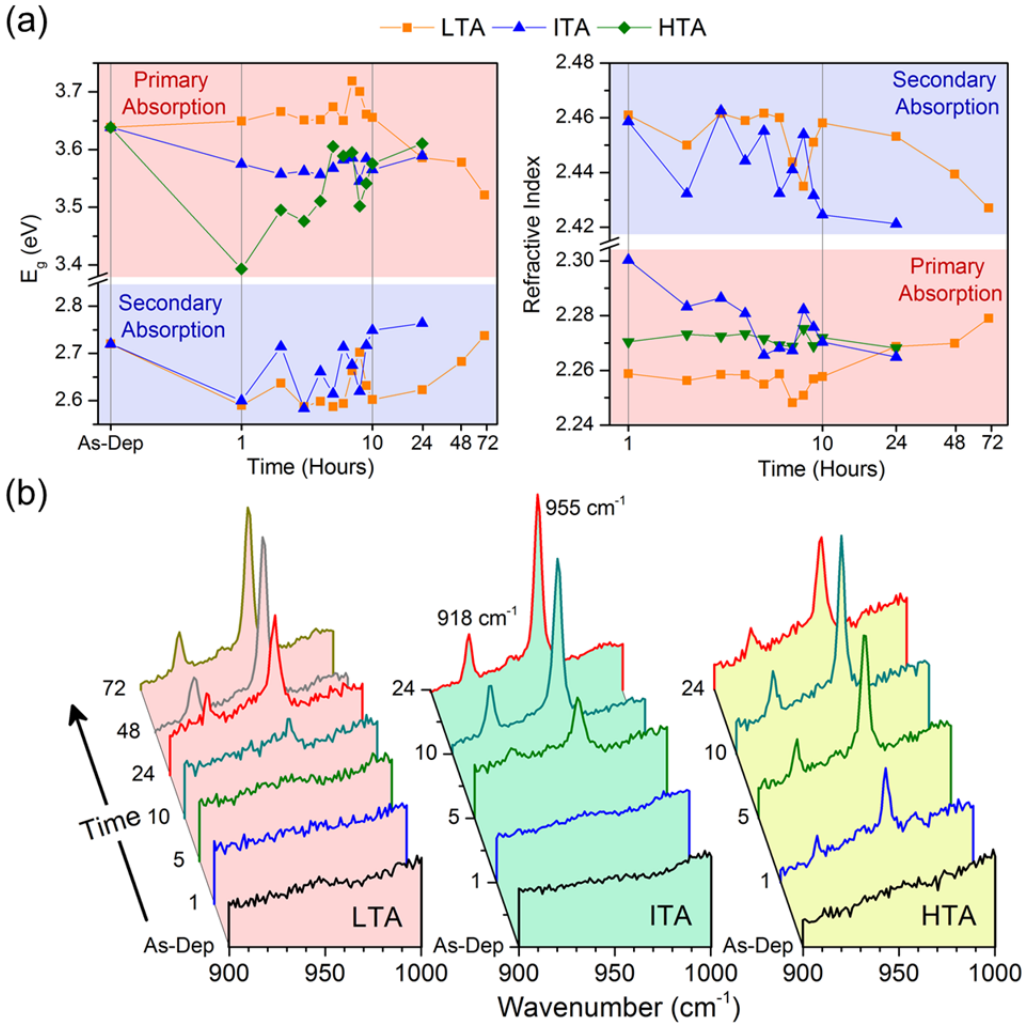


Figure 6.9. (a) Calculated E_g and n values for the primary and secondary absorption edges of the LTA, ITA and HTA treated films, respectively. (b) Time-dependent Raman scattering spectra of LTA, ITA and HTA treated samples showing the formation of the 918 cm^{-1} and 955 cm^{-1} vibrational peaks at each of the thermal treatment temperatures.

The formation of the characteristic Raman modes within the LTA samples confirm that the onset of TTF formation via inter-diffusion occurs at 200 ^{o}C. Species diffusion was considered by assuming random lattice diffusion of Si, O, Na species into the initially amorphous V_2O_5 film with net radial displacement of atomic or ionic diffusion unidirectionally from the substrate (into or indeed out of) the ~50 nm thick 5-layer dip-coated layer. The thermal diffusivity of the glass (~0.35 mm/s) ensures fast equilibration to the annealing temperature, leaving the temporal phase conversion process specifically a function of ionic diffusivity and atomic restructuring. Using the Si as the tracer (7% to 40% concentration increase upon TTF formation, *cf.* Figure 6.6 (c)), an average diffusion constant of just $D = 3.5 \times 10^{-15}$ cm^2 s^{-1} (for Na in sodium silicate glasses, $D = 10^{-10}$-10^{-11} cm^2 s^{-1}) is estimated from $L^2 = Dt$, where L is the diffusion length, D the diffusion coefficient and t the diffusion time. The Si species was examined as the tracer due to the large (~33%) change in the at%. The diffusion of species into the film is the faster process; subsequent diffusion within the developing TTF is slower, and confirmed from Raman scattering evidence of the onset of TTF formation (but prior to diffusion and subsequent complete chemical modification) and via XPS at% noted during the TTF formation.

The UV-Vis-NIR transmission characteristics of the samples indicates that to form the fully transparent TTF material, the extra thermal energy experienced by the ITA and HTA treated samples over longer time periods is required to fully convert the entire film (*cf.* Figure 6.1 (d)) and develop full broadband transparency.

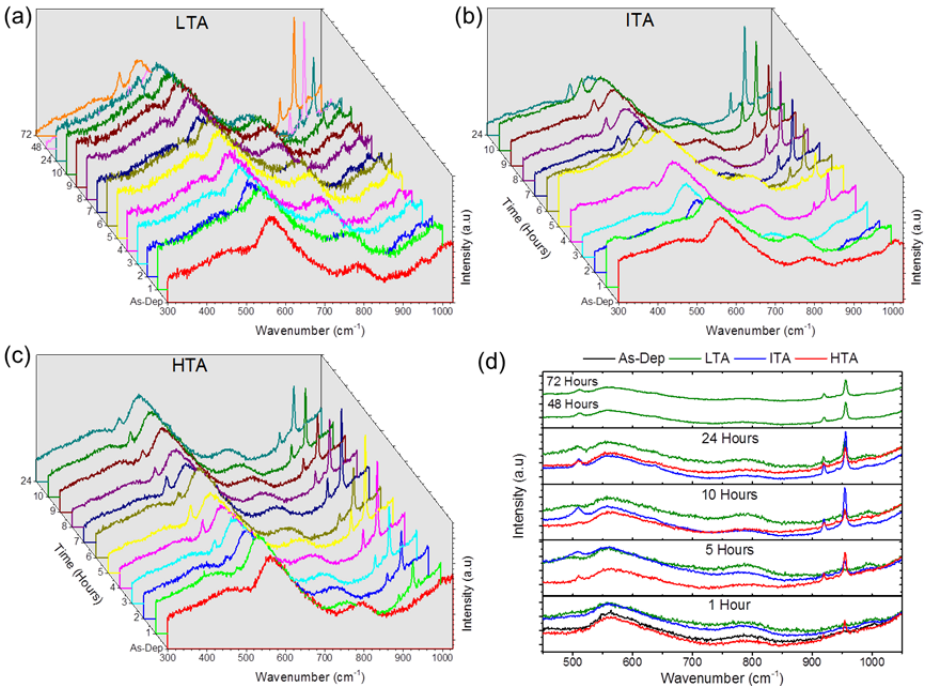


Figure 6.10. Time dependent Raman scattering spectroscopy for the (a) LTA, (b) ITA and (c) HTA samples. (d) Comparison between the Raman scattering spectra of the different samples at different of thermal treatment times.

6.4 Conclusions

A UV-Vis-NIR broadband ternary V-O-Na-Si mixed metal oxide transparent thin film material was demonstrated to form on glass through a diffusion controlled process from a solution processed dip-coated VO thin film. The method itself is a facile and cost-effective technique for the production of a transparent layer on the borosilicate glass surface that is conformal and generally free of cracks or pinholes. The final TTF material retains a low surface rms roughness of <1 nm and a defined composition and structure from the embedding and mixing of the V-O and Na-O and Si-O species. XPS, Raman scattering and XRD analysis confirm a TTF surface composition of $V_{0.04}O_{0.54}Si_{0.41}Na_{0.01}$, which contains a crystalline α-$NaVO_3$ component within a glassy matrix. The transparency of the TTF exceeds 90-97% absolute transmission across the UV to NIR wavelength range. The nature of O bonding within this transparent material modifies during annealing from a higher

proportion of NBO in the As-Dep V_2O_5 to a dominant BO configuration with Si-O and Na during the formation of the TTF.

During the annealing to form the TTF, an intermediate stage forms a multi layered system, with each layer exhibiting unique optical and structural characteristics analogous to a multi layered oxide system with a lower absolute transparency to both the as-deposited and TTF materials. The TTF formation was demonstrated to be possible at lower temperatures using initially thinner dip-coating, and provides a faster, thinner TTF optical coating on glass in shorter time, which is of benefit for incorporation into optoelectronic devices, (tandem) solar cells, LEDs and for optical coatings where enhanced and defined transmission/reflection characteristics are needed, but where high annealing temperatures must be avoided, all below softening temperatures for a range of glasses, optics and encapsulants. The approach may also allow low- or high-k binary, ternary or other dielectric oxide growth, and as an anti-tarnish barrier layer invisible to the human eye.

The adaptable processing techniques involved in the formation of a V-O-Na-Si based TTF material on glass substrates via precursor design and high rate dip-coating is practical for technologies in optics and photonics. Importantly, TTFT and optical coatings research and development for next generation display and interactive technologies require new materials with higher electronic mobilities, controllable thickness and refractive index, application-specific absorbance characteristics facilitates by doping using alternative metals than those reported here, and ease in processability. The latter is particularly important for devices or optics with complex or non-planar shapes. With the advent of flexible and shape-adaptable displays and screens, the use of plastic substrates is also increasing in importance owing to their light weight, flexibility, and low cost and the use of the substrate composition is an

intriguing method to dope, control and compositionally modify optical coatings. Indeed, this approach opens the door to using not only substrates, but coatings on substrates as metal or dopant sources for thermally driven diffusional modification of subsequent optical or optoelectronic coating materials.

6.5 References

1. Ellmer, K. Past achievements and future challenges in the development of optically transparent electrodes. *Nat. Photon* ***6***, 809-817 (2012).
2. Fortunato, E.; Barquinha, P.; Martins, R. Oxide Semiconductor Thin-Film Transistors: A Review of Recent Advances. *Adv. Mater.* ***24***, 2945-2986 (2012).
3. Granqvist, C. G. Electrochromics for smart windows: Oxide-based thin films and devices. *Thin Solid Films* ***564***, 1-38 (2014).
4. Chen, C.-P.; Chen, Y.-D.; Chuang, S.-C. High-Performance and Highly Durable Inverted Organic Photovoltaics Embedding Solution-Processable Vanadium Oxides as an Interfacial Hole-Transporting Layer. *Adv. Mater.* ***23***, 3859-3863 (2011).
5. Zhang, X.-L. *et al.* Anti-reflection resonance in distributed Bragg reflectors-based ultrathin highly absorbing dielectric and its application in solar cells. *Appl. Phys. Lett.* ***102***, 103901 (2013).
6. Wang, Y. *et al.* $Ag_2O/TiO_2/V_2O_5$ one-dimensional nanoheterostructures for superior solar light photocatalytic activity. *Nanoscale* ***6***, 6790-6797 (2014).
7. Dotan, H. *et al.* Resonant light trapping in ultrathin films for water splitting. *Nat. Mater.* ***12***, 158-164 (2013).
8. Pasquarelli, R. M.; Ginley, D. S.; O'Hayre, R. Solution processing of transparent conductors: from flask to film. *Chem. Soc. Rev.* ***40***, 5406-5441 (2011).
9. Faustini, M. *et al.* Hydrophobic, Antireflective, Self-Cleaning, and Antifogging Sol−Gel Coatings: An Example of Multifunctional Nanostructured Materials for Photovoltaic Cells. *Chem. Mater.* ***22***, 4406-4413 (2010).
10. Chen, D. Anti-reflection (AR) coatings made by sol–gel processes: A review. *Sol. Energy Mater. Sol. Cells* ***68***, 313-336 (2001).
11. Kats, M. A. *et al.* Enhancement of absorption and color contrast in ultra-thin highly absorbing optical coatings. *Appl. Phys. Lett.* ***103***, 101104 (2013).
12. Jang, J. *et al.* Transparent High-Performance Thin Film Transistors from Solution-Processed SnO_2/ZrO_2 Gel-like Precursors. *Adv. Mater.* ***25***, 1042-1047 (2013).
13. Si Joon, K.; Seokhyun, Y.; Hyun Jae, K. Review of solution-processed oxide thin-film transistors. *Jpn. J. Appl. Phys.* ***53***, 02BA02 (2014).
14. Lin, Y.-H. *et al.* High Electron Mobility Thin-Film Transistors Based on Solution-Processed Semiconducting Metal Oxide Heterojunctions and Quasi-Superlattices. *Adv. Sci.* ***2***, (2015).
15. Grill, A. *et al.* Progress in the development and understanding of advanced low k and ultralow k dielectrics for very large-scale integrated interconnects—State of the art. *Appl. Phys. Rev.* ***1***, 011306 (2014).
16. Lee, W.-J. *et al.* Large-Scale Precise Printing of Ultrathin Sol–Gel Oxide Dielectrics for Directly Patterned Solution-Processed Metal Oxide Transistor Arrays. *Adv. Mater.* ***27***, 5043-5048 (2015).
17. Choy, K. L. Chemical vapour deposition of coatings. *Prog. Mater Sci.* ***48***, 57-170 (2003).
18. Jeon, G. H. Recent progress in thin film processing by magnetron sputtering with plasma diagnostics. *J. Phys. D: Appl. Phys.* ***42***, 043001 (2009).
19. Schneller, T.; Waser, R.; Kosec, M.; Payne, D., *Chemical Solution Deposition of Functional Oxide Thin Films*. 1st ed.; Springer: London, 2013; p 796.

20. Jo, J.-W. *et al.* Highly Stable and Imperceptible Electronics Utilizing Photoactivated Heterogeneous Sol-Gel Metal–Oxide Dielectrics and Semiconductors. *Adv. Mater.* ***27***, 1182-1188 (2015).
21. Bao, X. *et al.* Simple O_2 Plasma-Processed V_2O_5 as an Anode Buffer Layer for High-Performance Polymer Solar Cells. *ACS Appl. Mater. Interfaces* ***7***, 7613-7618 (2015).
22. Banger, K. K. *et al.* Low-temperature, high-performance solution-processed metal oxide thin-film transistors formed by a 'sol–gel on chip' process. *Nat. Mater.* ***10***, 45-50 (2011).
23. Chang, J. H. *et al.* A solution-processed molybdenum oxide treated silver nanowire network: a highly conductive transparent conducting electrode with superior mechanical and hole injection properties. *Nanoscale* ***7***, 4572-4579 (2015).
24. Chen, Z. *et al.* Fabrication of Highly Transparent and Conductive Indium–Tin Oxide Thin Films with a High Figure of Merit via Solution Processing. *Langmuir* ***29***, 13836-13842 (2013).
25. Mizoshita, N.; Ishii, M.; Kato, N.; Tanaka, H. Hierarchical Nanoporous Silica Films for Wear Resistant Antireflection Coatings. *ACS Appl. Mater. Interfaces* ***7***, 19424-19430 (2015).
26. Faustini, M. *et al.* Preparation of Sol−Gel Films by Dip-Coating in Extreme Conditions. *J. Phys. Chem. C* ***114***, 7637-7645 (2010).
27. Minemawari, H. *et al.* Inkjet printing of single-crystal films. *Nature* ***475***, 364-367 (2011).
28. Meyers, S. T. *et al.* Aqueous Inorganic Inks for Low-Temperature Fabrication of ZnO TFTs. *J. Am. Chem. Soc.* ***130***, 17603-17609 (2008).
29. Grosso, D. How to exploit the full potential of the dip-coating process to better control film formation. *J. Mater. Chem.* ***21***, 17033-17038 (2011).
30. Thomas, S. R.; Pattanasattayavong, P.; Anthopoulos, T. D. Solution-processable metal oxide semiconductors for thin-film transistor applications. *Chem. Soc. Rev.* ***42***, 6910-6923 (2013).
31. Sunde, T. O. L. *et al.* Transparent and conducting ITO thin films by spin coating of an aqueous precursor solution. *J. Mater. Chem.* ***22***, 15740-15749 (2012).
32. O'Dwyer, C. *et al.* Bottom-up growth of fully transparent contact layers of indium tin oxide nanowires for light-emitting devices. *Nat. Nano.* ***4***, 239-244 (2009).
33. Lee, J.-Y.; Connor, S. T.; Cui, Y.; Peumans, P. Solution-Processed Metal Nanowire Mesh Transparent Electrodes. *Nano Lett.* ***8***, 689-692 (2008).
34. Watcharotone, S. *et al.* Graphene−Silica Composite Thin Films as Transparent Conductors. *Nano Lett.* ***7***, 1888-1892 (2007).
35. O'Dwyer, C.; Sotomayor Torres, C. Epitaxial growth of an antireflective, conductive, graded index ITO nanowire layer. *Front. Phys.* ***1***, (2013).
36. Street, R. A. Thin-Film Transistors. *Adv. Mater.* ***21***, 2007-2022 (2009).
37. Nomura, K. *et al.* Room-temperature fabrication of transparent flexible thin-film transistors using amorphous oxide semiconductors. *Nature* ***432***, 488-492 (2004).
38. Chiang, H. Q. *et al.* High mobility transparent thin-film transistors with amorphous zinc tin oxide channel layer. *Appl. Phys. Lett.* ***86***, 013503 (2005).
39. Ya-Hui, Y.; Yang, S. S.; Chen-Yen, K.; Kan-San, C. Chemical and Electrical Properties of Low-Temperature Solution-Processed In-Ga-Zn-O Thin-Film Transistors. *Electron Devic. Lett. IEEE* ***31***, 329-331 (2010).

40. Piccirillo, C.; Binions, R.; Parkin, I. P. Synthesis and Functional Properties of Vanadium Oxides: V_2O_3, VO_2, and V_2O_5 Deposited on Glass by Aerosol-Assisted CVD. *Chem. Vap. Deposition* ***13***, 145-151 (2007).
41. Paik, T. *et al.* Solution-processed phase-change VO_2 metamaterials from colloidal vanadium oxide (VO_x) nanocrystals. *ACS Nano* ***8***, 797-806 (2014).
42. Yang, Z.; Ko, C.; Ramanathan, S. Oxide Electronics Utilizing Ultrafast Metal-Insulator Transitions. *Annu. Rev. Mater. Res.* ***41***, 337-367 (2011).
43. Tong, Z. *et al.* Improved electrochromic performance and lithium diffusion coefficient in three-dimensionally ordered macroporous V_2O_5 films. *J. Mater. Chem. C* ***2***, 3651-3658 (2014).
44. Tauc, J., *The Optical Properties of Solids*. Academic Press: New York, 1966.
45. Akaltun, Y.; Yıldırım, M. A.; Ateş, A.; Yıldırım, M. The relationship between refractive index-energy gap and the film thickness effect on the characteristic parameters of CdSe thin films. *Opt. Commun.* ***284***, 2307-2311 (2011).
46. Ravindra, N. M.; Ganapathy, P.; Choi, J. Energy gap–refractive index relations in semiconductors – An overview. *Infrared Phys. Techn.* ***50***, 21-29 (2007).
47. Castriota, M. *et al.* Evolution from vanadium pentoxide xerogel to sodium-containing vanadates in thin films on ITO-coated glasses. *Ionics* ***13***, 205-211 (2007).
48. Castriota, M. *et al.* Anomalous enhancement of Raman scattering of metal oxide film deposited on thermally treated ITO-coated glass substrates. *Chem. Phys. Lett.* ***478***, 195-199 (2009).
49. de Waal, D. Vibrational spectra of the two phases of $NaVO_3$ and the solid solution Na ($V_{0.66}P_{0.34}$) O_3. *Mater. Res. Bull.* ***26***, 893-900 (1991).
50. Seetharaman, S.; Bhat, H. L.; Narayanan, P. S. Raman spectroscopic studies on sodium metavanadate. *J. Raman Spectrosc.* ***14***, 401-405 (1983).
51. Morris, M. *et al.* Standard x-ray diffraction powder patterns. *Nat. Bur. Stand.* ***25***, 67 (1981).
52. Evans, H. Metamunirite, a new anhydrous sodium metavanadate from San Miguel County, Colorado. *Mineral. Mag.* ***55***, 509-513 (1991).
53. Nesbitt, H. W. *et al.* Bridging, non-bridging and free (O_{2-}) oxygen in Na_2O-SiO_2 glasses: An X-ray Photoelectron Spectroscopic (XPS) and Nuclear Magnetic Resonance (NMR) study. *J. Non-Cryst. Solids* ***357***, 170-180 (2011).
54. Mekki, A. *et al.* Structure and magnetic properties of vanadium–sodium silicate glasses. *J. Non-Cryst. Solids* ***318***, 193-201 (2003).
55. King, S. W. *et al.* Valence and conduction band offsets at low-k a-SiO_xC_y:H/a-SiC_xN_y:H interfaces. *J. Appl. Phys.* ***116***, 113703 (2014).
56. Bell, F. G.; Ley, L. Photoemission study of SiO_x ($0 \leq x \geq 2$) alloys. *Phys. Rev. B* ***37***, 8383-8393 (1988).

Chapter 7

Contact Transfer Doping of Solution Processed V-O-Na-Si Thin Films and Nanowires on Transparent Metal Oxide Substrates

Abstract

A contact transfer doping method is demonstrated for solution processed mixed metal oxide thin films and nanowire dispersions directly on transparent metal oxide substrates. Different methods for exploiting inter-diffusion effects to form and dope thin film materials on substrates that do not have mobile ionic species was developed. A contact diffusion technique involving the deposition of VO thin films on diffusion layer FTO substrates and subsequent pressure contacting of a donor glass on the surface enabled the formation of V-O-Na-Si nanowire meshes on the surface of FTO after thermal annealing. A method for the deposition of planar and templated V-O-Na-Si thin films using Na-SiO_2 and SiO_2 electrodeposited surfaces coated in VO thin films was also developed. The addition of Na species in the electrodeposition electrolyte was found to be essential for the fabrication of both α-$NaNO_3$ and β-$NaNO_3$ thin films.

7.1 Introduction

The formation of a transparent V-O-Na-Si thin film was discussed in Chapter 6. This composite, made up of crystalline α-$NaVO_3$ within a glassy matrix, was formed through thermally induced inter-diffusion processes between a VO dip-coated thin film and borosilicate glass substrate. Previously, the deposition of the V-O-Na-Si thin films was limited to the borosilicate glass substrates on which they were deposited. In this chapter, two different methods are studied for forming V-O-Na-Si materials onto FTO substrates, i.e. glass substrates with FTO diffusion barrier/resistant layers.

Two different deposition techniques are utilised for depositing the V-O-Na-Si thin film material on substrates with a diffusion barrier on top of a glass substrate. A contact diffusion technique was devised to form an effectively transparent thin film composed of a nanowire mesh surface morphology. The second technique described here involves the formation of the V-O-Na-Si phase from V_2O_5 dip-coated onto an electrodeposited layer composed of a mixture of SiO_2 and Na (Na-SiO_2) on a conductive FTO substrate. Films containing only SiO_2 are also deposited using the same electrodeposition method where there is no Na-containing salt added to the electrolyte. The composite vanadium-containing materials are formed through inter-diffusion with a dip-coated VO thin film during annealing. For both methods the inter-diffusion process is used to form V-O-Na-Si related materials, namely a V-Na-SiO_2 and V-SiO_2, which are terms used to denote vanadium containing Na-SiO_2 and SiO_2 thin film materials.

The range of emerging materials, such as the V-O-Na-Si family of materials discussed in this chapter, are under investigation for use in modern electronics and devices as dielectrics and when appropriately doped, as high field-effect mobility

channel materials in TFTs, for example.[1-3] The range of applications for new metal oxide materials and structures are desired for use as different components within modern devices particularly for thin film electronics.[4-9] A range of different surface morphologies and structures for the V-O-Na-Si materials are possible using the different deposition techniques highlighted in this chapter. By exploiting inter-diffusion phenomena, transparent phases of thin and thick films, and crystalline nanowire networks of V-O-Na-Si is proven in the presence of SiO_2 and Na^+ ions on a range of substrates. This solution based approach for diffusion doping of oxide thin films is potentially interesting as a general method for phase modification of materials through a cost-effective and facile solution processable method.

7.2 Experimental

7.2.1 Thin Film Formation and Processing

For contact diffusion depositions, thin films of V_2O_5 were deposited onto FTO substrates with a 1000:10:1 (IPA : Alkoxide : H_2O) precursor solution through dip-coating. Cleaned borosilicate glass was placed on the surface of the thin film and held in place with a weight to ensure equalised and intimate contact between the glass and V_2O_5 thin film. Annealing at 300 ^oC was performed in a conventional oven for 72 hours and an enclosed furnace was used for treatments at 450 ^oC and annealed for 6-8 hours.

Na-SiO_2 and SiO_2 thin films were electrodeposited using an electrolyte solution containing Tetraethyl Orthosilicate (TEOS) as the active precursor and a $NaNO_3$ salt additive. To electrodeposit Na-SiO_2 thin films the electrolyte contained both TEOS and $NaNO_3$ as outlined in Chapter 3. SiO_2 thin films were prepared from

the same electrolyte without the addition of $NaNO_3$. The thin films were electrodeposited onto FTO substrates at a constant potential for set deposition times. V-Na-SiO_2 and V-SiO_2 thin films were formed by dip-coating a VO layer onto the electrodeposited Na-SiO_2 and SiO_2 thin films. Subsequent thermal treatments were used to facilitate the inter-diffusion processes.

7.2.2 Analysis Techniques

The thin film surface morphology was examined with both AFM and SEM. SEM images were collected top-down and at a 45^o incident angle. Raman scattering spectroscopy was collected on a Renishaw InVia Raman spectrometer using a 514 nm 30 mW laser source. Spectra were collected and focused onto the samples using a 50× objective lens. Mapping of the intensity of Raman vibrational modes was accomplished using a computerised movable microscope stage. XPS spectra were acquired on an Oxford Applied Research Escabase XPS system.

7.3 Contact Diffusion Transfer

7.3.1 Deposition Process

In the contact diffusion process, a thin film of V_2O_5 is deposited onto a substrate as outlined in the previous chapters. The ITO or FTO coatings on glass act as diffusion barriers to ionic mobility, preventing diffusional movement of Si- and Na-species from the glass. A clean borosilicate glass piece is contacted with the surface of the V_2O_5 thin film and pressure is applied between the two and maintained during thermal treatment. The thermal treatment parameters were refined between samples to influence the thin film surface morphology. A thicker as-deposited V_2O_5

layer requires a higher temperature for the formation of the transparent region due to the increased amount of inter-diffusion needed to convert to the transparent phase.

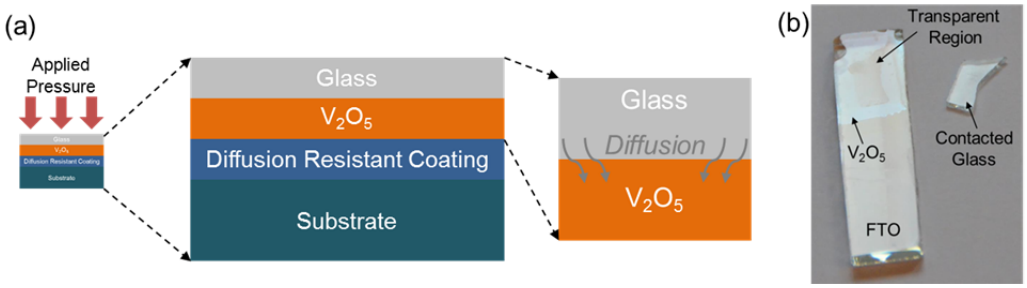


Figure 7.1. (a) Schematic of deposition technique for contact diffusion inter-diffusion process. (b) Optical image of a V_2O_5 thin film on FTO with a contact diffused area in the centre and the contacted glass used.

A schematic showing the deposition technique for contact inter-diffusion is shown in Figure 7.1 (a). Both the glass and V_2O_5 must be sufficiently clean to ensure a good contact between the two surfaces to enable inter-diffusion. A longer UV-O_3 cleaning step of 1 h is used to ensure that there is no residual organic matter left on either surface. A contact diffusion formed transparent region in the centre of a single layer of V_2O_5 on an FTO substrate is shown in the optical image of Figure 7.1 (b). The contacted glass had a distinctive shape, which is evident on the surface of the V_2O_5 thin film after the inter-diffusion processes occurred during thermal treatment. As will be shown, this transparent region comprises the V-O-Na-Si transparent phase. The transparent region was formed during a 72 hours thermal treatment at 300 ^{o}C. The long thermal treatment period was required to enable the contact diffusion process at this temperature. In the V-O-Na-Si thin films prepared in the previous chapter, the 300 ^{o}C temperature for 12 h was sufficient for the inter-diffusion to occur due to the conformal interface between the glass and the thin film as a result of the dip-coating deposition. In the contact inter-diffusion process a greater thermal

energy or longer treatment time is required to allow diffusion across the interface between two surfaces.

7.3.2 Surface Morphology and Vibrational Spectra

The surface morphology of both the FTO substrate and a dip-coated V_2O_5 thin film on the surface is shown in Figure 7.2 (a), the SEM settings (working distance, contrast and accelerating voltage) were kept consistent during acquisition of both images. The FTO substrate has a granular morphology, but is conformally covered by the dip-coated V_2O_5 thin film. Secondary electron intensity from the underlying FTO substrate means the FTO grains are visible through the V_2O_5 thin film in Figure 7.2 (a) similar to the effect on Au substrates shown in Figure 5.3. During the annealing the glass substrate is kept in contact with the V_2O_5 thin film shown in Figure 7.2 (a).

In Figure 7.2 (b) SEM images of the contact diffused transparent region from Figure 7.1 (b) are shown. The surface of the transparent region shows the formation of a nanowire mesh morphology. The nanowires are spread across the surface of the transparent region in different concentrations. The outer areas of the transparent region have the highest concentration of nanowires while the inner regions have a lower concentration. Surface SEM images of the inner and outer regions are shown in Figure 7.2 (b) and a larger image of the nanowire mesh is provided in Figure 7.2 (c), which indicated a relatively uniform coverage of long nanowires with random orientation across the surface.

The Raman scattering spectra for the V_2O_5 and transparent regions is shown in Figure 7.2 (d). For comparison, the Raman spectra of the V-O-Na-Si vibrational

modes for the TTF formed directly on a glass substrate is included in Figure 7.2 (d). As expected, the initial dip-coated V_2O_5 thin film forms the characteristic orthorhombic crystal structure expected from V_2O_5 (*cf.* Chapters 4 and 6). The transparent region shows the formation of the characteristic vibrational modes for the V-O-Na-Si material which originate from the α-$NaVO_3$ phase. However, the modes are shifted from 918 cm^{-1} and 955 cm^{-1}, to 925 cm^{-1} and 951 cm^{-1} respectively. These shifts are attributed to size and stress effects on the crystalline α-$NaVO_3$ phase that forms within the glassy matrix.

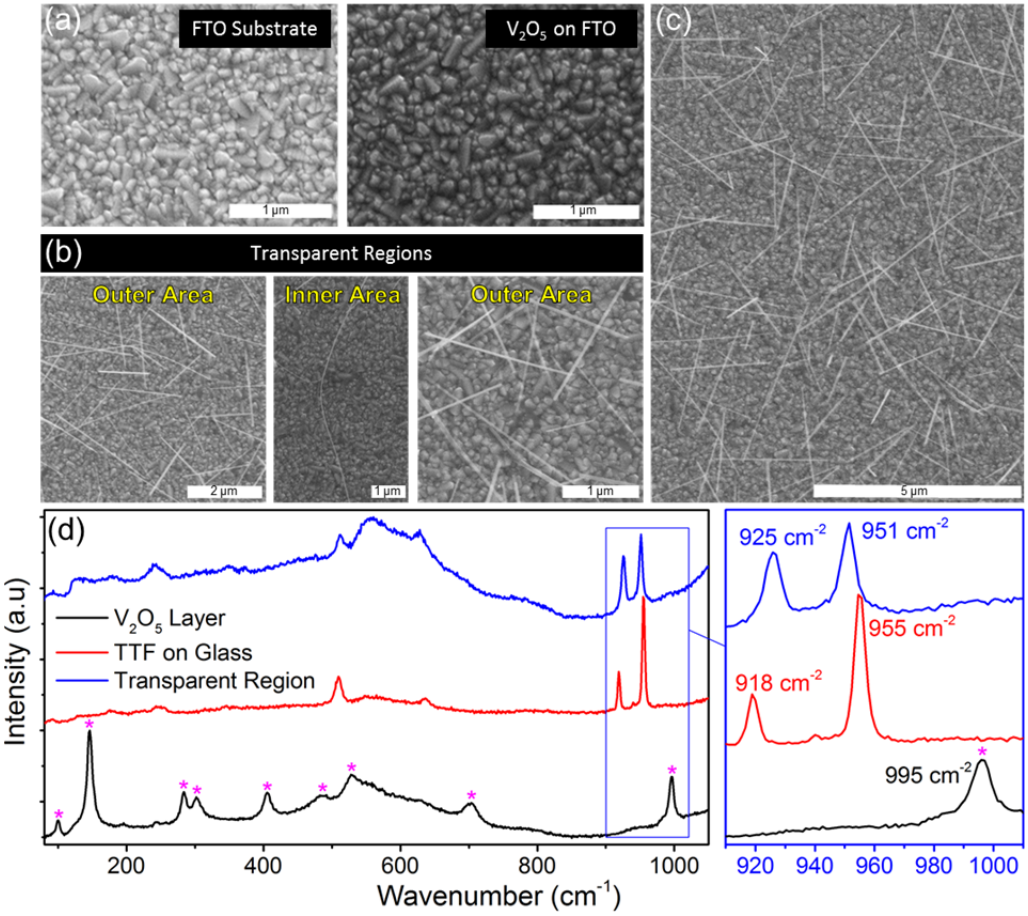


Figure 7.2. SEM images of the (a) FTO substrate and V_2O_5 thin film. (b) SEM images showing the nanowire mesh morphology of the inner, outer and inner regions of the transparent contact diffusion region. (c) Larger SEM image of the nanowire mesh morphology of transparent region for a contact diffused film showing the uniformity of the nanowires. (d) Raman scattering spectroscopy of V_2O_5 thin film and a TTF formed on glass compared to the spectra of the transparent region formed through contact diffusion showing the formation and shifting of characteristic vibrational modes for both materials.

The red and blue shifting of the 918 cm^{-1} and 955 cm^{-1} to 925 cm^{-1} and 951 cm^{-1} modes respectively may be due to effects such as compressive/tensile stresses or the increase or decrease of the crystalline structure size. The red and blue shifting of the major Raman vibrational mode due to tensile and compressive respective stresses was measured by Dombrowski *et al.* for silicon nanostructures.[10] Similarly, the formation of 1D nanowires and the associated decrease in size can cause a red-shift in the characteristic modes due to phonon confinement effects and scattering as found for other nanowire systems.[11-12] The shifting of the Raman modes can be due to a number of factors such as stress and changes to crystal size which alter the length of the vibrational bonds.

An alternative contact diffusion experimental procedure involving thicker dip-coated V_2O_5 films was performed in order to alleviate some of the effects mentioned above in the material that formed from a single (~10 - 15 nm) V_2O_5 layer annealed at 300 ^oC for a long period of time (72 h). The thickness of the VO layer was increased to ~30 nm by dip-coating 3 layers in succession. The thicker VO layer ensures a larger amount of V species is available for the formation of the nanowires. The annealing temperature was also increased to 450 ^oC and the annealing time decreased to 6 h. The higher annealing temperature allows for a shorter processing time thus decreasing the amount of time that the samples must be stressed.

The morphology of the transparent region for a contact diffused sample with a 3 layer (~30 nm) thick V_2O_5 thin film thermal treated at 450 ^oC for 6 h is shown in Figure 7.3. The SEM figure in Figure 7.3 (a) shows the large nanowire mesh coating that forms on the surface of the outer transparent region. The inset in Figure 7.3 (a) is a magnified view of the nanowire mesh. Nodes are apparent on the surface of the nanowire mesh and a higher SEM magnification of these nodes is shown in Figure

7.3 (b). Nanowires radially spread from a centre mass within these nodes resulting in a larger localised nanowire concentration. Formation of the nodes is attributed to the presence of a defect or raised region on the V_2O_5 thin film where the nanowires radially grew from due to a localised change in the pressure with the donor glass substrate. However, the overall deposit shows a very high and relatively uniform dispersion of nanowires on the TCO surface, each composed of the mixed metal oxide transparent phase.

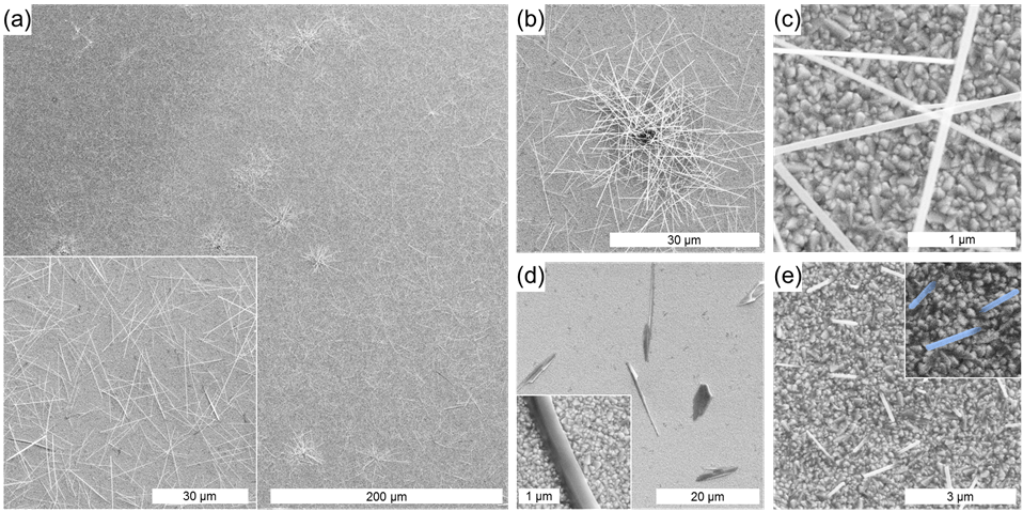


Figure 7.3. SEM images of the surface of a transparent region formed on a 3 layer thick V_2O_5 thin film thermally treated at 450 ^oC for 6 hrs. SEM images of (a) high concentration region of nanowires with presence of nanowire nodes, (b) zoomed in image of a nanowire node and (c) higher magnification image of nanowires. SEM images from the inner area of the transparent region showing (d) large ribbon/shard structures and (e) rods formation.

A higher magnification SEM image of the nanowires is shown in Figure 7.3 (c). The nanowires have a uniform morphology and appear to be ribbon shaped with a larger nanowire diameter than nanowire thickness. The fibrous morphology of the nanowires is common in both vanadium oxide nanomaterials[13] and $NaVO_3$ structures.[14] The V-O-Na-Si material formed through the contact diffusion process

may be predisposed to forming ribbon like nanowires due to the influence of the VO and $NaVO_3$ materials, which can explain the nanowire morphology.

In Figure 7.3 (d, e) SEM images of areas within the centre of the contact diffusion-formed transparent region are shown. In these areas the formation of larger shards surrounded by regions of smaller rods of the V-O-Na-Si material can be seen on the surface. Seeded growth of nanowires is a commonly used method for the preparation of meshes[15]; in this case the VO grains discussed in Chapter 4 may act as the seeds for the inter-diffusion process since they conformally coat the granular FTO substrate. The granular FTO surface may facilitate formation of the nanostructures as there are small spaces between the granular substrate and contacted glass to allow the growth of the nanowires from the V_2O_5 grains. Shown in Figure 7.3 (e) and highlighted with false colour images in the inset, the tail of the rods can be seen protruding from the surface of the thin film suggesting that their formation is seeded from the surface and continue to grow through continued contact with the glass substrate which supplies the required Na and Si diffusion species.

Raman scattering spectroscopy was used to examine the different regions on the surface of the transparent region. Raman vibrational spectra for two different regions of the transparent sample are shown in Figure 7.4 (a) with orthorhombic V_2O_5 as a comparison. The formation of the 954 cm^{-1} and 918 cm^{-1} modes indicative of α-$NaVO_3$ are present in the Raman spectra.[16-17] There is no evidence of shifting due to stress and size effects as found in the 10 – 15 nm initial VO thin film thickness samples formed at 300 ^oC. The formation of the characteristic Raman modes implies that the thicker 30 nm V_2O_5 thin film coupled with a shorter and higher temperature thermal treatment (450 °C for 6 h) forms the same V-O-Na-Si phase containing α-$NaVO_3$ as discussed in Chapter 6.

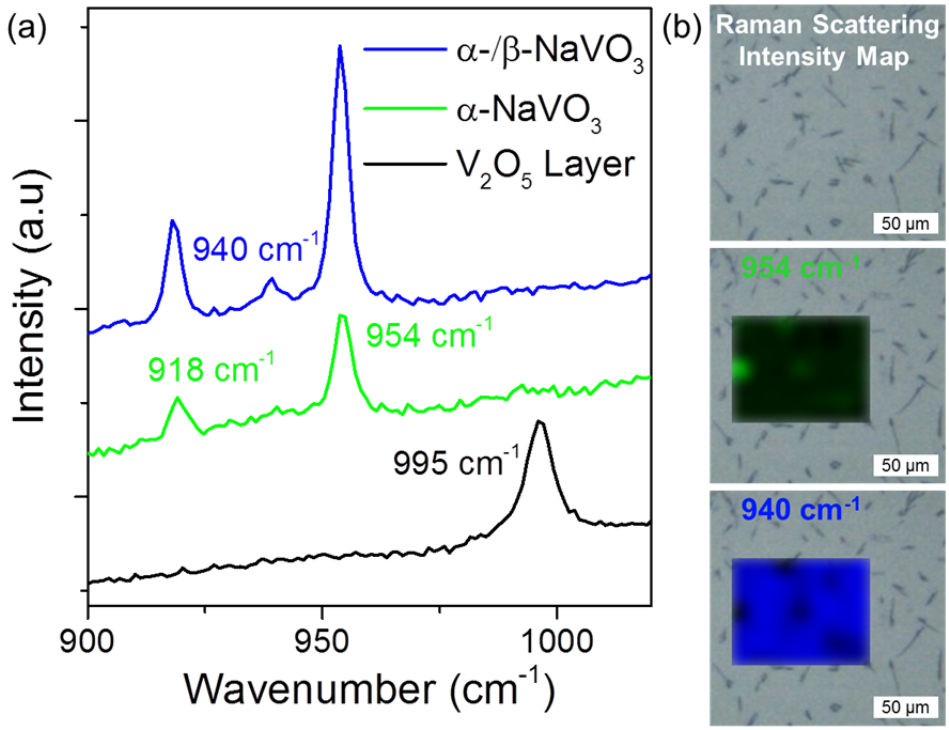


Figure 7.4. (a) Raman scattering spectra of V_2O_5 thin film and two different areas of the transparent region showing evidence of the formation of α-$NaVO_3$ within the nanowires. The presence of the 940 cm^{-1} is also shown in certain areas which are indicative of traces of β-$NaVO_3$ being present. (b) Raman scattering spectroscopy intensity map of the centre of the transparent region showing the areas where the 954 cm^{-1} and 940 cm^{-1} modes increase in intensity.

The presence of a secondary vibrational mode at 940 cm^{-1} in the blue spectra of Figure 7.3 (a) is attributed to the presence of β-$NaVO_3$ in the nanowires[14, 16-17] at specific areas within the transparent region surface. Using Raman intensity mapping of the 940 cm^{-1} (corresponding to β-$NaVO_3$) and 955 cm^{-1} (corresponding to α-$NaVO_3$) modes, shown in Figure 7.3 (b), an area within the inner part of the transparent region was scanned and 2D x-y intensity maps at each wavenumber of interest across the surface was acquired. The 955 cm^{-1} vibrational mode is found primarily in the larger shards while the intensity of the 940 cm^{-1} mode is higher in the areas between these shards.[16-17] The areas containing the shards and rods was the same as those shown in Figure 7.3 (d, e).

It is known from investigation of these phases in mineral deposits, that the formation of α-$NaVO_3$ occurs at higher temperatures after β-$NaVO_3$ is formed.[16] On the nanoscale, the regions that show spectroscopic evidence of β-$NaVO_3$, such as the rods, may be due to the nanowires having insufficient thermal energy to further undergo diffusion and form α-$NaVO_3$ nanowires. The stunted growth of the β-$NaVO_3$ rods compared to the long α-$NaVO_3$ nanowires found on the outer regions of the transparent regions may be due to a non-uniform pressure gradient across the contact diffusion site.

7.3.3 HRTEM of Contact Diffusion V-O-Na-Si Surface

In order to determine the structure and morphology of the nanowires formed through the contact diffusion mechanism, thin films of VO were dip-coated onto the surface of Si_3N_4 TEM grids as previously shown in Chapter 4. The VO coated Si_3N_4 TEM grids were annealed at 450 ^oC for 6 h contacted to a cleaned glass piece. After annealing, the surface of the Si_3N_4 TEM grids were examined using Raman scattering spectroscopy and HRTEM.

A low magnification HRTEM image of the nanowires and structures formed on the surface of the Si_3N_4 TEM grids is shown in Figure 7.5 (a). The HRTEM image shows the surface contains large quantities of nanowires and other nanostructured materials, such as shards and sheets. The presence of different morphologies of nanowires and structures is attributed to the contact diffusion mechanism affected by the smooth Si_3N_4 surface compared to the granular FTO in earlier experiments, and may also as a result of flexure in the 10 nm thick Si_3N_4 free-standing substrate. Any flex would prevent consistent areal pressure to the contacted

glass piece. A long nanowire is shown in the HRTEM image of Figure 7.5 (b). The interior of the nanowire is darker denoting a denser inner surface while the surrounding material is less dense. This type of deposit can be seen in many areas of the low magnification image of Figure 7.5 (a). This structure may be a composite of the V-O-Na-Si materials that are formed during the contact diffusion process and may not have fully formed the desired α-$NaVO_3$ or β-$NaVO_3$ phase. The structure is similar to that seen for core-shell nanowires with amorphous or less dense coatings of an inner structure.[18-20]

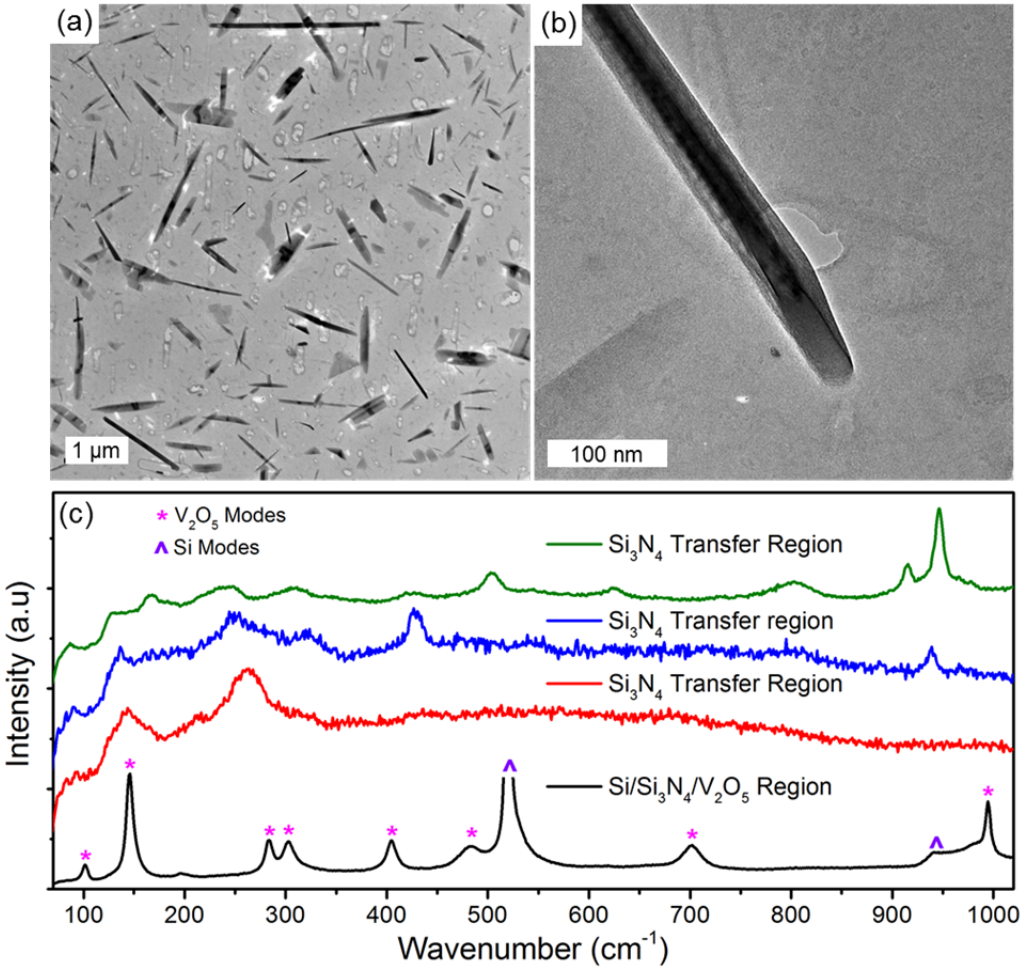


Figure 7.5. (a) Low magnification HRTEM image of the nanostructures formed on a contact diffused surface deposited on a Si_3N_4 TEM grid. (b) HRTEM image of a nanowire displaying a dense interior. (c) Raman scattering spectra of contact diffused transfer sections showing the formation of the vibrational modes for V_2O_5 on Si and those corresponding to V-O-Na-Si materials.

Raman scattering spectroscopy was performed on the contact diffused Si_3N_4 TEM grids after annealing and the spectra are shown in Figure 7.6 (c). The Raman scattering spectra from various regions on the surface show the formation of orthorhombic V_2O_5 on top of Si, in the non-windowed areas of the substrate. In the Si_3N_4 free-standing window regions, evidence of different vibrational modes is found. Raman vibrational modes corresponding to the formation of the β-$NaVO_3$ phase is shown in the green spectra of Figure 7.5 (c) while the other spectra show the formation of neither orthorhombic V_2O_5 nor α-/β-$NaVO_3$.

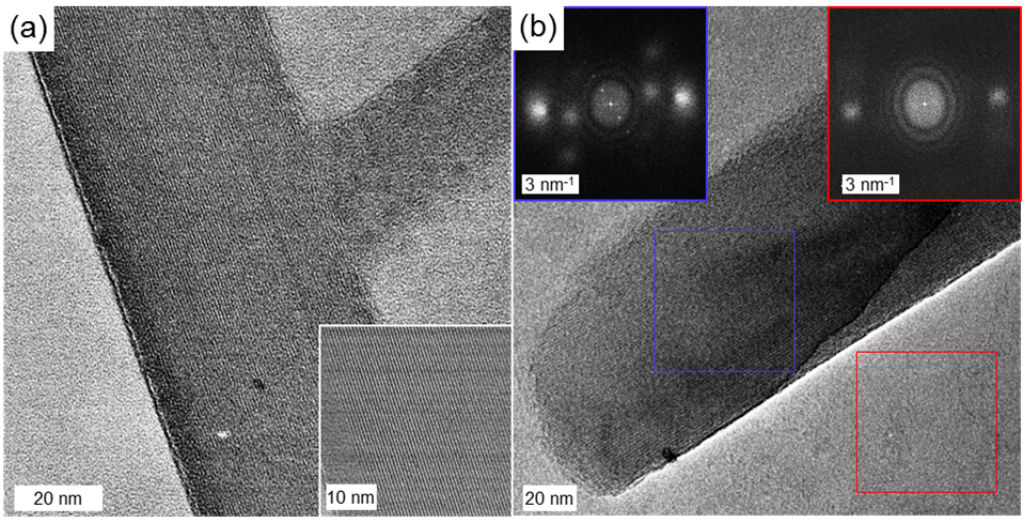


Figure 7.6. HRTEM images of two nanostructures showing formation of a single crystalline structure. The insets of (b) show the FFT diffraction pattern of the indicated regions.

To further analyse the nanowires formed on the surface of the Si_3N_4 TEM grids, regions exhibiting crystallinity were studied with two such nanowire structures shown in Figure 7.6. The two nanowires shown in Figure 7.6 show the diffraction from crystal planes which are indicative of single crystal structures. In Figure 7.6 (b), the Si_3N_4 substrate contributes an amorphous/polycrystalline diffraction pattern as shown in the indicated inset. The crystalline d-spacing for the nanowire in Figure 7.6 (a) is 0.6494 nm while the d-spacing of Figure 7.6 (b) shows a larger value of 1.205

nm which do not match up to known $NaVO_3$ d-spacings. The TEM analysis of the nanowires formed through the contact diffusion process shows the formation of crystalline structures.

Both the Raman scattering spectroscopy and HRTEM analysis performed on the contact diffused nanowires formed on Si_3N_4 TEM grids were inconclusive for the exact phases present of the structures. Further testing and analysis will be required for utilising the planar TEM deposition technique to analyse the nanostructures as the fragility of the Si_3N_4 TEM grids may have impacted upon the amount of pressure exerted on the glass contacted VO thin film thus altering the formation of desired V-O-Na-Si phase structures.

The contact diffusion mechanism for transfer doping of thin films between a V_2O_5 thin films on diffusion barrier layer and, and a borosilicate glass substrate source demonstrates the capability of utilising the inter-diffusion mechanism discussed in chapter 6, and surface roughness nucleation sites to form nanowire network morphologies of V-O-Na-Si transparent materials. Thin film morphologies utilising nanowire structures are used for applications in photovoltaics[21], TCOs[22-23], sensors[24] and optical coatings.[25] These materials are deposited in a variety of ways while the inter-diffusion technique outlined in this section demonstrates the capability of nanowire formation through the mechanical contacting of a donor material. This technique can potentially be expanded to other materials and diffusion products: through the ion-exchange of Na with Li in borosilicate glass[26] it may be possible to encourage the formation of Lithium-intercalated V_2O_5 for use in applications such as thin film batteries.

7.4 Planar Electrodeposition Formation of Na-SiO_2 and V-Na-SiO_2

Conductive substrates can be coated with a range of materials using electrodeposition. The electrodeposition process used in this chapter was adapted from a technique outlined by Walcarius *et al.* for the deposition of mesoporous SiO_2 thin films on a range of substrates.[27] The process involves the electrochemical generation of OH^- groups at the surface of the substrate through the application of a constant negative voltage across the cell.[27-28] The generation of OH^- groups at the surface of the substrate facilitates the hydrolysis and polycondensation of the TEOS depositing a solid thin film of SiO_2 material.[29-31] Two types of planar thin films were deposited by electrodeposition. The first deposition was a Na-SiO_2 mixture where Na was added to the TEOS-based electrolyte with a $NaNO_3$ salt additive. The resulting electrodeposited thin film was analysed using XPS and is composed of predominantly SiO_2 with some Na species present. The second electrodeposition thin film formed contained only SiO_2, without any $NaNO_3$ added to the electrolyte. SEM analysis of the resulting Na-SiO_2 and SiO_2 electrodeposited films shows a rough surface morphology. Subsequent coating with VO through dip-coating and annealing can form a phase of the V-O-Na-Si material through interdiffusion processes. The influence of sodium in the inter-diffusion process was determined through analysis of the two types of thin film depositions.

7.4.1 Effect of Electrodeposition Voltage on Structure and Vibrational Characteristics

For a planar electrodeposited Na-SiO_2 deposition on an FTO substrate, chronoamperometry was used at a constant applied voltage with the corresponding

current monitored over time. The applied current versus time profile for a planar Na-SiO_2 deposition at applied voltages of -2.5 V and -4 V for 10 s is shown in Figure 7.7 (a). After the constant negative electric potential is applied the electrodeposition current was found to decrease over time. The maximum current for the planar Na-SiO_2 deposition at -4 V is higher than that for the same deposition at -2.5 V. There is also a variation in the electrodeposition current vs. time profile between depositions at either applied voltage. The variations in the current vs. time profile between the two applied voltages in the 0.35 s – 2.85 s regions is attributed to the increased Faradaic processes at the substrate surface due to the differences in applied potential. After an initial rapid change in current, the reaction rate (current) increases slightly and thus film growth (as measured by the cumulative total charge passed) increases in time. Analysis of the total charge (Q_{Total}) for both applied voltages shows that the higher -4V applied voltage increases the total charge of the system from 0.10358 C to 0.10478 C. The increase of the applied voltage past -2.5 V did not result in a substantially larger charge through the system.

The electrodeposited Na-SiO_2 films were dip-coated with VO using the 1000:10:1 (IPA:Alkoxide:H_2O) precursor solution and subsequent annealing formed a V-Na-SiO_2 thin film through interdiffusion processes. The optical images in Figure 7.7 (b) show the as-deposited and thermal treated Na-SiO_2 and V-Na-SiO_2 thin films deposited at -2.5 V and -4 V potentials, respectively. The lower half of both of the thin films was coated with VO to form a staggered Na-SiO_2/V-Na-SiO_2 multi-layered deposit. After thermal treatment the interdiffusion V-Na-SiO_2 material forms on the lower surface of the thin films. Interdiffusion of the VO is seen in the optical images after thermal treatment through the optical clearing of the coated areas. The optical images in Figure 7.7 (b) show that the overall surface coverage of the Na-

SiO_2 films deposited at -2.5 V is superior to those of the films deposited at -4 V under identical deposition times in a similar electrolyte. In the Na-SiO_2 thin film deposited at -4 V, the outer edges of the FTO substrate are not coated while in the film deposited at -2.5 V the FTO surface is uniformly coated.

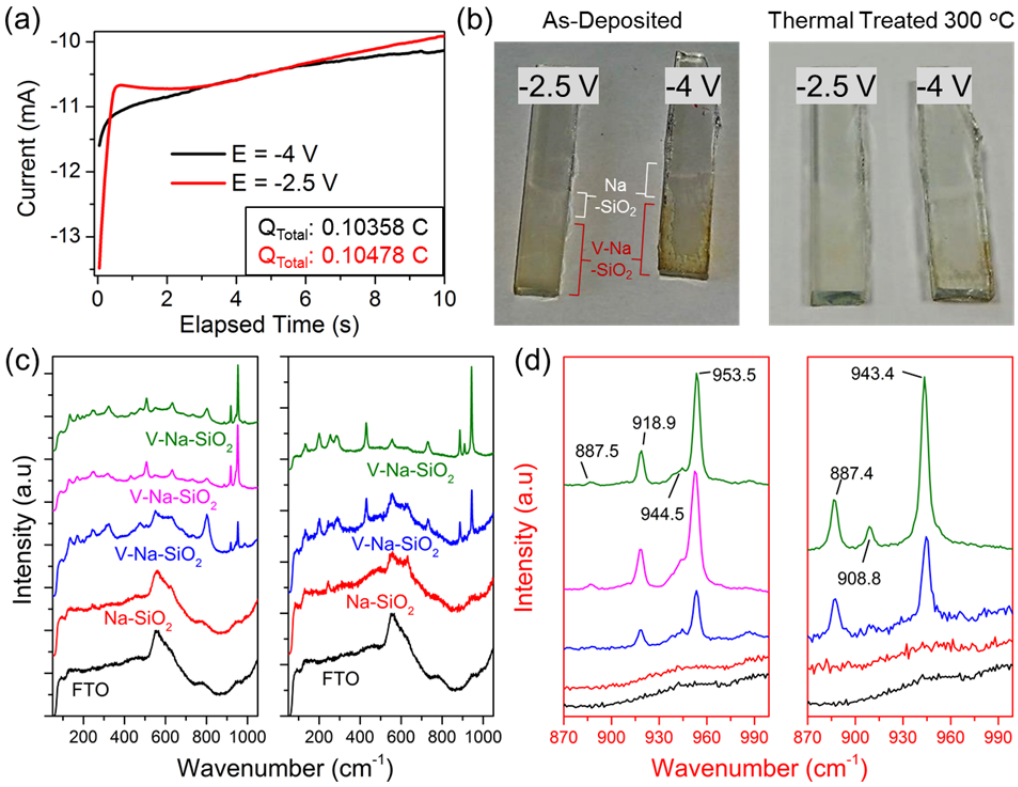


Figure 7.7. (a) Electrodeposited current over time profile for planar deposition of Na-SiO_2 and V-Na-SiO_2 on FTO at an applied voltage of -2.5 V and -4 V. The value for total charge is given for each applied voltage. (b) Optical images of as-deposited and heated electrodeposited Na-SiO_2 films with a 1 cm long dip-coated VO thin film. Raman scattering spectroscopy of (c) FTO, Na-SiO_2 and V-Na-SiO_2 films after thermal treatment at 300 ^oC for films electrodeposited at -2.5 V and -4 V. (d) Same Raman spectra as (c) zoomed into the 870 cm^{-1} - 1000 cm^{-1} wavenumber range.

The Raman scattering spectra for the thermally treated samples deposited at -2.5 V and -4 V is presented in Figure 7.7 (c, d) respectively. The Raman spectra for the FTO, Na-SiO_2 and V-Na-SiO_2 regions are shown where different characteristic peaks are evident in both samples. The Na-SiO_2 vibrational modes in the -4 V deposited Na-SiO_2 layer are more distinct with a higher intensity compared to the

background FTO spectrum than those of the -2.5 V deposited Na-SiO_2 layer. The higher electrodeposition voltage increases the packing and thickness of the Na-SiO_2 layer and therefore the sensitivity to the respective vibrational modes increases.

Different V-Na-SiO_2 characteristic vibrational modes for the films deposited at -2.5 V and -4 V are shown in the spectra of Figure 7.7 (c, d) each corresponding to either α-$NaVO_3$ or β-$NaVO_3$. The 887.4 cm^{-1} mode is present in both deposits and the other prominent α-$NaVO_3$ or β-$NaVO_3$ modes appear depending upon the Na-SiO_2 deposition voltage. The most prominent high wavenumber modes for the V-Na-SiO_2 film deposited at -2.5 V is 918 cm^{-1} and 953 cm^{-1} respectively. These two modes are characteristic of α-$NaVO_3$. The characteristic modes for the V-Na-SiO_2 film deposited at -4 V shows the vibrational modes for β-$NaVO_3$ at 908 cm^{-1} and 943 cm^{-1}.

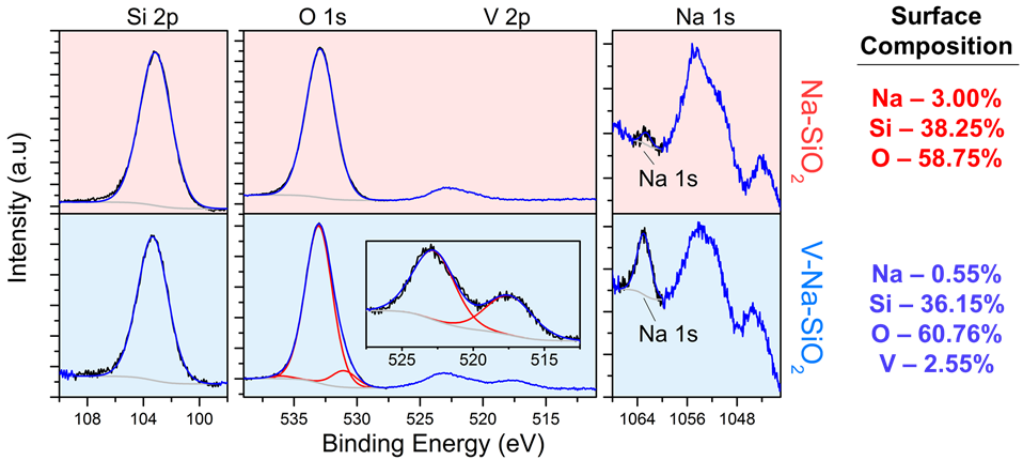


Figure 7.8. XPS spectrum for the Na-SiO_2 and V-Na-SiO_2 thin films showing the binding energies for the Si 2p, O 1s, V 2p and Na 1s peaks. The Auger peaks for SnO_2 and Sn are located at ~1055 eV and 1046 eV respectively and are attributed to areas of the FTO substrate being visible to the X-Ray spot. Surface composition was calculated from the survey XPS spectrum for Na, Si, O and V.

The X-ray photoelectron spectra from the Si 2p, O 1s, V 2p, Na 2p and Na 1s core-levels for both Na-SiO_2 and V-Na-SiO_2 thin films deposited at -2.5 V is

presented in Figure 7.8. There is no change to the Si 2p peak at 103.2 eV after the formation of the Na-SiO_2 material, which is to be expected due to the large amount of Na-SiO_2 present and low concentration of VO deposited on the surface. The O 1s peak has an extra shoulder contribution at 530.9 eV which is attributed to the formation of α-$NaVO_3$ on the surface through inter-diffusion processes. The V 2p peak is located at 517.7 eV correlates to the binding energy for V in $NaVO_3$.[32] Interestingly, the Na 1s increases in intensity after the inter-diffusion process occurs. The increase in the Na 1s is attributed to the diffusion of Na from within the Na-SiO_2 film to the surface for the formation of the V-Na-SiO_2 material.

Surface composition analysis using the XPS survey spectrum shows that the surface prior to VO deposition is composed of 3% Na, 38.25% Si and 58.75% O. Assuming that areas of the FTO substrate is in view of the X-ray beam due to the presence of the Sn and SnO_2 Auger peaks in Figure 7.8, the contribution of the bonded O species for FTO increases the percentage of O in the composition calculation. As the Si 2p peak is referenced to SiO_2, the assumption that Na species is deposited within the SiO_2 material leads to an estimation of the electrodeposited material to be $Na_{0.1}SiO_2$. After dip-coating and annealing, the Na species within the $Na_{0.1}SiO_2$ thin film inter-diffuses with the VO forming the V-Na-SiO_2 material.

The formation of α-$NaVO_3$ and β-$NaVO_3$ from -2.5 V and -4 V initially electrodeposited Na-SiO_2 thin films may be due to the effect of the electrodeposited surface during the annealing step. The formation of the α-$NaVO_3$ phase was investigated by Seetharaman *et al.* who showed that the initial β-$NaVO_3$ undergoes a phase change to α-$NaVO_3$ after thermal treatment at 420 ^oC and above.[16] This phase change occurs in the case of deposition at -2.5 V, but not for Na-SiO_2 films deposited at -4 V. The denser Na-SiO_2 material at -4 V may inhibit the inter-

diffusion of Na by increasing the diffusion distance and therefore halting the phase change from β-$NaVO_3$ to α-$NaVO_3$. As the formation of α-$NaVO_3$ is facilitated at electrodeposition voltages of -2.5 V for the planar depositions with little change to the total charge of the electrodeposition, the use of this voltage was chosen for preparing the Na-SiO_2 thin films for further study and analysis.

7.4.2 Thin Film Morphology of Na-SiO_2 and V-Na-SiO_2 Thin Films

The surface morphology of the Na-SiO_2 and V-Na-SiO_2 thin films deposited by electrodeposition at -2.5 V was studied due to the formation of the α-$NaVO_3$ phase after thermal treatment. The surface morphologies for planar Na-SiO_2 and V-Na-SiO_2 thin films was examined using top down and cross-sectional SEM microscopy. The cross-sectional SEM was performed at an incident angle of 45^o and allowed for the side profile of the deposits to be examined and the thickness to be approximated. A 45^o incident angle was chosen due to the difficulty in obtaining an SEM image at 0^o incident angle due to the high thickness (3 mm) of the non-conductive glass substrate beneath the FTO.

An SEM image of a clean FTO surface is shown in Figure 7.9 (a). The transparent FTO has a granular surface morphology with a thickness of ~350 nm. Both top down and 45^o angled surface images of an electrodeposited Na-SiO_2 thin film deposited at -2.5 V for 10s after thermal treatment is shown in Figure 7.9 (b-d). The surface morphology of the electrodeposited Na-SiO_2 film shows a surface composed of spherical particles, presumably the $Na_{0.1}SiO_2$ mixture. The SEM images (Figure 7.9 (c, d)) show that the thickness of the Na-SiO_2 thin films is larger than that of the dip-coated V_2O_5 thin films presented in the previous chapters. An

estimated thickness of ~500 – 800 nm is determined from the SEM images for the Na-SiO_2 thin films. Interestingly, SEM images show that the Na-SiO_2 thin film has a smooth uniform morphology under the spherical particles located on the surface. This initial compact layer coats the entire surface prior to the more granular top surface being formed.

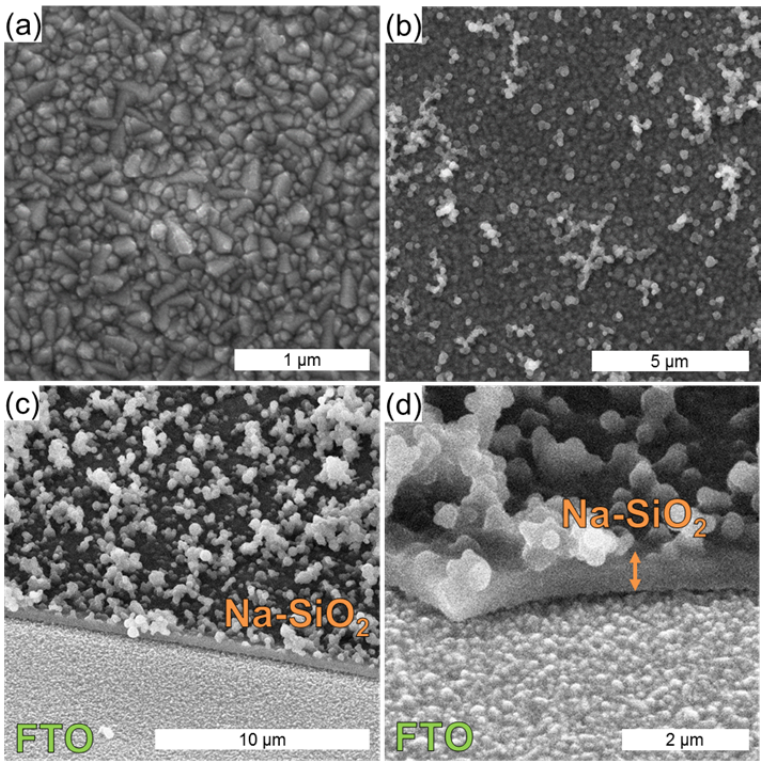


Figure 7.9. SEM images of (a) FTO substrate and (b – c) electrodeposited Na-SiO_2 film.

SEM images of V-Na-SiO_2 after thermal treatment is shown in Figure 7.10 (a-d). A surface morphology similar to those of the Na-SiO_2 thin films is seen which implies a conformal coating of VO is applied when forming V-Na-SiO_2. In Figure 7.10 (d) a coating is apparent on the particulate surface which is attributed to the formation of the V-O-Na-Si related material through inter-diffusion between the Na-SiO_2 and VO thin films. The role of the VO in the formation of the V-Na-SiO_2 thin

films does not have a noticeable effect on the resulting thin film thickness as evidenced in a comparison between both Figure 7.9 (d) and Figure 7.10 (d).

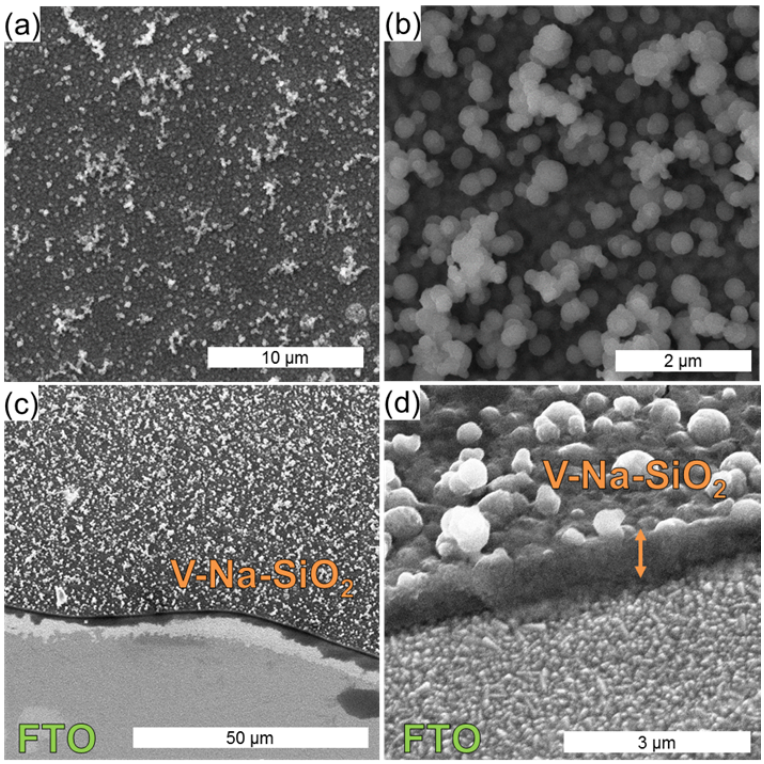


Figure 7.10. (a – d) SEM images of electrodeposited V-Na-SiO_2 film after thermal treatment.

The implications for inter-diffusion processes that do not detrimentally alter the initial surface will be of use for applications in nanoelectronic and optical devices where tight constraints on surface defects are required. The inter-diffusion process may in future be applied for the localised doping of materials and surfaces through either the application of contact diffusion or pre-depositing as demonstrated in the previous and current section respectively. By utilising pre-doped[26] or other such glasses and materials, it may be possible to expand the inter-diffusion process to a variety of dopants and metals for use in a range of thin film applications and devices.

7.5 Planar Electrodeposition Formation of SiO_2 and V-SiO_2

To ascertain the effect of Na species on the V-O-Na-Si inter-diffusion materials, thin films composed with only Si and O were deposited. The SiO_2 thin films were deposited using electrodeposition with the same electrolyte where no $NaNO_3$ salt was added. Electrodeposition was employed to form SiO_2 thin films which were subsequently dip-coated with VO to form a V-SiO_2 composite material. The electrodeposition voltage was kept in line with the Na-SiO_2 depositions at -2.5 V but the deposition time was increased in order to form thicker SiO_2 thin films on the surface of the FTO substrates as the $NaNO_3$ within the electrolyte affected the deposition rate. Annealing was performed as in the Na-SiO_2 case at 300 ^{o}C for 12 hours in a conventional oven. Raman scattering spectroscopy and SEM analysis methods were employed for determining the effect of the Na species on the formation of V-O-Na-Si based materials from contact transfer diffusion doping.

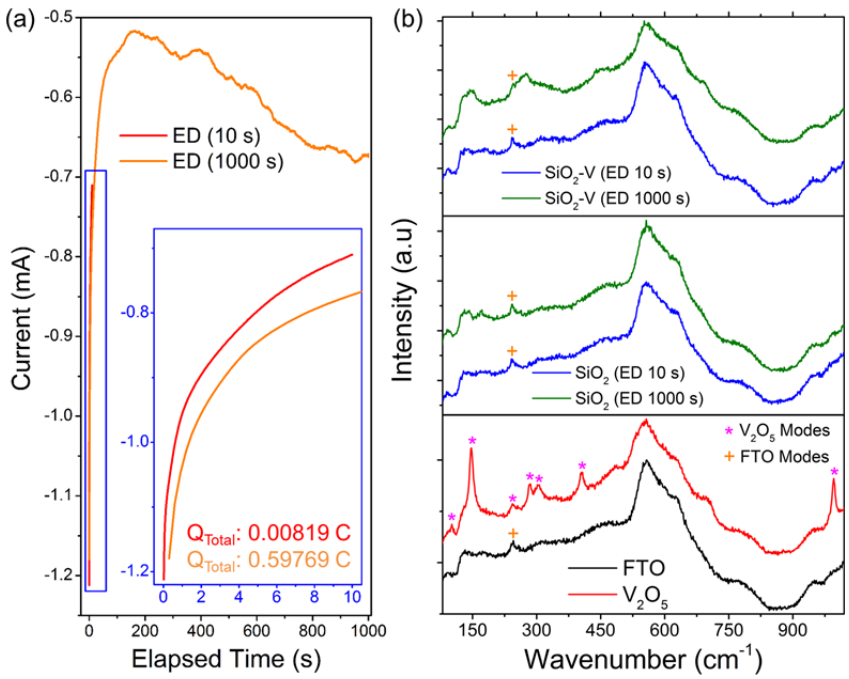


Figure 7.11. (a) Electrodeposition current over time profiles for planar depositions of SiO_2 thin films on FTO at an applied voltage of -2.5 V and deposition times of 10 s and 1000 s. (b) Raman scattering spectroscopy of planar electrodeposited depositions of SiO_2 and V-SiO_2 thin films after thermal treatment compared to FTO and orthorhombic V_2O_5.

In Figure 7.11 (a) the electrodeposition current over time profiles for planar depositions of SiO_2 thin films deposited at 10 s and 1000 s is shown. The two electrodeposited thin films have a similar current vs. time profile for the first 10 s. The total charge passed for the SiO_2 thin films electrodeposited for 10 s and 1000 s is 0.00819 C and 0.59769 C respectively. The total charge of the comparative 10 s Na-SiO_2 electrodeposition is two orders of magnitude larger than for SiO_2 electrodeposited over 10s. The longer deposition time was required for the SiO_2 compared to the Na-SiO_2 thin films due to the influence of the $NaNO_3$ within the electrolyte, such as alterations to the conductivity and pH, which can result in changes to the rate of OH^- production at the substrate interface required for the formation of a uniform thin film.[31]

Raman scattering spectroscopy was performed on the annealed SiO_2 and V-SiO_2 thin films deposited at 10 s and 1000 s to assess the vibrational mode structure of the V-O-Na-Si material from both electrodeposition growths. The role of Na in the inter-diffusion process was examined through analysis of the Raman scattering spectra of Figure 7.11 (b) and determining if the characteristic modes for the V-O-Na-Si inter-diffusion materials are present. Figure 7.11 (b) includes spectra of the vibrational modes of the FTO substrate and orthorhombic V_2O_5 to enable direct comparisons. The Raman scattering spectra for the SiO_2 and V-SiO_2 deposited at both 10 s and 1000 s do not show the formation of any of the characteristic modes for the V-O-Na-Si range of materials. However, the Raman spectra also do not show the formation of orthorhombic V_2O_5 which would be expected on the surface after annealing without the influence of inter-diffusion processes as shown in the red spectra of Figure 7.11 (b).

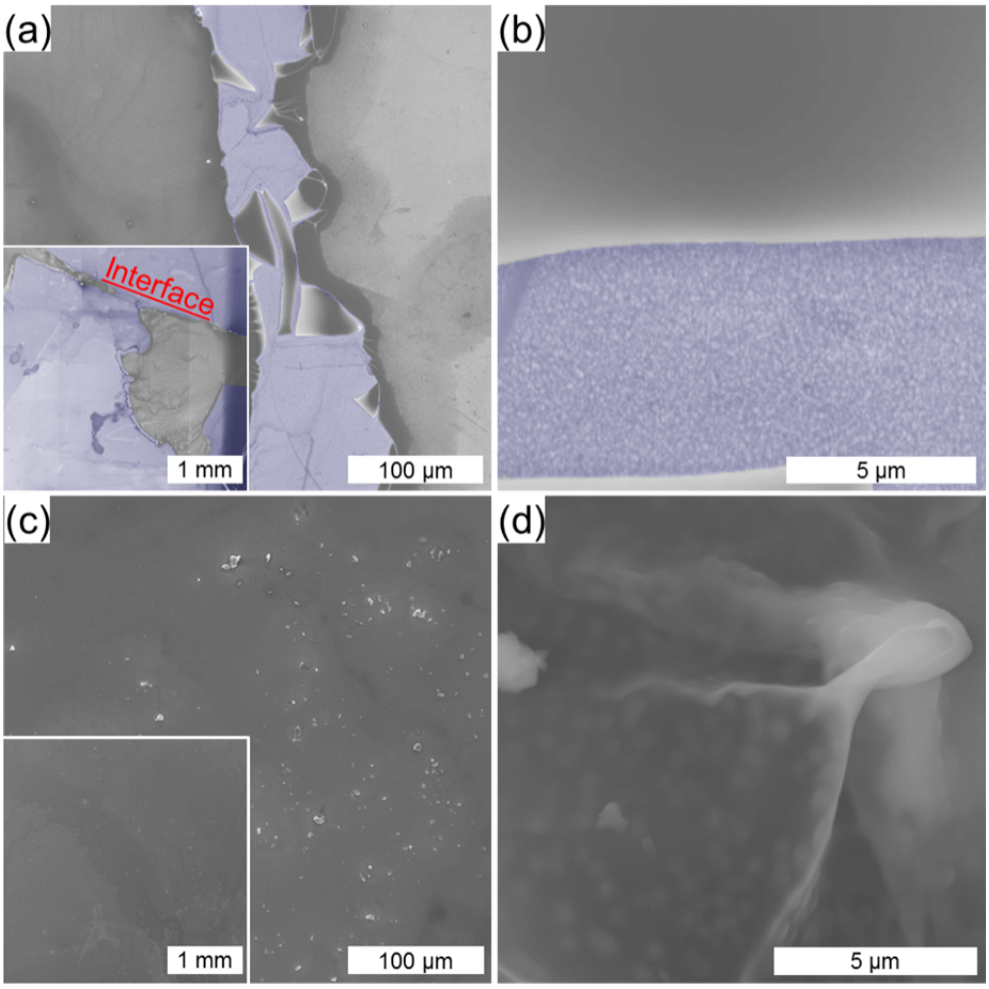


Figure 7.12. SEM images at different magnifications of planar as-deposited 10 s electrodeposited (a, b) SiO_2 and (c, d) V-SiO_2 thin films. (Blue regions highlight areas where uncovered FTO is seen)

To determine whether any morphological factors affected the formation of orthorhombic crystalline V_2O_5 on the surface of the SiO_2, SEM images of the samples before and after heating was obtained. SEM images of the as-deposited SiO_2 and V-SiO_2 thin films are shown in Figure 7.12 and Figure 7.13 for the thin films deposited at 10 s and 1000 s, respectively.

The SiO_2 thin films are shown in (a, b) and the V-SiO_2 thin films in (c, d) in both Figure 7.12 and Figure 7.13. The SiO_2 depositions at 10 s duration consist of non-uniform coatings with low surface coverage of the FTO substrate as shown in

Figure 7.12 (a, b). The electrodeposited film develops cracks and exposes the FTO substrate underneath (coloured in blue) upon drying, indicating a degree of internal porosity. The low magnification image in the inset of Figure 7.12 (a) shows the low surface coverage of the SiO_2 coating after 10 s electrodeposition time. The film formed after 1000 s exhibits greater surface coverage with a uniform morphology. Surface cracking is limited to be located close to the FTO/SiO_2 interface (Figure 7.13 (a, b)).

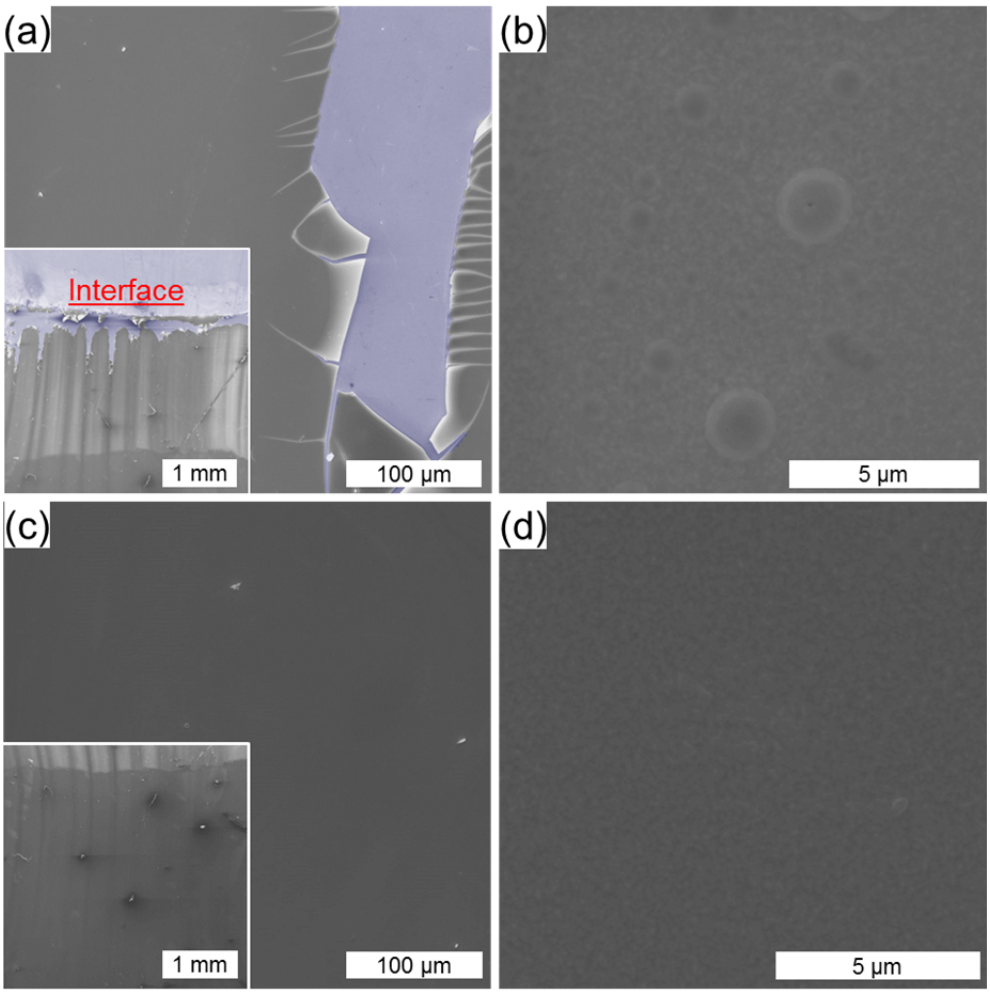


Figure 7.13. (a, b) SEM images at different magnifications of planar SiO_2 electrodeposited for 1000 s and (c, d) after coating with VO prior to annealing to form V-SiO_2. The higher surface coverage of the FTO substrate (blue regions) compared to the SiO_2 films electrodeposited for 10 s can be seen.

The V-SiO_2 coating deposited at 10 s is non-uniform and irregular due to the low surface coverage of the underlying SiO_2 as seen in Figure 7.12 (c, d). The SEM image in Figure 7.12 (d) shows the rough morphology of the as-deposited V-SiO_2 coating. By contrast, the as-deposited V-SiO_2 coating after 1000 s of growth shows a uniform surface morphology as shown in Figure 7.13 (c, d). The dip-coated VO thin film conformally coated the surface of the SiO_2 as previously discussed in Chapters 4, 5 and 6 describing VO coating of different substrates using the same technique.

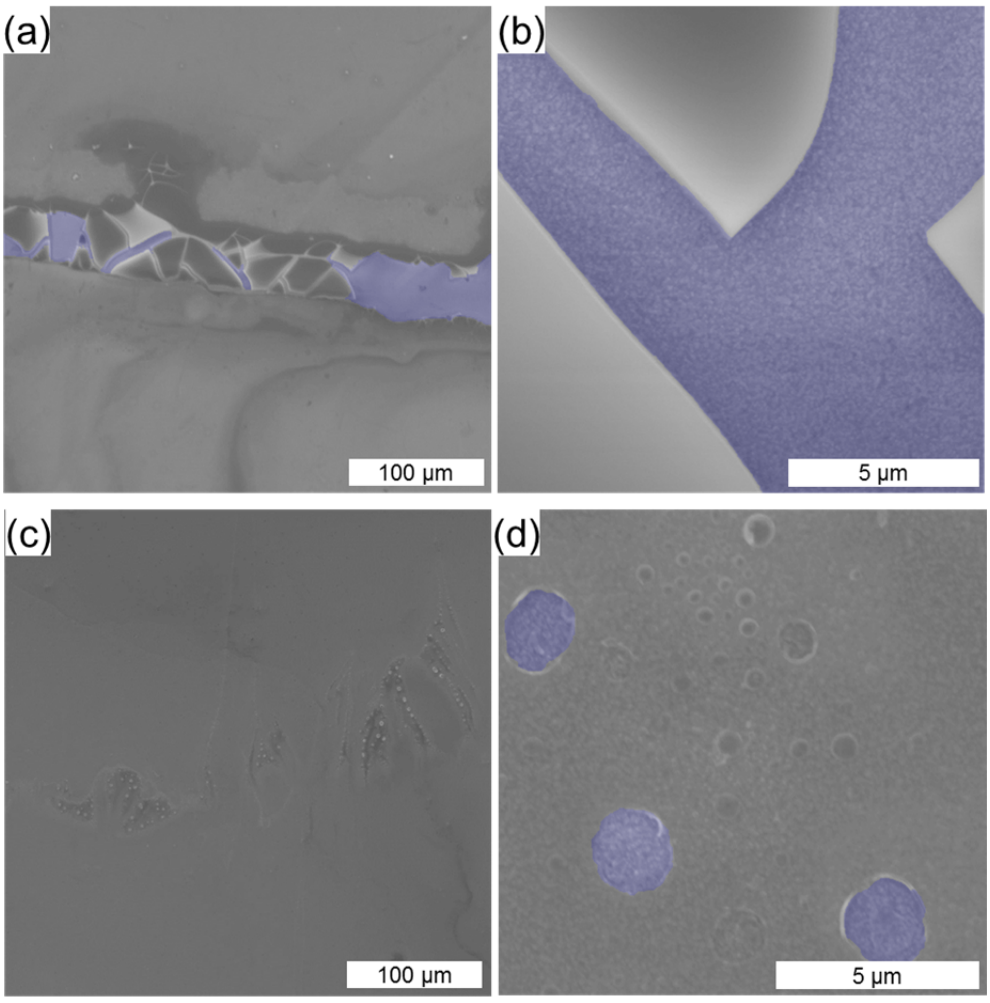


Figure 7.14. SEM images of planar annealed V-SiO_2 thin films formed from electrodeposited SiO_2 films deposited for (a, b) 10 s and (c, d) 1000 s. (blue areas denote FTO areas which are not coated in SiO_2)

SEM images of V-SiO_2 thin films deposited at 10 s and 1000 s formed after thermal annealing are shown in Figure 7.14 (a, b) and (c, d) respectively. For V-SiO_2 thin films formed in 10 s, the surface coverage after thermal treatment is low and the formation of the material is found only in regions where SiO_2 was deposited. The surrounding regions show the formation of orthorhombic V_2O_5 due to the lack of SiO_2 that facilitates inter-diffusion processes.

The V-SiO_2 thin films deposited at 1000 s have a smooth surface morphology as evidenced by the SEM images of Figure 7.14 (c, d). Small areas on the surface of the V-SiO_2 shows the presence of small 1 - 2 μm sized pinholes shown in Figure 7.14 (d). The pinholes mimic those examined previously on Au and ITO substrates but have a significantly larger average radius, 1.356 μm compared to 25.1 nm and 111.5 nm respectively for the Au and ITO substrates (see Chapter 5). The formation of the pinholes is attributed to regions on the SiO_2 electrodeposited thin film where the VO may not have adequately coated the surface resulting in pinhole formation from surface compaction of the thin films during thermal treatment.

The mass of the electrodeposited thin films can be calculated using the deposited materials density and Faraday's law where it is assumed that all of the charge is used for the formation of the thin film. The mass (m) can be calculated using:

$$m = \frac{\rho V_m Q}{2nF} \qquad \textit{(Eq. 7.1)}$$

where V_m is the molar volume of the electrodeposited material, n is the number of electrons transferred, Q is the charge and ρ is the density of the deposited material. In Figure 7.15 (a) a comparison of the charge vs. time and calculated mass vs. time for the Na-SiO_2 and SiO_2 electrodeposited thin films is shown. The V_m and ρ of the

Na-SiO_2 thin films was assumed to be the same as SiO_2 (V_m = 27.359 cm^3/mol, ρ = 2.62 g/cm^3) due to the low amount of Na species within the electrodeposited Na-SiO_2 thin film as calculated from XPS measurements. An n value of 4 was chosen due to the number electrons required for the electro generation of OH^- on the substrate surface that facilitates formation of SiO_2 by subsequent hydrolysis.[31] The calculated mass for the Na-SiO_2 thin film electrodeposited for 10 s is ~9.3 µg. This value is two orders of magnitude smaller than the 139.1 – 222.6 µg calculated from the 500 – 800 nm thickness measured using SEM in Figure 7.9 (d) and the dimensions of the substrate surface deposited upon. The calculated masses for the SiO_2 electrodeposited thin films at 10 s and 1000 s are 0.66 µg and 62.93 µg, respectively.

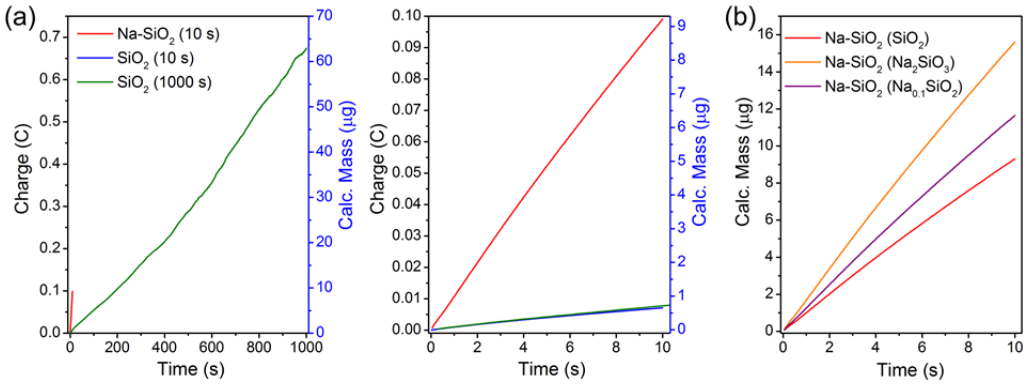


Figure 7.15. (a) Comparison of charge vs. time and calculated mass vs. time for the Na-SiO_2 and SiO_2 electrodeposited thin films. (b) Calculated mass vs. time for Na-SiO_2 electrodeposited thin films using constants for SiO_2, Na_2SiO_3 and $Na_{0.1}SiO_2$.

To determine the influence of V_m for various Na mole fractions in the Na-SiO_2 thin films, different mass values were recalculated assuming that the electrodeposited thin film formation is SiO_2, Na_2SiO_3 (a common sodium-silicate material) and the calculated $Na_{0.1}SiO_2$ material. In all cases, the Faradaic efficiency was again assumed to be 100%. The calculated V_m and ρ values used were 27.359

cm^3/mol and 2.65 g/cm^3, 46.589 cm^3/mol and 2.64 g/cm^3, 34.236 cm^3/mol and 2.65 g/cm^3, and as shown in Figure 7.15 (b), the masses range from 9.3 µg, 15.71 µg and 11.62 µg for the SiO_2, Na_2SiO_3 and $Na_{0.1}SiO_2$ respectively, an order of magnitude lower than the measured values. While the composition matches detailed spectroscopic examination, it is apparent that the $NaNO_3$ additive to the electrolyte affects not only on the composition but also the electrodeposited thickness. A change in the number of electrons exchanged per mole or the molar volume cannot account for the variation, nor does a rescaling due to a significant degree of internal porosity compared to the theoretical mass that describes a compact film formation – the SEM evidence shows a predominantly compact thin film formation with subsequent porous overgrowth. The current efficiency associated with SiO_2 formation can be written as

$$\eta = \frac{2nF}{mV_mQ} \qquad \textit{(Eq. 7.2)}$$

The current efficiencies for both durations of deposition are quite low and range from 0.06-0.09 (for 10 - 100 s) and the charge passed presumably gives rise to soluble reaction products with a considerable charge contribution to the reaction steps that leads to surface hydroxyl group coverage and subsequent hydrolysis (chemical as opposed to electrochemical formation).

The role of Na species in the inter-diffusion formation of V-O-Na-Si based materials was examined by depositing pure SiO_2 thin films from an electrodeposition electrolyte without the $NaNO_3$ additive. The resulting thin films were tuned to deposit a uniform coating on the surface by increasing the deposition time and VO was subsequently dip-coated onto the surface as before. The formation of the characteristic Raman vibrational modes of the V-O-Na-Si did not appear after thermal treatment, neither was evidence of orthorhombic V_2O_5 formation seen on V-

SiO_2 areas as shown in Figure 7.11 (b). As the formation of orthorhombic V_2O_5 is not found for the VO coated SiO_2 regions, it is assumed that the inter-diffusion processes occur between the Si, V and O species and form an amorphous, non-Raman active material. This information consolidates the findings from chapter 6, which demonstrated the formation of α-$NaVO_3$ crystalline phase with an amorphous medium. The α-$NaVO_3$ matrix has a characteristic Raman spectrum and XRD pattern which can be detected, but previous XPS measurements have shown large amounts of Si present on the surface accompanying the α-$NaVO_3$. This section provides definitive proof that the Si, V and O species also undergo inter-diffusion to form an amorphous glassy material, and that both Si and Na species are required to convert V_2O_5 to a highly visible transparent material as a film or as nanowires.

7.6 Templated Deposition of Na-SiO_2 and V-Na-SiO_2

Patterned substrates and thin films are used in a range of applications from electronic devices[33], optical coatings[34], sensors[35] and batteries.[36] In optics, different patterning techniques can alter the propagation of light through a range of materials, which can lead to improvements in applications such as photovoltaics where enhanced coupling, scattering, or absorption of light can be used to improve the efficiency of the devices.[34, 36-37]

Different methods are available for the deposition of patterned and structured substrates/thin films. Techniques for altering the surface chemistries in solution processed techniques, where alterations are made to the wettability of surfaces, can be employed for the preparation of patterns such as stripes, lines and single deposits.[38-41] Other solution processed methods are available that use these

advantageous liquid characteristics through the incorporation of nanoparticles and inclusions for promoting the use of a large variety of reproducible fabrication techniques.[42-43] These techniques can be applied to drop casting, thermal/sputter depositions and dip-/spin-coating, where substrates for a range applications, most notably SERS, can be manufactured.[42] The formation of interdigitated circuits and electrodes can also be of benefit for improving the efficiency of batteries and sensors by increasing the surface area available.[35, 44]

Here, custom 3D-printed templates were used in conjunction with electrodeposition processes to form templated Na-SiO_2 thin film structures. By coating the entire substrate with VO thin films and thermally treating the overall deposit, a patterned V-Na-SiO_2 thin film surrounded by V_2O_5 is formed, forming an in-plane heterojunction of conducting and non-conducting oxide with significantly different degrees of optical transparency. Macro-sized templates were prepared in order to demonstrate the concept whereby a combination of electrodeposition and inter-diffusion processes can form patterned transparent features of films and materials on substrates via contact transfer diffusion doping.

In Figure 7.16 (a), the electrodeposition current vs. time profile for a templated deposition is compared to the profile for a planar deposition as shown in section 7.4 and the associated total charge values for both electrodepositions is given. The templated deposition has a lower initial current with a difference in the profile shape noticeable between the two depositions between 0.3 s - 2 s. The decrease in total charge passed (from 0.10358 C to 0.02638 C) is attributed to a reduction in available surface area for the electrodeposition to occur.

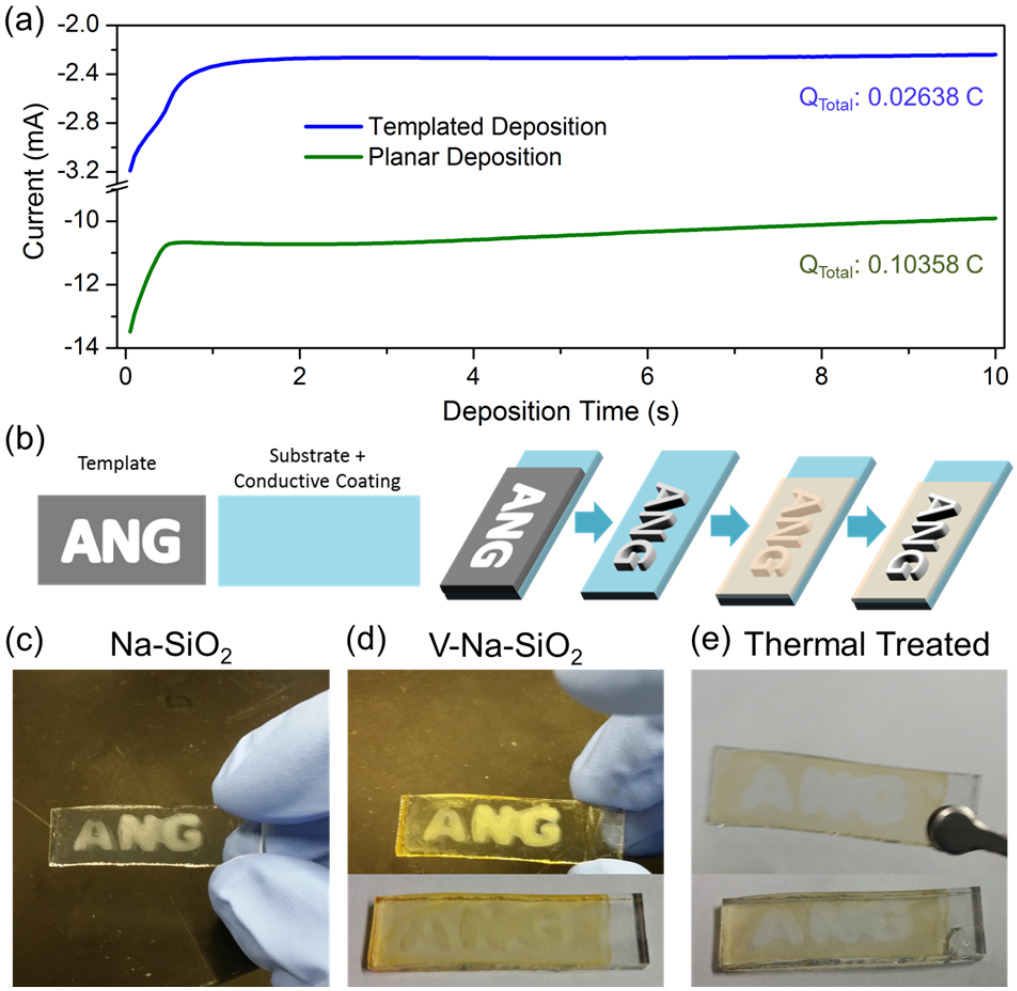


Figure 7.16. (a) Electrodeposited current vs. time profile for templated deposition on FTO at an applied potential of -2.5 V and the associated total charge values. (b) Schematic illustrating the method for producing templated samples. Optical images of (c) templated Na-SiO_2 on FTO, (d) templated Na-SiO_2 coated in VO prior to thermal treatment. (e) Optical images of (d) after thermal treatment with the V-Na-SiO_2 material surrounded by an orthorhombic V_2O_5 thin film.

A schematic of the procedure for depositing the templated Na-SiO_2 and V-Na-SiO_2 samples is shown in Figure 7.16 (b). A 3D printed template is placed in front of the bare FTO and the electrodeposition is performed resulting in a Na-SiO_2 deposit forming within the templated area which is then dip-coated with VO and thermally annealed. Optical images of the templated Na-SiO_2, as-deposited V-Na-SiO_2 and thermal treated V-Na-SiO_2 samples are shown in Figure 7.16 (c-e) respectively. The templated as-deposited Na-SiO_2 thin films appear to be optically

diffuse or bleached. A single VO thin film was dip-coated to the Na-SiO_2 at 2.5 mm/s and the resulting thin sample is shown in Figure 7.16 (d). The inset image shows how the VO conformally coats the surface and decreases the transmission of light through the templated region. After thermal treatment and subsequent inter-diffusion, the non-templated regions form orthorhombic V_2O_5 while the formation of V-Na-SiO_2 occurs on the templated region. The optical image and inset in Figure 7.16 (e) shows the resulting changes to the templated and non-templated thin films. The diffusive optical characteristics of the templated regions is restored after thermal treatment due to inter-diffusion processes and the formation of V-Na-SiO_2.

SEM images of an as-deposited Na-SiO_2 templated thin film is shown in Figure 7.17. The as-deposited sample shown in Figure 7.17 (a) has two distinct regions for allowing comparisons to be directly made: the top part (above the N) is uncoated templated Na-SiO_2 and FTO and the bottom part (below the N) is the same type of deposition but is coated with an as-deposited VO thin film. An overview SEM image of the written deposited is shown in Fig. 7.14(a) and the (i – iv) regions correspond to the images on the right hand side. After coating with VO, the surface of the FTO is conformally coated, Figure 7.17 (a) (ii). The SEM images show that the electrodeposited Na-SiO_2 film has a lower surface roughness to those previously studied in section 7.4. In comparison to the conformally VO coated FTO in Figure 7.17 (a) (iv) the VO coating on Na-SiO_2 is irregular and rough on the surface as shown in Figure 7.17 (a) (iii).

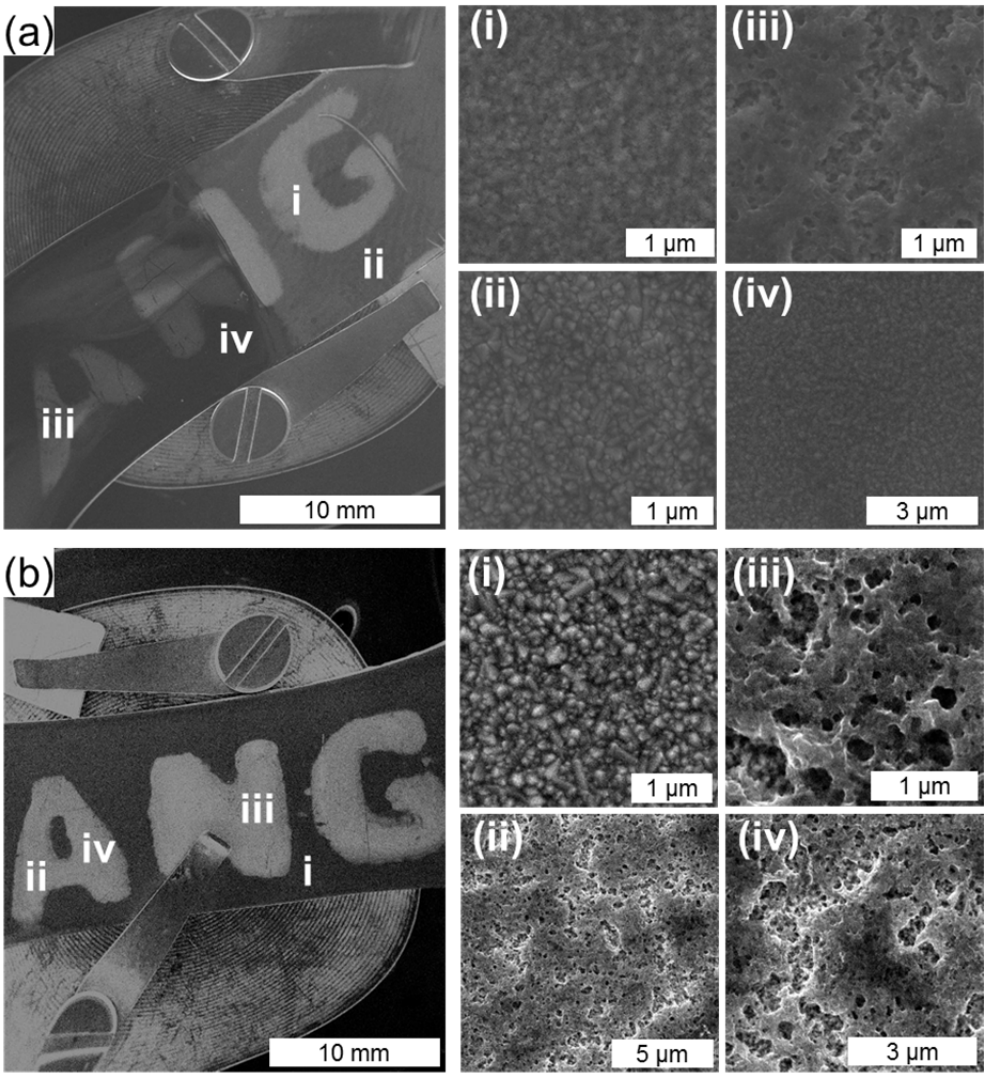


Figure 7.17. SEM images of templated Na-SiO_2 deposition on FTO. (a) as-deposited (i) VO thin film coating Na-SiO_2, (ii) VO thin film coating FTO, (iii) uncoated SiO_2 and (iv) uncoated FTO. (b) Thermally treated (i - iii) V-Na-SiO_2 and (iv) V_2O_5 coated FTO. The (i – iv) regions for (a) and (b) correspond to the images on the right hand side.

SEM images of a thermally treated fully coated V-Na-SiO_2 templated sample is shown in Figure 7.17 (b) with the different regions indicated with (i – iv) as previously done in Figure 7.17 (a). After thermal treatment, the V_2O_5 coated FTO retains a similar conformal coating discussed previously; however, the V-Na-SiO_2 regions, Figure 7.17 (b) (ii – iv), show the formation of a rough surface morphology. The rough morphology is due to non-conformal inter-diffusion processes with the

initially non-conformal VO on Na-SiO_2 coating. The orthorhombic V_2O_5 coating on the FTO retains its low surface roughness and conformal coating to the substrates granular surface.

The Raman scattering spectra acquired from various regions on a thermally treated V-Na-SiO_2 templated sample is shown in Figure 7.18. The FTO, Na-SiO_2 and V_2O_5 regions show the expected characteristic vibrational modes. The Raman scattering modes for the templated V-Na-SiO_2 regions do not show the presence of the characteristic vibrational modes for the V-O-Na-Si materials. The second V-Na-SiO_2 Raman spectrum shown in Figure 7.18 has evidence of a low intensity mode, 145 cm^{-1}, which can be attributed to the formation of orthorhombic V_2O_5.

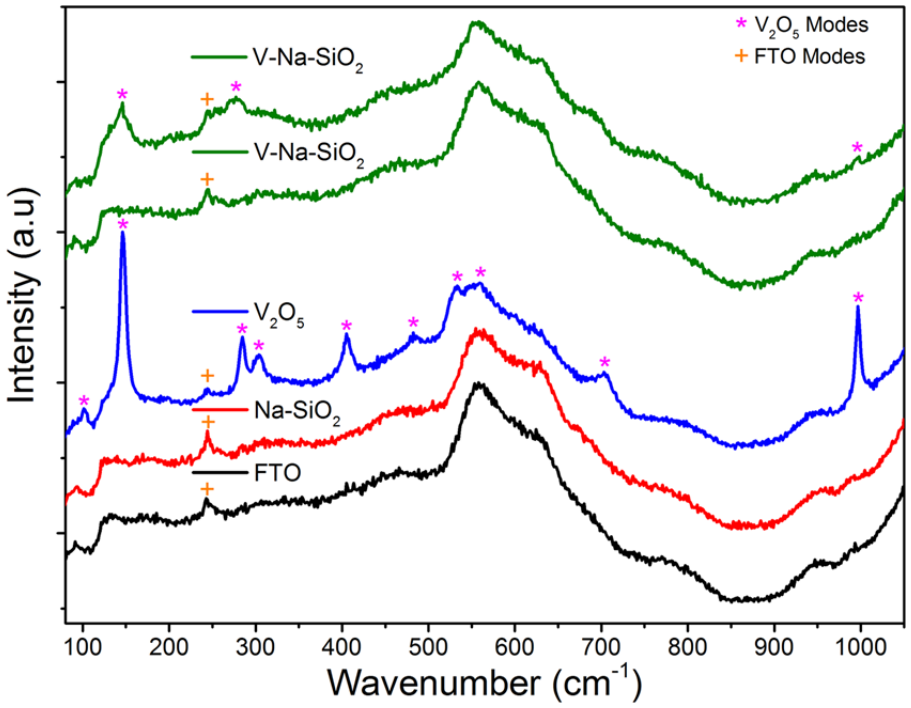


Figure 7.18. Raman scattering spectroscopy of different regions on a templated Na-SiO_2 and V-Na-SiO_2 thin film.

The lack of evidence for the formation of either large concentrations of orthorhombic V_2O_5 or the modes indicative of the presence of α-$NaVO_3$, to be

expected for full inter-diffusion, can be explained by examining the Na-SiO_2 patterning and non-conformal VO coating. The changes in packing of the surface from the electrodeposited templating may have affected the distribution of the Na species within the porous Na-SiO_2 thin film. As with the cases studied in sections 7.4, an increase in the required diffusion length of the Na species can limit the amount of Na available for the inter-diffusion formation of α-$NaVO_3$ at the surface of the deposit. Coupled with this effect, it was shown in section 7.5 that the inter-diffusion materials formed with Si, V and O are not Raman active. The non-conformal coating of the V_2O_5 on the surface of the Na-SiO_2 results in the formation of small concentrations of V_2O_5 on the Na-SiO_2 also, as evidenced in Figure 7.18. A rougher VO coating can also increase the required diffusion distance required for the inter-diffusion, thus regions of orthorhombic V_2O_5 formed with the glassy V-Si-O material, resulting in their low intensity in the Raman spectrum. The application of templated electrodeposited substrates incorporating inter-diffusion processes can be optimised for modifying functional materials and film that are useful in optical and electrical devices such as photovoltaics and photocatalytic materials.

7.7 Conclusions

Methods for the formation of V-O-Na-Si inter-diffused thin film materials on diffusion barrier layer substrates, such as FTO, were studied using a variety of techniques. A contact diffusion method was developed for the formation of nanowire mesh surfaces composed of α-$NaNO_3$ and β-$NaNO_3$ nanowires. The technique involves the facilitating of the inter-diffusion process through the contacting of a glass to the surface of a dip-coated VO thin film. Through the application of a constant pressure between the glass and FTO substrate during thermal annealing the

inter-diffusion process is enabled. The contacted glass contributes the donor Na and Si species for the formation of the V-O-Na-Si nanowires which grow in different concentrations and morphologies across the inter-diffusion formed region.

Both the initial VO thickness and annealing temperature/time affected the type of nanowire meshes formed, with red and blue shifting of the characteristic modes for the α-$NaNO_3$ and β-$NaNO_3$ materials due to stress and size effects. With a thicker initial VO thin film the formation of α-$NaNO_3$ and β-$NaNO_3$ nanowire regions is formed on the surface, with different regions corresponding to nanowires, shards and rods of both materials. HRTEM analysis of the nanowires formed on Si_3N_4 TEM grids show that the nanowires and other nanostructures may have core-shell characteristics and various crystalline structures and morphologies. This technique can potentially be expanded to other materials and diffusion products for the formation of complex nanowire mesh structures.

An electrodeposition technique was adapted for producing the V-O-Na-Si thin films on FTO in both planar and templated morphologies. In the electrodeposition of Na-SiO_2 and SiO_2 thin films, a cathodic potential was applied for the production of OH^- groups on the surface of the substrate which in turn facilitated the hydrolysis and polycondensation of an alkoxide TEOS solution which formed the solid thin film deposits. A large change in surface morphology and coverage was found between the electrodeposited Na-SiO_2 and SiO_2 thin films, where the SiO_2 thin films were electrodeposited from an electrolyte without a $NaNO_3$ additive. The $NaNO_3$ additive affected the thickness and morphology of the electrodeposited thin films by altering the Faradaic response of the electrolyte during electrodeposition.

The formation of the V-O-Na-Si inter-diffused material is affected by the applied electrodeposition voltage and the presence of Na species within the material. With the inclusion of Na species within the electrodeposited thin films, the formation of both α-$NaNO_3$ and β-$NaNO_3$ thin films is facilitated. The pure SiO_2 thin films electrodeposited without the $NaNO_3$ additive do not show evidence of the formation of α-$NaNO_3$ or β-$NaNO_3$ but also does not form pure orthorhombic V_2O_5 which shows that there is an inter-diffusion process between the dip-coated VO and SiO_2 which forms a non-Raman active material. Templated depositions of the V-O-Na-Si materials can be prepared through the use of custom 3D printed templates which allow for the deposition of intricate V_2O_5/V-Na-SiO_2 morphologies with well-defined interfaces and surface areas.

The work in this chapter highlights the range of technique available for the formation of V-O-Na-Si materials on diffusion layer substrates. The techniques and methods outlined in this chapter demonstrate that the direct deposition of VO materials onto glass substrates is not required for the inter-diffusion process to occur. Through increased research and development of the range of techniques possible for the application of inter-diffusion formation methods, a number of depositions can be devised and used for the formation and doping of materials of thin films from an underlying coating that facilitate diffusional movement of elemental or ionic species.

7.8 References

1. Jiang, J. *et al.* Recent Advances in Metal Oxide-based Electrode Architecture Design for Electrochemical Energy Storage. *Adv. Mater.* ***24***, 5166-5180 (2012).
2. Freund, H.-J.; Pacchioni, G. Oxide ultra-thin films on metals: new materials for the design of supported metal catalysts. *Chem. Soc. Rev.* ***37***, 2224-2242 (2008).
3. Chueh, C.-C.; Li, C.-Z.; Jen, A. K. Y. Recent progress and perspective in solution-processed Interfacial materials for efficient and stable polymer and organometal perovskite solar cells. *Energy Environ. Sci.* ***8***, 1160-1189 (2015).
4. Si Joon, K.; Seokhyun, Y.; Hyun Jae, K. Review of solution-processed oxide thin-film transistors. *Jpn. J. Appl. Phys.* ***53***, 02BA02 (2014).
5. Lee, D. H.; Chang, Y. J.; Herman, G. S.; Chang, C. H. A General Route to Printable High-Mobility Transparent Amorphous Oxide Semiconductors. *Adv. Mater.* ***19***, 843-847 (2007).
6. Lee, W.-J. *et al.* Large-Scale Precise Printing of Ultrathin Sol–Gel Oxide Dielectrics for Directly Patterned Solution-Processed Metal Oxide Transistor Arrays. *Adv. Mater.* ***27***, 5043-5048 (2015).
7. Jiang, Q. *et al.* Amorphous ZnAlSnO thin-film transistors by a combustion solution process for future displays. *Appl. Phys. Lett.* ***106***, 053503 (2015).
8. Thomas, S. R.; Pattanasattayavong, P.; Anthopoulos, T. D. Solution-processable metal oxide semiconductors for thin-film transistor applications. *Chem. Soc. Rev.* ***42***, 6910-6923 (2013).
9. Grill, A. *et al.* Progress in the development and understanding of advanced low k and ultralow k dielectrics for very large-scale integrated interconnects—State of the art. *Appl. Phys. Rev.* ***1***, 011306 (2014).
10. Dombrowski, K. F.; De Wolf, I.; Dietrich, B. Stress measurements using ultraviolet micro-Raman spectroscopy. *Appl. Phys. Lett.* ***75***, 2450 (1999).
11. Fukata, N. *et al.* Phonon confinement in silicon nanowires synthesized by laser ablation. *Physica B* ***376-377***, 864-867 (2006).
12. Viera, G.; Huet, S.; Boufendi, L. Crystal size and temperature measurements in nanostructured silicon using Raman spectroscopy. *J. Appl. Phys.* ***90***, 4175 (2001).
13. Pelletier, O. *et al.* A Detailed Study of the Synthesis of Aqueous Vanadium Pentoxide Nematic Gels. *Langmuir* ***16***, 5295-5303 (2000).
14. Evans, H. Metamunirite, a new anhydrous sodium metavanadate from San Miguel County, Colorado. *Mineral. Mag.* ***55***, 509-513 (1991).
15. Geaney, H. *et al.* High Density Growth of Indium seeded Silicon Nanowires in the Vapor phase of a High Boiling Point Solvent. *Chem. Mater.* ***24***, 2204-2210 (2012).
16. Seetharaman, S.; Bhat, H. L.; Narayanan, P. S. Raman spectroscopic studies on sodium metavanadate. *J. Raman Spectrosc.* ***14***, 401-405 (1983).
17. de Waal, D. Vibrational spectra of the two phases of $NaVO_3$ and the solid solution Na $(V_{0.66}P_{0.34})$ O_3. *Mater. Res. Bull.* ***26***, 893-900 (1991).
18. Lauhon, L. J.; Gudiksen, M. S.; Wang, D.; Lieber, C. M. Epitaxial core-shell and core-multishell nanowire heterostructures. *Nature* ***420***, 57-61 (2002).
19. Tang, J. *et al.* Solution-processed core-shell nanowires for efficient photovoltaic cells. *Nat. Nano* ***6***, 568-572 (2011).
20. Ramasamy, P.; Seo, D.-M.; Kim, S.-H.; Kim, J. Effects of TiO_2 shells on optical and thermal properties of silver nanowires. *J. Mater. Chem.* ***22***, 11651-11657 (2012).

21. Mehra, S.; Christoforo, M. G.; Peumans, P.; Salleo, A. Solution processed zinc oxide nanopyramid/silver nanowire transparent network films with highly tunable light scattering properties. *Nanoscale* ***5***, 4400-4403 (2013).
22. Lee, J.-Y.; Connor, S. T.; Cui, Y.; Peumans, P. Solution-Processed Metal Nanowire Mesh Transparent Electrodes. *Nano Lett.* ***8***, 689-692 (2008).
23. Chang, J. H. *et al.* A solution-processed molybdenum oxide treated silver nanowire network: a highly conductive transparent conducting electrode with superior mechanical and hole injection properties. *Nanoscale 7*, 4572-4579 (2015).
24. Ramgir, N. S.; Yang, Y.; Zacharias, M. Nanowire-Based Sensors. *Small* ***6***, 1705-1722 (2010).
25. O'Dwyer, C. *et al.* Bottom-up growth of fully transparent contact layers of indium tin oxide nanowires for light-emitting devices. *Nat. Nano.* ***4***, 239-244 (2009).
26. Moakes, G.; Bottomley, L. A.; Janata, J. Doping of Glass with Lithium Ion. *Anal. Chem. 77*, 1106-1110 (2005).
27. Walcarius, A.; Sibottier, E.; Etienne, M.; Ghanbaja, J. Electrochemically assisted self-assembly of mesoporous silica thin films. *Nat. Mater.* ***6***, 602-608 (2007).
28. Sayen, S.; Walcarius, A. Electro-assisted generation of functionalized silica films on gold. *Electrochem. Commun.* ***5***, 341-348 (2003).
29. Sibottier, E.; Sayen, S.; Gaboriaud, F.; Walcarius, A. Factors Affecting the Preparation and Properties of Electrodeposited Silica Thin Films Functionalized with Amine or Thiol Groups. *Langmuir* ***22***, 8366-8373 (2006).
30. Walcarius, A.; Sibottier, E. Electrochemically-Induced Deposition of Amine-Functionalized Silica Films on Gold Electrodes and Application to Cu(II) Detection in (Hydro)Alcoholic Medium. *Electroanal.* ***17***, 1716-1726 (2005).
31. Collinson, M. M.; Higgins, D. A.; Kommidi, R.; Campbell-Rance, D. Electrodeposited Silicate Films: Importance of Supporting Electrolyte. *Anal. Chem.* ***80***, 651-656 (2008).
32. Mezentzeff, P.; Lifshitz, Y.; Rabalais, J. W. Compositional and chemical modifications of V_2O_5 and $NaVO_3$ induced by N_{2+} bombardment. *Nucl. Instruments Methods in Phys. Res. Sec.* ***44***, 296-301 (1990).
33. Hoeppener, S.; Maoz, R.; Sagiv, J. Constructive Microlithography: Electrochemical Printing of Monolayer Template Patterns Extends Constructive Nanolithography to the Micrometer−Millimeter Dimension Range. *Nano Lett.* ***3***, 761-767 (2003).
34. Niu, W. *et al.* 3-Dimensional photonic crystal surface enhanced upconversion emission for improved near-infrared photoresponse. *Nanoscale* ***6***, 817-824 (2014).
35. Shirahata, N. *et al.* Reliable Monolayer-Template Patterning of SnO_2 Thin Films from Aqueous Solution and Their Hydrogen-Sensing Properties. *Adv. Func. Mater.* ***14***, 580-588 (2004).
36. Armstrong, E.; O'Dwyer, C. Artificial opal photonic crystals and inverse opal structures - fundamentals and applications from optics to energy storage. *J. Mater. Chem. C* ***3***, 6109-6143 (2015).
37. Liao, J. *et al.* Enhancement of the up-conversion luminescence of Yb_{3+}/Er_{3+} or Yb_{3+}/Tm_{3+} co-doped $NaYF_4$ nanoparticles by photonic crystals. *J. Mater. Chem. C* ***1***, 6541-6546 (2013).
38. Wang, Y.; McCarthy, T. J. Dip-coating deposition on chemically patterned surfaces: a mechanistic analysis and comparison with topographically patterned surfaces. *Langmuir* ***30***, 2419-2428 (2014).

39. Tian, D.; Song, Y.; Jiang, L. Patterning of controllable surface wettability for printing techniques. *Chem. Soc. Rev.* ***42***, 5184-5209 (2013).
40. Noguera-Marín, D.; Moraila-Martínez, C. L.; Cabrerizo-Vílchez, M. A.; Rodríguez-Valverde, M. A. Transition from Stripe-like Patterns to a Particulate Film Using Driven Evaporating Menisci. *Langmuir*, (2014).
41. Corrales, T. P. *et al.* Spontaneous Formation of Nanopatterns in Velocity-Dependent Dip-Coated Organic Films: From Dragonflies to Stripes. *ACS Nano*, (2014).
42. Amarandei, G.; O'Dwyer, C.; Arshak, A.; Corcoran, D. Fractal Patterning of Nanoparticles on Polymer Films and Their SERS Capabilities. *ACS Appl. Mater. Interfaces* ***5***, 8655-8662 (2013).
43. Higgins, A. M.; Jones, R. A. L. Anisotropic spinodal dewetting as a route to self-assembly of patterned surfaces. *Nature* ***404***, 476-478 (2000).
44. Pikul, J. H. *et al.* High-power lithium ion microbatteries from interdigitated three-dimensional bicontinuous nanoporous electrodes. *Nat. Commun.* ***4***, 1732 (2013).

Chapter 8

Conclusions

8.1 Introduction

In this chapter, a brief conclusion summarizing the results of Chapters 4 to 7 is presented. Possibilities for future work are also outlined in this chapter.

8.2 Dip-Coated V_2O_5 Thin Film Formation

A better understanding of solution processed thin film formation characteristics, specifically the role of alkoxide solution precursors, can lead to higher quality thin film coatings for academic and industrial applications. In Chapter 4, thin films of V_2O_5 were deposited onto transparent ITO coated glass substrates to investigate the formation characteristics of the alkoxide based solution precursor. The effects of PAD and changes in the solvent-alkoxide dilution on surface morphology, structure, optoelectronic properties and crystallinity for both bulk and uniform thin film depositions was studied through the application of drop-casting and dip-coating deposition techniques. Sub-100 nm thin films were prepared using a fast-rate dip-coating technique where low rms roughness and a defect free surface coupled with high optical transmission in the visible region were found for low concentration depositions. The application of PAD techniques was investigated with the aim of improving the thin film morphology and surface structure. The reduction in surface discontinuities was linked to the change from a granular surface structure with normal precursor solutions to a polycrystalline structure in precursors containing PEG. The work demonstrated that H_2O additive and alteration of viscosity and precursor composition by PAD were promising for the preparation of very uniform thin films during high rate dip-coating where the surface morphology and structure can be engineered through facile changes to the liquid solution.

8.3 Optimizing V_2O_5 Dip-Coated Thin Film Depositions

Surface thin film defects can be detrimental in the operation of devices such as TFTs and solar cells, where defects such as pinholes can cause short circuiting and therefore decrease the device efficiency, effectiveness and lifetime. In Chapter 5 the formation of pinhole defects in solution-processed thin films deposited from alkoxide based precursors was studied. Pinhole defects were examined for V_2O_5 thin films deposited on both Au and ITO where the different surface properties of the substrates affected the size and spatial dispersion of the pinholes. The average size of the pinholes formed on Au and ITO substrates was 25.1 nm and 111.5 nm respectively. While the average size of the pinholes are different, the percentage of the total surface area covered in pinholes was comparable at ~ 8% for both substrates. It was found that the formation of the pinhole defects on the surface of the thin films was due to spinodal instabilities and dewetting effects of the liquid precursor solution which occurs during the formation stage of the deposition. A nanofluid stage, where the alkoxide hydrolyses as inclusions within the liquid precursor after dip-coating, was attributed to the spinodal and dewetting effects. Through the application of PAD and changes in the alkoxide:IPA dilution ratios, as outlined in Chapter 4, the formation of pinhole defects can be halted and allows for the formation of highly uniform thin films deposited through solution processed methods in an ambient deposition atmosphere.

8.4 Transparent Thin Film Deposition via Substrate Diffusion Doping

In Chapter 6, a thermally induced inter-diffusion process between a glass substrate and solution processed VO thin film was analysed and demonstrated to

facilitate the formation of a V-O-Na-Si transparent mixed metal oxide material. The inter-diffusion allowed a fully transparent material to form with a surface composition of $V_{0.0352}O_{0.547}Si_{0.4078}Na_{0.01}$. The V-O-Na-Si thin film was composed of an α-$NaVO_3$ structure within a glassy matrix, which was determined through combination of Raman scattering spectroscopy and thin film XRD analysis. A high broadband transparency across the UV-NIR spectra range exceeding 90-97% absolute transmission coupled with a low surface roughness and small amount of defects was apparent for the V-O-Na-Si thin film. The formation of new materials and the possible inclusion of inter-diffusion processes for the doping of thin film device components can help decrease the reliance on high cost deposition and processing techniques currently employed for the preparation of modern technologies and devices.

8.5 Contact Transfer Doping of Solution Processed V-O-Na-Si Thin Films and Nanowires on Transparent Metal Oxide Substrates

In Chapter 7 methods for the deposition of V-O-Na-Si inter-diffused thin films materials on diffusion layer substrates was studied. Different techniques were examined for the deposition of the V-O-Na-Si thin films, ranging from a contact diffusion method and processes incorporating electrodeposited Na-SiO_2 and SiO_2 thin films. Nanowire mesh morphologies were formed on the surface of the diffusion layer substrates through the contacting of a glass to a dip-coated VO thin film after thermal annealing. Both the initial VO thin film thickness and annealing temperature/time affected the morphology and structure of the nanowire meshes which grew on the surface with different concentrations, morphologies and structures. The contact diffusion technique can potentially be adapted and expanded

to other material and diffusion products for the formation of complex nanowire mesh structures.

A second method for the deposition of V-O-Na-Si materials on the surface of diffusion barrier layers was developed which utilised an electrodeposition process to form Na-SiO_2 and SiO_2 thin film deposits onto the surface. Inter-diffusion processes were initiated through annealing of a dip-coated VO thin film. With the inclusion of Na species within the electrodeposited thin films, the formation of both α-$NaNO_3$ and β-$NaNO_3$ thin films is facilitated while pure SiO_2 thin films electrodeposited without the $NaNO_3$ additive do not show evidence of the formation of α-$NaNO_3$, β-$NaNO_3$ or pure orthorhombic V_2O_5 which shows that there is an inter-diffusion process between the dip-coated VO and SiO_2. Using the electrodeposited technique and custom 3D printed stencils, templated depositions of the V-O-Na-Si materials can be prepared allowing for the deposition of intricate V_2O_5/V-Na-SiO_2 morphologies.

8.6 Summary of Conclusions

- Solution processed thin films were coated onto a variety of substrates using a fast-rate dip-coating method.
- When deposited on the substrate, the thin film forms through hydrolysis and undergoes a transition to a nanofluid prior to solidification.
- Surface defects such as pinholes and hillocks can form on the surface of thin films due to spinodal and dewetting effects on the liquid film during the nanofluid development stage.

- PAD and precursor solution changes can be employed to alter the resultant thin film morphologies.
- Surface defect formation can be halted through the application of PAD and precursor : solvent changes by altering the formation characteristics during the nanofluid stage of development.
- The optical properties of V_2O_5 were related to the surface crystal structure, with decreases of the E_g evident from changes of a granular to polycrystalline surface structure.
- An innovative inter-diffusion technique was demonstrated for the formation of a transparent V-O-Na-Si metal oxide material.
- The V-O-Na-Si material is composed of α-$NaVO_3$ within a glassy matrix with a high broadband transparency of 90-97% across the UV-Vis-NIR spectrum.
- Deposition of V-O-Na-Si materials on diffusion layer substrates is possible through contact diffusion and VO coating of electrodeposited substrates
- Contact diffusion depositions form crystalline nanowire mesh surface morphologies on granular FTO substrates through the annealing of a dip-coated VO thin film contacted to glass.
- Thin films of Na-SiO_2 and SiO_2 can be deposited on FTO using electrodeposition and subsequent annealing of a dip-coated VO thin film can form V-O-Na-Si materials through inter-diffusion.

8.7 Future Work

8.7.1 Solution Processed Thin Film Device Applications

Solution processed thin film deposition methods are becoming a sought after and versatile technique for both academia and industry.[1-2] The use of solution processing is desirable due to the low cost and the scalability of the technique for depositing large surface area thin film coatings.[2] The application of solution processing developed in this thesis can be utilised in next-generation electronics and optoelectronics, such as TFTs and photovoltaics, particularly those that must be curved or flexible. A schematic of a typical TFT is shown in Figure 8.1, where solution processed methods can be used to deposit individual or multiple thin film components. The realisation of fully solution processed devices and materials with high electronic and optical quality depositions is projected to lower the cost to both the manufacturer and consumer, but can also provide alternative methods for iterative layer deposition and composition control at complex oxide interfaces, which is a pressing research area for enhancing field effect mobilities for fast switching transitors.[3]

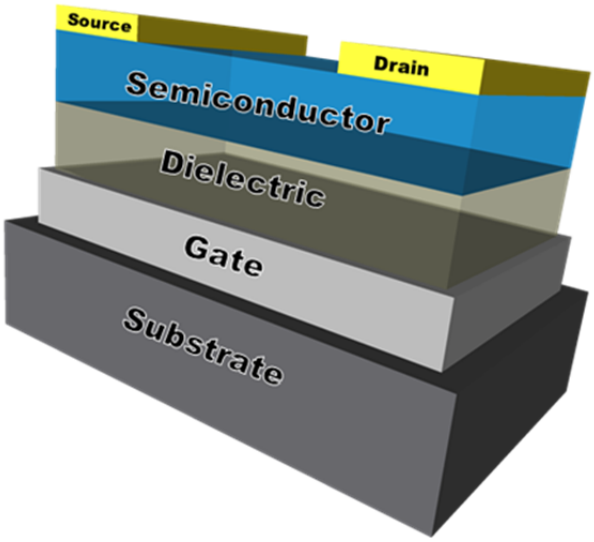


Figure 8.1. Schematic of a TFT Device with a back-gated morphology.

Through the application of the techniques examined in this project, from defect control methods and utilisation of inter-diffusion processes for material formation and doping, components for use in TFTs and other optoelectronic devices can be synthesised. In Figure 8.2, a schematic of a possible solution-processed TFT with the inclusion of an inter-diffusion material, such as a VO thin film, is shown. For optimum performance characteristics of the TFT, an ideal inter-diffusion material will have mobile species available for diffusing into the dielectric to a high-k material while also having available species for the preferential doping of the semiconducting channel layer. Additionally, alternative complex oxide interfaces for even higher mobility amorphous mixed metal oxide semiconductors may be possible by facilitating inter-diffusion of dopant metallic species whose s-orbital electron facilitate electronic conduction in an amorphous ionic mixed metal oxide material. The solution processed technique lends itself to this role due to the capability of the method for the preparation of thin films containing a range of different materials through facile solution alterations.[4]

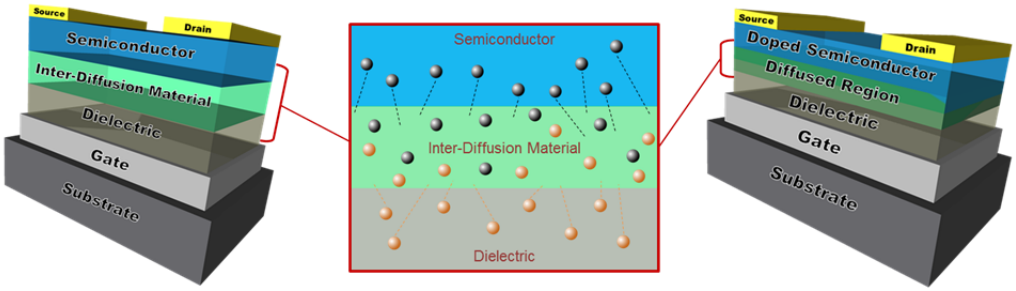


Figure 8.2. Schematic of a TFT deposited using solution processed methods and incorporating an inter-diffusion layer for the formation of a high-k dielectric and doping of the semiconductor through preferential material deposition.

The preparation of state-of-the-art devices, ranging from TFTs and TTFTs, to photovoltaics and optical coatings, can be deposited using the techniques outlined in this thesis in principle. The methods can be altered for the deposition of both pure

and mixed phase materials on a variety of substrates. Through careful choice of solution-processable oxide materials and dopants from appropriate soluble precursors, the deposition of dielectric and conductive oxides and interfaces may be possible in the near future.

8.7.2 Precursor Solution Nanofluid

Further research is possible on the formation characteristics of the alkoxide based precursor through analysis of the nanofluid deposition stage. This research can be performed by analysing the formation of the solid bulk-like material from droplets of the precursor solution. Research into nanofluid and other liquid systems where dewetting, hydrolysis, demixing or crystallization/solidification is affected, controlled, enhanced or retarded from inclusions such as nanoflakes or nanoparticles in the deposit is being reported in order to determine the forces that govern the formation of various patterns such as the coffee ring effect and other dewetting/spinodal depositions in a variety of liquid media.[5-9] This technique can be applied to determine particle size distributions within a solution through analysis of the resulting pattern, where larger particles converge on the centre of the coffee ring and smaller particles on the outer edge.[10]

The dewetting effects of alkoxide based solution precursors are of interest due to the dynamic nature of the material solidification and conversion to an oxide during hydrolysis. The alkoxide based solution hydrolyses to form the deposit during solvent evaporation. This hydrolysis stage is a dynamic effect that is not completed until the material is fully formed; the dewetting and spinodal effects are therefore halted during this stage due to the densification of the material as discussed in

Chapter 5. Figure 8.3 shows optical images of a vanadium alkoxide precursor solution droplet recorded at specific time intervals after deposition on a glass substrate. As the time increases after deposition, the hydrolysis of the alkoxide within the solvent can be viewed as they experience dynamic forces in the formation of the material, which also includes liquid volume loss from drying and changes in the molar volume of the material from the inorganic phase to the oxide. After the full hydrolysis and formation of the thin films the surface cracking due to dewetting is seen on the surface of the deposit.

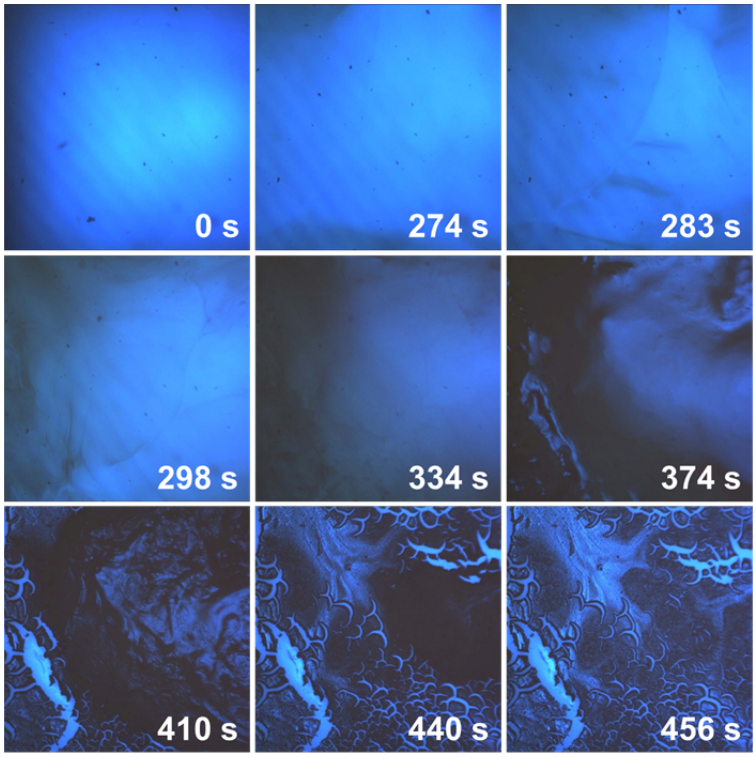


Figure 8.3. Optical images over time of a vanadium alkoxide precursor solution droplet. The effect of dewetting and spinodal decomposition on the surface formation is evident through the morphology of the resultant material. (The blue colour is due to an optical filter).

The final film microstructure (of the as-deposited film) depends on several factors such as the structure, size and dispersion of nanoscale inclusions within the films, how reactive such species are, and whether or not such inclusion influence

dewetting or solidification from known viscosity coating on short (fast) or long (slow) timescale, where volatility and evaporation rates as opposed to gravitational draining, may dominate the hydrolysis. In such cases, knowledge and measurement of shear and capillary forces are also important. Technologically, such fundamental investigations will be important especially for diffusion doping, where pinholes will form continuous defect through single or multi-layered coatings. Even if infilled with subsequent layers, pinholes define regions that are not doped with the species from the underlying substrate and so the factors that control coating of oxides is critical for layer on layer formation of important electronic oxide for device applications. For future work, this process can be further examined and related to known nanofluid processes. Through the analysis of dynamic alkoxide formation within a solvent, a method for altering the dewetting mechanisms can be developed and applied to solution processed techniques such as dip-/spin-coating in order to improve thin film depositions.

8.7.3 Advanced Electrodeposition Templating

The application of templating for the deposition of V-O-Na-Si templated thin films was examined in Chapter 7. This technique can be expanded to investigate the possibility of forming more intricate templated thin films and spatially patterned film formation. The inter-diffusion process can be further utilised for the deposition of interdigitated electrodes with different V_2O_5 and V-O-Na-Si regions, and serve as a model to be adapted to oxides of other materials and phases. These types of interdigitated surfaces can be used in applications such as supercapacitors, batteries and electronic devices.[11-13]

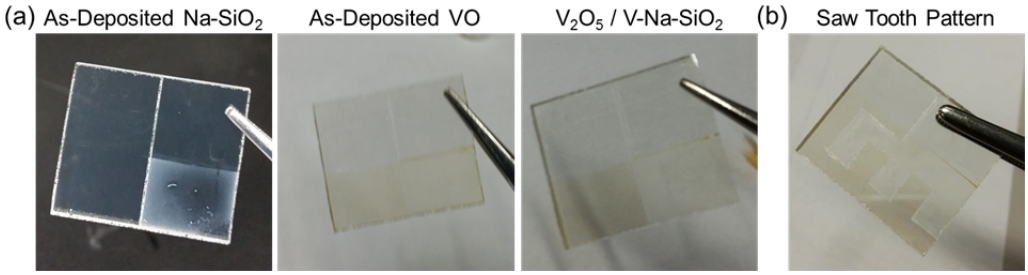


Figure 8.4. Optical images of interdigitated V_2O_5 / V-Na-SiO_2 samples on FTO with a (a) simple planar and (b) saw tooth pattern.

In Figure 8.4 optical images are shown of two interdigitated V_2O_5/V-Na-SiO_2 samples on FTO. The samples were prepared by creating conductive pathways on the surface of the FTO using 3D printed template covers, to allow for selective electrodeposition of the Na-SiO_2 material on the surface. The FTO was scored down to the glass substrate to separate out independent conductive regions on the substrate. For the first sample, a simple planar pattern was prepared and is shown in Figure 8.4 (a) while a more complex pattern which increases the interface area between the two materials by using a saw tooth design is shown in Figure 8.4 (b). The Na-SiO_2 material is electrodeposited onto one of the surfaces and the whole sample is then coated with a VO thin film with subsequent annealing forming the orthorhombic V_2O_5 and V-Na-SiO_2 materials on each section respectively. Thermal annealing may then facilitate diffusional doping and conversion to alternative or even alternating phases, or to infer a different conductivity, optical transparency or surface morphology on site-specific regions on transparent conductive materials. Through the use of advanced lithography techniques for the formation of large area interdigitated conductive electrodes, this method could be applied for the preparation of a new range of devices for applications in electronics and energy storage/generation using solution processed methods for the deposition of the active materials on the surface.

8.8 References

1. Choi, H. W.; Zhou, T.; Singh, M.; Jabbour, G. E. Recent developments and directions in printed nanomaterials. *Nanoscale **7***, 3338-3355 (2015).
2. Schneller, T.; Waser, R.; Kosec, M.; Payne, D., *Chemical Solution Deposition of Functional Oxide Thin Films*. 1st ed.; Springer: London, 2013; p 796.
3. Franklin, A. D. Nanomaterials in transistors: From high-performance to thin-film applications. *Science **349***, (2015).
4. Park, S. *et al.* In-Depth Studies on Rapid Photochemical Activation of Various Sol–Gel Metal Oxide Films for Flexible Transparent Electronics. *Adv. Func. Mater.* ***25***, 2807-2815 (2015).
5. Alizadeh Pahlavan, A.; Cueto-Felgueroso, L.; McKinley, G. H.; Juanes, R. Thin Films in Partial Wetting: Internal Selection of Contact-Line Dynamics. *Phys. Rev. Lett.* ***115***, 034502 (2015).
6. Anyfantakis, M.; Baigl, D. Dynamic photocontrol of the coffee-ring effect with optically tunable particle stickiness. *Angew. Chem. Int. Ed. Engl.* ***53***, 14077-14081 (2014).
7. Anyfantakis, M. *et al.* Modulation of the Coffee-Ring Effect in Particle/Surfactant Mixtures: the Importance of Particle–Interface Interactions. *Langmuir **31***, 4113-4120 (2015).
8. Luo, Y. *et al.* Nematic Order Drives Macroscopic Patterns of Graphene Oxide in Drying Drops. *Langmuir **30***, 14631-14637 (2014).
9. Amarandei, G. *et al.* Effect of Au Nanoparticle Spatial Distribution on the Stability of Thin Polymer Films. *Langmuir **29***, 6706-6714 (2013).
10. Hendarto, E.; Gianchandani, Y. B. Size sorting of floating spheres based on Marangoni forces in evaporating droplets. *J. Micromech. Microeng.* ***23***, 075016 (2013).
11. Pikul, J. H. *et al.* High-power lithium ion microbatteries from interdigitated three-dimensional bicontinuous nanoporous electrodes. *Nat. Commun.* ***4***, 1732 (2013).
12. Nystrom, G. *et al.* Self-assembled three-dimensional and compressible interdigitated thin-film supercapacitors and batteries. *Nat. Commun.* ***6***, 7259 (2015).
13. Zhao, C. *et al.* Three dimensional (3D) printed electrodes for interdigitated supercapacitors. *Electrochem. Commun.* ***41***, 20-23 (2014).